THE DC NANOGRID HOUSE: CONVERTING A RESIDENTIAL BUILDING FROM AC TO DC POWER TO IMPROVE ENERGY EFFICIENCY

by

Jonathan Ore

A Dissertation

Submitted to the Faculty of Purdue University

In Partial Fulfillment of the Requirements for the degree of

Doctor of Philosophy

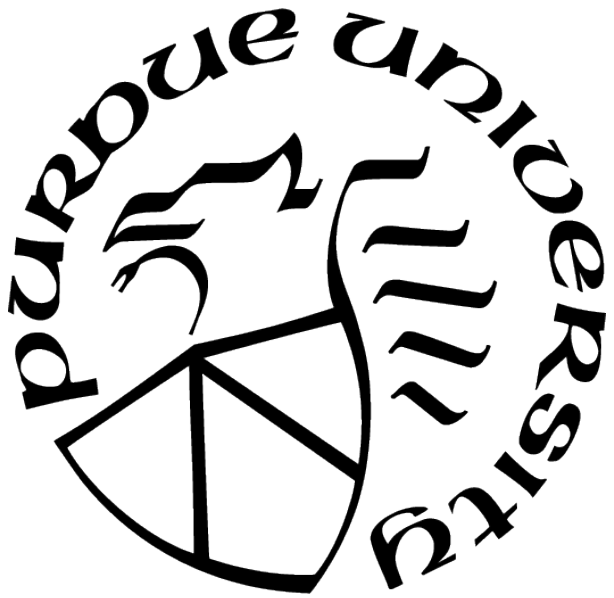

School of Mechanical Engineering

West Lafayette, Indiana

May 2021

THE PURDUE UNIVERSITY GRADUATE SCHOOL
STATEMENT OF COMMITTEE APPROVAL

Dr. Eckhard Groll, Chair

School of Mechanical Engineering

Dr. Peter Meckl

School of Mechanical Engineering

Dr. Stanislaw Żak

School of Electrical Engineering

Dr. Scott Sudhoff

School of Electrical Engineering

Approved by:

Nicole Key

To my wife, Michelle Lane Ore, and her ceaseless support of all my aspirations.

ACKNOWLEDGMENTS

The author would like to convey his sincere gratitude and humbleness to his research advisor and department head, Professor Eckhard Groll, for the opportunity to join the thermal science research area, and to take on such a fascinating and interdisciplinary project. Without his wisdom, patience, and reassurance, this project would surely occupy a shadow of its present achievements. In addition, the author is profoundly grateful for the support of each of the committee members, their unique individual characteristics, and invaluable mentorship throughout the program: Professor Peter Meckl for his kindness and encouragement to pursue the degree, Professor Stanislaw Żak for his wise counsel and excellent sense of humor, and Professor Scott Sudhoff for his insights and assistance into all things electrical. The author has also benefited from the tutelage of practical and relevant coursework under each member of the committee, which has proven to be indispensable throughout the pursuit of this doctoral degree.

Special thanks is also extended to the Center for High Performance Buildings (CHPB) and its member constituents, without whom this research could not have been a success. The author is thankful for the organization as a whole, the individual Project Management Subcommittee (PMS) members over each phase of the project, and the many years of financial endorsement, which have sustained both the material development of the lab space and the research appointments to this project. The author is also thankful for the National Renewable Energy Laboratory (NREL) for their collaboration with this research, and their financial assistance during the terminal year of the author's graduate studies. Furthermore, the author is grateful for the very many collaborators and vendors who have collectively backed this project and donated equipment to further its progress.

The author is particularly appreciative of his friends and colleagues throughout this endeavor, who have each provided exceptional support and made the academic journey survivable. Though there are far too numerous individuals to recognize, the author would like to highlight a few of special importance: Horacio Flores, Lucien Culot, Phil Teague, Dr. André Moraes, Dr. Riley Barta, Dr. Davide Ziviani, Dr. Orkan Kurtulus, Parveen Dhillon, Vatsal Shah, Fatih Meral, Andreas Hoess, Leon Brendel, Ife Ibitayo, and the entire Groll

family. In addition to these, the author also thanks Julayne Moser for her overwhelming encouragement to join the PhD program at the start, and for the incredible flexibility extended while beginning the academic journey remotely.

Lastly, the author would like to extend his heartfelt thankfulness to the members of his family, particularly to his parents Daniel and Grace Ore, and to his wife, Michelle Ore. Of most crucial acknowledgement is reserved for Michelle, who has stood by the author's side as a loving and compassionate wife throughout nearly a decade of marriage. Across multiple cancer diagnoses, long-distance separations, challenging work-life balances, and the never ending pursuit of academic degrees, Michelle has remained a concrete pillar of encouragement through thick and thin, never faltering in her unceasing selflessness. Even while pursuing her own doctoral degree and working full-time as an oncological registered nurse, she has dedicated a tremendous allotment of her own personal time to making this research effort achievable. It is unequivocally her encouragement and support that enabled the completion of this document, and for this the author is forever indebted to her.

TABLE OF CONTENTS

LIST OF TABLES

LIST OF FIGURES

LIST OF SYMBOLS

A	Volume Area	(m^3)
C_d	Coefficient of discharge	$(-)$
d	Conductor spacing	(m)
f	Signal frequency	(Hz)
gpm	Gallons per minute	$(gallons/min)$
h	Specific enthalpy	(kJ/kg)
I_x	Rotational inertia at node x	$(kg \cdot m^2)$
k_0	Fixed constant	$(-)$
k_d	Normalized air density factor	$(-)$
$\dot{m}$	Mass flow	(kg/s)
p	Pressure	(kPa)
P	Real Power	(kW)
$p.f.$	Power factor	$(-)$
Q	Reactive power	$(kVAR)$
$\dot{Q}$	Cooling capacity	(W)
r	Conductor radius	(m)
S	Apparent power	(kVA)
$SHGC$	Solar Heat Gain Coefficient	$(-)$
T	Temperature	$(^{\circ}C)$
T	Time period	(s)
$U - Factor$	Heat loss metric	$(W/(m^2 \cdot K))$
v_x	Voltage magnitude at node x	(V)
V	Voltage	(V)
V_c	Disruptive voltage	(V)
$\dot{V}$	Volumetric air flow	(m^3/s)

VT	Visible Transmittance	$(\%)$
$\dot{W}$	Power	W
Y	Expansion Factor	$(-)$
Z_{xy}	Impedance between nodes x and y	(Ω)
θ_x	Signal Frequency at node x	(Hz)
ρ	Density	(kg/m^3)
τ_x	Time-relaxation parameter at node x	(s)
ω	Specific humidity	$(-)$

ABBREVIATIONS

air	Air
app	Appliance
Avg	Average
controlled	Controlled quantity
delivered	Net capacity
evap	Evaporator
indoor	Indoor
Line	Conductor Line
measured	Measured quantity
nozzle	Nozzle box
ppm	Parts per million
total	Total
water	Water
1, 2, 3, …	State points

NOMENCLATURE

AC	Alternating Current
ACRE	Agronomy Center for Research and Education
ADC	Analog to Digital Converters
AHU	Air Handling Unit
AMQP	Advanced Message Queuing Protocol
ASCE	American Society of Civil Engineers
AWG	American Wire Gauge
BES	Bulk Electric System
BJT	Bipolar Junction Transistor
CAES	Compressed Air Energy Storage
CAN	Controller Area Network
CDD	Cooling Degree Day
CEC	California Energy Commission
CHP	Combined Heat and Power
CIGRÉ	International Council on Large Electric Systems
COP	Coefficient of Performance
CS	Chip Select
CT	Current Transformer
DAC	Digital to Analog Converters
DAQ	Data Acquisition
DC	Direct Current
DER	Distributed Energy Resource
DOE	U.S. Department of Energy
ECC	Energy Control Center
ECI	Enhanced Conversion Innovation
EER	Energy Efficiency Ratio
EIA	Energy Information Administration
EMC	Electromagnetic Compatibility

EMCB	Energy Management Circuit Breakers
EMI	Electromagnetic Interference
EMS	Energy Management System
EPRI	Electric Power Research Institute
ERCOT	Electric Reliability Council of Texas
ESD	Electrostatic Discharge
EV	Electric Vehicle
FEMA	Federal Emergency Management Agency
FERC	Federal Energy Regulatory Commission
HDD	Heating Degree Day
HEV	Hybrid Electric Vehicle
HIL	Hardware in the Loop
HPC	Historical Preservation Committee
HVAC	Heating, Ventilation, and Air Conditioning
HVDC	High Voltage Direct Current
I/O	Input/Output
I2C	Inter-Integrated-Circuit
IC	Integrated Circuit
IEA	International Energy Agency
IEC	International Electrotechnical Commission
IEEE	Institute of Electrical and Electronics Engineers
IoT	Internet of Things
IT	Information Technology
K&T	Knob and Tube Wiring
KPI	Key Performance Indicator
LBNL	Lincoln Berkeley National Laboratory
LED	Light-Emitting Diode
LVDC	Low Voltage Direct Current
MIPS	Modular Inverter Power System

MISO	Master-In Slave-Out
MOM	Message-Oriented Middleware
MOSI	Master-Out Slave-In
MPPT	Maximum Power Point Tracking
MQTT	MQ Telemetry Transport protocol
MSRP	Manufacturer's Suggested Retail Price
MTU	Measuring Transmitting Units
NERC	North American Electric Reliability Corporation
NI	National Instruments
NOAA	National Oceanic and Atmospheric Administration
NREL	National Renewable Energy Laboratory
NRHP	National Register of Historic Places
OEM	Original Equipment Manufacturer
OS	Operating System
OSI	Open System Interconnection
PaaS	Platform as a Service
PFC	Power Factor Correction
PID	Proportional-Integral-Derivative
PIR	Passive Infrared
PoC	Proof of Concept
PoE	Power over Ethernet
PV	Photovoltaic
QA	Quality Assurance
QoS	Quality of Service
REST	Representational State Transfer
RMS	Root Mean Square
ROW	Right-Of-Way
RTOS	Real-Time Operating System
SBC	Single-Board Computer

SCADA	Supervisory Control and Data Acquisition
SCL	Serial Clock
SDA	Serial Data
SDS	Sustainability Development Scenario
SEER	Seasonal Energy Efficiency Ratio
SEIA	Solar Energy Industry Associates
SGHC	Solar Heat Gain Coefficient
SoC	System on a Chip
SPI	Serial Peripheral Interface
SPOF	Single Point of Failure
SSR	Solid State Relay
STOMP	Simple Text Oriented Messaging Protocol
TED	The Energy Detective
TXV	Thermostatic Expansion Valve
UART	Universal Asynchronous Receiver Transmitter
UI	User Interface
UPS	Uninterruptible Power Supply
USD	US Dollars
VAC	AC Voltage
VDC	DC Voltage
VLAN	Virtual Local Area Network
VM	Virtual Machine
VSD	Variable Speed Drive
VT	Visual Transmittance
WH	Water Heater
WWSIS	Western Wind and Solar Integration Study

ABSTRACT

The modern U.S. power grid is susceptible to a variety of vulnerabilities, ranging from aging infrastructure, increasing demand, and unprecedented interactions (e.g., distributed energy resources (DERs) generating energy back to the grid, etc.). In addition, the rapid growth of new technologies such as the Internet of Things (IoT) affords promising new capabilities, but also accompanies a simultaneous risk of cybersecurity deficiencies. Coupled with an electrical network referred to as one of the most complex systems of all time, and an overall *D+* rating from the American Society of Civil Engineers (ASCE), these caveats necessitate revaluation of the electrical grid for future sustainability. Several solutions have been proposed, which can operate in varying levels of coordination. A microgrid topology provides a means of enhancing the power grid, but does not fundamentally solve a critical issue surrounding energy consumption at the endpoint of use. This results from the necessary conversion of Alternating Current (AC) power to Direct Current (DC) power in the vast majority of devices and appliances, which leads to a loss in usable energy. This situation is further exacerbated when considering energy production from renewable resources, which naturally output DC power. To transport this energy to the point of application, an initial conversion from DC to AC is necessary (resulting in loss), followed by another conversion back to DC from AC (resulting in loss).

Tackling these losses requires a much finer level of resolution, namely that at the component level. If the network one level below the microgrid, i.e. the nanogrid, operated completely on DC power, these losses could be significantly reduced or nearly eliminated altogether. This network can be composed of appliances and equipment within a single building, coupled with an energy storage device and localized DERs to produce power when feasible. In addition, a grid-tie to the outside AC network can be utilized when necessary to power devices, or satisfy storage needs.

This research demonstrates the novel implementation of a DC nanogrid within a residential setting known as *The DC Nanogrid House*, encompassing a complete household conversion from AC to DC power. The DC House functions as a veritable living laboratory, housing three graduate students living and working normally in the home. Within

the house, a nanogrid design is developed in partnership with renewable energy generation, and controlled through an Energy Management System (EMS). The EMS developed in this project manages energy distribution throughout the house and the bi-directional inverter tied to the outside power grid. Alongside the nanogrid, household appliances possessing a significant yearly energy consumption are retrofitted to accept DC inputs. These modified appliances are tested in a laboratory setting under baseline conditions, and compared against AC equivalent original equipment manufacturer (OEM) models for power and performance analysis. Finally, the retrofitted devices are then installed in the DC Nanogrid House and operated under normal living conditions for continued evaluation.

To complement the DC nanogrid, a comprehensive sensing network of IoT devices are deployed to provide room-by-room fidelity of building metrics, including proximity, air quality, temperature and humidity, illuminance, and many others. The IoT system employs Power over Ethernet (PoE) technology operating directly on DC voltages, enabling simultaneous communication and energy supply within the nanogrid. Using the aggregation of data collected from this network, machine learning models are constructed to identify additional energy saving opportunities, enhance overall building comfort, and support the safety of all occupants.

1. INTRODUCTION

1.1 Background

At the end of August in 1831, a young chemist by the name of Michael Faraday was experimenting with electromagnetic induction in an attempt to induce electricity into a coil of wire using a permanent magnet. Until this point in time, electricity could only feasibly be generated by one of two methods: (a) static electricity through mechanical means (e.g., friction), or (b) chemical reaction through a voltaic battery. It was already known that electrical current in a coil was capable of magnetizing a piece of iron, but the reverse process was still unknown. That is, until 1831, when Faraday attempted to slide a magnet through a piece of tube wrapped in a copper wire, and discovered that the connected galvanometer, a machine capable of measuring electrical current, registered a twitch in its needle. For the first time in history, a generator of electrical power had been created [1].

Faraday, along with many other scientists of the day (Ampere, Henry, Maxwell, Joule, Kelvin, and many others) expanded on this groundbreaking discovery, and laid the foundation for the modern understanding of electrical power generation and energy conversion into other forms. These insights produced a number of critical inventions, including the electric generator and motor, phonograph, telephone, light bulb, and more [2]. Most significantly, these developments established the principles for all modern power transmission and distribution, which is integrated into nearly every aspect of modern society. Since its discovery, electricity is typically classified into one of two forms: Direct Current (DC) or Alternating Current (AC), which would lead to a fierce debate over which form should function as the basis for transmission. Though AC ultimately prevailed as the victor, an understanding of the power grid (referred to henceforth as the *macrogrid*) elements and its historical evolution are critical to addressing modern obstacles hindering its performance, and reevaluating AC versus DC in terms of the primary means of energy transmission and distribution.

1.2 Power Transmission and Distribution

As electrical energy consumption has increased, so too has the challenge of generating, storing, transmitting, and distributing it across wide geographical regions. In the specific aspect of transmission, the power dissipated in a conductor is proportional to the square of the resistance of that conductor. Since conduction length itself is proportional to its resistance, transmission over long distances faced a distinct obstacle, which both AC and DC designs initially struggled to contend with. According to Ohm's Law described in Equation 1.1, the same amount of power can be transmitted by varying the respective current and voltage.

$$P = I \times V \tag{1.1}$$

Returning to the previous dilemma of power lost in the conductor, power lost is also proportional to the amount of current flowing through it. As a result, maintaining the same level of power transmission by modulating a higher voltage and simultaneously reducing the current would thus minimize the Ohmic power losses in a conductor. This solution is an essential element in modern power distribution (both AC and DC), which uses transmission lines with voltages typically scaled in kilovolts, although megavolt ranges have been employed as well. An illustration of the common transmission line voltages and their usage within the U.S. is depicted in Figure 1.1.

Alongside transmission, power distribution serves the critical role of interfacing between the transmission systems and individual consumers. Within the U.S. (and more generally North America), the transmission and distribution network has developed in a geospatial fashion, leading to connections and interconnections based on geography rather than strictly energy and power transportation needs. Consequently, the last century of expansion has established the overarching macrogrid, representing an immensely complex system made up of a huge network of interconnected transmission lines, generators, loads, and power electronics. The grid, formally maintained under the North American Electric Reliability Corporation (NERC), is divided into two major and three minor interconnections arranged spatially across the continent [4]. A graphic illustrating each interconnection entity is de-

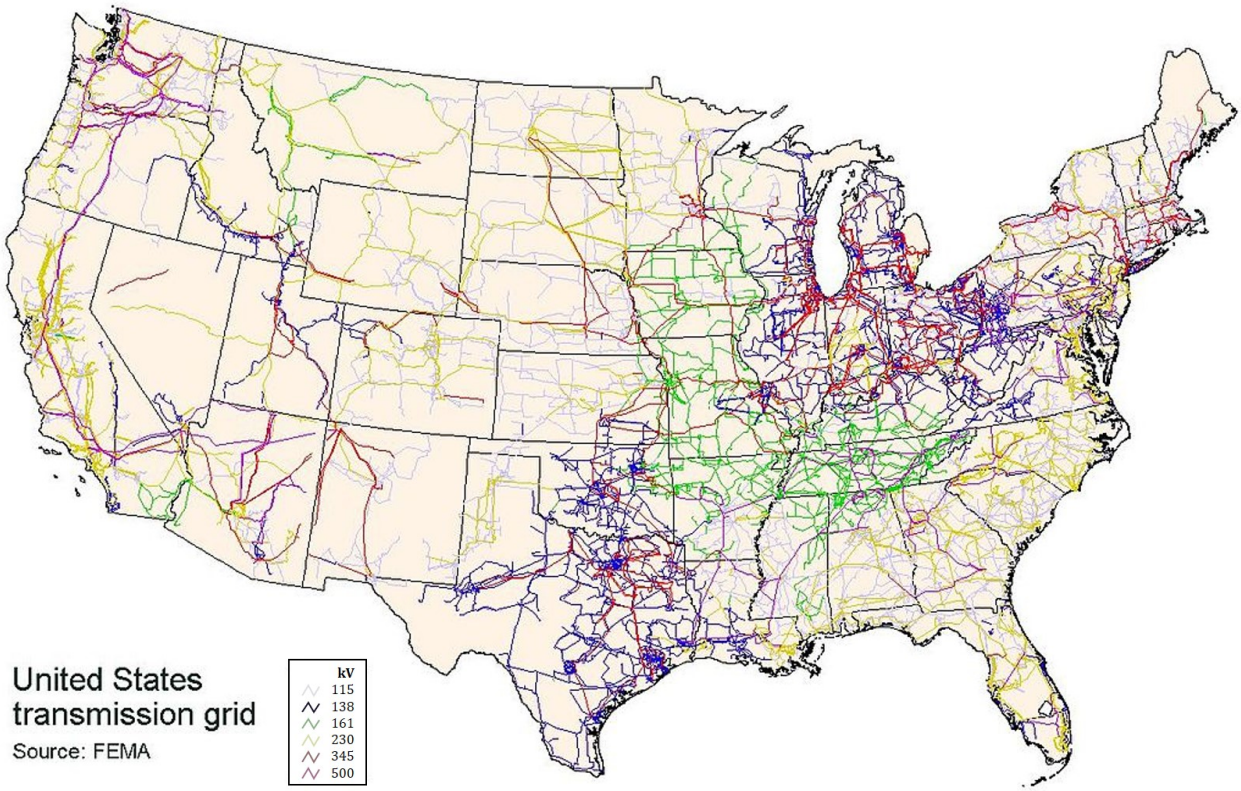

Figure 1.1. U.S. transmission line voltage arrangement[3].

tailed in Figure 1.2, and a second image representing the corresponding relative electricity consumption of each of the three major interconnections is shown in Figure 1.3. The grid design, originating in the 1880's based on Nikola Tesla's alternating current (AC) architecture, was largely motivated by cost, materials, and technology which suited high-voltage AC transmission, and low-voltage AC consumption. Individual power generators merged over time to coalesce in a mesh of generation capability, resulting in the power grid's *bottom-up* approach of construction. These historical design motivators hold significant influence over the present-day grid's stability, reliability, control, and scalability [5].

1.2.1 The War of Currents

At the end of the 19th century, engineering heavyweights Nikola Tesla, George Westinghouse, and Thomas Edison battled over what would become the foundation for present-day

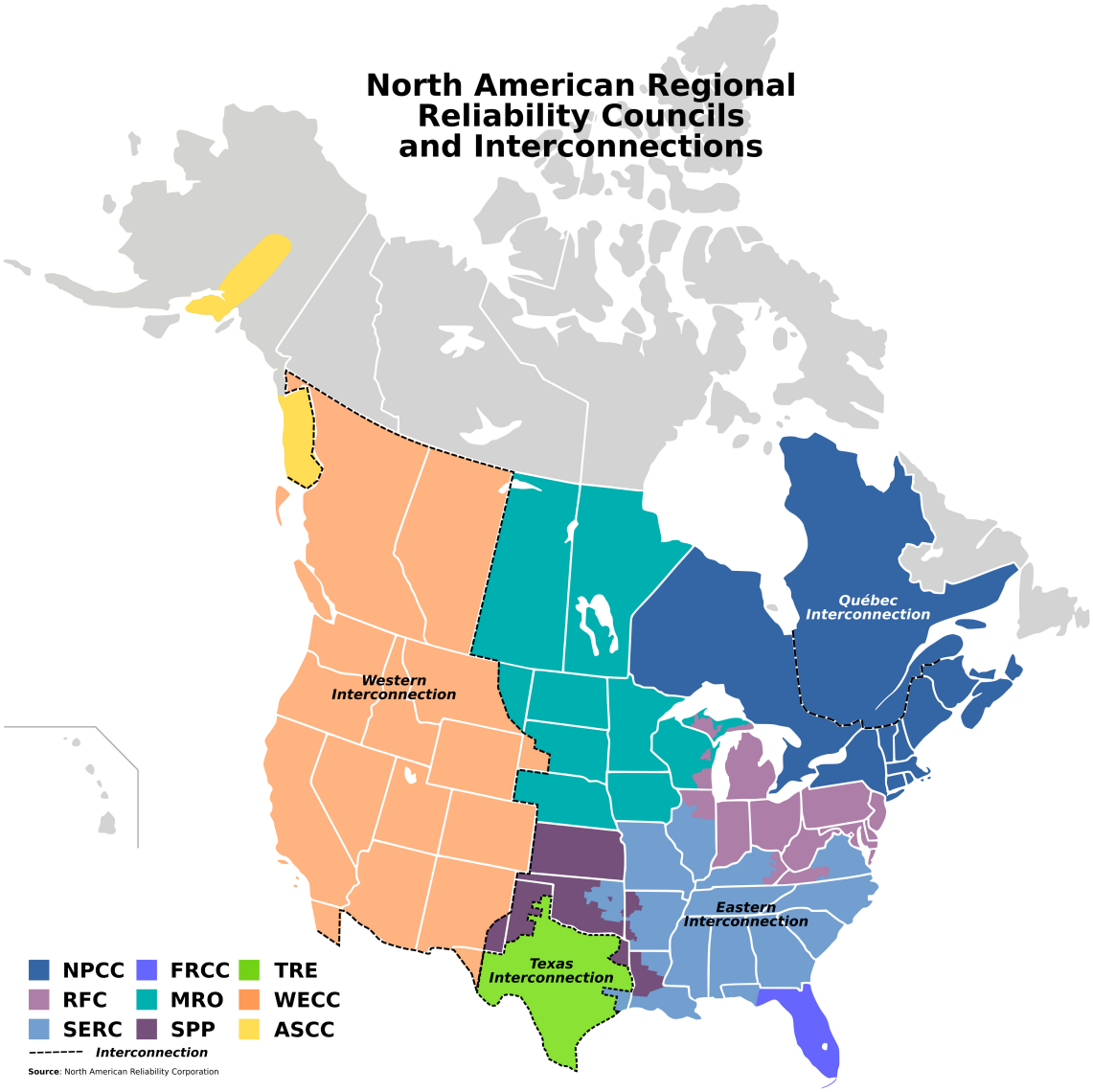

Figure 1.2. NERC interconnections map [4].

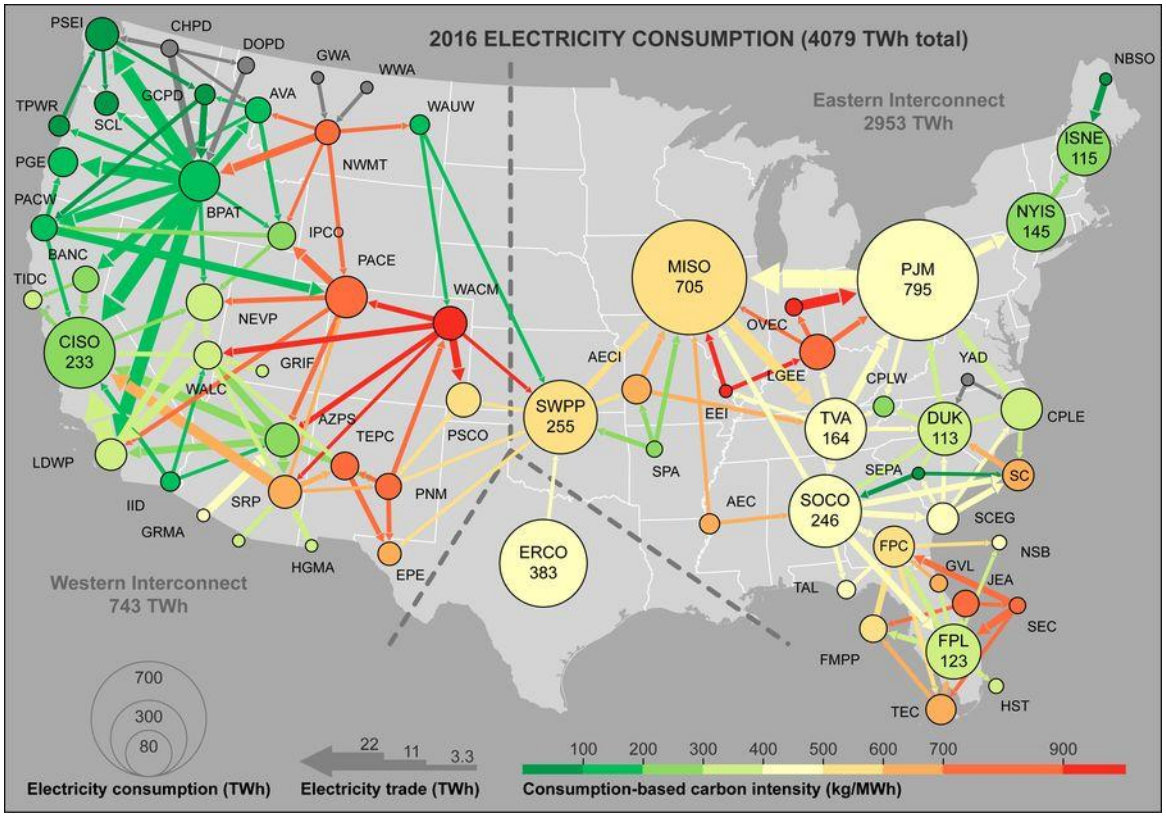

Figure 1.3. Electrical consumption and interconnection strength by region within the U.S. in 2016 [6].

electricity distribution. Edison supported a Direct Current (DC) driven framework, while Tesla and Westinghouse argued for an AC architecture, and ultimately, AC reigned victorious. A major asset of AC at the time was its ability to be converted to higher and lower voltages, giving it a critical advantage over DC. The battle was clinched during the Chicago World's Fair in 1893, during which Westinghouse successfully underbid Edison to supply power to the Fair. This demonstration of AC power consequently resulted in the Niagara Falls Power Company awarding Westinghouse a major contract to construct a power generator for the falls. In 1896, the Niagara Falls hydroelectric power plant was successfully launched, providing power to the Buffalo, NY area. Following this success, General Electric shifted its investment into AC power, securing AC as the predominant means of power distribution in the U.S. [7].

1.2.2 Historical Failures of the Macrogrid

The development of the AC-based power grid has been rife with challenges since its inception. The advent of increasing energy demands within the U.S. has resulted in escalated strain on the power grid, bringing into question its capacity to support future needs. The spatial layout of the power grid in North America makes it especially vulnerable to cascading failures, with the Federal Energy Regulatory Commission (FERC) explaining that a loss of merely nine key substations out of 55,000 could result in a country-wide blackout [8]. Modern technological innovations have fostered a greater dependency on the grid, coupling it with nearly every aspect of contemporary society. Unfortunately, the grid has not experienced a parallel rate of growth alongside technology, with some estimates reporting on the order of trillions of dollars necessary for repairs and upgrades to return to a nominal performance level. In 2017, the American Society of Civil Engineers (ASCE) scored the U.S. energy system with a grade of a $D+$ for overall reliability, citing aging distribution lines, capacity bottlenecks, and climate impacts as leading factors in their evaluation [9].

A critical component affecting the grid's stability is the geographical coupling of the underlying networks. A multitude of studies, including those of popular social networks, reveal that systems with random structures are far more stable than their systematic counterparts, owing in part to the reduced presence of critical nodes [10]. Similar to a Jenga tower, the removal of crucial elements in an ordered structure can quickly result in catastrophic failure, as witnessed in the 2003 northeast power outage which affected over 50 million people across the U.S. and Canada [11]. Many studies have been conducted surrounding failures of the grid; the most prominent blackouts in North America have been collected and listed in Table 1.1.

Most recently, the winter storm event in the southern U.S. resulted in power lost for millions of customers, affecting those as far north as Oregon and as far south as Mexico [12]. In Texas alone, approximately five million customers were without power for several days, resulting in financial costs estimated at over $200 billion US Dollars (USD), the highest impact in Texas' history [13]. In addition to the economic implications, a multitude of other entities were affected, including public infrastructure, food and water availability, en-

vironmental resources, and healthcare provisions. Many factors contributed to the resulting region's grid outage, including failures of nearly every type of power generation resource, overwhelming demand at a historical record high, and limited interconnection throughput available with other geographical regions to provide stabilizing measures (as reflected in Figure 1.3) [14]. Though renewable energy was frequently reprimanded for its role in the overall system's failures, five times more natural gas power capacity was taken offline from the storm as compared to wind power [15]. Regardless of the individual energy source, the Electric Reliability Council of Texas (ERCOT), which functions as the main agency behind the Texas Interconnection, claimed that the grid was mere seconds from a complete system blackout, which would have led to far more devastating outcomes [16]. Concerns over the electrical grid's resiliency in the face of natural disasters and other failures are a critical motivator for consideration of future designs.

Table 1.1. Significant blackout events in the U.S. [11], [12], [17]–[19]

Date	Location	Customers Impacted	Primary Cause
13-Mar-1989	Quebec, New York	5,828,000	Solar flare
14-Dec-2002	Western U.S.	2,100,000	Winter Storm
14-Aug-2003	Eastern U.S., Canada	55,000,000	Cascading failure
18-Sep-2003	Southeastern U.S.	2,590,000	Hurricane Isabel
23-Oct-2005	Southeastern U.S.	3,200,000	Hurricane Wilma
27-Aug-2011	Eastern U.S.	5,000,000	Hurricane Irene
10-Sep-2017	Southern U.S.	7,600,000	Hurricane Irma
01-Nov-2019	Northeastern U.S., Canada	2,000,000	Major Storm
10-Feb-2021	Texas, Southern U.S., Mexico	5,000,000	Winter Storm

1.3 Power Electronic Converter Efficiencies

Further challenging the state of the electrical grid is the needs of consumer and industrial equipment at the grid endpoints. Most modern devices and appliances require direct current (DC) input, stipulating the distributed AC voltage to be transformed. This includes cell phones, TVs, computers, printers, game consoles, light-emitting diode (LED) lighting, electric vehicles (EVs), and many others, all of which require DC power [20]. Each voltage

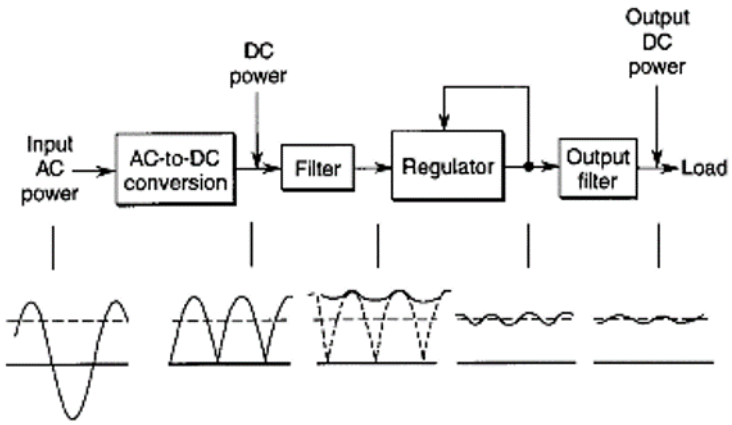

Figure 1.4. Generalized power rectification process from AC to DC [22].

transformation from AC to DC, or DC to AC, results in energy loss due to conversion and inversion inefficiencies. The general process of AC to DC conversion, known as rectification, is reflected in Figure 1.4. In the beginning of the conversion process, the AC input voltage is typically stepped down from 120 VAC or 240 VAC (in the case of residential use) to a significantly lower level, such as 12 VAC, through the use of a transformer. The next stage involves a rectification process in which the negative phase of the AC waveform is removed, as illustrated in the second graphic in Figure 1.4. This can be accomplished using a bridge rectifier configuration, which typically arranges four diodes working together to electrically reshape the input AC signal. Once the signal has been rectified, the next step includes power factor correction (PFC) circuits, and filtering to ensure the sinusoidal waveform resolves into a more constant signal. This filter can be constructed from a combination of inductor, capacitor, and resistance circuit elements working together to smoothen the signal. The final stages include regulation, to maintain the DC signal at a desired voltage level, and additional filters to remove ripples, noise, and other non-DC characteristics of the voltage signal. Other topologies for AC to DC power conversion exist, including Active Front End (AFE), single phase systems, and various specialized configurations [21].

The power electronics utilized during the conversion process are each associated with some loss of usable energy through heat loss, parasitic elements, skin effect, eddy currents, and many others [23]. Surveys of the field indicate that approximately 30% of all AC power

generated is processed through power electronics and conversion, resulting in between 15% to 40% of energy lost due to dissipative effects [24], [25]. A recent experimental study by the Lawrence Berkeley National Laboratory (LBNL) confirmed these findings, estimating the average power lost in consumer-grade power supplies to be approximately 32% [26]. With the demand for energy generation increasing, a proportional rise in the amount of energy passed through power electronics is also expected, thereby resulting in further power lost due to these inefficiencies.

The losses associated with various AC and DC conversion and inversion processes is a prime mover for the topic of modern electrical topologies, but continues to persist as a significant source of contention surrounding the explicit degree of benefit. Challenges to clarifying and simplifying these issues include the vast array of converter technologies and types, continuing developments from novel research efforts, manufacturer specifications versus actual performance, and the use-cases and scenarios under which findings are reported. As an example, [27] reported peak load conversion efficiencies from high voltage AC to low voltage DC of approximately 95%. However, several common household devices studied by [28] described conversion efficiencies for devices such as a laptop, LED, phone charger, fan, and 1 kW inverter as low as 87%, 49%, 71%, 60%, and 65%, respectively. Similarly, [29] indicated typical AC to DC conversion efficiencies of common appliances, including refrigerators, computers, televisions, lighting, and water heaters of approximately 87%, 80%, 85%, 82%, and 88%, respectively. As a result, although peak conversion efficiency studies frequently record values in the high 90^{th} percentile range for all manner of conversion combinations (i.e., AC-AC, AC-DC, DC-AC, DC-DC), ordinary devices usually fall significantly short of this range.

An intrinsic aspect of the various conversion mechanisms and their impact on the overall electrical architecture's benefit encompasses the specific location where the conversion needs to occur. Under an AC scheme, energy generated from renewable sources is fundamentally DC in nature (even from wind turbines) but must be converted to AC to be distributed within the home. Multiple studies have indicated potential improvements through the use of a DC-based architecture ranging from 14% [30], 18% [31], and even as high as 30% [32] over AC-equivalent counterparts. These achievements are made feasible in part by

(a) isolating primary AC-DC conversion processes to one central, highly specialized and efficient module, (b) instituting multiple high-efficiency DC-DC conversion devices driven by a principal DC bus, and (c) eliminating multiple conversion losses from energy generation and storage elements. In the case of an AC-based micro/nanogrid, the potential utilization path for wind power generation could include as many as six or more conversion stages (e.g., AC-DC (from generation), DC-AC (for distribution), AC-DC (for initial storage), DC-AC (for subsequent distribution), AC-DC (for appliance rectification stages), and DC-AC (for motor consumption)).

1.4 Macrogrid Stability Challenges

1.4.1 Reactive Power

A particular challenge of AC systems involves contending with two different types of power — real power, P, which holds the capability to do useful work, and reactive power, Q, which occurs when electrical current and voltage phasors are out phase. A description of phasors and their use in electrical calculations is detailed further in Appendix A. Reactive power occurs due to the presence of inductors and capacitors, which dissipate no power but still impact the circuit current and voltage. Devices can be considered to either consume or produce reactive power depending on the phase relationship between the current and voltage. If current lags behind the voltage in a device, then it consumes reactive power, but if current leads the voltage instead, the device produces reactive power. Reactive power and real power are related by the apparent power, S, which is given by Equation 1.2 [33].

$$S = \sqrt{P^2 + Q^2} \quad (VA) \tag{1.2}$$

Certain devices, such as a transformer, require magnetic fields in order to operate, and thus need to consume reactive power from a circuit. As a result, it is necessary for AC transmission lines to provide a specific amount of both real and reactive power to operate correctly. However, an overabundance of reactive power decreases the amount of real power

available, and therefore the ability to perform useful work. This relationship is described by the power factor, given in Equation 1.3 [33].

$$p.f. = \frac{P}{|S|} \quad (-) \tag{1.3}$$

In order to improve power distribution efficiency, the power factor needs to be increased, resulting in the general need for PFC devices in AC systems. This leads to a greater dependency on power electronics, increased cost, and more opportunities for component failures.

1.4.2 System Dynamics

Across the power grid, electrical loads absorb both real and reactive power, and generators inject them at individual nodes. Loads and generators each maintain unique response dynamics, and result in power fluctuations in time. The process in which these elements interact is known as *swing equations*, which describe the power balance and dynamics of the grid over a sufficiently long time period. The primary relationship is given in Equation 1.4,

$$I_x\ddot{\theta_x} + \tau_x\dot{\theta_x} + j\tau_x^{(v)}\dot{v_x} = P_x + jQ_x - V_x \sum_{(x,y)} \frac{V_x^* - V_y^*}{Z_{xy}^*} \tag{1.4}$$

where the indices x and y indicate two individual nodes in the power system, I_x is the rotational inertia of a turbine generator, θ_x is the frequency of the AC signal being transmitted, and Z_{xy} represents the complex impedance of the electrical line between the nodes [34]. The asterisks over the voltage and impedance on the right side of Equation 1.4 denote complex conjugation. During steady state operation, Equation 1.4 balances to zero, but realistically these dynamics are constantly changing, with generators and their turbines acting like coupled oscillators [5]. As a result, the grid can be perceived as a three-dimensional contour of potential energy, which behaves as a function of both the phase and voltage at a given location.

In this three-dimensional energy space, local minima are sought between given nodes to identify areas of stability. Near these locations, small perturbations in voltage or phase can be realized without destabilizing the system. However, as load conditions or other

environmental aspects change, so do the contours, and the system can become unstable. In these situations, the potential energy will seek a path to zero, known as *voltage collapse*, in which the system is no longer able to sustain adequate voltage levels [35]. This problem significantly escalates in complexity when transitioning from the aforementioned two-node base case to the present day electrical grid, involving tens of thousands of nodes, each with unique dynamics and responses.

1.4.3 Renewable Energy Integration

Introducing renewable energy generators to the electrical grid institutes an entirely new type of interaction — that of probabilistic dynamics. Unlike providers such as coal or nuclear power plants, renewable resources such as wind and solar include an uncertainty in their generation and cannot be controlled to meet demand in the same manner as their fixed provider counterparts. Grid stability is often analyzed using an $(N-1)$ criterion, which indicates whether Equation 1.4 possesses a steady-state solution when a critical generator or transmission line is removed from the set of N power grid elements [34]. Since renewable energy provides an inconsistent supply over time, the $(N-1)$ criterion becomes an inadequate measure to consider stability, and alternative methods are necessary.

Instead of employing deterministic analysis, integrated renewable energy generators can be visualized using a probabilistic distribution to identify possible deviations from a current forecasted state. In this way, a feasibility region of acceptable states and an infeasibility region of states resulting in failures can be obtained. The stability analysis can then be expressed as locating the most probable fluctuations within the power grid nodes that shift the current state from a feasibility region to an infeasibility region, which can be achieved by finding the maximum of the error surrounding the feasibility region. These problems are highly complex in nature and represent a significant challenge in the field of AC research [5], [36].

An important topic surrounding the discussion of renewable energy integration is its general impact to the grid stability. The current U.S. Administration has criticized the usefulness of these resources, with the FERC chairman suggesting that coal power plants are

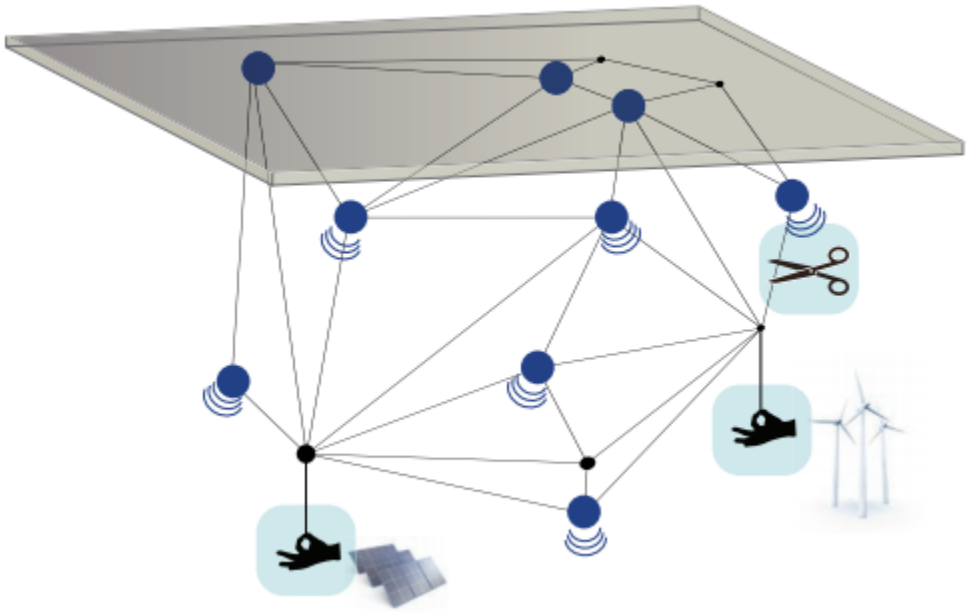

Figure 1.5. Renewable energy stability interactions visualization [39].

underappreciated and deficient in funding with respect to their value towards baseload power generation [37]. A study conducted by the U.S. Department of Energy (DOE) suggested that power outages should be mitigated by approving policy measures to extend coal and other baseload power plant operation lifetimes, and expediting approval for permitting new projects. In addition, the report also suggested that the addition of increasing amounts of solar photovoltaics and other renewable resources without mass or mechanical inertia may pose a threat to reliability and expected electrical behavior [38].

Providing a different perspective on this topic, research conducted by the National Renewable Energy Laboratory (NREL) entitled, "Western Wind and Solar Integration Study", determined that these types of renewable energy sources required no radical shift in stability procedures. The report surveyed transient stability in the Western Interconnection (see Figure 1.2) and concluded that adequate frequency response during disturbances was maintained. A useful graphic representing the interaction of renewable resources and other grid elements is depicted in Figure 1.5. As illustrated in the diagram, individual blue masses indicate generators supplying power to the system loads, which are represented by tension in the lines connecting the generators. Solar and wind generators are shown by the hand-icons,

demonstrating the ability to provide power but no other control. The scissor-icon portrays a disturbance-event (e.g., loss of a generator, loss of a transmission line, etc.), which will result in the individual generators and lines being dislodged, representing instability. If the disturbance-event is too significant (e.g., too many transmission lines are lost), the system will become uncontrollable and cannot return to a stable state.

Additional study is necessary to better understand the dynamics of renewable resources, but early findings suggest that grid stability is not inherently hindered by their presence [39]. In addition, battery systems interspersed throughout the grid offer mitigation to any stability offset produced by renewable resources. Deployment of such storage devices in a variety of locations (utilities, commercial facilities, residential homes, etc.) affords a buffer, and can be used to enhance overall grid stability [40]. Although the cost of storage technologies remains a present challenge, technologies are consistently improving and the presence of battery storage offers another layer of resiliency against power distribution interruptions.

1.5 Macrogrid Transmission and Distribution Losses

Beyond conversion losses at endpoints, a nontrivial amount of energy is also lost during power transmission and distribution. Considering the worst case in which renewable energy generators produce nominal DC power, end-to-end losses include the initial DC to AC conversion, AC transmission losses, individual distribution losses, and finally rectification losses at the point of use in AC to DC conversion. According to the U.S. Energy Information Administration (EIA), approximately 5% of electricity transmitted is lost due to grid inefficiencies [41]. Between 2000 and 2015, more than 172 quads of electricity were transferred through the U.S. electrical grid, equivalent to approximately 50 trillion kWh. From distribution losses alone, the amount of energy dissipated would be sufficient to power 306,000 houses over the same time period, assuming an average consumption of 914 kWh per house per month [42]. As revealed by the EIA in Figure 1.6, more than half (65%) of all energy processed through the electric power sector is lost during the generation, transmission, distribution, and unplanned consumption from power plants [43].

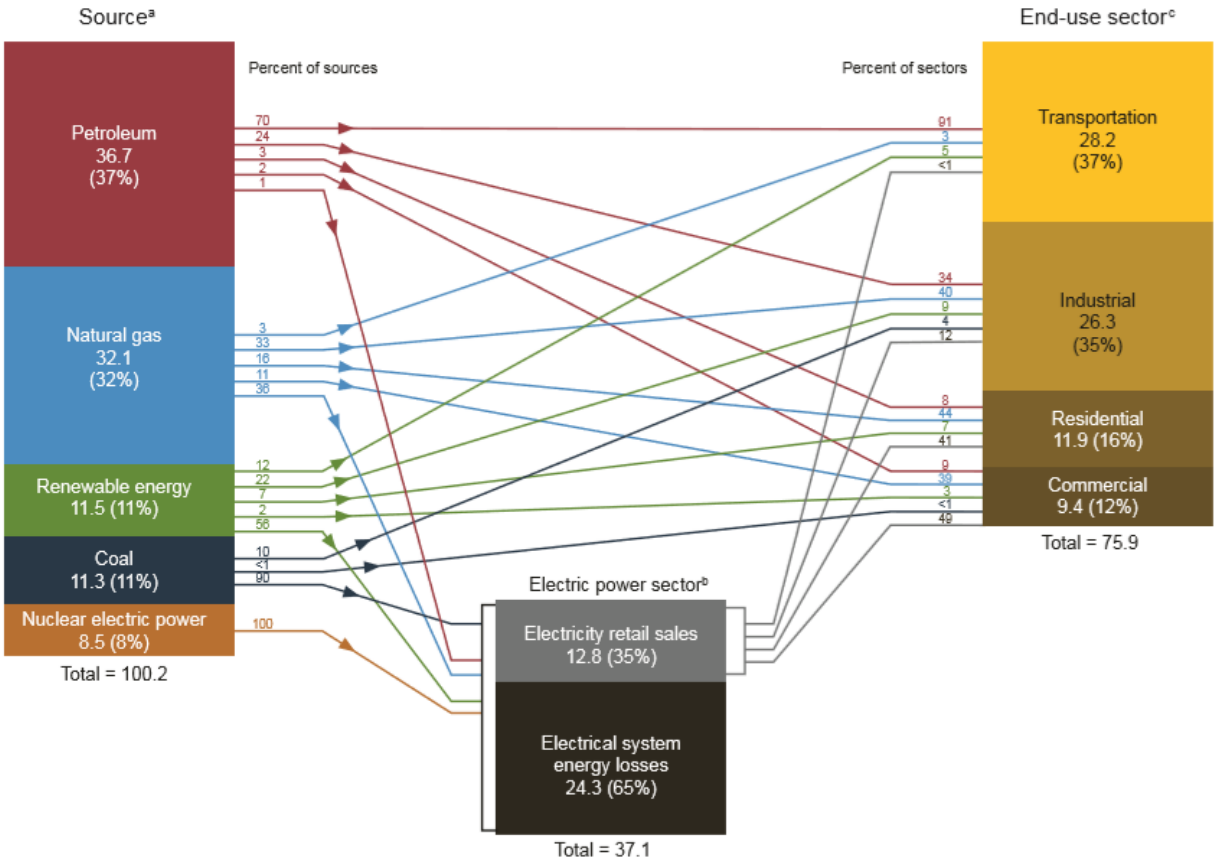

Figure 1.6. U.S. electrical energy consumption by source and end-use sector in 2019 [43].

An individual study in New York identified utility transmission losses of up to 5.8% and distribution losses of up to 4.6%; however, these values were obtained *after* utilities had enacted a variety of improvements to reduce losses in the distribution system. Ultimately, AC transmission and distribution schemes must contend with an array of loss-mechanisms, including but not limited to: (1) ohmic losses, (2) corona losses, and (3) other distribution losses [44].

Owing in part to technological developments and reduced electrical complexity of DC-DC conversions, DC-driven systems afford opportunities to provide significantly higher conversion efficiencies. One significant advantage of DC current is the avoidance of the *skin effect*, which is an electrical phenomenon plaguing AC signals [45]. In a conductor carrying an AC voltage, the distribution of the current tends to accumulate closer to the surface, thus giving the effect its name. As a consequence of this increased current density, the asso-

ciated resistance of the conductor experiences a corresponding increase, leading to energy losses. The presence of the skin effect is proportional to the frequency of the electric signal, and therefore does not occur with DC voltages. Another detractor of AC is known as the *proximity effect*. Similar to the skin effect, this phenomenon is proportional to the signal's frequency, and increases a conductor's resistance in a proportional fashion. The proximity effect occurs in part due to the generation of magnetic fields by an AC signal, which introduces eddy currents in conductors close by. AC transmission lines must be specially designed to mitigate these losses, but cannot wholly avoid them [46]–[48]. Finally, *corona discharge* is another type of power loss associated with transmission lines, and can be observed by an ultraviolet emission, visible purple aura, and often an audible noise. This effect is the result of ionization of the surrounding air due to high voltages, and results in energy loss through a conductor.

To illustrate the comparison between AC and DC losses under these effects, a short example assessing the corona discharge is demonstrated. Using Peek's formula in Equation 1.5, the power loss associated with the corona effect is proportional to the signal's frequency,

$$P = \frac{k_0}{k_d}(f + 25)\sqrt{\frac{r}{d}}(V - V_c)^2 \times 10^{-5} \quad (W/m) \tag{1.5}$$

where k_0 is a fixed constant, k_d is the normalized air density factor, f is the voltage signal frequency, r is the conductor radius, d is the conductor spacing, V is the root-mean-square (RMS) phase-neutral voltage, and V_c is the RMS disruptive voltage in each phase [49]. Using sample values to demonstrate with a 60 Hz, 442 kV AC signal and a 3.5 cm conductor radius, the corona effect calculates to a 3.3% loss in energy transmission. Since the value of f in Equation 1.5 for a DC signal is zero, the corresponding corona loss will be lower as compared to an AC signal with the same environmental conditions. Performing the calculation again for a DC signal with the same voltage and conductor parameters but with a pure, 0 Hz DC signal yields a reduction in power loss of approximately 240% [50].

1.6 The Second War of Currents - Generating a Case for DC

1.6.1 High Voltage DC Transmission

Similar to high voltage AC, high voltage DC (HVDC) can also be employed to transfer power over long distances while minimizing electrical losses. The first HVDC transmission lines were constructed in the 1950's in both Sweden and Italy, with dozens of new projects presently under construction or completed [51]. In 2019, China demonstrated an HVDC link using a 1,100 kV transmission line over a span of 3,300 km, supporting a maximum bulk power transfer of 12 GW [52]. With installations such as these, both intra- and intercontinental networks are feasible, with a host of benefits in contrast to AC equivalent systems.

Costs for transmission lines are associated with a variety of parameters, including occupied space for transmission line towers (known as right-of-way (ROW)), physical cost of towers, conduction line costs, electrical equipment and terminators, and other necessary power electronics. DC transmission has the immediate benefit over AC via its conductor real-estate needs; while AC requires three conductors to carry power (hot, line, and neutral), DC only requires two (positive and negative). Since high voltage AC transmission lines require a minimum amount of spacing between conductors to avoid ground-faults and arcing, HVDC transmission also benefits from requiring a smaller ROW through spacing management between its two conductors as opposed to three. The reduced amount of conduction material also affords smaller conductor losses, such as ohmic losses discussed in the previous section, and the avoidance of other AC-specific losses, such as the skin effect [53]. Figure 1.7 demonstrates the comparison of ROW for HVDC and AC transmission line options supplying 2 GW of power.

An economic analysis of high voltage AC and DC transmission can be performed in consideration of the specific costs associated with each system configuration. As Figure 1.8 indicates, a *break-even* distance occurs where the capital investment for an HVDC system is more cost-effective than the corresponding AC system. Several studies have determined this distance to be approximately 500 km, but there are some caveats with this calculation [53]. When directly compared to HVDC, more AC transmission lines are often required to provide sufficient stability between endpoints, thereby increasing overall cost. In addition,

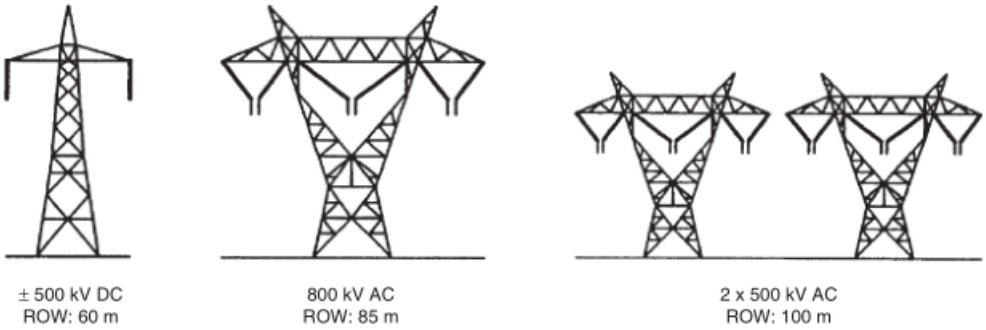

Figure 1.7. AC vs. DC. transmission line ROW [53].

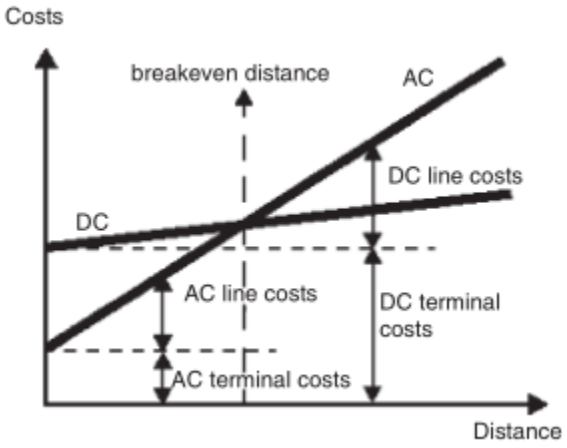

Figure 1.8. High voltage AC vs. DC break-even comparison [53].

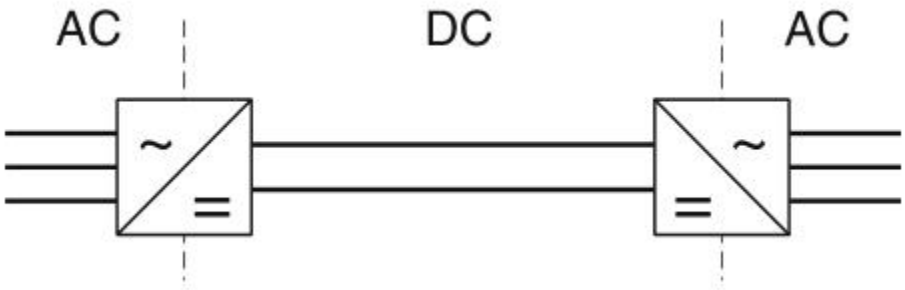

Figure 1.9. Point-to-point HVDC transmission line integration into existing AC infrastructure [54].

as discussed in the previous section, AC transmission lines must contend with both *real* and *reactive* power consumption and generation, and therefore require switching stations along a transmission path to appropriately manage power distribution [55]. As a result, the true benefit for HVDC is underappreciated when performing a pure comparison in transmission and equipment costs. Specific advantages of HVDC transmission compared to a functionally equivalent AC system include reduced conduction losses, isolation between origin and terminal connections, frequency-agnostic and independent connections, and enhanced stability contributions to upstream and downstream AC systems [54]. Finally, a HVDC transmission system can also integrate directly into an existing AC distribution network through the use of point-to-point connections, as illustrated in Figure 1.9.

1.6.2 Hybrid and Electric Vehicles

In consideration of the convoluted problems facing the current AC grid architecture, the proliferation of devices and appliances requiring DC power, and the rapid growth of DC producing renewable energy generators, the motivation for reexamination of a DC-driven architecture is clear. The advent of hybrid electric vehicles (HEVs) and EVs has revealed a direct demand for DC, poised to reveal explosive growth in the coming decades. During 2018, a little more than 1% of the 95 million passenger and commercial vehicles sold worldwide were electrically driven. However, the International Energy Agency (IEA) anticipates this value to increase up to 30% by 2030, yielding approximately 228 million new EVs on the road [56]. In addition to the associated increase in electricity demand, these vehicles will also require a fundamental shift in infrastructure to adequately supply them. Current statistics and future estimated increases in EV representation are detailed in Figure 1.10. This massive projected increase in DC electricity demand compels a fundamental reconsideration of the grid's distribution mechanisms in order to satisfy future needs, and avoid undesirable environmental impacts.

In addition, the expansion of DC producing renewable resources into the grid's energy portfolio also motivates further consideration of a DC architecture. In 2015, the IEA determined that renewable energy constituted 64% of new electricity generating capacity within

the U.S. [57]. This considerable increase can be visualized in Figures 1.11 and 1.12. In 2018, solar power generated 570 TWh of electricity, and under the current Sustainability Development Scenario (SDS) is expected to increase to over 3 PWh by 2030 as indicated in Figure 1.13 [58]. With the appreciable increase in DC power generation, overall electricity consumption, and new devices coming online requiring a DC supply, a unique approach to future grid designs is necessary.

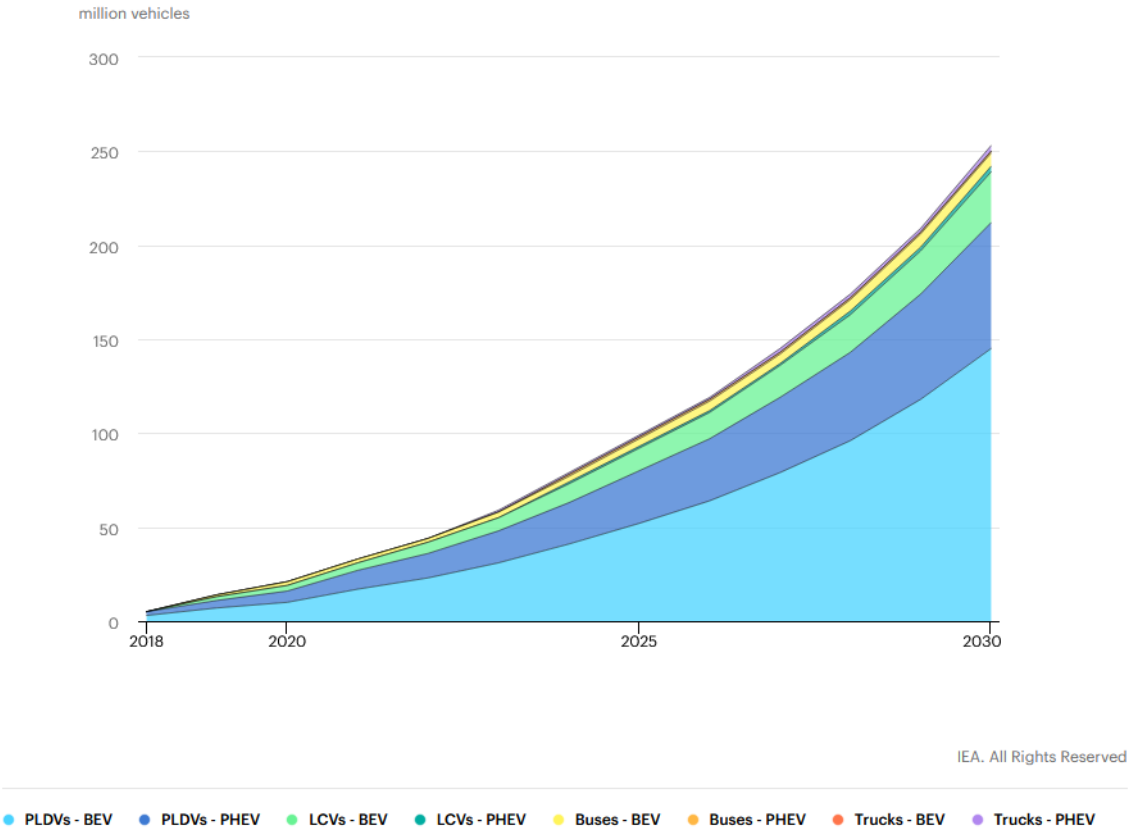

Figure 1.10. Projected EV growth within the U.S. by 2030 [59].

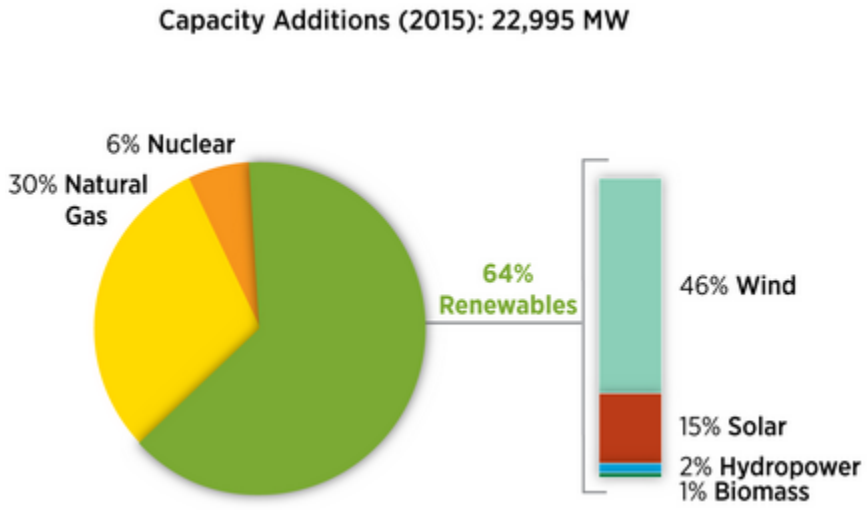

Figure 1.11. U.S. renewable energy capacity additions in 2015 [57].

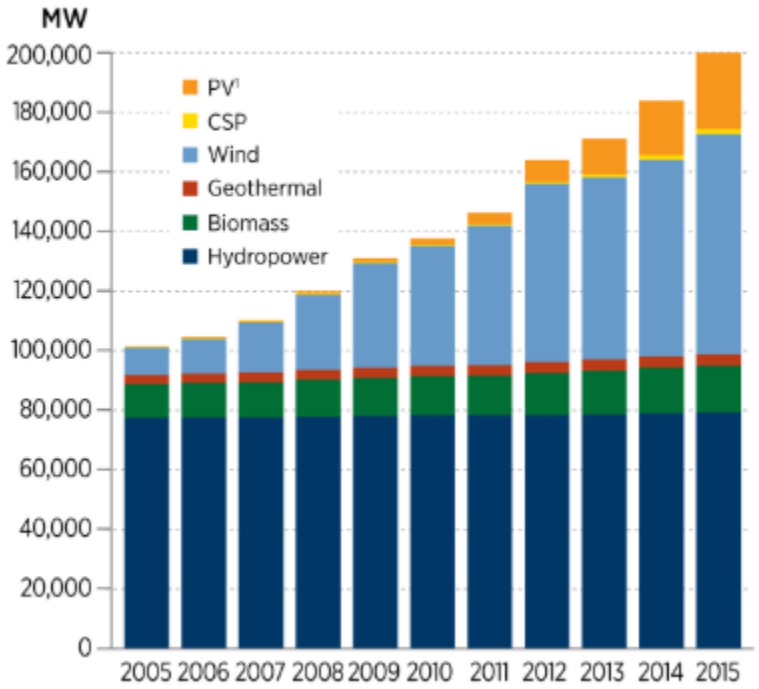

Figure 1.12. U.S. renewable energy capacity increase between 2005 and 2015 [57].

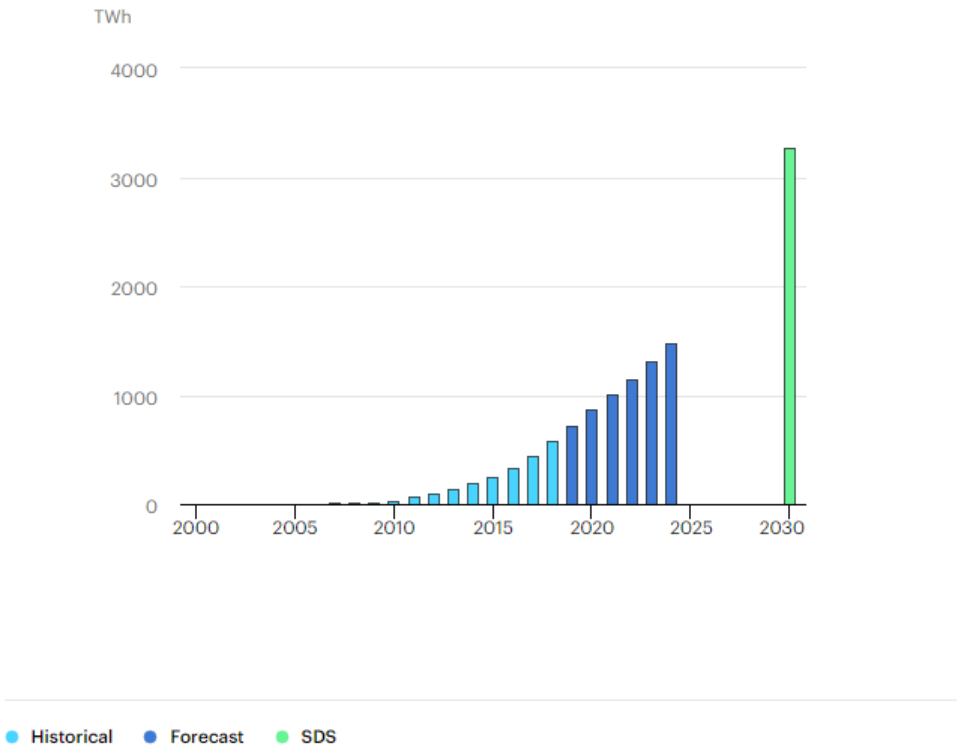

Figure 1.13. Projected increase in solar energy within the U.S. by 2030 [58].

1.6.3 Energy Consumption Characterization

In a survey of 24 countries representing 92% of energy consumed worldwide during 2018, the IEA determined that residential consumers represented up to 20% of the end-use of energy, as indicated in Figure 1.14. Of this sector, space heating and cooling accounted for more than half of energy consumed as shown in Figure 1.15, positioning heating, ventilation, and air-conditioning (HVAC) systems as key points of interest for analysis. Appliance energy consumption followed in second, accounting for another one-fifth of residential net energy consumed [60].

Owing in part to their significant representation of total energy consumption and homogeneity of specific load types, residential spaces occupy a pivotal juncture in the path toward the future architecture of the electrical grid. Many studies have evaluated the individual characteristics of residential loads, such as [61]–[64], for the purposes of assessing

Figure 1.14. End-use energy consumption by sector during the 2018 year [60].

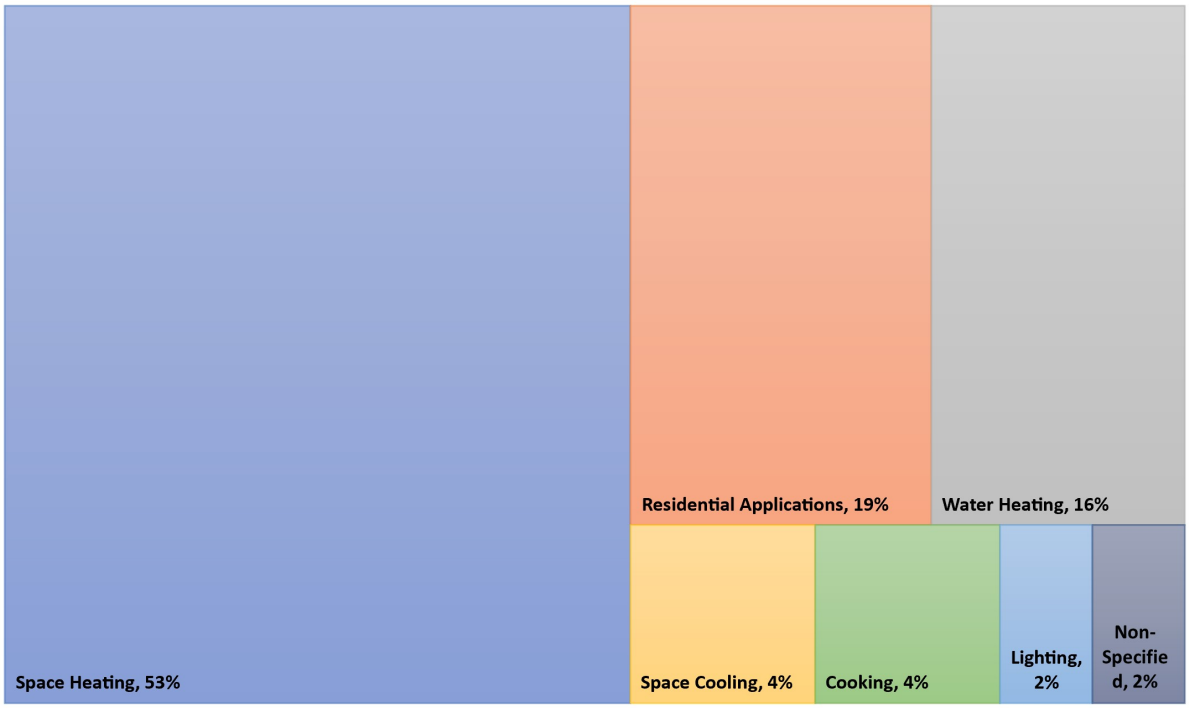

Figure 1.15. End-use energy consumption breakdown in residential environments during the 2018 year [60].

both demand side management and the opportunity for retrofit suitable with DC power. In particular, [63] classified common residential electrical loads as either (a) lighting, (b) electronics, (c) heating elements, or (d) motor loads. Of these, all but the heating elements were surmised to benefit from a direct-DC supply or suitable DC-retrofit compared to the baseline AC versions.

1.6.4 Distributed Energy Resources

As the macrogrid increases in size and throughput, so do its stability challenges and supply requirements. In addition, higher instantaneous power demands can lead to cascading failures during disruptions, as evidenced by many of the blackout events during the past several decades [11]. These obstacles can be overcome with the help of a newly emerging asset – distributed energy resources, or DERs. According to NERC, a DER is, "any resource on the distribution system that produces electricity and is not otherwise included in the formal NERC definition of the Bulk Electric System (BES)" [65, p. 1]. As a result, DERs occupy a broad range of resources, including energy storage, renewable energy generation, EV charging stations, back-up generators, and even microgrids themselves. Fundamentally, to be classified formally as a DER an entity must be capable of producing electricity, thus supporting the inclusion of energy storage systems. Interestingly, individual equipment and devices which maintain their own storage may also function as a DER (such as an EV) if the electrical connection is bidirectional [65].

With the acceleration in deployment of renewable energy generation, especially that of solar photovoltaics (PV) and wind power, the macrogrid is presented with an increasingly diverse supply of energy resources. Unlike traditional base load power plants, such as coal and nuclear, renewable resources are frequently volatile and therefore unsuitable for satisfaction of base load power demands. Instead, these systems are far more effective for responding to transient shifts in demand, such as intermediate loads arising during the daytime in winter and summer seasons. If these sources are coupled with energy storage systems, such as compressed air energy storage (CAES), pumped heat energy storage, or other conventional battery storage systems, the variability of energy generation can be significantly mitigated.

In addition, storage systems within the macrogrid provide a relaxation to the demands on other generation processes, and bolster the stability of the neighboring grid elements.

Opponents to the integration of renewable energy sources and the larger composite of DERs have argued that due to their inherently unstable nature, these resources are unreliable and thus incapable of replacing established fossil-fuel based power generation sources. Contrary to this suggestion, multiple studies have recognized the considerable benefit of incorporating sources such as wind and solar PV, as [66] confirmed in their multiphase Western Wind and Solar Integration Study (WWSIS). The WWSIS report sought to understand whether the macrogrid (specifically the Western Interconnection) could withstand the inclusion of extensive amounts of wind and solar energy generation without inducing instabilities and resulting in undesirable strain to the overall system. Far from any unfavorable impact, the WWSIS's first phase determined that up to 35% of the region's power production could be substituted by wind and power generation without requiring significant restructuring of the grid. Furthermore, the same modification would also provide an equivalent benefit to the environment roughly similar to removing up to 36 million cars off the road (compared to the existing system operation). Utility and operation costs were also discovered to decrease under the addition of these renewable resources, and transmission segments could provide better utilization due to the locality of energy generation. Finally, distributing the points of energy generation geographically was also recognized to reduce variability in production, as the prevalence of wind and solar conditions becomes proportionally more consistent as the spatial size of the region considered increases [66].

1.6.5 Microgrids and Nanogrids: Highway to Health

One proposed solution to the expanding energy issues are the concepts of the *microgrid* and *nanogrid*. As defined by the U.S. DOE, a microgrid is represented by a group of loads and distributed energy resources (DERs), which have a defined electrical boundary from other entities, can be controlled as a single body, and maintain the ability to either interact with the grid, or disconnect and operate independently in an islanding mode [67]. The International Council on Large Electric Systems (CIGRÉ) provides a similar interpretation,

further specifying that DERs include all manner of energy generation in the microgrid (e.g., fossil fuels, combined heat and power (CHP), PV, wind, etc.), and storage devices can possess a diverse collection of implementations (e.g., electrical, mechanical, gravitational, thermal, chemical, etc.) [68]. To this end, a microgrid is a unit which can coexist alongside conventional electrical distribution mechanisms, but affords the capability to operate on its own if necessary. Furthermore, the microgrid can distribute energy back to the grid if required, offering an additional advantage to stability. With respect to this terminology, the existing overall electrical grid is often referred to as the macrogrid.

Similar to microgrids, nanogrids offer much of the same benefits on a much smaller scale. While a microgrid might encompass an entire neighborhood of interconnected houses, a power plant, and local energy storage, a nanogrid could be comprised of a single home with a solar installation. Lincoln Berkeley National Laboratory (LBNL) defines a nanogrid to represent a single controllable entity with at least one load, and at least one connection to external grids (either a larger microgrid, the overall macrogrid, etc.) [69]. A critical difference from the microgrid, however, is the requirement for storage; a nanogrid may or may not have energy storage integrated into its design. As a result, by its formal definition a nanogrid is not required to support islanding operation.

Microgrids and nanogrids are not required to stipulate a specific voltage for distribution, although DC is very commonly used in both. These systems benefit from their flexibility to integrate into a panoply of applications, ranging from industrial facilities, commercial buildings, cul-de-sacs, individual homes, and many other structures. A prominent member in the DC-space, the EMerge Alliance, has helped to establish a variety of microgrids, including many of those indicated in Figure 1.16.

Data centers are a specific application with significant benefit from the microgrid architecture. One of the most crucial aspects of these facilities is resiliency regardless of equipment failure, inclement weather, or other unexpected disturbances [71]. Data centers often include Uninterruptible Power Supplies (UPS) which house DC batteries for energy storage. Due to the conversion losses associated with DC to AC conversion (and vice versa), employment of a DC microgrid topology provides a significant opportunity for energy savings, with LBNL identifying up to a potential 28% reduction in energy consumption when compared to an

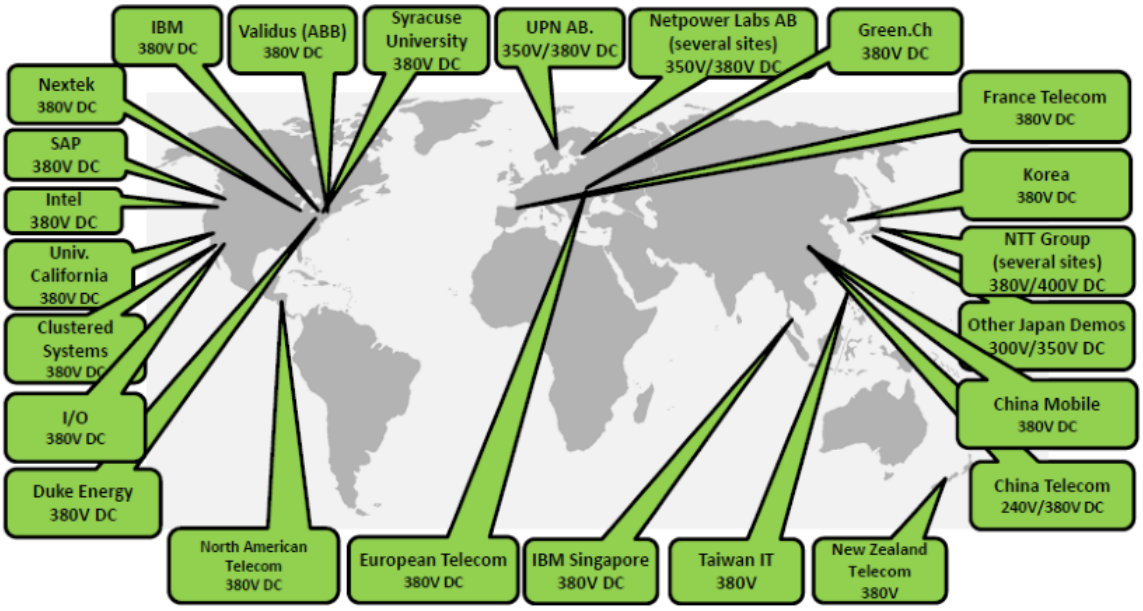

Figure 1.16. DC microgrid deployments around the world [70].

equivalent AC-based system [72]. In a similar finding, a study of a Duke Energy data center employing a 380 VDC solution determined an energy savings of approximately 15% compared with the same architecture driven by AC [73]. As a result, the capacity for DC systems to provide significant savings over their AC counterparts has been demonstrated in a variety of applications, and continues to be investigated in contemporary research.

Microgrids and nanogrids offer a bottom-up solution to transmission and distribution challenges, requiring minimal coordination and the flexibility to function alongside the existing AC infrastructure. With integrated battery storage, these topologies offer resiliency to grid disruptions, load-balancing opportunities, and ready compatibility with DC power producing renewable energy sources. Nanogrids continue these benefits one step further, yielding configurations with reduced conversions between distribution and devices, and increasing the potential for energy savings. Combining these systems with DC-compatible devices and furthering retrofit-research into additional appliances capable of supporting DC could render AC the minority in power distribution, rather than the predominant entity.

1.7 Research Objectives and Approach

Though field research has established the potential benefits of DC systems in specific industrial and commercial applications, the experimental implementation of topologies such as the microgrid and nanogrid within the residential space is a topic devoid of significant investigation. Existing studies include topics such as:

- Theoretical or limited hardware in the loop (HIL) analyses of residential nanogrid implementations [30], [74]–[85]
- Experimentation with low-voltage DC applications [81], [86], [87]
- Isolated appliance DC retrofits [63], [88]–[92]
- Individual microgrid/nanogrid converter topology design [29], [77], [78], [93]
- Microgrid/nanogrid control system applications [94]–[96]
- Energy Management System (EMS) or Battery Management System (BMS) development [61], [62], [64], [97]–[104]

Although wide coverage of subjects has been demonstrated, no completely DC-retrofitted residential structure currently exists within the U.S. suitable of sustaining all its encompassed loads, from small to large. As a result, this research seeks to perform the following unique contributions:

- Instrument and analyze a lived-in residential home to identify device and appliance electrical characteristics, opportunities for energy savings, and historical usage trends.
- Collaborate with industry partners and other vendors to investigate potential retrofits for appliances to ensure their compatibility with DC voltages, and perform laboratory testing of such devices to electrically characterize their performance and observe their behavior under a variety of load conditions.
- Design a novel DC nanogrid infrastructure for the residential home, sized sufficiently for its energy demands and integrated with energy storage and generation equipment.

- Implement the DC nanogrid within the home alongside the existing AC infrastructure, and progressively transition devices and appliances from AC to DC supply.
- Design and deploy a novel Internet of Things (IoT) network using microcontrollers and sensors, and leveraging DC power-based technologies such as Power over Ethernet (PoE).
- Develop and program an EMS and BMS to manage electrical distribution, battery storage and discharge, macrogrid-nanogrid interactions, mitigate and broadcast fault detection, and ensure safety for occupants of the home.
- Monitor the DC nanogrid implementation over a sufficient time period to determine opportunities for improvement, enhancement, and additional optimization using novel techniques such as machine learning.

1.8 Overview

With respect to the objectives outlined in the previous section, the structure of this thesis is laid out in the following manner. In Chapter 2, the residential home under study is instrumented and monitored to establish baseline energy consumption. In addition, the building is significantly renovated to improve its energy efficiency and consumption, and analyzed to determine its year-over-year performance. In Chapter 3, a heat pump unit is retrofitted to accommodate DC input, and is instrumented in psychrometric chambers with a DC power supply to analyze its performance. An unmodified heat pump unit is simultaneously installed in the DC House to provide a reference for comparison, using a variety of thermal performance methodologies. In Chapter 4, the DC Nanogrid system development and architecture is discussed, along with its construction, energy and control system mechanisms, and safety topics surrounding its operation. In Chapter 5, a state-of-the-art IoT monitoring system is developed and deployed in the home, providing real-time feedback of building parameters, environmental conditions, and safety notifications. Finally, Chapter 6 summarizes these efforts and suggests future research thrusts.

2. RESEARCH ENVIRONMENT, INSTRUMENTATION, AND RENOVATIONS

2.1 Modernization and Electrification

The residential home under study is a two-story 1920's era home, referred to henceforth as the *DC Nanogrid House*, and houses three graduate students who live and work in the dwelling. As a result, the DC Nanogrid House serves as a veritable *living lab*, providing a realistic environment in which energy consumption and other parameters can be evaluated. The house occupies a 595 m^2 lot with a detached garage, and contains 208 m^2 of floor space. In order to establish a consistent baseline of electrical energy consumption, the house was first completely electrified, replacing natural gas appliances with electrical versions. In addition, the utility connection to the home was upgraded from 200 A to 400 A service to support modernization of the home and additional loads coming online.

As part of the modernization, the kitchen in the DC Nanogrid House was completely renovated, adding new appliances furnished by Whirlpool Corporation. New circuits were installed to support the water heater, heat pump, and kitchen appliances added to the home. Non-functioning receptacles were removed and replaced, along with new light switches, light fixtures, and disconnect switches for new devices. Knob and tube wiring (K&T) were removed and replaced with conventional AC wiring, as well as new terminations, mounting hardware, conduit, fittings, and other needed accessories. Outside views of the DC Nanogrid House are provided in Figures 2.1 and 2.2, and floorplans for each floor are illustrated in Figure 2.3.

Figure 2.1. DC Nanogrid House — street view.

Figure 2.2. DC Nanogrid House — rear view.

Figure 2.3. DC Nanogrid House floorplan.

2.2 Home Improvements and Renovations

2.2.1 Basement Waterproofing

Following the electrification and major appliance installations, many aspects of the DC Nanogrid House were improved and renovated. Of primary concern was the basement; owing to the house's age, the drain pipes in the basement floor were directly connected to the main sewer line. As a result, during intense rainfall, the drainage pipes would often become overloaded, and backfill into the basement. In addition, an abundance of water exists in the soil near the home, penetrating the basement walls and leaving behind a white substance known as *efflorescence* (see Figure 2.4). Outside of potential health repercussions, the presence of water poses a significant danger to electrical systems (especially those operating on DC). As discussed in later sections, substantial care must be devoted to grounding and protection of DC systems to ensure arcing and ground-faults do not occur. Water in close proximity of these systems presents an undesirable potential conduction path, as well as a hazard to electrical components and circuitry [105].

Since multiple paths existed for water entry into the basement, and insufficient drainage to process backfills, a perimeter drainage system was designed and installed. A waterproofing

Figure 2.4. Presence of efflorescence on basement walls before waterproofing.

specialist, AdvantaClean, was contacted for support with this project, and with the assistance of a plumber, performed the following tasks:

- Installation of an AdvantaDrain Interior Perimeter Drain System along all basement walls
- Installation of a 0.37 kW S-2 Superior Sump Pump with sealed lid basin
- Installation of a condensate drain for heat pump air handling unit (AHU) and water heater (WH)
- Installation of a 9 m discharge line on the east side of the home
- Application of white anti-microbial infused coating to exterior foundation walls

Figure 2.5. Cracked ceramic drainage pipes.

Figure 2.6. Drainage pipe after repairs.

Figure 2.7. Excavation of foundation for sump pump and drain system installation.

Figure 2.8. Completed installation of the sump pump.

Figure 2.9. Sealed sewer line access with hydraulic cement.

Figure 2.10. Completed condensation drainage line installation.

During this process, multiple broken pipes were discovered due to deterioration of the clay material used in the original lines. These were repaired by Haan Plumbing Service and Summers Plumbing Heating & Cooling to ensure proper and safe drainage. Figures 2.5 and 2.6 illustrate the before and after photographs of the repaired piping, Figures 2.7 and 2.8 show the excavation and installation of the perimeter drain and sump pump, Figure 2.9 shows the sealant of the sewage line entry to the basement with hydraulic cement, and finally, Figure 2.10 shows the condensation drainage for the AHU and WH.

2.2.2 Insulation Renovations

The next area of improvement surrounded energy efficiency of the home. After several winter months in 2018 yielding over $400 electricity bills, investigation of the structure revealed two primary opportunities for renovation: (1) wall insulation, and (2) windows. Owing to the age of the house, insulation was nearly non-existent and suspected to be a significant culprit of extensive heating usage. USA Insulation of Indianapolis was contacted for support with foam-injection into the walls, using R-5.1 per inch. In addition, band joists, rim joists, and sill plates in the basement were air sealed using spray foam, as shown in Figure 2.11.

Figure 2.11. Basement spray foam installation.

Outside of the basement, the attic insulation was also determined to be well-below the recommended amount for the given geographical location. As Figure 2.12 indicates, homes in the northeast region of Indiana should maintain insulation levels of between R38 to R60, with recommendations for existing structures to use a minimum of R49 [106].

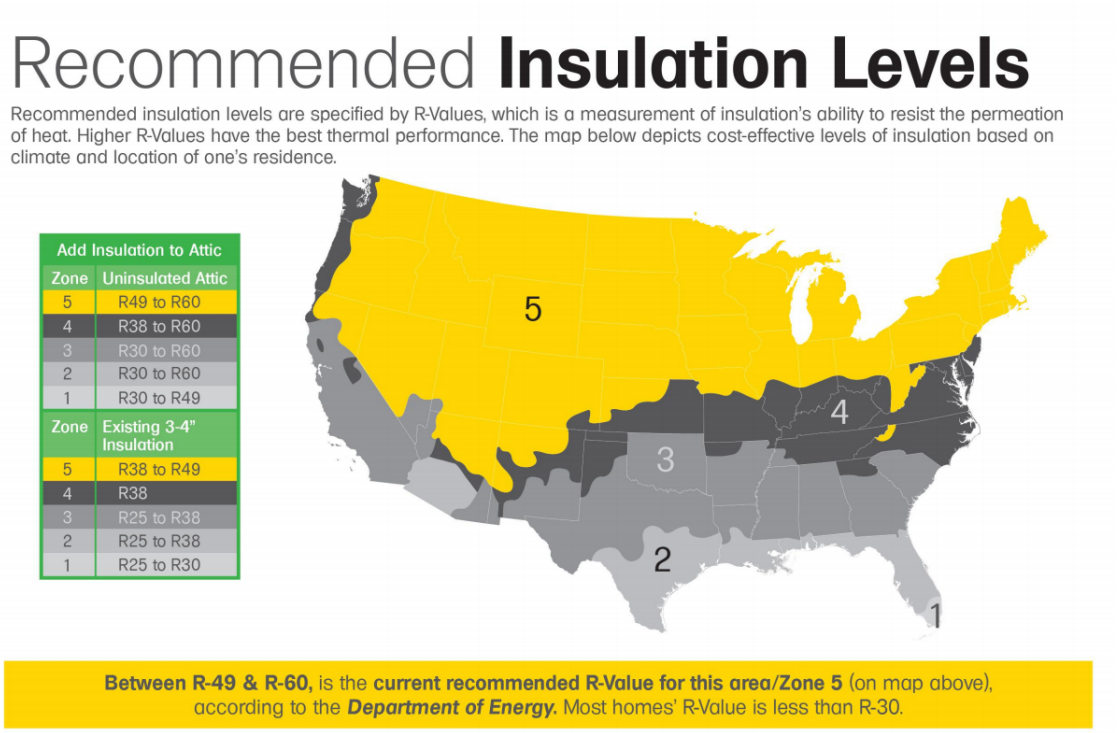

Figure 2.12. U.S. DOE recommended insulation levels by geographical location [106].

Prior to the insulation renovations in the attic, less than R-20 was measured, with some locations having nothing at all. To rectify this, Owens Corning Pro-Cat blown-in fiberglass insulation with an R-60 level was installed into the attic, with before and after comparisons provided in Figure 2.13 and Figure 2.14. This type of insulation passes odor emission requirements, corrosion and fungi resistances, water vapor absorption limitations under 5%, and possesses noncombustible characteristics.

Figure 2.13. DC House attic with less than R-20 insulation.

Figure 2.14. DC House attic after installing R-60 fiberglass blown-in insulation.

2.2.3 Window Renovations

In addition to insulation, the windows of the DC Nanogrid House were single-pane configurations, many of which were original to the construction period of the house. 35 windows existed in the house, six contained in the basement, and 29 between the first and second floors. A survey of each window determined approximately 1/3 to be non-functional, and another 1/3 to be in disrepair. Many of the windows in the basement were also broken or cracked, further diminishing the thermal insulation of the home.

A further challenge of the house was its location in the West Lafayette historical district, requiring any exterior changes to undergo scrutiny by the Historical Preservation Committee (HPC). The HPC mandated that replacement windows had to comply with a number of stipulations, including material choice, color, grill pattern, and dimensions. To assist with these issues, Lowes was contacted for replacement options which would satisfy the HPC requirements. An application was submitted and approved by the HPC, specifying Pella Lifestyle Series wood double-hung windows with Pella AdvancedComfort^{TM} Low-E Insulating Glass with Argon, blocking up to 85% of ultraviolet rays [107]. The Liftestyle Series windows are ENERGY STAR$^{®}$ certified, saving on average up to $538 and 2814 kg of CO_2 in a home per year when compared to a structure using single-pane windows [108]. The performance ratings of the windows are given by:

- U-Factor of 1.42
- Solar Heat Gain Coefficient (SGHC) of 0.25
- Visible Transmittance (VT) of 0.47

The U-Factor defines the rate of heat loss through the material, the SGHC is a dimensionless value between 0 and 1 representing the fraction of solar radiation admitted through a window, and the VT is the amount of light in the visible-spectrum which passes through the window [109]. The installation of the windows in the sun room of the house is shown in Figure 2.15. Rather than replace the six broken and cracked basement windows, these were instead boarded up and internally insulated with FOAMULAR R-5.1 rigid foam board

insulation. Before and after illustrations of these improvements are shown in Figures 2.16 and 2.17.

Figure 2.15. DC Nanogrid House Pella window installation.

Figure 2.16. Basement window before improvements.

Figure 2.17. Basement window after improvements.

2.2.4 Exterior Improvements and Additions

In addition to the major improvements to the inside of the house, several functional and aesthetic changes were performed to its exterior. To deter unwanted foot-traffic through the yard and potential vandalism to the home or Purdue property, a 43 m wooden fence with park-rail styling along the south-side of the home was installed. In addition, the broken down fence along the west-side of the property was also repaired and replaced with a new 10.5 m wooden shadowbox fence. These installations are shown in Figure 2.18. In addition, the side-door of the house was broken and provided little thermal insulation during the heating and cooling seasons. As a result, this was replaced with a Larson mid-view white storm door with coil-wrapped wood trim. All exterior improvements to the home were approved by the West Lafayette HPC.

2.2.5 Lab Space Development

To support the research activities in the DC House, the basement was further remodeled to develop a functional lab space area. Before waterproofing activities, this consisted of a temporary desk in the northwest corner of the basement, as shown in Figure 2.19. After renovations were completed, the back office area on the east side of the basement was completely overhauled to accommodate the new lab space construction. After significant renovations to the room, the current setup now includes a dedicated electronic workbench, multiple workstations for development and office use, an interface for the nanogrid control system, and a shelving area for storage. These improvements are illustrated in Figure 2.20 and Figure 2.21.

Figure 2.18. DC Nanogrid House fencing installation.

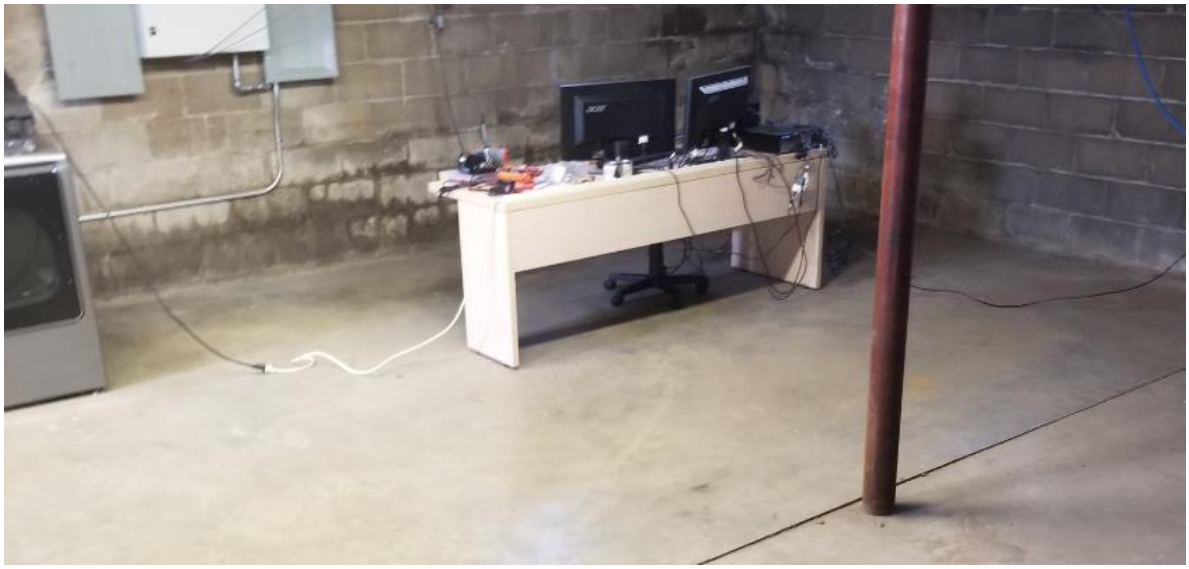

Figure 2.19. DC Nanogrid House temporary lab space.

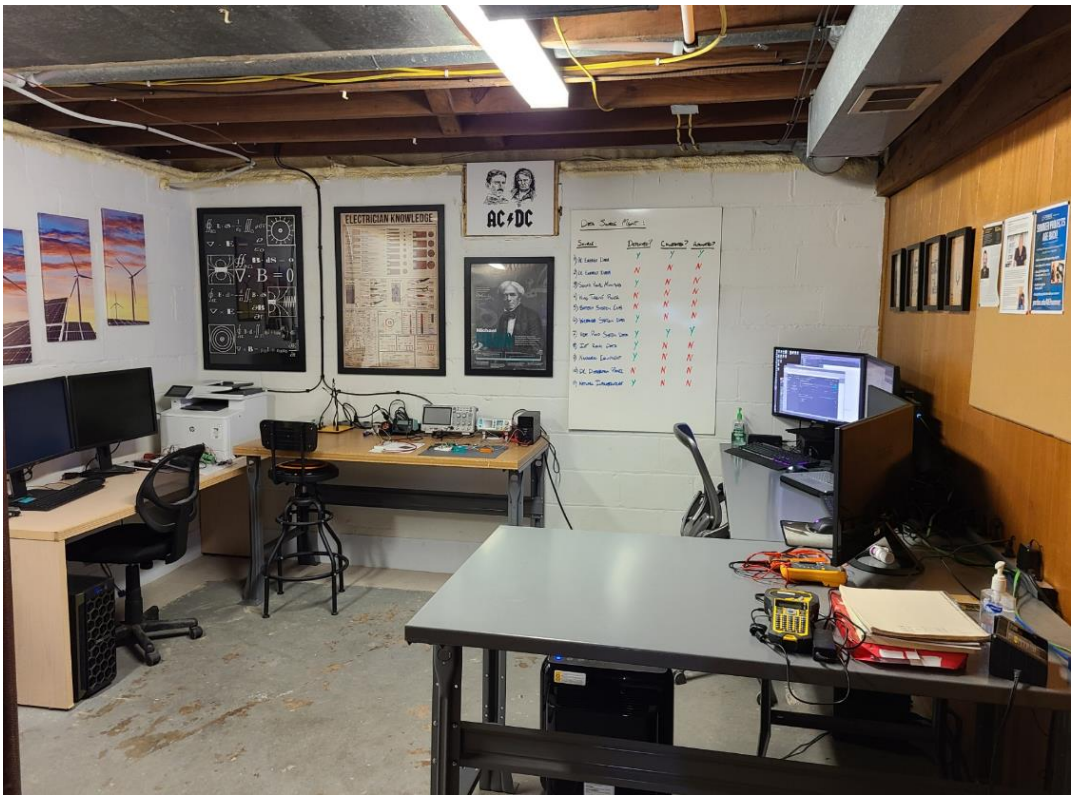

Figure 2.20. DC Nanogrid House renovated lab space.

Figure 2.21. DC Nanogrid House storage area.

2.3 DC House Data Acquisition Systems

2.3.1 Electrical Load Center Instrumentation

In order to construct a baseline metric for the energy consumption of devices and appliances under the conventional AC configuration, the load centers of the home were instrumented with Wi-Fi supported circuit breakers equipped with energy monitoring and remote control capabilities. These *smart breakers*, referred to as Energy Management Circuit Breakers (EMCBs), were designed in a partnership between Eaton and the Electric Power Research Institute (EPRI) [110]. With its traditional split-phase 120/240 VAC residential configuration, the DC Nanogrid House served as a desirable candidate for field testing the EMCB modules. 24 of the load center circuits were fitted with an EMCB module, and four were monitored externally using a power meter. An illustration of an EMCB device is shown in Figure 2.22, and the load centers before and after modification are provided in Figures 2.23 and 2.24, respectively.

Figure 2.22. Eaton EMCB Wi-Fi circuit breaker module.

Figure 2.23. AC load panels before modifications.

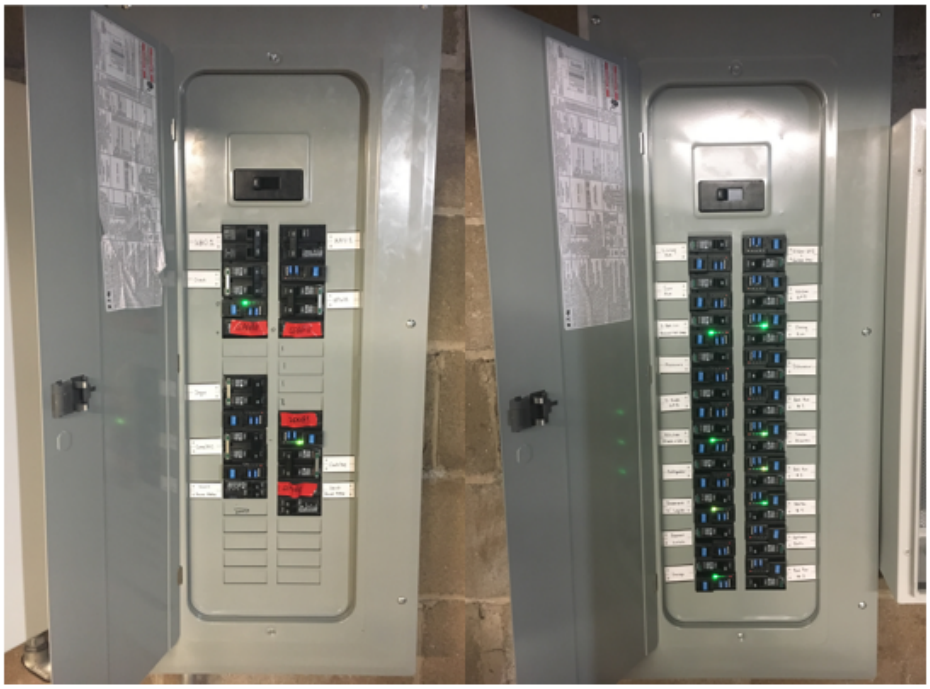

Figure 2.24. AC load panels after EMCB installation.

The breakers and their recorded data were made available on online portals through Duke Energy and Eaton, providing the capability to download and access individual circuit data on a monthly basis. Depictions of the portals are shown in Figures 2.25 and 2.26. Electrical data parameters collected by the EMCBs approximately every 15 minutes are shown in Table 2.1.

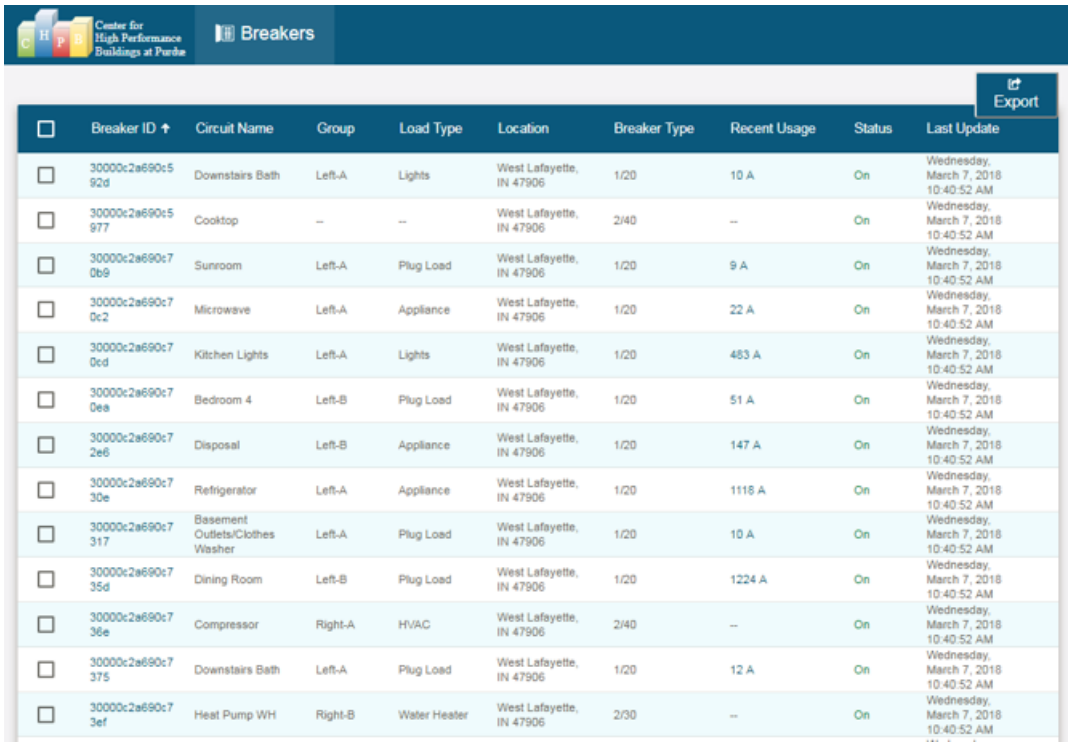

Breaker ID	Circuit Name	Group	Load Type	Location	Breaker Type	Recent Usage	Status	Last Update
30000c2a690c592d	Downstairs Bath	Left-A	Lights	West Lafayette, IN 47906	1/20	10 A	On	Wednesday, March 7, 2018 10:40:52 AM
30000c2a690c5977	Cooktop	--	--	West Lafayette, IN 47906	2/40	--	On	Wednesday, March 7, 2018 10:40:52 AM
30000c2a690c70b9	Sunroom	Left-A	Plug Load	West Lafayette, IN 47906	1/20	9 A	On	Wednesday, March 7, 2018 10:40:52 AM
30000c2a690c70c2	Microwave	Left-A	Appliance	West Lafayette, IN 47906	1/20	22 A	On	Wednesday, March 7, 2018 10:40:52 AM
30000c2a690c70cd	Kitchen Lights	Left-A	Lights	West Lafayette, IN 47906	1/20	483 A	On	Wednesday, March 7, 2018 10:40:52 AM
30000c2a690c70ea	Bedroom 4	Left-B	Plug Load	West Lafayette, IN 47906	1/20	51 A	On	Wednesday, March 7, 2018 10:40:52 AM
30000c2a690c72e6	Disposal	Left-B	Appliance	West Lafayette, IN 47906	1/20	147 A	On	Wednesday, March 7, 2018 10:40:52 AM
30000c2a690c730e	Refrigerator	Left-A	Appliance	West Lafayette, IN 47906	1/20	1118 A	On	Wednesday, March 7, 2018 10:40:52 AM
30000c2a690c7317	Basement Outlets/Clothes Washer	Left-A	Plug Load	West Lafayette, IN 47906	1/20	10 A	On	Wednesday, March 7, 2018 10:40:52 AM
30000c2a690c735d	Dining Room	Left-B	Plug Load	West Lafayette, IN 47906	1/20	1224 A	On	Wednesday, March 7, 2018 10:40:52 AM
30000c2a690c736e	Compressor	Right-A	HVAC	West Lafayette, IN 47906	2/40	--	On	Wednesday, March 7, 2018 10:40:52 AM
30000c2a690c7375	Downstairs Bath	Left-A	Plug Load	West Lafayette, IN 47906	1/20	12 A	On	Wednesday, March 7, 2018 10:40:52 AM
30000c2a690c73ef	Heat Pump WH	Right-B	Water Heater	West Lafayette, IN 47906	2/30	--	On	Wednesday, March 7, 2018 10:40:52 AM

Figure 2.25. Duke Energy portal providing EMCB data.

The EMCBs are UL489 listed circuit breakers, satisfying requirements for marine use, naval use, UPS use, software specifications, overcurrent protection, Electromagnetic Compatibility (EMC), and motor overload protection [111]. As a result, the EMCBs could be installed into the AC load centers without additional components or protective circuitry. In addition, the Wi-Fi connection of the devices allows for bi-directional communication; the devices report data described in Table 2.1, and a user can enable or disable specific breakers using the Duke Portal shown in Figure 2.25. The load center circuit types and monitors are indicated in Table 2.2.

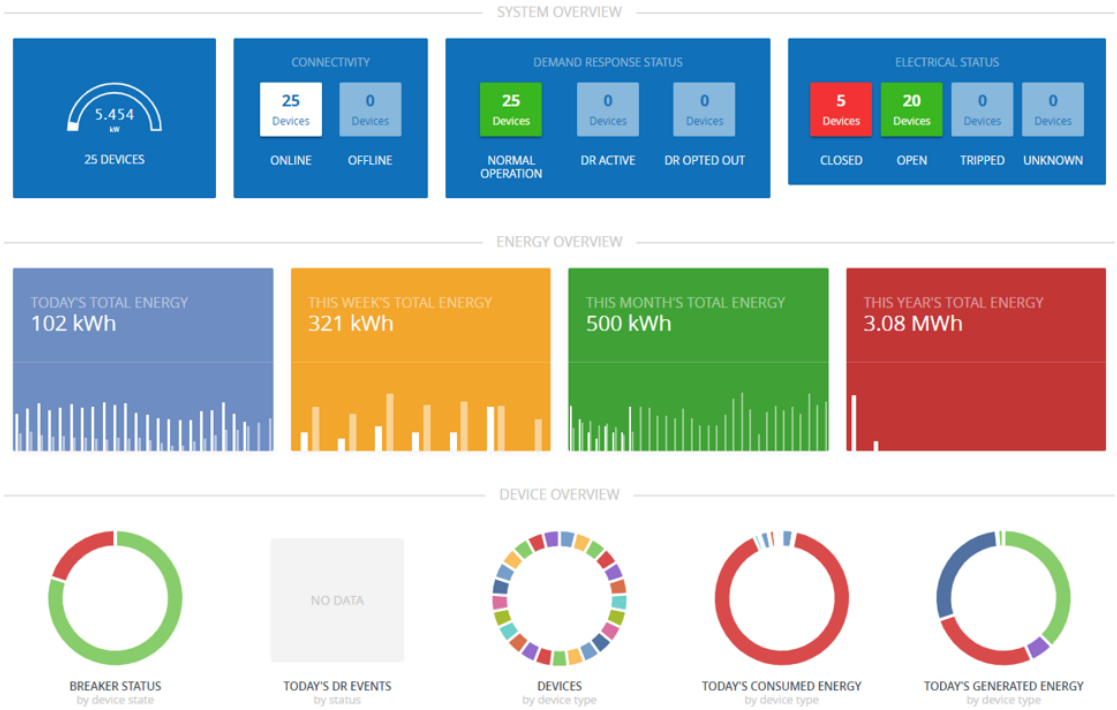

Figure 2.26. Eaton portal providing EMCB data.

Table 2.1. EMCB electrical parameters collected

Parameter	Unit
Elapsed measurement time	[s]
AB Line-Line Voltage	[V]
AN Line-Neutral Voltage	[V]
BN Line-Neutral Voltage	[V]
Phase A Current	[A]
Phase B Current	[A]
Frequency	[Hz]
Power Consumption (real)	[kW]
Energy Consumption	[kWh]

Table 2.2. AC load panel circuit type and measurement method.

Circuit Description	Load Type	Breaker Type	Monitoring Method
Downstairs Bathroom	Lighting	1 Pole / 20 A	EMCB
Downstairs Bathroom	Outlets	1 Pole / 20 A	EMCB
Cooktop	Appliance	2 Pole / 40 A	EMCB
Garbage Disposal	Appliance	1 Pole / 20 A	EMCB
Dishwasher	Appliance	1 Pole / 20 A	EMCB
Microwave	Appliance	1 Pole / 20 A	EMCB
Refrigerator	Appliance	1 Pole / 20 A	EMCB
Kitchen	Lighting	1 Pole / 20 A	EMCB
Kitchen	GFCI Outlets	1 Pole / 20 A	EMCB
Basement	Outlets	1 Pole / 20 A	EMCB
Basement	Lighting	1 Pole / 20 A	EMCB
Dining Room	Outlets	1 Pole / 20 A	EMCB
Heat Pump Outdoor Unit	Appliance	2 Pole / 40 A	EMCB
Upstairs Bathroom	Outlets	1 Pole / 20 A	EMCB
Clothes Dryer	Appliance	2 Pole / 30 A	EMCB
Clothes Washer	Appliance	1 Pole / 20 A	EMCB
Smoke Detectors	Device	1 Pole / 20 A	EMCB
Bedroom #1	Outlets	1 Pole / 20 A	EMCB
Bedroom #2	Outlets	1 Pole / 20 A	EMCB
Bedroom #3	Outlets	1 Pole / 20 A	EMCB
Bedroom #4	Outlets	1 Pole / 20 A	EMCB
Living Room	Outlets	1 Pole / 20 A	EMCB
Sun Room	Outlets	1 Pole / 20 A	EMCB
Water Heater	Outlets	2 Pole / 40 A	EMCB
Oven	Appliance	2 Pole / 40 A	Power Monitor
Air Handling Unit – Fan	Appliance	2 Pole / 40 A	Power Monitor
Air Handling Unit – Heater	Appliance	2 Pole / 40 A	Power Monitor

Since the EMCBs were currently in the prototype stage, a secondary measurement system was installed to avoid downtime. This system, known as The Energy Detective (TED®) Pro Home, uses current transformers (CTs) coupled with voltage measurements of each of the 120 VAC phases to obtain the energy and power calculations for each load panel circuit. The TED system is comprised of an Energy Control Center (ECC) connected to up to two Measuring Transmitting Units (MTUs). Each MTU supports up to two TED Spyder devices, which can each support up to eight CT inputs. In total, an ECC can measure up to 32 circuits. The TED system records voltage and current measurements once per minute with an accuracy greater than ±2% [112]. A depiction of the TED system in shown in Figure 2.27, with two 200 A CTs, an ECC, and an MTU laid out from left to right, and the TED Pro Home user interface (UI) in the background. An illustration of the TED Spyder and individual CT sensors is shown in Figure 2.28. The TED system installed in the DC Nanogrid House AC load centers is displayed in Figures 2.29 and 2.30.

Figure 2.27. TED Pro Home system components.

Figure 2.28. TED Spyder and CT devices.

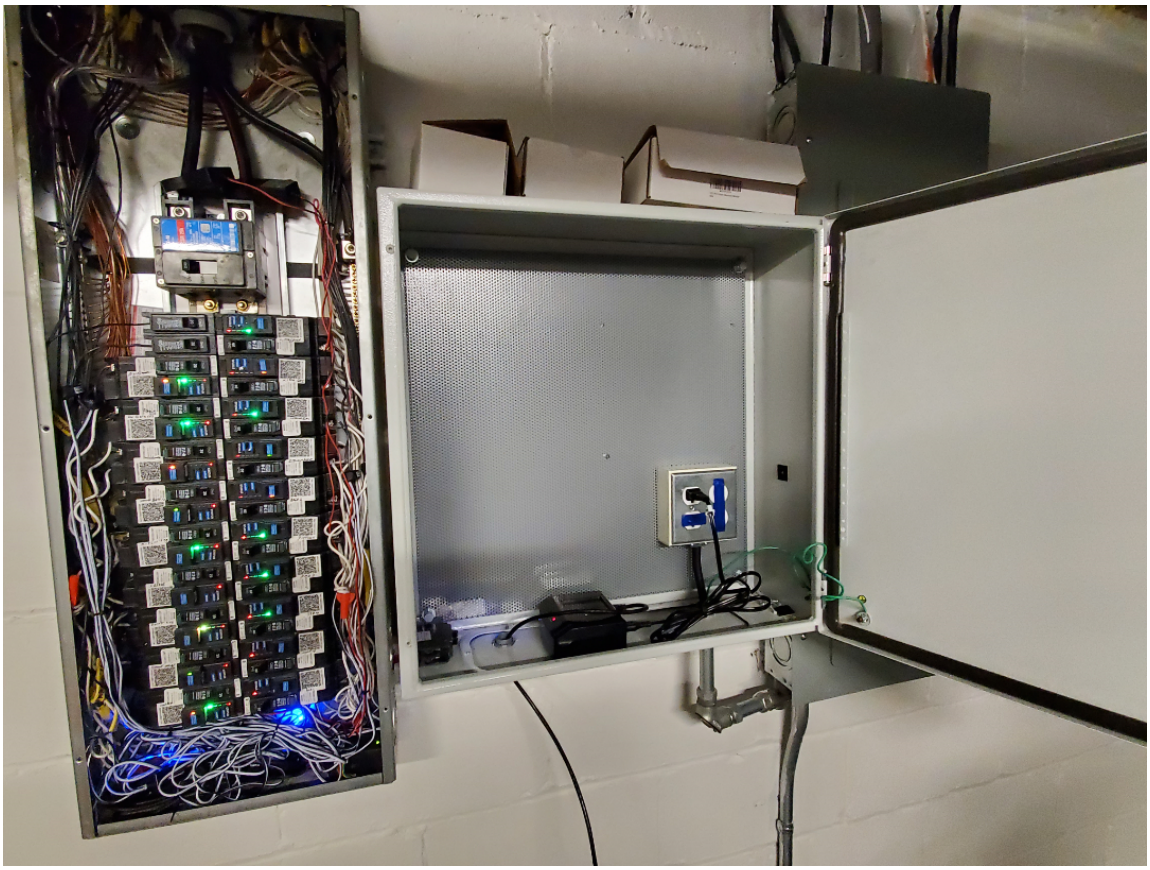

Figure 2.29. AC Load Center #1 TED Pro Home installation.

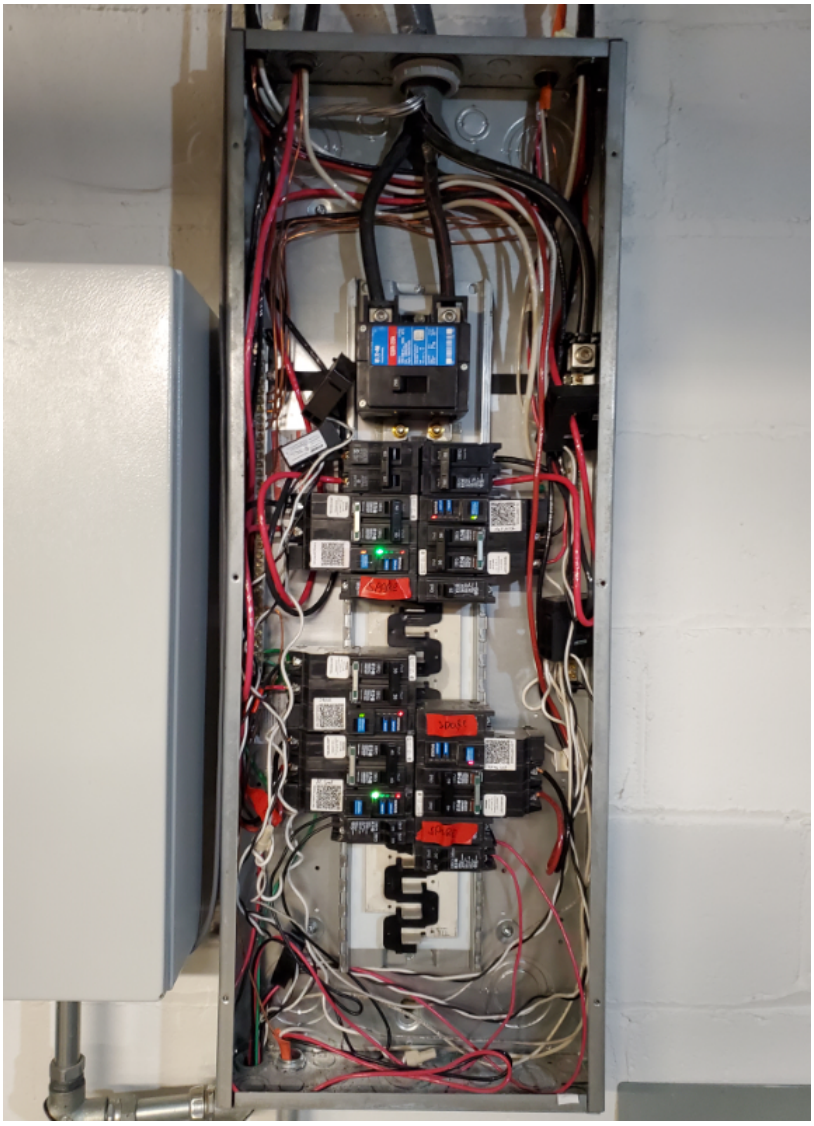

Figure 2.30. AC Load Center #2 TED Pro Home installation.

The load center circuit and CT specifications for the TED system are detailed in Table 2.3.

Table 2.3. AC load panel TED CT type and connection.

Circuit Description	CT Size	Spyder Device #	Port
Garbage Dispoal	20 A	1	1
Bedroom #3	20 A	1	2
Kitchen GFCI	20 A	1	3
Smoke Alarms	20 A	1	4
Dining Room Outlets	20 A	1	5
Bedroom #4 Outlets	20 A	1	6
Bedroom #2 Outlets	20 A	1	7
Upstairs Bathroom Lighting	20 A	1	8
Dishwasher	20 A	2	1
Downstairs Bathroom Outlets	20 A	2	2
Bedroom #1 Outlets	20 A	2	3
Clothes Washer	20 A	2	4
Microwave	20 A	2	5
Basement Outlets	20 A	2	6
Living Room Outlets	20 A	2	7
Basement Lighting	20 A	2	8
Heat Pump Outdoor Unit	60 A	3	1
Air Handling Unit – Heater	60 A	3	2
Clothes Dryer	60 A	3	3
Water Heater	60 A	3	4
Air Handling Unit – Fan	60 A	3	5
Cooktop	60 A	3	6
Oven	60 A	3	7
TED ECC Unit	20 A	3	8
Kitchen Lighting	20 A	4	1
Sun Room Outlets	20 A	4	2
Downstairs Bathroom Lighting	20 A	4	3
Refrigerator	20 A	4	4
Communication server receptacle	60 A	4	5
Emerson Ovation Circuit #1	60 A	4	6
Emerson Ovation Circuit #2	60 A	4	7
TED MTU Unit	60 A	4	8

2.3.2 Heat Pump Instrumentation

In addition to the electrical monitoring systems, a Yokogawa GM10 modular data acquisition (DAQ) system was installed, supplied with modules capable of measuring thermocouples, pulse inputs, and analog inputs. For thermocouples, the Yokogawa system provides ±0.2 °C accuracy for measurements between 0 °C and 400 °C, and (±0.1% of reading plus 0.2 °C) for measurements between −200 °C and 0 °C. For voltage measurements, the Yokogawa system provides an accuracy of (±0.01% of reading plus 2 mV) [113]. This DAQ system was initially used to record thermocouple instrumentation from the single and variable-speed Carrier Greenspeed outdoor heat pump unit, energy measurements from the indoor air handling unit and water heater, and water flow rates for the main and hot water supplies. The system configuration for these measurements is collected in Table 2.4. The original Carrier 3.5 ton single-speed unit and its replacement Carrier 4 ton variable-speed unit are depicted in Figure 2.31.

Table 2.4. Yokogawa GM10 DAQ instrumented Carrier unit and energy monitoring configuration

Device Description	DAQ Sensor ID	Sensor Type	Units
Compressor Suction Temperature	1	Thermocouple	°C
Compressor Shell Temperature (Top)	3	Thermocouple	°C
Indoor Coil Temperature (AHU)	4	Thermocouple	°C
Liquid Line – Indoor Temperature	5	Thermocouple	°C
Compressor Discharge Temperature	6	Thermocouple	°C
Outdoor Coil Temperature	7	Thermocouple	°C
Compressor Shell Temperature (Bottom)	8	Thermocouple	°C
Compressor Shell Temperature (Middle)	9	Thermocouple	°C
Suction Line – Indoor Temperature	10	Thermocouple	°C
Indoor Ambient Air Temperature	103	Thermocouple	°C
Indoor AHU Fan Pulse Sensor	201	Pulse	-
Indoor AHU Aux Heater Pulse Sensor	202	Pulse	-
Main Water Supply Pulse Sensor	203	Pulse	-
Hot Water Supply Pulse Sensor	204	Pulse	-
Indoor AHU Fan Energy	A1	Analog	kWh
Indoor AHU Aux Heater Energy	A2	Analog	kWh
Main Water Supply Flow Rate	A3	Analog	gpm
Hot Water Supply Flow Rate	A4	Analog	gpm

These thermocouple sensors can be used to indicate the times of the day when the heat pump unit is run, as exemplified in measurement recordings shown in Figures 2.32 and 2.33. The corresponding peak in Figure 2.32 and valley in Figure 2.33 reveal the period of the heat pump's operation. In particular, the compressor shell surface temperatures were measured to perform thermodynamic analysis in later studies. The instrumented compressor locations are described in Figure 2.34, and the remaining thermocouples instrumented in the indoor and outdoor units are represented in a refrigeration cycle schematic shown in Figure 2.35.

Figure 2.31. Carrier Greenspeed outdoor single and variable-speed heat pump unit comparison.

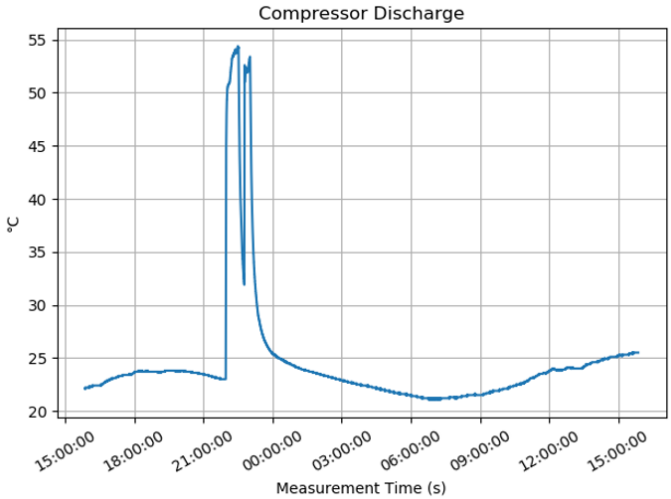

Figure 2.32. Compressor discharge temperature versus time of day.

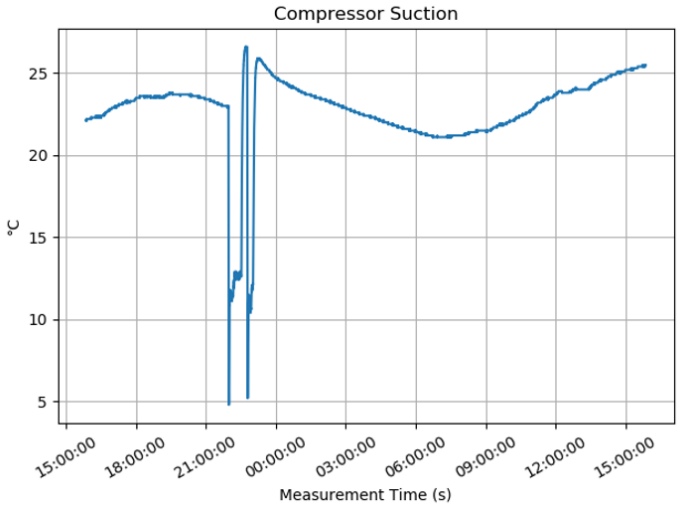

Figure 2.33. Compressor suction temperature versus time of day.

Figure 2.34. Compressor shell surface temperature instrumentation locations.

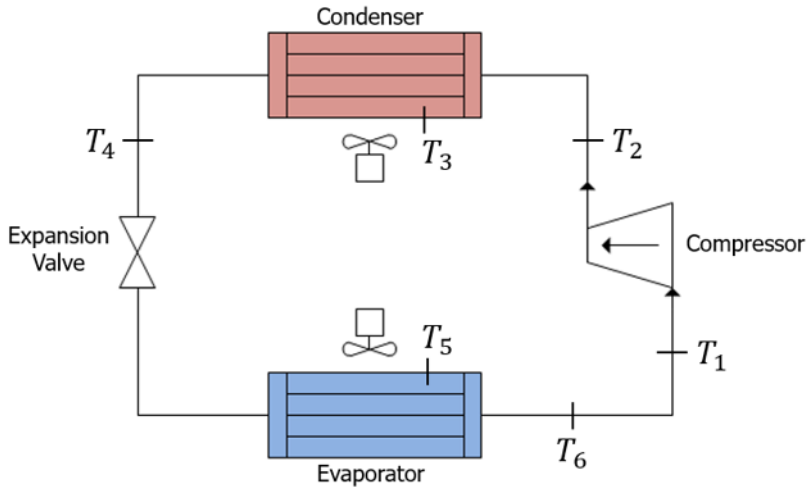

Figure 2.35. Heat pump refrigeration cycle temperature instrumentation locations (cycle in cooling mode).

During the third year of the project, the Carrier 4 ton variable-speed unit was replaced with a Trane 4-ton 18 seasonal energy efficiency ratio (SEER) split-system air-source heat pump suitable for retrofit to DC power. To enable AC-baseline data collection for comparison against the DC-retrofitted unit, an unmodified off-the-shelf unit running on 240 VAC was installed at the DC House and instrumented for thermal and electrical performance analysis. The energy monitors from the Yokogawa GM10 DAQ were moved to the TED system, as indicated in Table 2.3, and the thermocouples were reassigned to the Trane unit as described in Table 2.5. The physical locations of the thermocouples are depicted in Figures 2.36, 2.37, 2.38, 2.39. In addition to the thermocouples, the indoor heat pump unit is also equipped with differential pressure sensors, airflow and temperature measurements, and return side relative humidity and temperature sensors. Differential pressure measurements of the return and supply air sides are made by two Setra Multi-Range General Pressure Transducer modules, capable of measuring between ±1 kPa with a ±1.0% full-scale root sum square method. The Setra modules require a 13 to 30 VDC excitation, which is sustained by a PoE input driven through a 48 VDC to 24 VDC DC-DC converter. This system setup is depicted in Figure 2.40.

Table 2.5. Yokogawa GM10 DAQ instrumented Trane unit configuration.

Device Description	DAQ Sensor ID	Sensor Type	Units
Indoor Unit - Supply Side West #1	T001	Thermocouple	°C
Indoor Unit - Supply Side West #2	T002	Thermocouple	°C
Indoor Unit - Supply Side West #3	T003	Thermocouple	°C
Indoor Unit - Supply Side East #1	T004	Thermocouple	°C
Indoor Unit - Supply Side Northwest	T005	Thermocouple	°C
Indoor Unit - Supply Side East #2	T006	Thermocouple	°C
Indoor Unit - Supply Side East #3	T007	Thermocouple	°C
Indoor Unit - Supply Side East #4	T008	Thermocouple	°C
Indoor Unit - Supply Side Northeast	T009	Thermocouple	°C
Indoor Unit - Supply Side West #4	T010	Thermocouple	°C
Indoor Unit - Return Side #1	T011	Thermocouple	°C
Indoor Unit - Return Side #2	T012	Thermocouple	°C
Indoor Unit - Return Side #3	T013	Thermocouple	°C
Indoor Unit - Return Side #4	T014	Thermocouple	°C
Indoor Unit - Return Side #5	T015	Thermocouple	°C
Indoor Unit - Return Side #6	T016	Thermocouple	°C
Indoor Unit - Return Side #7	T017	Thermocouple	°C
Indoor Unit - Return Side #8	T018	Thermocouple	°C

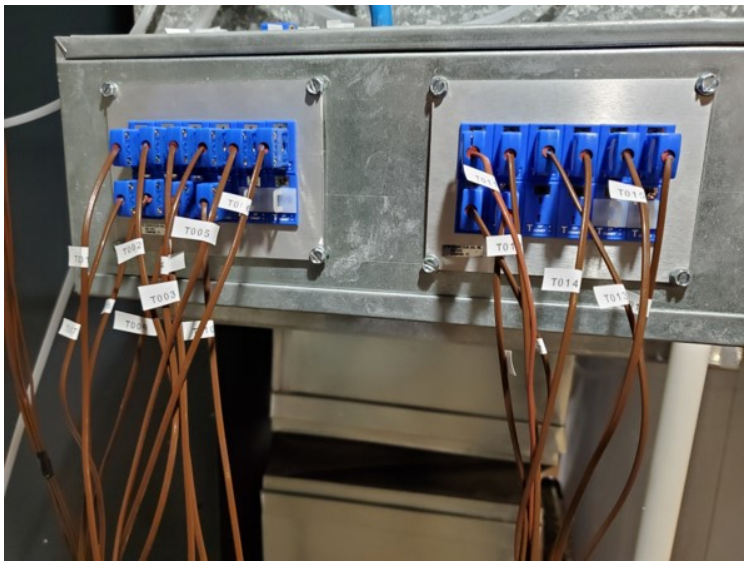

Figure 2.36. Yokogawa GM10 DAQ thermocouple interface panel.

Figure 2.37. Thermocouple instrumented locations on the supply (west) side of the indoor unit.

Figure 2.38. Thermocouple instrumented locations on the supply (east) side of the indoor unit.

Figure 2.39. Thermocouple instrumented locations on the return side of the indoor unit.

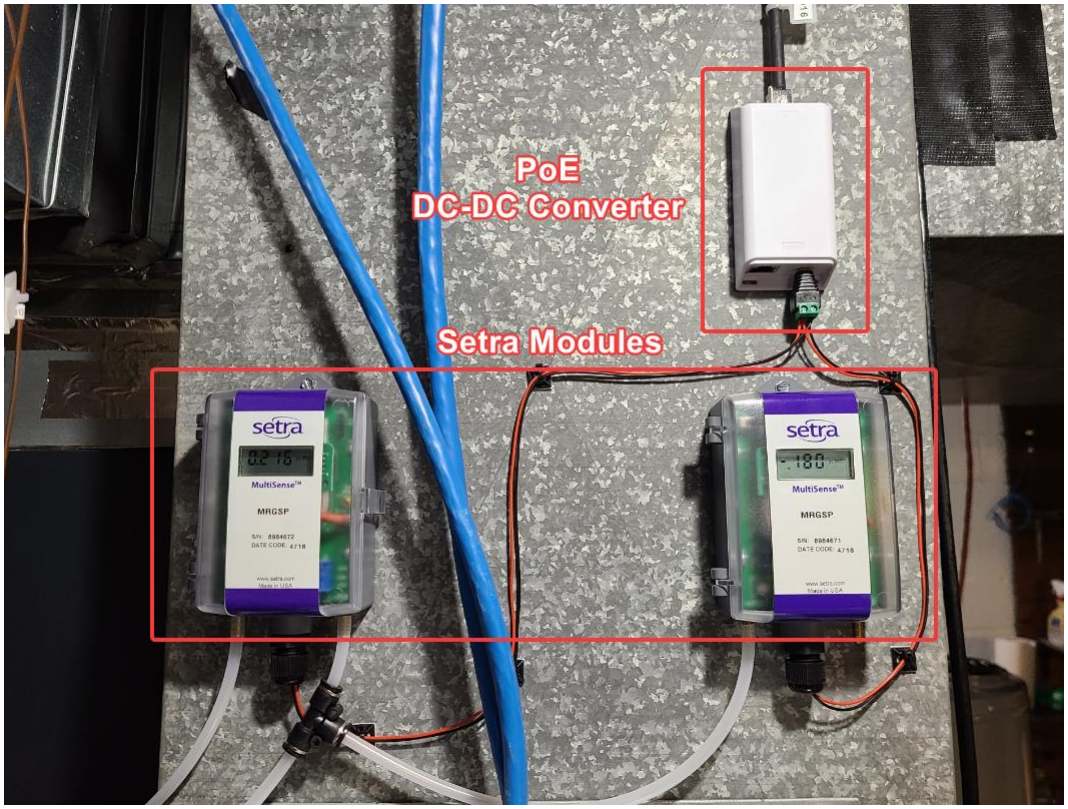

Figure 2.40. Instrumented Setra differential pressure modules on the indoor heat pump unit.

Airflow measurements of the indoor unit's supply air are performed by an Ebtron GTx116-P+ module, with two individual probes suitable for measurements between 0 m/s to 25.4 m/s at ±2% accuracy. Air temperature measurements are also provided, with a calibration range from −30 °C to 70 °C at an accuracy of ±0.083 °C. The Ebtron module requires an excitation of 24 VAC, which was not readily available in the laboratory area; to supply this, a common 24 VAC, 40 VA doorbell transformer was implemented off the existing 120 VAC wiring. This input method will be modified to a DC-driven inverter in the near future. The instrumented Ebtron system is shown in Figure 2.41.

Temperature and humidity measurements in the return air side are measured by a Vaisala HMDW110 series transmitter, which contains a probe enclosed in a flange inserted into the ductwork. The transmitter temperature and humidity sensors are each powered individually by the same PoE-driven 24 VDC power supply as the aforementioned Setra modules, and supports measurement readings over a Modbus RS485 communication channel. Tempera-

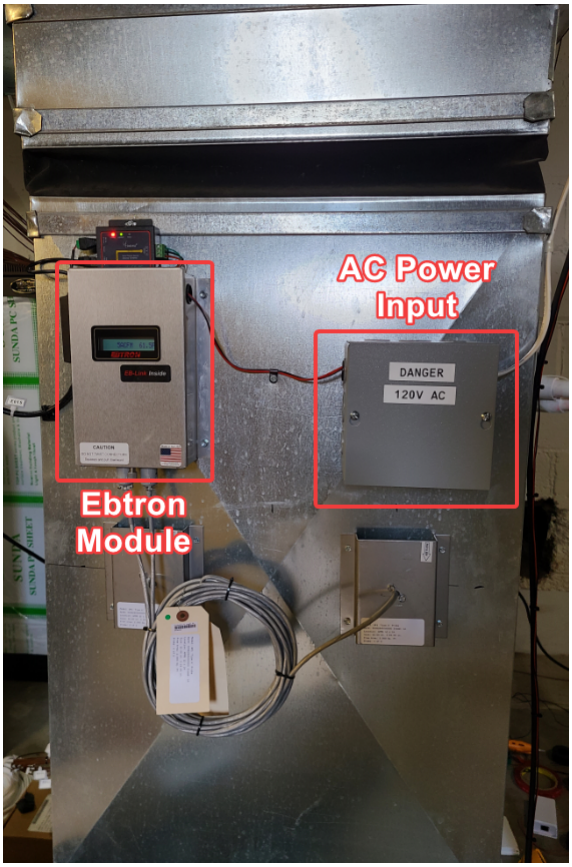

Figure 2.41. Instrumented Ebtron airflow module on the indoor heat pump unit.

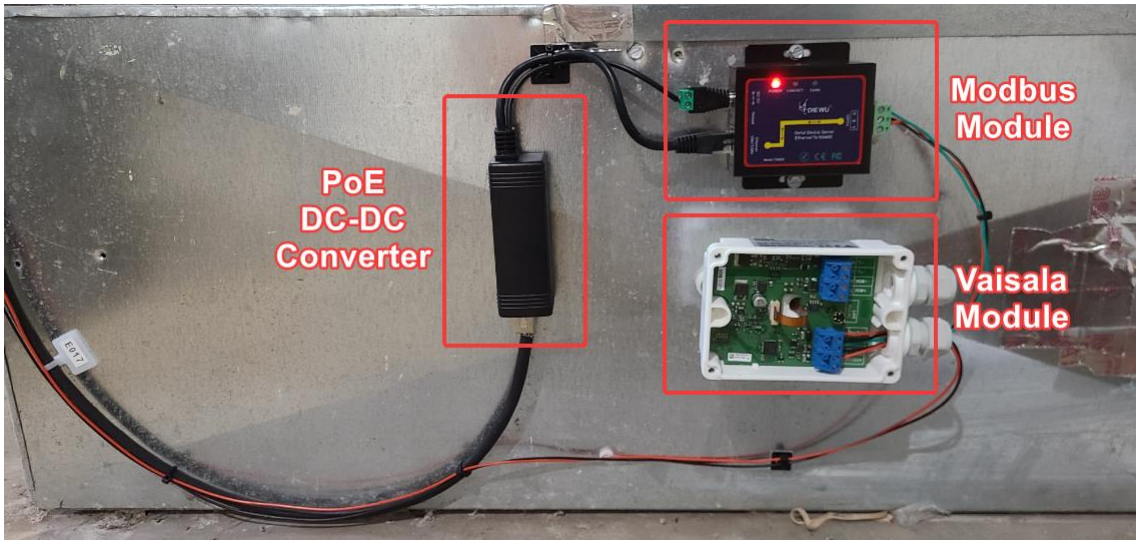

Figure 2.42. Instrumented Vaisala temperature and relative humidity module on the indoor heat pump unit.

tures can be measured in the range of −40 °C to 60 °C with an accuracy of ±0.2 °C. Relative humidity measurements are supported in the range of 0 to 100%, with accuracies between ±2% and ±4% depending on the current temperature setpoint range. The instrumented Vaisala system is shown in Figure 2.42.

2.3.3 Building Instrumentation

Each room of the DC Nanogrid House is outfitted with a prototype IoT board, which supports the collection of a wide array of building metrics. Every IoT board is identical in construction, and includes:

- 48 VDC to 5 VDC PoE power supply / DC-DC converter
- Raspberry Pi 4 Model B 4GB single board computer (SBC)
- ESP32 Espressif system on a chip (SoC) microcontroller
- Flying Fish MQ-7 gas sensor
- DHT22 temperature and relative humidity sensor
- BME280 environmental sensor
- MAX4465 microphone sensor
- GY-49 ambient light sensor
- Passive infrared (PIR) motion sensor

Power and communication are simultaneously provided using a gigabit PoE CAT6A RJ45 cable connected to the on-board PoE splitter. A summary of each data source and its corresponding measurement range and accuracy (if applicable) is detailed in Table 2.6, and an image of the prototype IoT board is demonstrated in Figure 2.43. The development of the modules, data collected, and software implementation is discussed in further detail in Chapter 5.

Table 2.6. Instrumented building IoT sensor specifications.

Sensor Type	Chip Name	Measurement Range	Accuracy
Air Quality	MQ-7	[20 ppm, 2000] ppm CO2	N/A
Environmental	DHT22	[0, 100] % RH [-40, 80] °C	±2% RH ±0.5 °C
Environmental	BME280	[0, 100] % RH [-40, 85] °C [30, 110] kPa	±3% RH ±1.0 °C ±0.1 kPa
Sound	MAX4466	[20, 20000] Hz	N/A
Light	GY-49	[0.045, 188000] Lux	N/A
Motion	PIR	[-90, 90] °	N/A

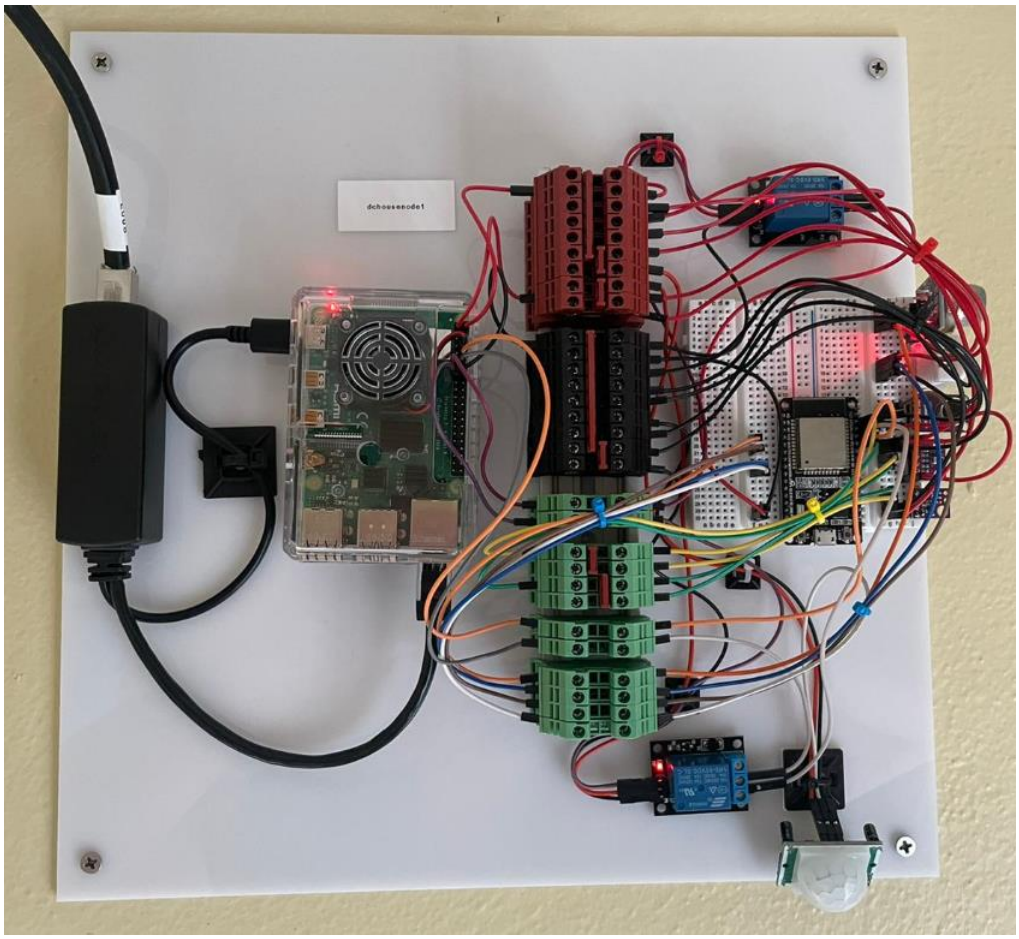

Figure 2.43. IoT prototype board used to instrument each room of the DC Nanogrid House.

2.3.4 Local Weather Station

A significant impact to building energy consumption arises from climate and local environmental conditions. As indicated in Figure 1.15, space heating, cooling, and water heating represent the largest categories of energy consumption across all U.S. households, and are directly impacted by these conditions. Previous research has revealed that weather conditions can significantly impact HVAC energy consumption, lighting utilization, and potential renewable energy generation from sources such as wind and solar [114]. Monitoring of local weather conditions enables direct feedback of these operations, and establishes an understructure for forecasting future conditions, both internal and external to a building. This is particularly meaningful for settings with integrated renewable energy sources, which are especially volatile to dynamic environmental circumstances [115]. In these situations, substantial energy fluctuations can occur within timescales of seconds and minutes rather than hours or days, prompting additional instrumentation to sufficiently leverage such resources.

While the primary objective of this research is to implement a novel DC electrical distribution system in a residential use-case, achieving enhanced energy efficiency is the overarching goal. As a result, investigation into possible instrumentation to support equipment specifications and potential areas of improvement revealed the benefit of installing a hyperlocal weather station directly adjacent to the home. Utilization of environmental measurements could yield insights into anticipated solar power generation, projected thermal load and demand, ambient lighting needs, and opportunities to implement machine-learning control of individual appliances and loads in the building. In addition, forecasted energy production and consumption could also be used to manage onsite battery energy storage and distribution to optimize electrical energy consumption from the external macrogrid and internal nanogrid. These objectives can be achieved through the division of forecasts into short-term (minutes, hours, and days), medium-term (months and seasons), and long-term (years) categories driven by fuzzy logic or neural-network based algorithms [116], [117]. These forecasts can then be supplied as inputs into the DC House's EMS and BMS to drive desired control methodology.

The weather station's sensor specifications are described in Table 2.7, and the installed structure on the DC Nanogrid House is depicted in Figure 2.44. The integration and analysis of the collected data along with the software development for this system are discussed in further detail in Chapter 5.

Figure 2.44. DC Nanogrid House weather station installation.

Figure 2.45. Waterproof Carflex conduit PoE routing from weather station controller to the DC House and connected radiation shield.

Figure 2.46. Close-up view of the weather station wind vane, anemometer, and light sensor.

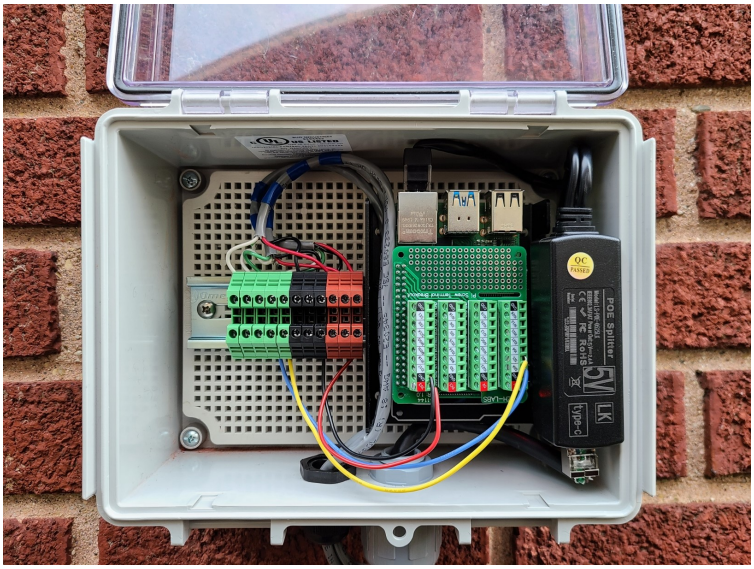

Figure 2.47. Waterproof enclosure containing terminal connections, SBC controller, and PoE input.

Table 2.7. Instrumented weather station sensor specifications.

Sensor Model	Sensor Description	Measurement Type	Communication Interface
SI1145	Ambient Light Sensor	UV Index/Infrared/Visible Light	I2C
SS451A	Omnipolar Hall Effect Sensor	Wind Speed/Precipitation Level	PWM
AS5600-ASOM	Hall Effect Sensor	Wind Direction	I2C
BMP280	Digital Pressure Sensor	Pressure	I2C
MCP9808	Digital Temperature Sensor	Temperature	I2C
HTU21D	Digital Relative Humidity Sensor	Relative Humidity	I2C
SGP30	Digital Multi-Pixel Gas Sensor	TVOC, CO2	I2C

2.4 Building and Equipment Energy Consumption Performance Analysis

2.4.1 Survey of Heat Pump Field Testing

Multiple studies have been conducted detailing test setup and configuration for heat pump energy analysis. One such study acknowledges that heating in colder climates can consume up to 60% of the total energy expended each year. Further supporting this is a DOE analysis, which revealed that buildings in the U.S. represent approximately 40% of the total energy consumed across all categories. With this information, the study sought to examine heat pump energy usage inside a military barracks through a demonstration of practical field testing at Camp Atterbury near Edinburgh, Indiana. In this particular environment, two individual rooms were studied and supplied by two independent HVAC systems. The building material was established on a concrete slab with stone tiling, and walled by concrete cinderblocks. An attic above the rooms contains insulated ductwork within an unconditioned space. The heat pump and other HVAC equipment were housed outside the barracks in an unconditioned mechanical room. This study identified set points for heating and cooling to be 20 °C to 23.3 °C, respectively. The complete area of the barracks was measured to be 488 m^2, divided evenly between both rooms [118].

Another study surveyed 22 homes in the Phoenix, AZ area to assess the current operating performance of their heat pumps against the manufacturer-specified capacity. Proctor [119] discovered that a nontrivial number of the units installed possessed suboptimal performance, with a meager 18% being correctly charged with refrigerant. The homes sampled within this

study were also discovered to be noncompliant with ASHRAE ventilation standards up to 82% of the time. The average house surveyed was a three-bedroom home containing an attic, with approximately 195 m^2 of floor space. 16 of the 22 homes contained one air conditioning system, while the remainder possessed two. Blower door experiments were performed to observe the level of air infiltration into the homes, with the study results revealing 75% of the samples falling below the minimum ventilation criteria of the referenced ASHRAE 62-1989 standard [120]. To resolve these substandard performance deficiencies, Proctor recommended better feedback to the technicians installing the HVAC systems, and increased accountability for all parties involved to comply with published manufacturer and building standards.

Research performed at the ReNEWW (Retrofitted Net-zero Energy, Water, and Waste) House project directly next door to the DC House investigated HVAC performance in a hybrid air-hydronic system to achieve net-zero energy. This study revealed the improvement of the system effectiveness measured in kWh/°C during various heating seasons. The ReNEWW House is also a 1920's era style home, which underwent a significant renovation process to improve the building's energy efficiency and reduce consumption. This included the replacement of a natural gas furnace and split-system air condition unit with the air-hydronic system discussed in this study. One of the primary motivations behind this research involves the lack of attention on existing residential structures; while new buildings are often the concentration of energy improvement efforts and associated energy-saving legislation, existing buildings require similar attention in the way of retrofit and renovation. Caskey and Groll [121] recognize new home constructions constitute approximately 14% of existing homes, while those built before 1980 represent over 50% of the population. This is a challenging situation which can be even further strained by protection and preservation societies and city ordinances.

2.4.2 Preliminary Building Improvements Analysis

A key theme of the DC Nanogrid House project surrounds the improvement of energy efficiency and reduction of overall energy consumption, primarily by means of electrical interface. However, electrical and thermal energy management are closely linked, and as

such are closely evaluated synchronously in this study. As described in the previous section, the house was fully instrumented with electrical and thermal instrumentation to provide monitoring across a variety of devices and inputs. Due to the home's geographic location, it subsequently endures temperatures below freezing for at least four months of the year on average. Based on this information, the heating and cooling devices were anticipated to consume the most amount of energy over the course of the year. Data collected from 2018 confirms this hypothesis, as illustrated in Figure 2.48 and 2.49. Motivated by this information, the heat pump has been targeted as a priority for electrical retrofit to DC power.

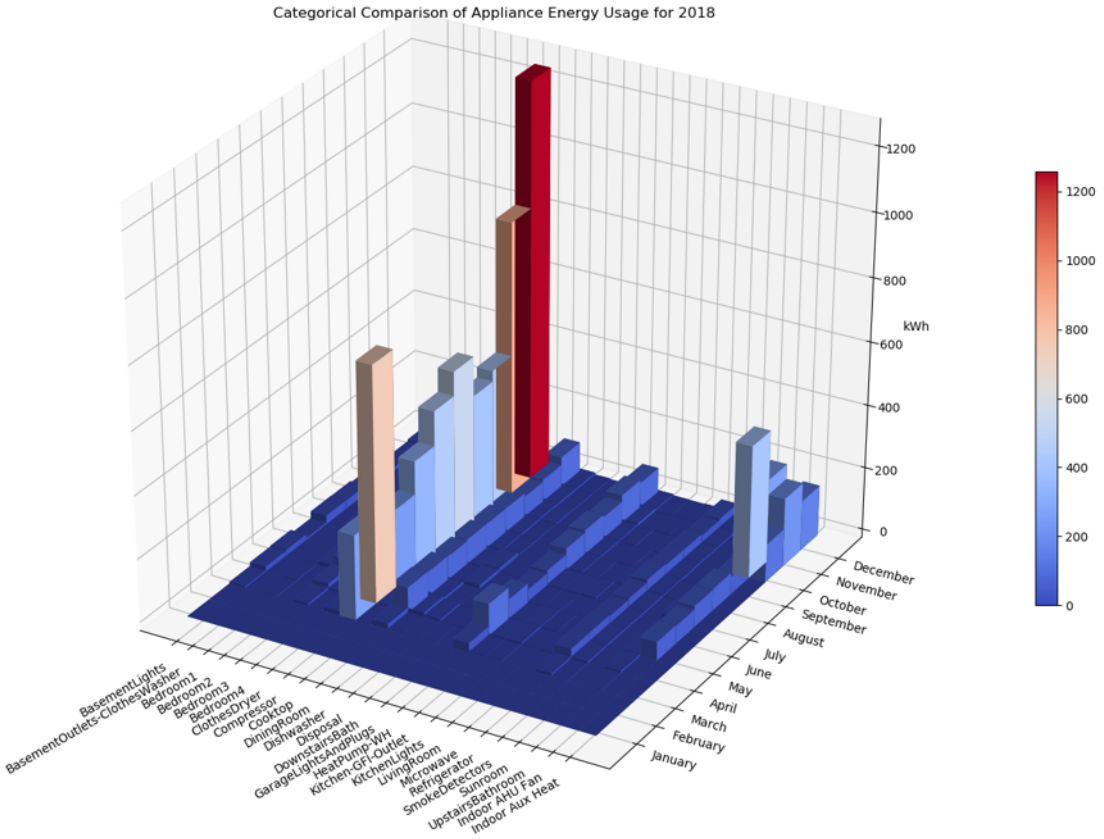

Figure 2.48. Categorical energy consumption by device in the DC Nanogrid House during 2018 measured in kWh.

Consistency of heating and cooling schedules across both heat pump units was essential for establishing a reference point of comparison. Owing to the increased capacity of the variable-speed heat pump, the evaluation of energy consumption is performed on the heat

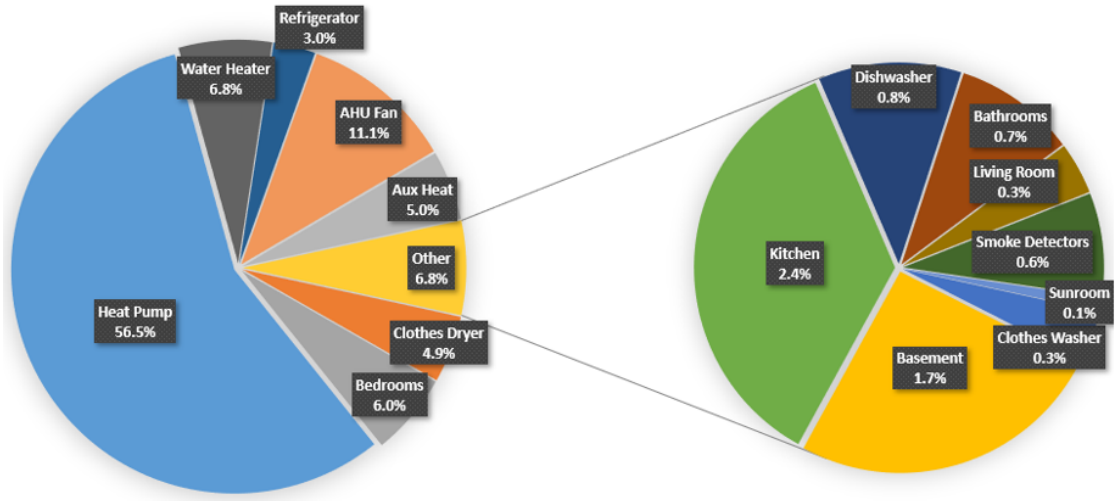

Figure 2.49. Categorical energy consumption by device in the DC Nanogrid House during 2018 measured by percentage.

pump unit and the house as a composite, rather than equipment versus replacement equipment. The timeline shown in Table 2.8 and the corresponding research context therefore develop three scenarios to analyze:

1. Fixed-Speed Heat Pump without Insulation
2. Fixed-Speed Heat Pump with Insulation
3. Variable-Speed Heat Pump with Insulation

The results of this research examine Scenario 1 against Scenario 2, and Scenario 1 against Scenario 3. Data used to investigate these findings was generated using electrical data collected from the EMCB modules described in Section 2.3.1, and historical weather data obtained from multiple National Oceanic and Atmospheric Administration (NOAA) sources.

The method of analysis performed is similar to that shown in Caskey and Groll (2017), utilizing the heating degree day (HDD) and cooling degree day (CDD) terminology. Using hourly weather data collected by NOAA from stations near West Lafayette, IN, these values can be calculated using the following formulae detailed in Equations 2.1 and 2.2.

$$HDD = 1hr \times (18.3°C - T_{Avg,Ambient}) \times \frac{1day}{24hr} \tag{2.1}$$

Table 2.8. DC Nanogrid House building modification events and timeline.

Scenario Name	Modification Description	Event Date
Scenario 1	Baseline Period – Fixed-Speed Heat Pump	04/01/2018 – 08/31/2018
Scenario 2	Insulation Installed	09/01/2018 – 10/18/2018
-	Variable-Speed Heat Pump Installed	10/18/2018 – 10/22/2018
Scenario 3	Evaluation Period	10/23/2018 – 04/01/2019

Table 2.9. Heat Pump monthly energy and CDD system effectiveness summary.

Date	CDD [Days]	CDD [°C]	Heat Pump Energy [kWh]	Heat Pump Energy/CDD [kWh/°C]
May, 2018	29	104.18	233.43	2.24
June, 2018	29	124.64	359.30	2.88
July, 2018	26	124.71	453.00	3.63
August, 2018	31	151.89	529.50	3.49
Scenario 1 - Total	**115**	**505.41**	**1575.23**	**3.12**
September, 2018	17	89.21	298.03	3.34
October, 2018	9	32.39	92.69	2.86
Scenario 2 - Total	**26**	**121.61**	**390.72**	**3.21**

$$CDD = 1hr \times (T_{Avg,Ambient} - 18.3°C) \times \frac{1day}{24hr} \tag{2.2}$$

A histogram of weather statistics for the West Lafayette, IN area between April, 2018 and April, 2019 is illustrated in Figure 2.50, with average daily temperatures organized into bin sizes of 2.75 °C. As the histogram reveals, the heating and cooling temperature modes are approximately 22.7 °C and 0.7 °C, respectively. The strategy of binning temperature data is aligned with the ASHRAE methodology to evaluate heat pump performance [122]. Based on the timeline of events in Table 2.8, an HDD characterization allows for a comparison between Scenario 1 and Scenario 3, while a CDD allows for a comparison between Scenario 1 and Scenario 2. Finally, the monthly system effectiveness and energy usage are tabulated over the course of the year in Table 2.9 and Table 2.10, allowing for a more direct comparison.

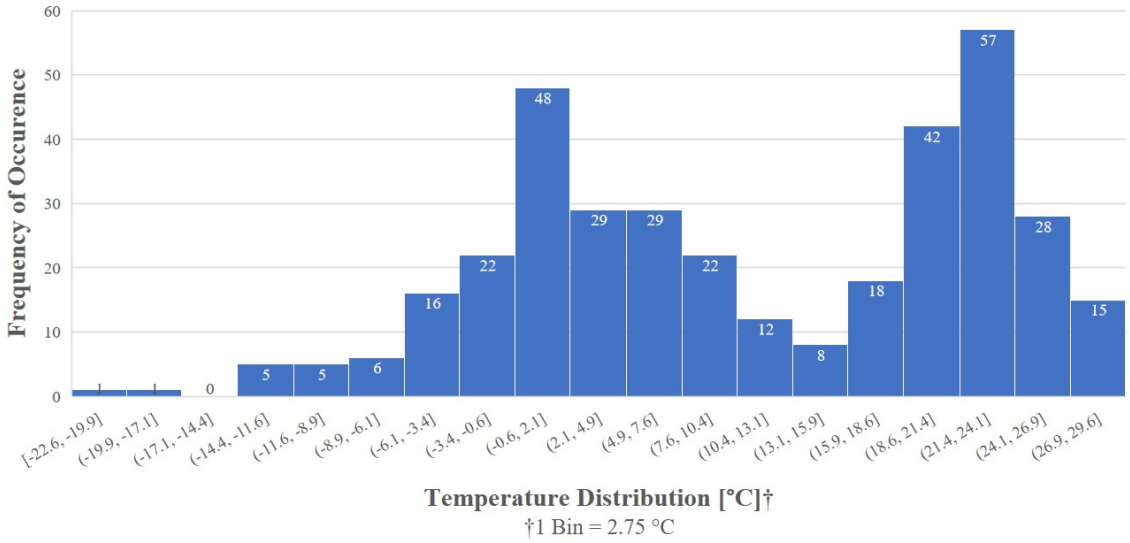

Figure 2.50. Histogram of daily average temperatures in West Lafayette, In between April, 2018 and April, 2019.

Table 2.10. Heat Pump monthly energy and HDD system effectiveness summary.

Date	HDD [Days]	HDD [°C]	Heat Pump Energy [kWh]	Heat Pump Energy/HDD [kWh/°C]
April, 2018	29	334.05	770.69	2.31
May, 2018	2	3.36	5.97	1.78
July, 2018	1	1.51	5.17	3.42
Scenario 1 - Total	**32**	**338.92**	**781.83**	**2.31**
September, 2018	7	21.46	124.69	5.81
October, 2018	22	223.43	339.11	1.52
Scenario 2 - Total	**15**	**112.14**	**273.43**	**2.44**
November, 2018	30	485.72	872.29	1.80
December, 2018	31	533.66	1262.47	2.37
January, 2019	31	697.34	2054.62	2.94
February, 2019	25	472.58	1275.81	2.70
March, 2019	30	475.64	1155.82	2.43
Scenario 3 - Total	**156**	**2753.1**	**6810.18**	**2.47**

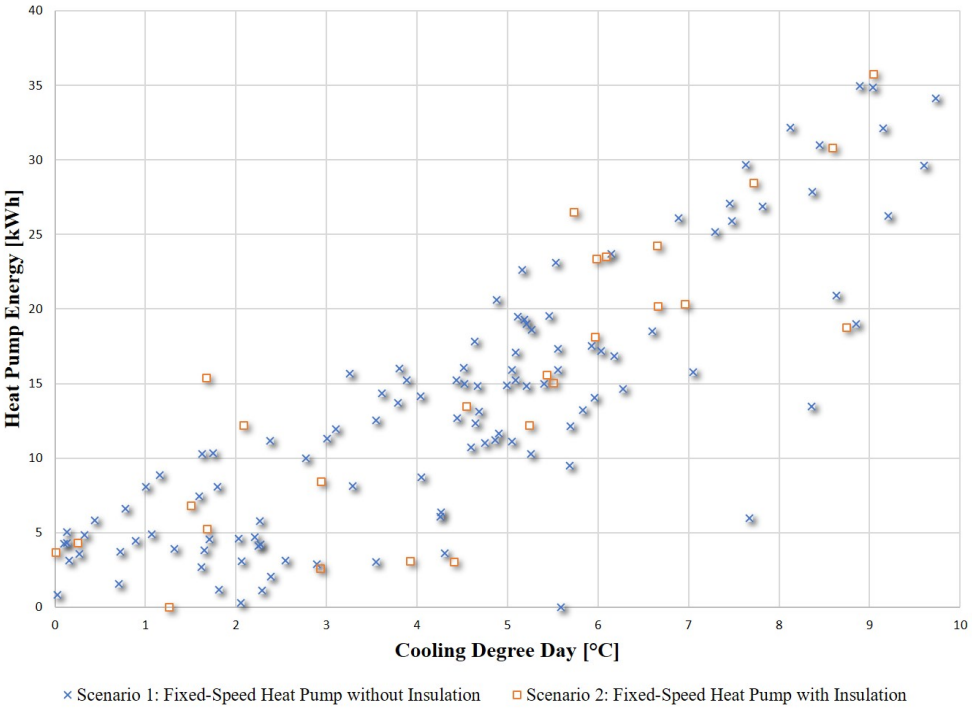

Figure 2.51. Heat pump system energy consumption as a function of CDD.

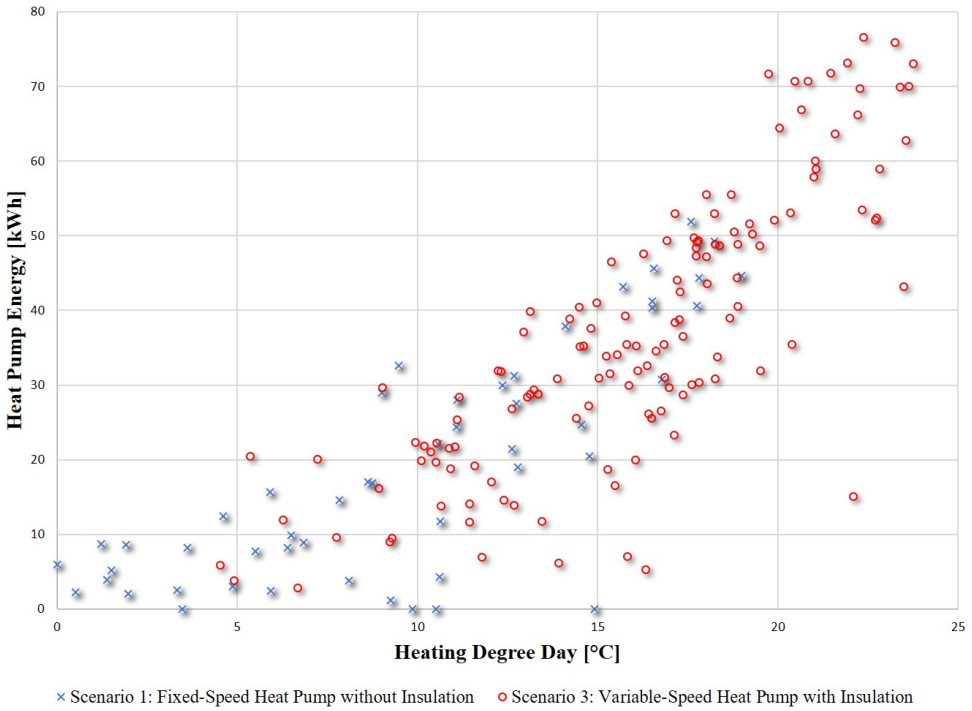

Figure 2.52. Heat pump system energy consumption as a function of HDD.

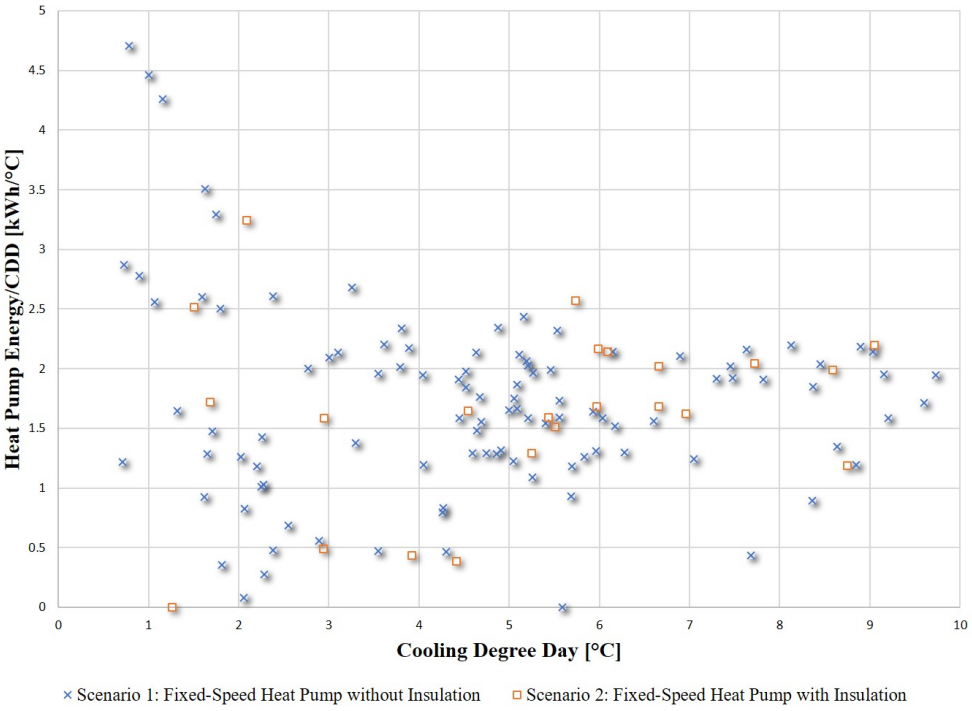

Figure 2.53. Heat pump system effectiveness as a function of CDD.

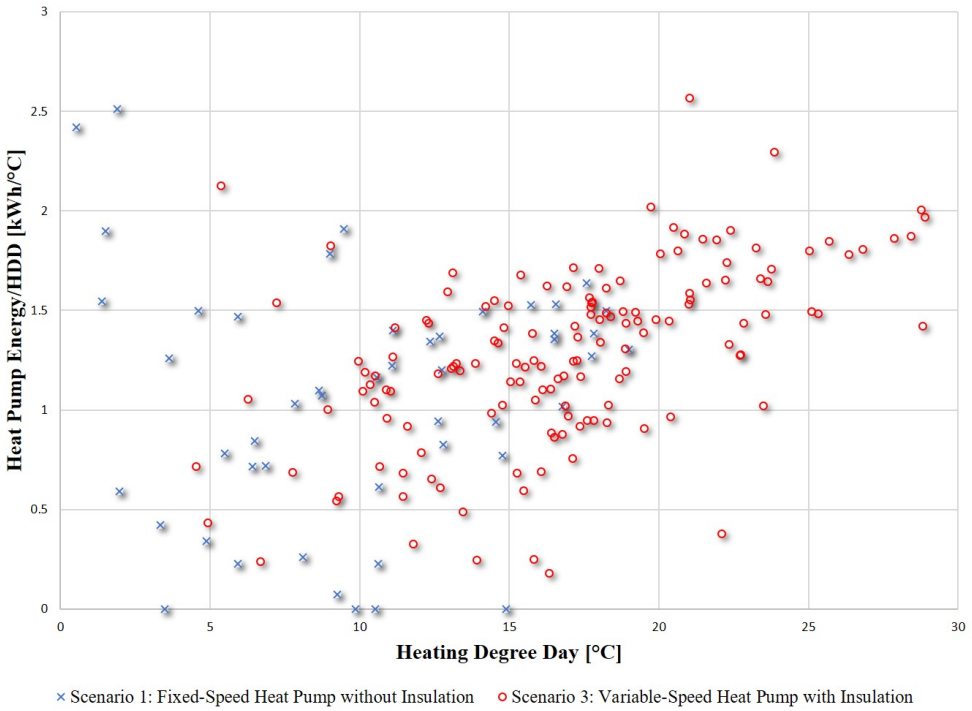

Figure 2.54. Heat pump system effectiveness as a function of HDD.

A major finding in Figures 2.51 and 2.52 is the consistency of heating and cooling energy with respect to the daily HDD or CDD value. It can be seen from Figure 2.51 that the Scenario 1 evaluation of just the fixed-speed heat pump without any insulation revealed a coefficient of determination, or R^2, of 0.65, and the Scenario 2 evaluation of the fixed-speed heat pump with insulation yielded an R^2 of 0.70. A similar increase is observed in Figure 2.52, with the Scenario 1 evaluation revealing an R^2 of 0.28 and the Scenario 3 evaluation of the variable-speed heat pump with insulation yielding an R^2 of 0.76. The R^2 value provides an explanation for the variation in the heat pump energy expended as a function of the heating or cooling degree day value. The HDD evaluation in Table 2.10 is of particular interest, owing to the significant increase in heating degree values towards the end of 2018 and beginning of 2019. These trends are confirmed in Figure 2.53 and Figure 2.54, which present decreased ratio of energy expenditures even at extensive swings in the HDD and CDD values. Over the course of subsequent heating and cooling seasons, the effectivity ratios summarized in Table 2.9 and Table 2.10 are anticipated to follow in a decreasing manner.

This particular study sought to evaluate the performance improvement of a heat pump amongst varying environmental conditions, equipment configurations, and home renovations. The results captured here reflect a statistical improvement in the consistency of heating and cooling energy expended by the heat pump as a function of time, which aligns with the installment of insulation into the home's walls. Over the one-year period of study in the West Lafayette, IN region, the greatest frequency of modal ambient temperatures above and below the 18.3 °C (65 °F) reference point occurred at 24 °C (75.2 °F) and −1 °C (30.2 °F), or HDD and CDD values of 19.3 °C (34.8 °F) and 5.7 °C (10.2 °F), respectively. When considering ambient temperature recordings in localized temperature bins around these values, a comparison from Scenario 1 to Scenario 2 at the CDD value reveals a change in system effectiveness from 3.12 kWh/°C to 3.21 kWh/°C, or approximately 2.9%. Performing a similar comparison of Scenario 1 to Scenario 3 at the HDD value reveals an improvement of system effectiveness from 2.31 kWh/°C to 2.47 kWh/°C, or approximately 6.5%. The discrepancy in improvement between Scenario 1 to Scenarios 2 and 3 can be explained by the

deficiency of data points obtained during Scenario 2, which is confirmed by the overall system improvement at Scenario 3.

2.4.3 Building Modifications Longitudinal Study

Continuing the analysis described in Section 2.4.2, a complete longitudinal study was conducted on the summation of all equipment modifications and building renovations occurring since the inception of the DC Nanogrid House project. The building and landscape pose an additional level of complexity to its overall objectives owing in part to its historical nature; however, its composition represents a more realistic depiction of the challenges facing common residential buildings in existence today [89]. The National Register of Historic Places (NRHP) database currently estimates over 90,000 individual historic locations in the U.S. territories as of April, 2008 [123]. Thus, holistic examination of building energy studies must critically consider the options available for renovating and refurbishing historical structures, yielding further importance to the outcomes of this study.

A summary of all data sources employed in this study's analysis is summarized in Table 2.11. These sources serve the dual purpose of evaluating energy consumption over the project period, and also providing a baseline of AC energy usage to compare against the subsequent DC implementation.

Table 2.11. Longitudinal study data source summary.

Label	Data Source	Data Reported	Reporting Frequency	Reporting Period
A	Utility Readings	Energy Consumption	Monthly	January 2018 - Present
B	Wi-Fi Circuit	Energy Consumption Power Quality Electrical Supply Characteristics	15 Minutes	March 2018 - September 2019
C	Wi-Fi Current Transformers	Energy Consumption Power Quality (limited) Electrical Supply Characteristics	Minutely	October 2019 - Present
D	Heat Pump Manufacturer	Energy Consumption	Secondly	July 2019 - November 2019
E	Regional Weather Station	Local Weather Data	Hourly	January 2018 - Present

While aggregate building and individual appliance energy data is available over the entire period of study, specific insights from electrical characteristics are limited to those collected

in source B in Table 2.11. The original Wi-Fi circuit breakers installed provided comprehensive characteristics of the AC load panels, including phase frequency, phase voltage, phase current, real power, reactive power, apparent power, and power factor measurements every 15 minutes. The current transformers in source C instrumented after this point provide voltage, real power, and power factor approximations, but do not yield reactive or apparent power measurements. In addition, source B data was made available as MongoDB export, and can be sampled or analyzed indefinitely. Data collected by source C is made available only over a representational state transfer (RESTful) API, and thus can only be queried during a finite window of time. Furthermore, only HTTP requests made each minute from the API can retrieve specific power quality information, requiring a third-party polling solution to be implemented and Wi-Fi service to be continually available. As a result, distinctive insights into individual device characteristics are variable and inconsistent after the period outlined in source B.

The devices represented in source B also experienced some disruptions during their period of operation. Like the devices in source C, they also operated on Wi-Fi and were vulnerable to service interruptions and other network issues. Whenever a network dropout occurred, data continued to be collected internally until service was restored. After this point, the accumulated data was then posted to the database at the next timestamp (rather than backfilling the previously missed timestamps). As a result of this behavior, preceding days with missing data can only be approximated by an average of the accumulated data posted at the next available timestamp.

Since each modification made to the DC House or its equipment will fundamentally affect its intrinsic thermodynamic characteristics, a baseline is necessary upon which to compare other measurements against. There are a variety of ways in which a building's average dry-bulb temperature can be influenced, including appliance and electronic heat dissipation, occupant body heat transfer, solar irradiance incident on the house's surface, and quality of a structure's insulation (Tabatabaei et al. 2017). Periods between individual modifications to the DC House do not afford sufficient time to reassess structural thermodynamic quantities for each new configuration, and thus effective energy expenditure in the form of space heating and cooling during each period is compared against the baseline evaluation period rather

than establishing individual balance point temperatures for each new configuration. Under this strategy, the DC House system effectiveness can be calculated during heating and cooling cycles against the measured external ambient temperature, and improvements are indicated by relative comparison to the baseline period.

This approach intuitively alludes to the HDD and CDD nomenclature described in Section 2.4.2, which is also used extensively in ASHRAE standards and other building energy studies [122], [124]–[126]. Typically, HDD and CDD values are identified based on a building's inherent balance point temperature, but the aforementioned methodology eschews this step and instead selects common baseline values upon which all configurations are analyzed against. To this end, a reference balance point temperature of 18.3 °C (65 °F) is established to determine heating and cooling degree values during a given configuration period. Since these values can be quantified by any unit of time, each period is discretized into hourly quantities, and therefore the respective heating degree and cooling degree quantities can be expressed using Equations 2.3 and 2.4.

$$Heating\,Degree\,Hours\,(HDH) = \sum_{j=day}^{period} \sum_{i=hour}^{24} (T_{balance} - T_{i,ambient}) \tag{2.3}$$

$$Cooling\,Degree\,Hours\,(CDH) = \sum_{j=day}^{period} \sum_{i=hour}^{24} (T_{i,ambient} - T_{balance}) \tag{2.4}$$

In these equations, $T_{balance}$ signifies 18.3 °C (65 °F). Using these definitions, weather data for each configuration period can be processed and binned appropriately with its associated heating or cooling designation and magnitude.

Over the total evaluation period from March 22nd, 2018, to June 1st, 2020, six major improvements were performed to the house, transforming its ability to effectively heat and cool the building space. Throughout this timeframe, many notable weather conditions occurred, particularly the infamous polar vortex of 2019 [127]. Based on this, the consideration of meteorological data is essential for suitable analysis during each configuration. Table 2.12 details each modification to the DC House, its respective identifier, and the period over which it initiated its impact. Every modification is assumed to be fully installed at the

beginning of its configuration period, and maintains its impact over all future periods (with the exception of the heat pump equipment replacement described in Configuration 2). As a result, each configuration's comparison to the original baseline period represents the relative improvements of the sum of all modifications performed up to, and including, the particular period under consideration. Each period and its encompassed hourly dry-bulb temperature is illustrated in Figure 2.55, and the relative hourly temperature difference to the selected balance point temperature is detailed in Figure 2.56.

Table 2.12. Longitudinal study configuration periods and descriptions.

Configuration Identifier	Description	Configuration Period	Days In Period
Baseline	Fixed-Speed Heat Pump Installed	03/22/2018 – 08/31/2018	163
Configuration 1	Foam-Injection Insulation Installed	09/01/2018 – 10/17/2018	47
Configuration 2	Variable-Speed Heat Pump Installed	10/18/2018 – 08/21/2019	308
Configuration 3	Basement Windows Repaired	08/22/2019 – 10/02/2019	42
Configuration 4	1st/2nd Floor New Windows Installed	10/03/2019 – 11/20/2019	49
Configuration 5	Resistive Heater Installed	11/21/2019 – 06/01/2020	194

Obtaining the contiguous heat pump energy consumption from sources B, C, and D described in Table 2.11 required an amalgamation of each data source and type over the entirety of the evaluation period. From source B, this amounted to an extraction of energy data collected every 15 minutes from the MongoDB file, and then totaling these values for each day. From source C, the RESTful API was polled minutely, downloaded and processed, and similarly totaled to determine each day's energy consumption. From source D, data obtained from the manufacturer was received in the form of real power draw at discrete intervals, usually in 1-2 second intervals. To obtain the energy consumption for these readings, the real power measurements were collected over a day, and converted to energy in kWh using the following formula described in Equation 2.5:

$$\begin{aligned} Energy\,Consumption\,[kWh] &= \sum_{configperiod} \int_{t_0=midnight}^{t_1=midnight} P(t)dt/3600 \\ &\approx \sum_{configperiod} \sum_{k=t_i}^{24hrs} P[k]\Delta t_i/3600 \end{aligned} \tag{2.5}$$

$P[k]$ represents the instantaneous power measured over a discrete interval, which is multiplied by the corresponding discrete time interval using a Riemann Sum representation, and finally

divided by 3600 to convert from kJ to kWh. Combining the energy data from sources B, C, and D, and then associating each day's heat pump energy consumption for heating or cooling usage culminates in the graphic shown in Figure 2.57. Similar in structure to Figure 2.56, heat pump energy consumption while hourly ambient temperature fell below the balance point is represented by heating above the x-axis, and correspondingly for cooling below the x-axis.

With the heat pump's energy consumption for heating and cooling operation obtained over the course of the entire evaluation period, this data can then be compared with the heating and cooling degree values presented in Figure 2.57. Summing the degree hours together over each day, as detailed in Equations 2.3 and 2.4, yields a net degree-hour total which can then be superimposed over the heating and cooling energy consumption shown in Figure 2.57. The result of this process is indicated in Figure 2.58, where the same heat

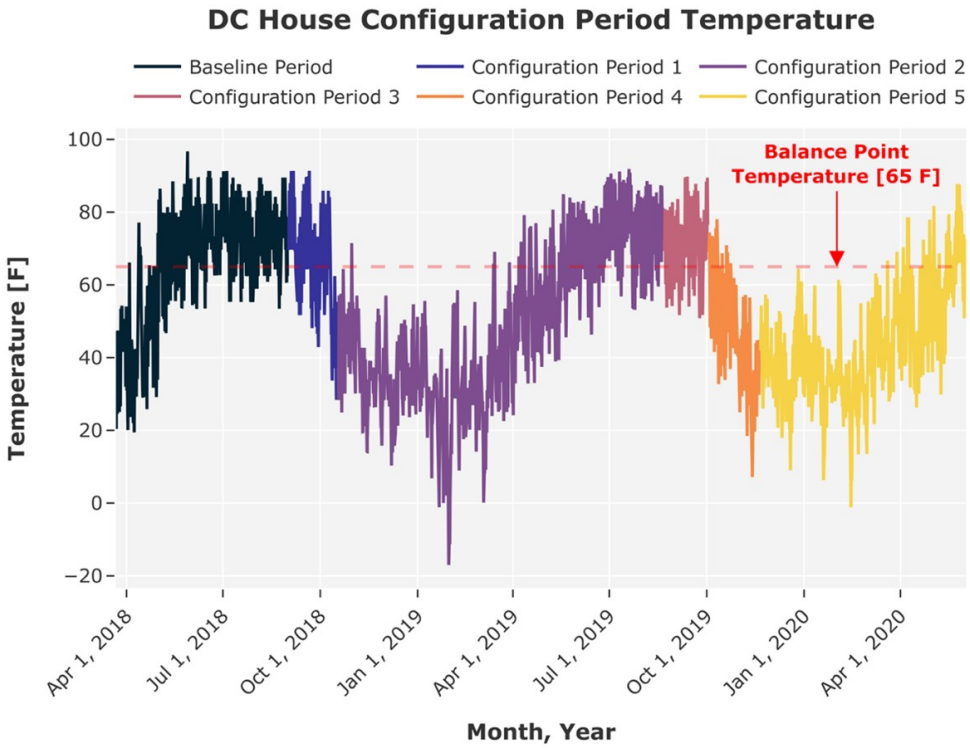

Figure 2.55. Configuration period ambient outdoor dry-bulb temperature reported in hourly intervals over the evaluation period.

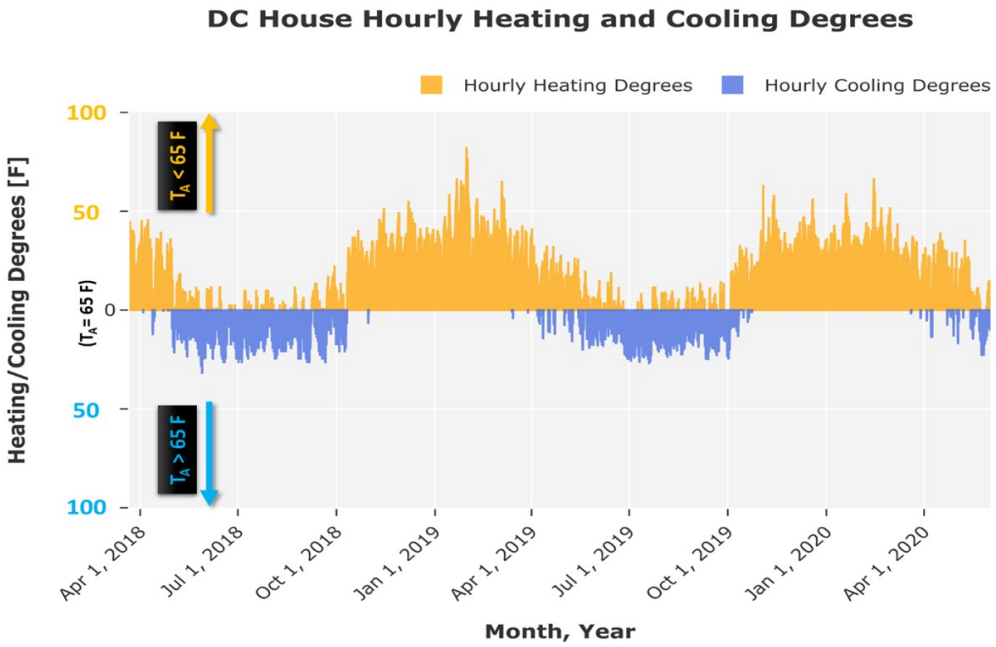

Figure 2.56. Ambient outdoor dry-bulb temperature reported in hourly intervals with respect to the balance point temperature (18.3 °C /65 °F) over the evaluation period.

pump energy consumption from Figure 2.57 is overlaid with the hourly degree totals for each day previously detailed in Figure 2.56.

Using the data collected in Figure 2.58 makes it possible to evaluate the heat pump system effectiveness over the duration of each configuration period. The effectiveness is a measure of the heat pump energy expended to provide heating or cooling to a space, with respect to the heating or cooling degree hours observed during its operation. For example, if the ambient temperature was observed to be 4.4 °C (40 °F) over one hour, thus giving a cooling-degree value of 13.9 °C (25 °F), and the heat pump used 50 kWh during that hour, its system effectiveness would be 3.60 kWh/°C-hr (25 kWh/°F-hr). If another hypothetical heat pump could sufficiently heat the same space using 25 kWh, its system effectiveness would instead be 1.80 kWh/°C-hour (1 kWh/°F-hr). Therefore, a smaller system effectiveness generally represents more efficient operation, so long as sufficient heating or cooling is provided to the space. Table 2.13 and Table 2.14 summarize these attributes over each individual configuration period.

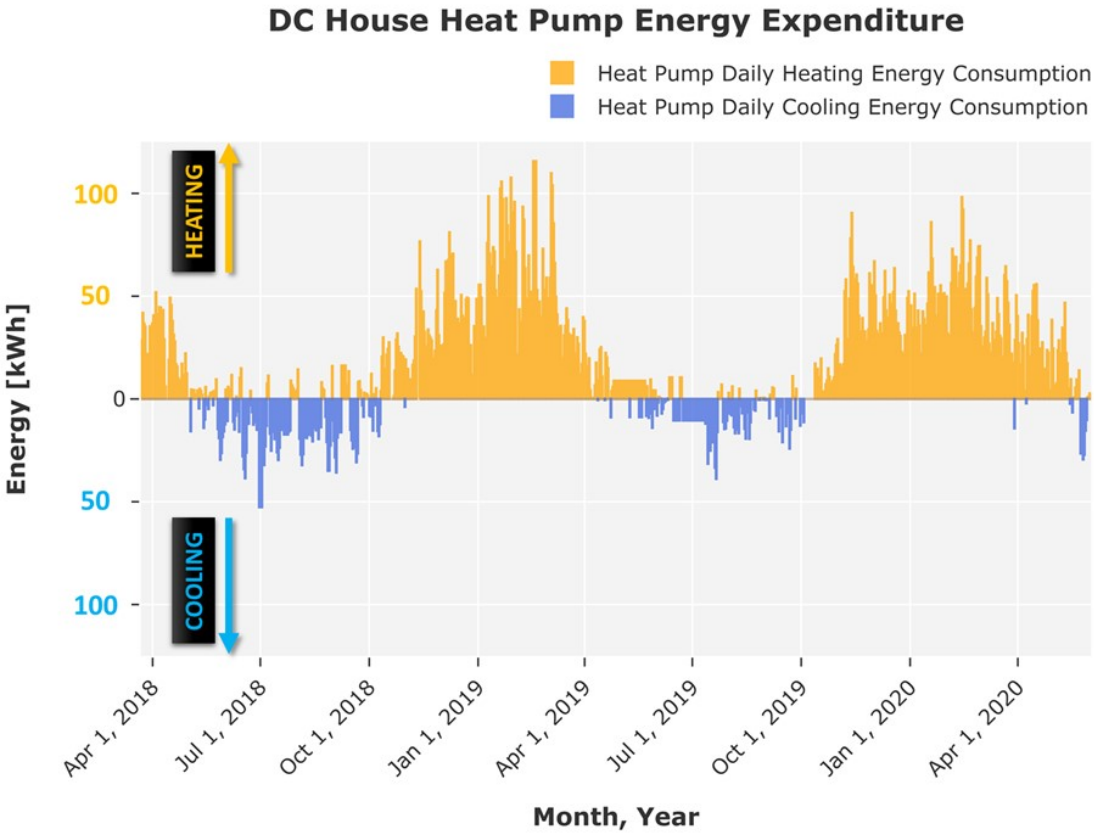

Figure 2.57. Daily heat pump energy consumption over the entirety of the evaluation period expressed in terms of heating and cooling operation.

The results of this project indicate the value of performing renovations to historical structures, as indicated in Table 2.13 and Table 2.14. If the representative improvement value from each configuration is multiplied by the weighted sum of heating or cooling hours it represents during the total evaluation period, the average improvement for heating and cooling energy efficiency is observed to be 2.38% and 31.3%, respectively. The modest gain with heating efficiency is certainly reasonable, as several configuration periods included exceedingly cold winters (especially the polar vortex endured in Configuration Period 2). Several additional factors would be valuable to supplement this data, such as infrared thermal scans of the home. In addition, the humidity of the inside and outside air could also be taken into account, as this also affects the comfortability of the indoor space and whether or not the residents elect to perform additional heating/cooling. In summary, the results shown in

this analysis indicate the usefulness of the degree-day methodology to perform comparative analyses of structural renovations, especially those with historical attributes.

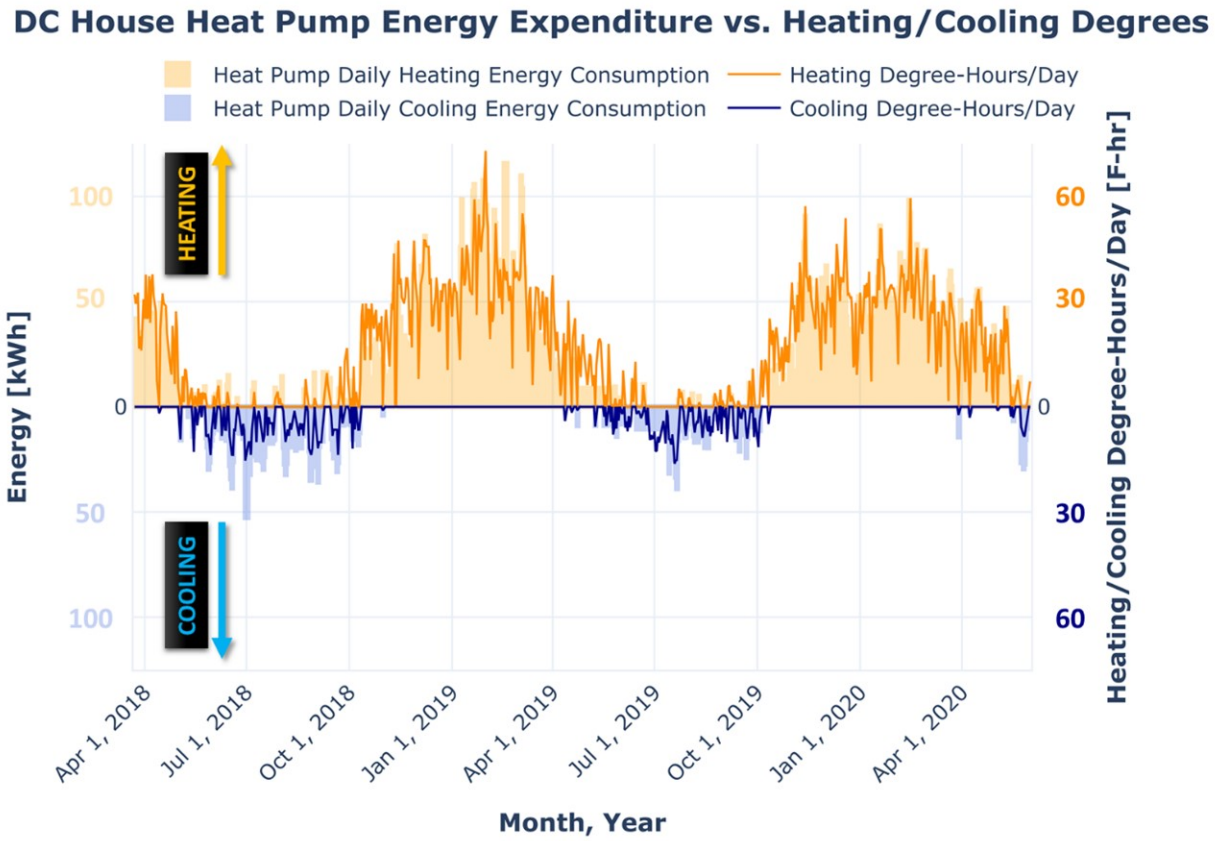

Figure 2.58. Daily heat pump energy consumption over the entirety of the evaluation period expressed in terms of heating and cooling operation.

Table 2.13. Heating system effectiveness by configuration period.

Configuration Identifier	Std. Dev. HDH/Day [°F-hr/day]	Avg. HDH/Day [°F-hr/day]	Total HDH [°F-hr]	Heat Pump Energy [kWh]	System Effectiveness [kWh/°F-hr]	Improvement [%]
Baseline	12.26	15.26	23222.9	1269.3	0.0547	REF
Configuration 1	8.50	11.16	5334.1	258.1	0.0484	+11.5
Configuration 2	14.22	26.32	139639.0	7814.8	0.0560	-2.4
Configuration 3	3.48	4.83	1231.2	35.6	0.0289	+47.0
Configuration 4	11.87	21.57	22559.3	1058.2	0.0469	+14.2
Configuration 5	11.84	24.81	105087.5	6748.0	0.0642	-17.5
NET	13.47	24.18	298078.0	15914.8	0.0534	+2.38

Table 2.14. Cooling system effectiveness by configuration period.

Configuration Identifier	Std. Dev. CDH/Day [°F-hr/day]	Avg. CDH/Day [°F-hr/day]	Total CDH [°F-hr]	Heat Pump Energy [kWh]	System Effectiveness [kWh/°F-hr]	Improvement [%]
Baseline	6.44	10.38	24443.9	1530.5	0.0626	REF
Configuration 1	6.67	10.41	6507.5	407.8	0.0626	-0.1
Configuration 2	6.38	10.06	20602.7	850.2	0.0413	+34.1
Configuration 3	5.97	9.28	6778.6	172.2	0.0254	+59.4
Configuration 4	2.93	4.61	498.0	11.3	0.0226	+63.8
Configuration 5	5.73	7.09	2807.7	159.3	0.0567	+9.4
NET	6.34	9.54	37690.3	1600.8	0.0425	+31.3

3. APPLIANCE RETROFIT AND EXPERIMENTAL ANALYSIS

3.1 Motivation for DC-Retrofitted Appliances

A survey of modern devices and appliances reveals an extensive presence of DC-power consumption, which is traditionally satisfied through the use of AC to DC conversions at the point of use. In a residential setting, the proliferation of these conversion operations are frequently associated with undesirable performance characteristics, resulting in the loss of useful power. Converters are traditionally divided into one of four categories:

- AC →DC: Rectification
- DC →AC: Inversion
- DC →DC: Chopper
- AC →AC: Cycloconverter

Although all four serve specific purposes, the first three are primarily used in residential settings, especially rectification. Rectifiers can be found in nearly every household device, including HVAC systems, refrigerators, washers and dryers, TVs, computers, and many others. In DC-centered architecture, losses from rectification stages can be mitigated or eliminated entirely, increasing the overall efficiency of appliances and devices. Furthermore, in the case where the DC distribution voltage is different from the DC voltage needed in an individual device, DC-DC converters (i.e., choppers) are often at least as efficient, if not greater than, an AC-DC rectifier [128]. Several studies have outlined possible functional equivalents of traditional AC conversion processes for appliances and devices supplied by a DC architecture; an air-conditioning system and an LED system are demonstrated in Figures 3.1 and 3.2.

Using DC conversions can mitigate energy loss, improve system performance, and in a growing number of cases reduce the overall system cost and complexity. In addition, environments incorporating renewable energy generation sources can naturally integrate the

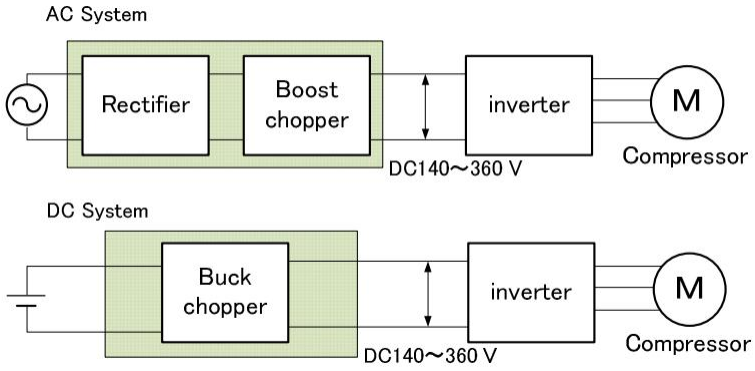

Figure 3.1. Functional equivalent AC system and DC system conversions for an air conditioner appliance [128].

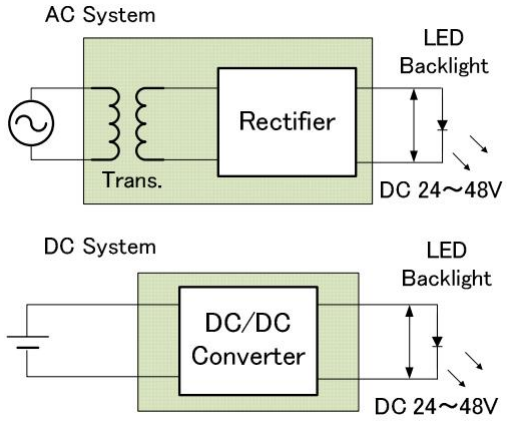

Figure 3.2. Functional equivalent AC system and DC system conversions for an LED device [128].

naturally generated DC energy without instituting a multitude of unnecessary rectification and inversion processes in between. Even in the case of equipment stipulating an AC voltage for a motor or drive, such as that illustrated in Figure 3.1, the supplied AC power from the input must still be initially rectified to a DC voltage. As a result, DC-centralized systems afford the opportunity to bypass rectification stages, and utilize a high-efficiency chopper if necessary. To summarize these benefits across all household devices, Figure 3.3 highlights the degree of benefit for individual loads and their respective device-type category [31]. Within this graphic, DC-connected and DC-converted loads would receive a measurable benefit from a DC distribution source. DC-indifferent loads would not inherently benefit from a

DC-source, and could either be voltage-agnostic (e.g., a heater) or implement a DC to AC inverter to achieve equivalent AC-supplied functionality.

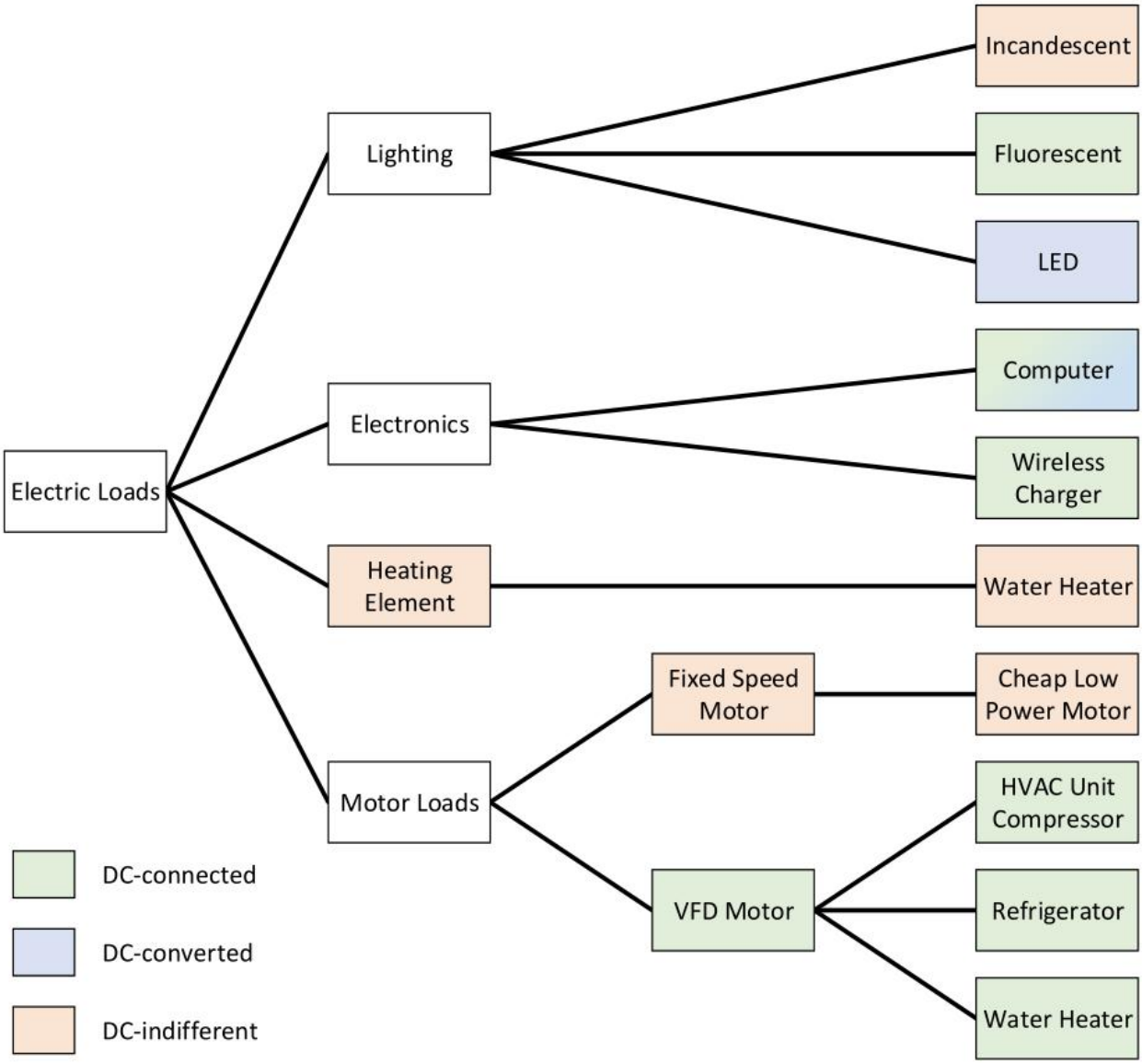

Figure 3.3. Degree of benefit for loads potentially connected to a DC distribution source [31].

3.2 AC Heat Pump Baseline Performance

One of the largest energy consumers in a residential setting is typically the heat pump equipment, providing heating and cooling to the home. A survey performed by the IEA affirms this, estimating that space heating and air conditioning represent up to 49% of average U.S. household energy consumption [129]. As a result, electrical retrofit of the heat pump from an AC to DC configuration affords a significant opportunity for energy savings and an increase in efficiency. To better understand its baseline AC electrical requirements, the off-the-shelf Trane 14 kW air-source variable-speed heat pump unit was closely studied during the summer of 2018. The electrical data used was processed from a MongoDB database provided by Duke Energy, and correlated with weather data obtained from NOAA. Electrical power characteristics of the heat pump over several months are shown in Figures 3.4, 3.5, 3.6, and 3.7, and energy consumption patterns are detailed in Figures 3.8, 3.9, 3.10, and 3.11. The electrical characteristics summarized by month are also tabulated in Table 3.1.

Table 3.1. Heat pump electrical characteristics during cooling months in 2018.

Month	**Average Power [kW]**	**Max Power** [kW]	**Energy Consumption** [kWh]	**Power Factor** [-]
May, 2018	0.312	3.363	223.620	0.992
June, 2018	0.523	3.250	359.303	0.990
July, 2018	0.769	4.460	551.840	0.989
August, 2018	0.718	3.187	513.479	0.992

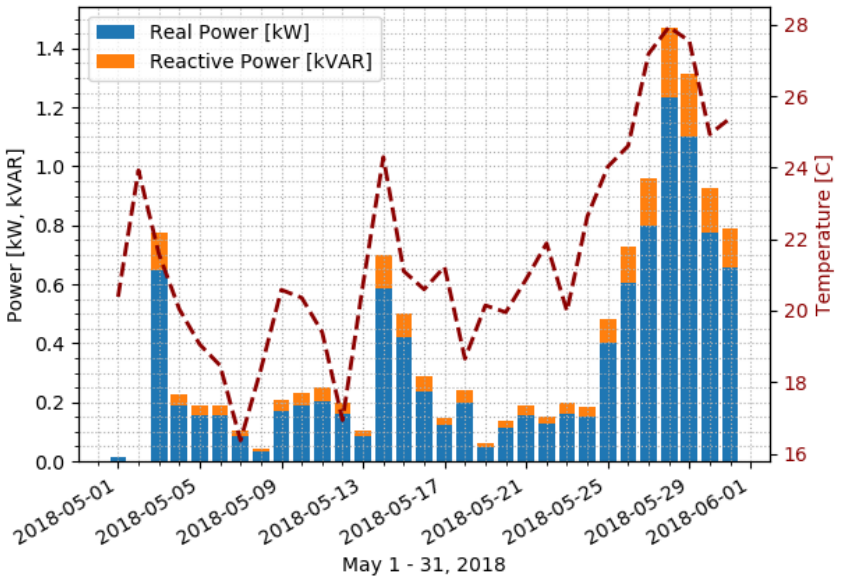

Figure 3.4. Heat pump daily real and reactive average power consumption in May, 2018.

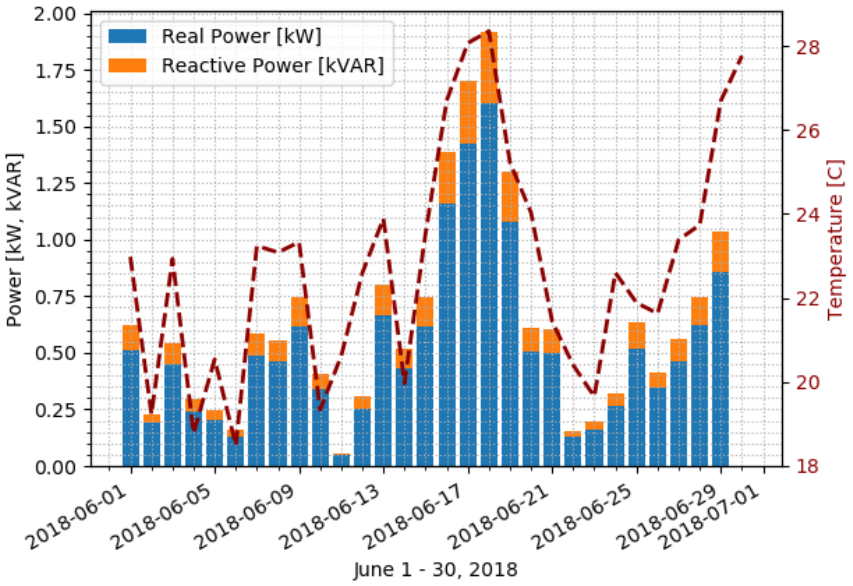

Figure 3.5. Heat pump daily real and reactive average power consumption in June, 2018.

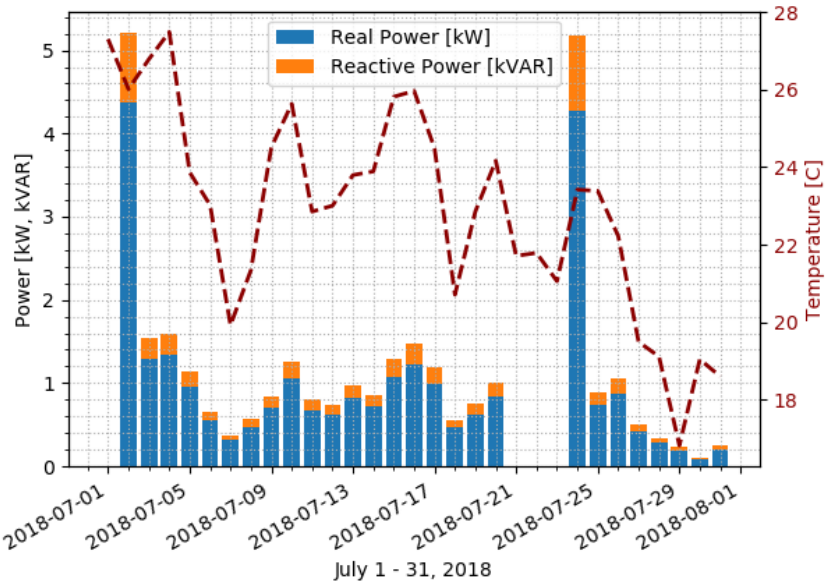

Figure 3.6. Heat pump daily real and reactive average power consumption in July, 2018.

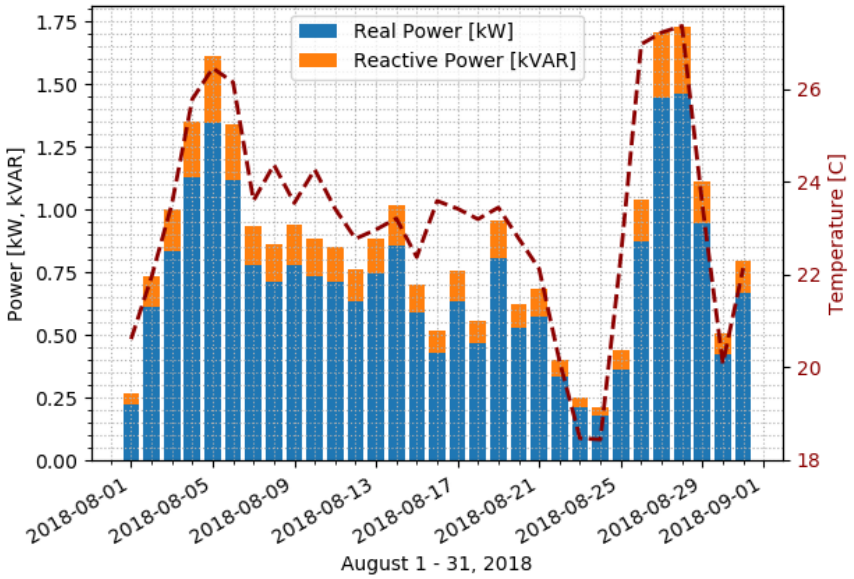

Figure 3.7. Heat pump daily real and reactive average power consumption in August, 2018.

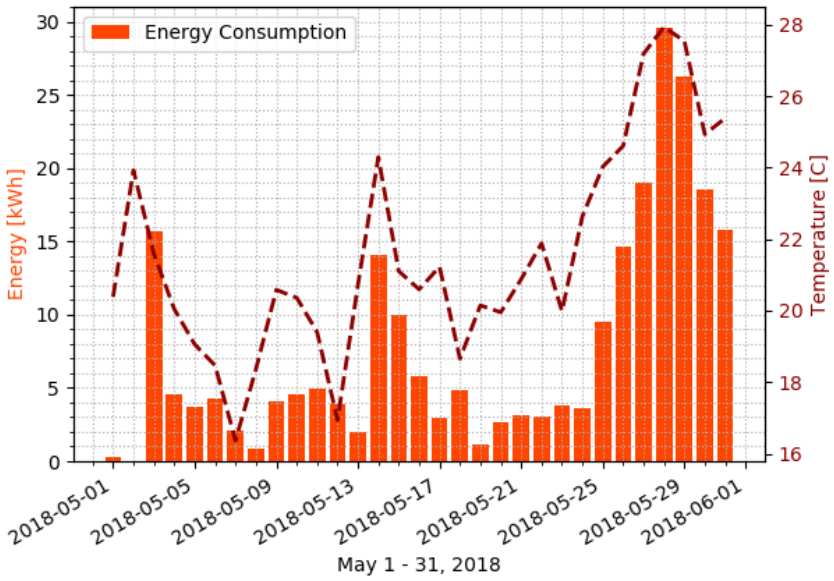

Figure 3.8. Heat pump daily average energy consumption in May, 2018.

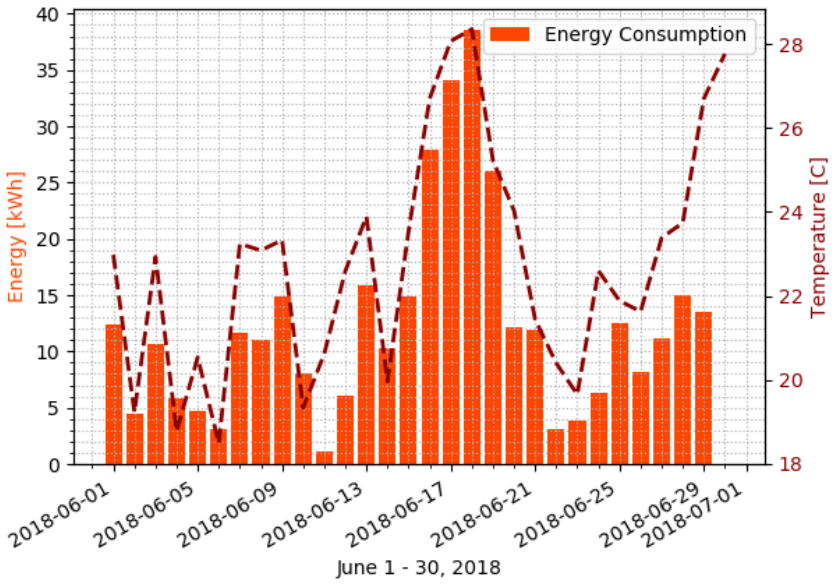

Figure 3.9. Heat pump daily average energy consumption in June, 2018.

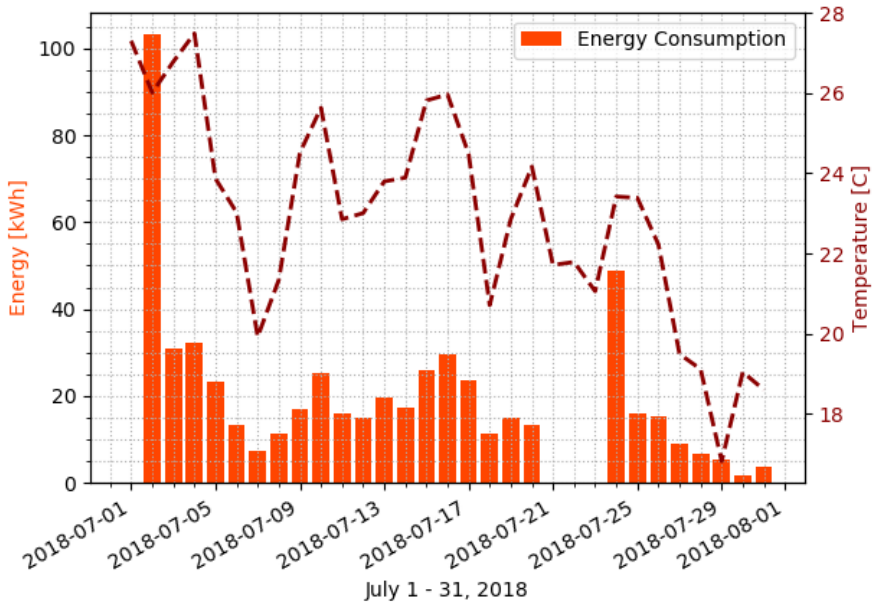

Figure 3.10. Heat pump daily average energy consumption in July, 2018.

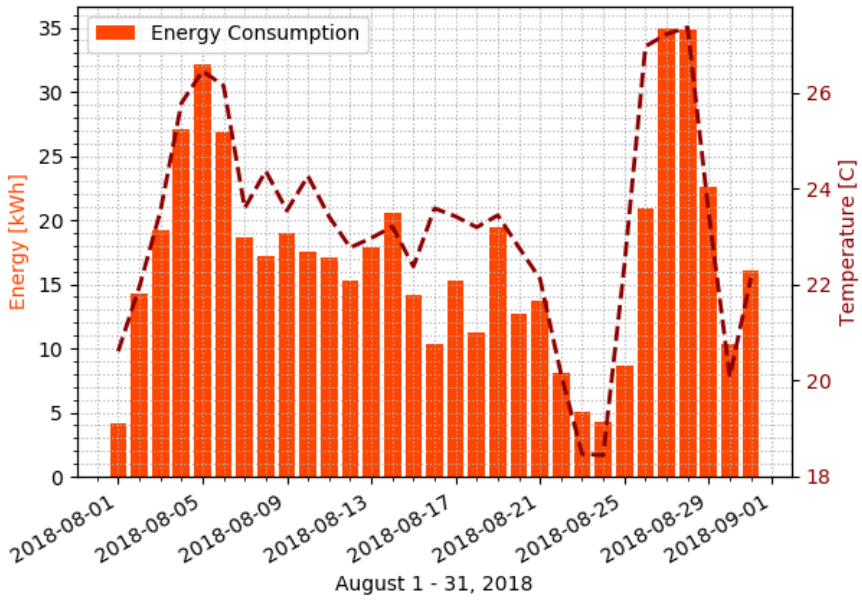

Figure 3.11. Heat pump daily average energy consumption in August, 2018.

3.3 Hybrid AC/DC Heat Pump Testing

As described in the preceding chapters and sections, the heat pump is positioned as a primary candidate for electrical retrofit to DC power, owing to its considerable consumption of energy with respect to other household appliances and devices. To study this experimentally, the off-the-shelf Trane heat pump unit described in Section 3.2 is compared to a second hybrid unit, intended for use with DC testing. This second unit, modified to accept both 240 VAC and 350 VDC, was installed in the psychrometric chambers at the Ray. W. Herrick Laboratories. The DC Nanogrid is simulated through the use of a variable-voltage 15 kW DC power supply. The environmental conditions inside and outside the DC House are emulated using two adjacent psychrometric chambers, capable of replicating conditions between -20 °C (-4 °F) and 55 °C (130 °F), and 15% to 100% relative humidity. AC and DC electrical configurations using a retrofitted hybrid heat pump are tested under a variety of cooling conditions, and compared with thermal and electrical performance metrics. Further testing conditions and topics of investigations are then considered for future study.

3.3.1 Testing Specifications and Methodology

To provide a basis for comparison across the various electrical configurations, an off-the-shelf variable speed heat pump with a scroll compressor was selected and retrofitted to accept both AC and DC electrical supply inputs. Using conventional residential AC power, the modified unit operates on a nominal split-phase 240 VAC input. Under the DC configuration, the modified unit operates on nominal bi-polar 350 VDC input, with undervoltage and overvoltage limits at 250 VDC and 400 VDC, respectively. The internal thermal configuration in the modified unit remained unchanged in order to ensure commonality. The results within this chapter evaluate thermal and electrical performance with both AC and DC power conditions using the retrofitted AC/DC hybrid unit. Future investigation will then consider this data against an unmodified unit installed at the DC House operating on standard 240 VAC.

A specific advantage of the DC-based electrical configuration arises from the difference in current consumption of the heat pump. The maximum power of the heat pump is rated

at 6.96 kW, which can be used to determine the maximum current load under a 120 VAC split-phase configuration as shown in Equation 3.1.

$$I_{AC} = P_{AC}/V_{AC} \tag{3.1}$$

Under this relationship, the maximum current is found to be approximately 29 A. If the voltage is then increased to 350 VDC for the DC connection, the maximum current is proportionally decreased to 20 A instead. Equation 3.1 can be rewritten to describe the loss of power with respect to the line resistance, as is shown in Equation 3.2.

$$P_{Loss} = I_{AC}^2 \times R_{Line} \tag{3.2}$$

From this equation, it is clear that the loss of power associated with resistance in the system is reduced in proportion to the squared inverse of current. As a result, halving the current requirement for a component could potentially reduce its electrical line transmission power losses by a factor of one-fourth. In the specific case of the heat pump under study in this paper, the decrease in current requirements from 29 A to 20 A affords a theoretical maximum reduction in line power loss of up to 52%, assuming equivalent resistances.

Although the line power consumption represents only a small portion of the energy consumed by the heat pump system, the savings become more significant over larger distances and across numerous appliances. These losses also result in a voltage drop between supply and appliance, potentially reducing performance and introducing system instability. Additional current requirements also impose an increase in the wire gauge, resulting in higher costs and even further possible line losses.

In a traditional electrical design for many industrial and commercial drives and motors, a supplied three-phase AC voltage is passed through a bridge rectifier, converting it to a usable DC voltage as shown in Figure 3.12.

In the case of the hybrid heat pump, the internal control mechanisms of the retrofitted components have been designed to accept both conventional AC voltage and DC input. The hybrid nature of the modified heat pump is made feasible in part by the capability of the bridge rectifier configuration described previously in Figure 1.4 to allow DC voltage to pass

through without significant impedance. In the case of a pure DC voltage, which is constant without any sinusoidal component, the diodes or thyristors shown in Figure 3.12 exercise virtually no impact on the path of current outside of a small voltage drop, and therefore do not inhibit the processing of the DC input. The remaining conversion stages described in Figure 1.4 (filter, regulator, etc.) also have no significant impact on an input DC voltage, and thus the DC voltage specified in the DC Link region of Figure 3.12 remains satisfied.

3.3.2 Hybrid Heat Pump Specifications

Initial experimental data for the hybrid heat pump was collected using a 230 VAC connection available within the psychrometric chambers. Within the U.S., 220 VAC to 240 VAC are generally understood as synonymous, and thus the DC House and psychrometric laboratory setting can be considered electrically equivalent for future studies. The hybrid heat pump under study is a 14.07 kW air-source split-system design, accepting either 240 VAC or 350 VDC as inputs. Indoor and outdoor components of the heat pump were installed separately in individual psychrometric chambers to properly emulate realistic environmental conditions at the DC House. The outdoor unit contains a compressor, condenser, outdoor

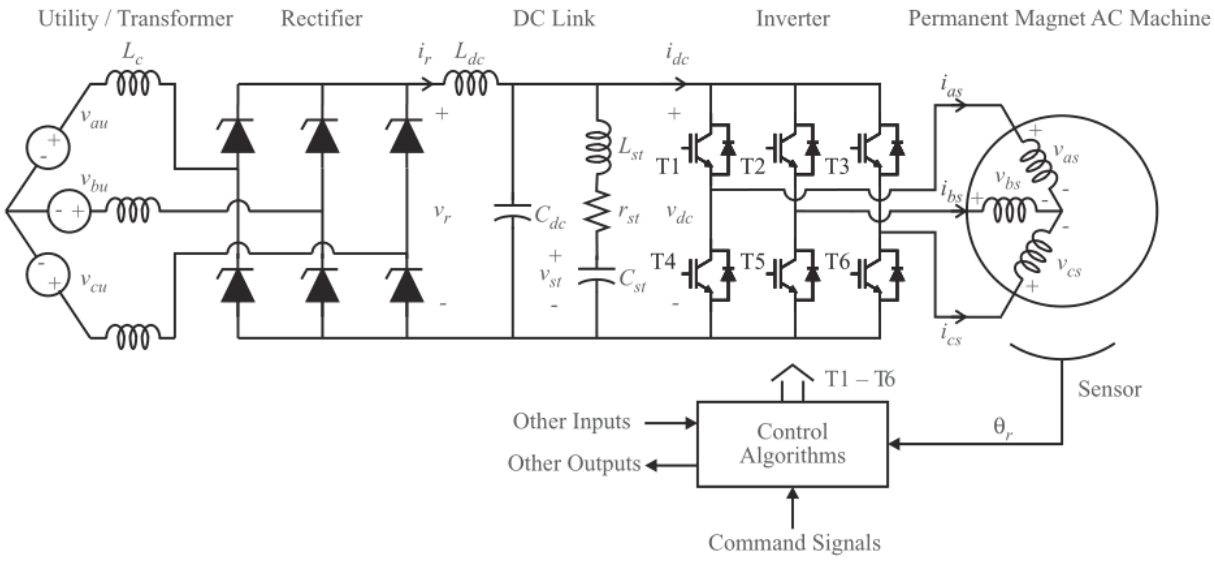

Figure 3.12. Three-phase motor drive circuit emphasizing conversion and inversion power electronics [130].

fan, and a four-way valve, while the indoor unit includes the evaporator, thermostatic expansion valve (TXV), and indoor fan. The heat pump unit contains a scroll compressor, and a manufacturer SEER value of 18. The nominal indoor airflow rate is 2379 m^3/h, and the hybrid system is charged with 6.1 kg of R410A. The heat pump system is composed of a variable speed compressor, an indoor fan with variable volume flow rate, and an outdoor fan with a variable speed motor. The specifications are summarized in Table 3.2.

Table 3.2. Hybrid heat pump testing configuration summary.

Electrical configurations	Cooling capacity	SEER rating	Refrigerant	Testing environment
240 VAC / 350 VDC	14.07 kW	18	R410A	Psychrometric Chambers

3.3.3 Equipment Setup and Data Collection

Laboratory data from the hybrid heat pump was collected using a National Instruments cRIO-2091 data acquisition system (DAQ) with a LabVIEW based visual interface for inspection and logging. Watt transducers were individually installed to monitor the AC power consumption of the indoor unit fan, and the outdoor unit fan and compressor. When employing the DC power configuration, cumulative system power was monitored using the 15 kW MagnaPower variable-voltage DC power supply. DC power was distributed to the indoor unit using 20 m of 10 AWG wire, and to the outdoor unit using 10 m of 6 AWG wire. Thermal data collected was evaluated using both air and refrigerant enthalpy methods to determine the cooling capacity. A schematic summarizing the psychrometric chamber layout and refrigeration loop configuration is provided in Figure 3.13, with the state point descriptions given in Table 3.3.

Thermophysical properties from the psychrometric test setup were determined through the use of the Engineering Equation Solver (EES) software [131]. In addition, state points 1 — 5 and 7 in Figure 3.13 could be calculated from the measured pressure and temperature values of the refrigerant. State point 6 between TXV and the evaporator was obtained assuming both an isenthalpic expansion across the TXV device and negligible pressure drop

Table 3.3. Hybrid heat pump state point definitions.

State Point	Description
1	Compressor Inlet
2	Compressor Outlet
3	Condenser Inlet
4	Condenser Outlet
5	EXV Inlet
6	EXV Outlet
7	Evaporator Inlet
8	Evaporator Outlet

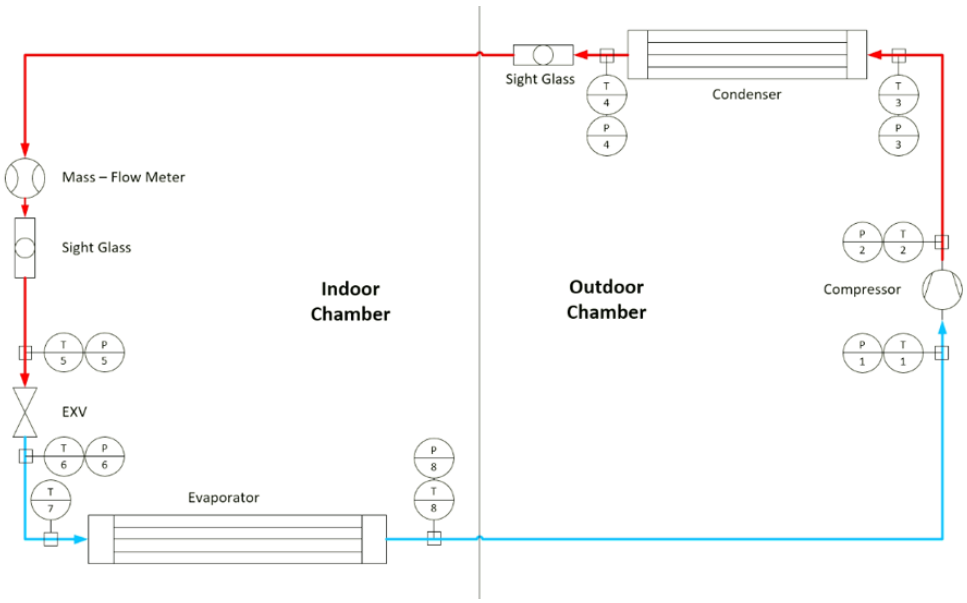

Figure 3.13. Hybrid heat pump cooling configuration schematic — psychrometric chamber setup.

at the outlet of the TXV and evaporator. The refrigerant mass flow was determined using a Coriolis mass flow meter configured for liquid phase between state points 4 and 5.

Cooling capacity of the hybrid heat pump could be calculated through two separate means, and then compared to determine the accuracy of the system measurements. Using

a First Law energy balance and the given assumptions at each state point, the evaporator cooling capacity can be computed from Equation 3.3.

$$\dot{Q}_{evap} = \dot{m}\Delta h_{evap} = \dot{m}(h_7 - h_6) \tag{3.3}$$

The net capacity is then calculated by taking the difference between the cooling capacity of the evaporator from Equation 3.3, and the additional heat added to the system from the indoor fan. The amount of heat was assumed approximately equivalent to the overall power consumption of the indoor unit, resulting in the relationship given by Equation 3.4.

$$\dot{Q}_{delivered} = \dot{Q}_{evap} - \dot{W}_{indoor} \tag{3.4}$$

Alternatively, the hybrid heat pump cooling capacity could also be determined using an air-side approach. In this evaluation, the overall air-side capacity can be calculated again by considering a First Law energy balance applied to the indoor unit. Within this energy balance, the difference in enthalpy of the air flow is accounted for, along with the phase change of water condensed within the unit, yielding Equation 3.5.

$$\dot{Q}_{delivered} = \dot{m}_{air}\Delta h_{evap} - \dot{m}_{water}h_{water} \tag{3.5}$$

In order to evaluate Equation 3.5, calculation of the mass of air flow is needed. This can be determined by analyzing the volume flow rate of the nozzle box in line with the indoor unit's duct work, which is designed in compliance with ASHRAE Standard 37-2009 [132]. The volumetric flow rate is calculated iteratively using Equation 3.6.

$$\dot{V}_{air} = Y\sqrt{\frac{2\Delta p_{nozzle}}{\rho_{air}}}\sum_{0}^{k} C_d A_i \tag{3.6}$$

The expansion factor, Y, and coefficient of discharge, C_d, in Equation 3.6 are defined in ASHRAE Standard 37-2009, and the area of the duct work, A_i was specified during system

installation [132]. With the volumetric flow rate obtained, the air flow mass can be solved by multiplying by the air density as illustrated in Equation 3.7.

$$\dot{m}_{air} = \dot{V}_{air}\rho_{air} \tag{3.7}$$

In addition to the mass of the air flow, the mass of the condensed water flow is also needed to evaluate Equation 3.5. EES is used to calculate the inlet air enthalpy, outlet water enthalpy, and outlet air enthalpy, provided the necessary inputs are given. This includes the air dry-bulb temperature, which is measured with a 3×3 thermocouple grid situated between the inlet and outlet of the indoor unit, the relative humidity of inlet air using a relative humidity sensor, and the dew point of the outlet air. The dew point is determined through a periodic sampling of the air at the rate of 1 L/min, which is then processed through a chilled mirror dew point sensor. The relationship between these values calculated in EES is detailed in Equation 3.8.

$$\dot{m}_{water} = \dot{m}_{air}(\omega_2 - \omega_1) \tag{3.8}$$

Finally, the heat pump coefficient of performance (COP) can be tabulated by dividing the system cooling capacity by its power consumption, as defined in Equation 3.9.

$$COP = \frac{\dot{Q}_{delivered}}{\dot{W}_{total}} \tag{3.9}$$

3.3.4 Testing Methodology

The hybrid heat pump with variable-speed components was tested in accordance with the guidelines set by AHRI. To establish common baseline testing conditions for both the AC and DC electrical configurations, psychrometric indoor and outdoor room conditions were specified from test conditions A, B, C, D, and E from Table 8 of the AHRI Standard 210/240 [133]. The compressor was operated near full speed during each test, but not explicitly controlled under either AC or DC configuration.

The test conditions performed are collected into a matrix shown in Table 3.4. Each test case was performed under both the 230 VAC and 350 VDC configuration under steady state conditions, and monitored for thermal and electrical characteristics every few seconds. This data was subsequently post-processed using the EES software at the conclusion of the testing.

Table 3.4. Hybrid heat pump psychrometric-based test matrix.

Test case	Cycle configuration	Indoor Temperature [°C]	Indoor Relative Humidity [%]	Outdoor Temperature [°C]	Indoor Relative Humidity [%]
1	Cooling	26.7	51.1	35	39.6
2	Cooling	26.7	51.1	27.8	39.6
3	Cooling	26.7	51.1	30.6	39.6
4	Cooling	26.7	51.1	27.8	39.6
5	Cooling	26.7	51.1	19.4	39.6

The test matrix described in Table 3.4 is also leveraged to evaluate the COP and the Energy Efficiency Ratio (EER) ratings for the hybrid heat pump system. These ratings, along with the SEER calculation, are standard methods used to rate the heating and cooling performance of U.S. heat pumps. A seasonal analysis is necessary to characterize the benefits of a variable speed system, which come in the form of the ability to match part-load conditions. The COP and EER ratings are used in this study to quantify the thermal performance of each test case under the AC and DC configurations of the hybrid heat pump.

3.3.5 AC and DC Testing Results

The results of the hybrid heat pump testing under the AC and DC electrical configurations of the test matrix in Table 3.4 are detailed in Table 3.5 and Table 3.6.

The cooling capacity, COP, and EER measured in each of the test cases was acquired using the refrigerant method calculation. Although these capacities were similar in magnitude between AC and DC configurations, the thermal state points of the refrigeration cycle maintained some significant differences, especially at the compressor suction temperature.

Table 3.5. Hybrid heat pump 230 VAC test results.

Test case	Electrical configuration [VAC]	Cooling capacity [kW]	Indoor power [kW]	Outdoor power [kW]	Total power [kW]	COP [-]	EER [-]
1-AC	230	12.8	0.4478	3.6204	4.0682	3.15	10.8
2-AC	230	14	0.4515	3.1088	3.5603	3.93	13.4
3-AC	230	13.6	0.3357	3.2627	3.5984	3.78	12.9
4-AC	230	14.1	0.3238	3.0835	3.4073	4.14	14.1
5-AC	230	15.4	0.3568	2.5475	2.9043	5.30	18.1

Table 3.6. Hybrid heat pump 350 VDC test results.

Test case	Electrical configuration [VAC]	Cooling capacity [kW]	Total power [kW]	COP [-]	EER [-]
1-DC	350	13.3	3.9050	3.38	11.3
2-DC	350	14.1	3.3260	4.24	14.1
3-DC	350	13.9	3.4557	4.02	13.9
4-DC	350	14.3	3.2429	4.41	14.3
5-DC	350	15.8	2.8138	5.62	15.8

To consider these more closely, the thermal characteristics of the first test case under both the AC and DC configurations are presented in Table 3.7.

Table 3.7. Hybrid heat pump test case 1 thermal characteristics.

Test case	Electrical configuration [V]	Indoor Air Flow $[m^3/s]$	Compressor suction superheat [C]	Compressor suction temperature [C]	Compressor suction pressure [kPa]	Compressor discharge temperature [C]	Compressor discharge pressure [kPa]
1-AC	230	0.6269	24.6	33.9	1016	81.2	3003
1-DC	350	0.6892	6.1	15.0	997.6	81.6	3002

As Table 3.7 reveals, the DC configuration maintained a higher indoor air flow rate under steady state conditions and a significantly lower compressor suction temperature. The state points for the AC and DC configurations under test case 1 are further illustrated in the P-h diagrams shown in Figure 3.14 and Figure 3.15.

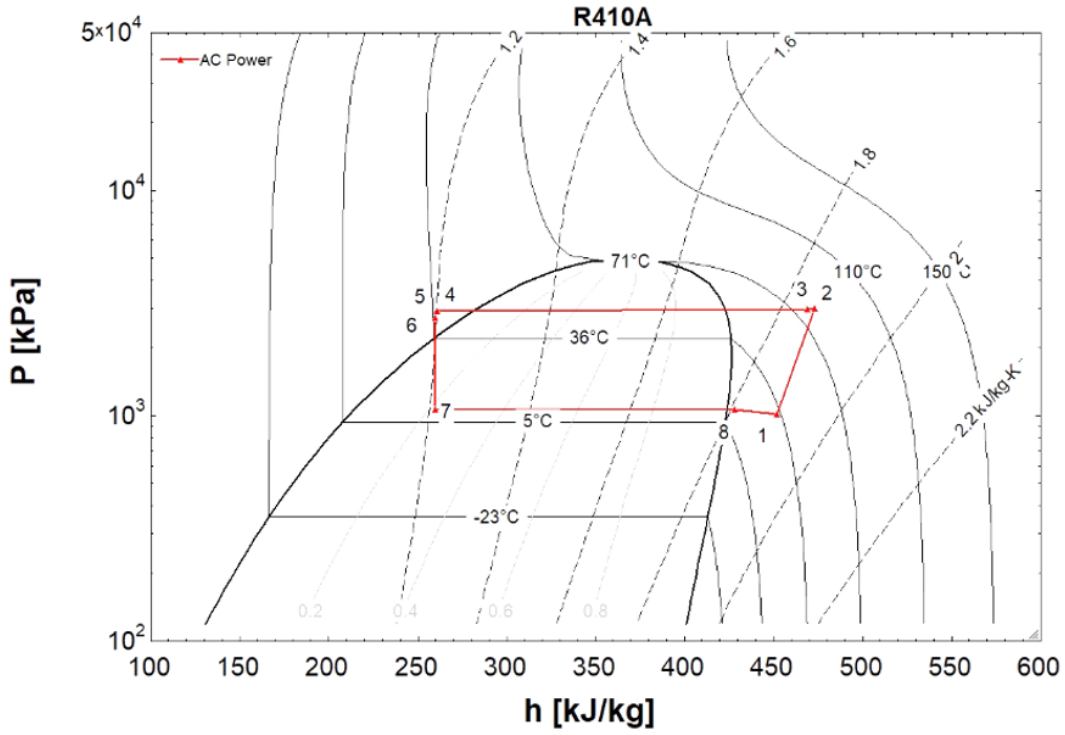

Figure 3.14. P-h diagram for the AC-powered test case 1.

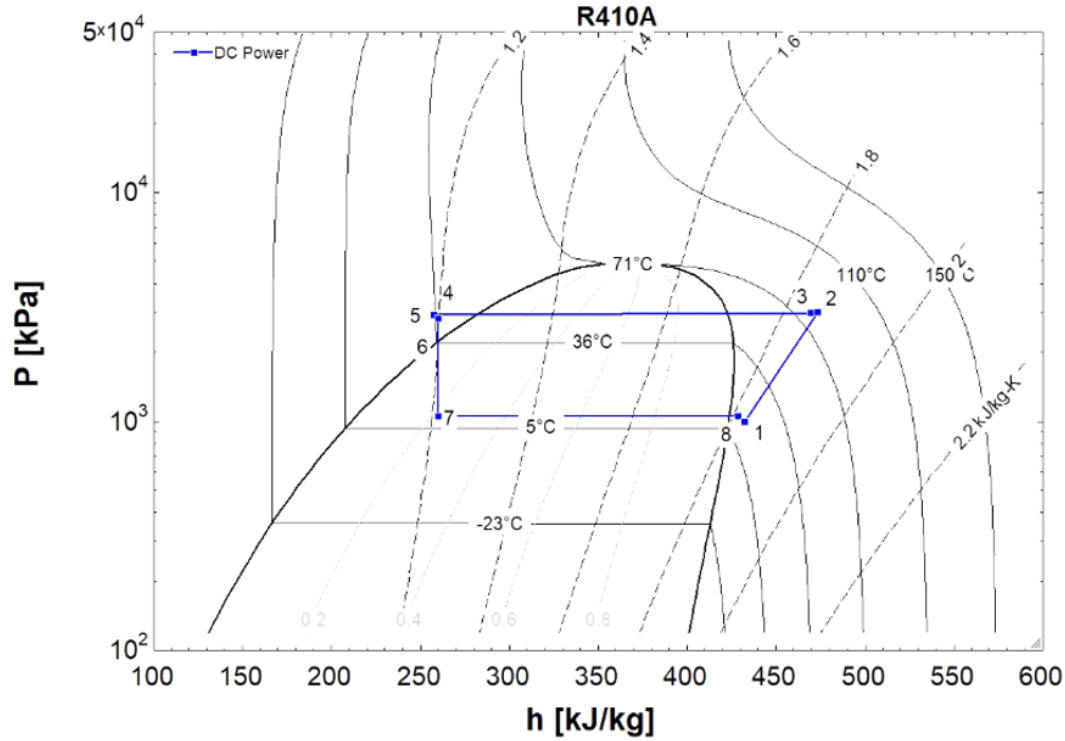

Figure 3.15. P-h diagram for the DC-powered test case 1.

Since the compressor speed was controlled automatically by the heat pump, this may have resulted in the differences observed. In addition, the drive operation under DC conditions could not be readily evaluated against those under the AC configuration without supplemental manufacturer data. As a result, these factors demonstrated a need for further instrumentation and analysis to determine the source of the differences. Additional DC-watt transducers are planned for installation on the indoor and outdoor units for increased fidelity of the power consumption, as well as coordination with service data to extract the compressor speeds in post-processing.

3.3.6 DC Measurement Uncertainty Analysis

The DC power supply served as both the representative DC Nanogrid supply for the hybrid heat pump, and the monitoring device to capture the heat pump total power consumption. As a result of the significant dependence on this unit, uncertainty of the supply and monitoring capabilities is considered. From the supply side, the manufacturer specifications indicate an output load regulation of ±0.01% of full-scale voltage under a voltage control mode. In addition, an input line regulation of ±0.004% of full-scale voltage is maintained under the same voltage control. Load regulation in this case refers to the capacity of the power supply to maintain a specified output voltage while the load is varying, and line regulation describes the ability of the power supply to maintain the same specified output voltage while the input supply power to the power supply is varying. Collectively, these represent a combined uncertainty of ±0.011%. This is calculated using a quadratic sum, which describes the uncertainty in measurements x, …, y, which are used to compute an uncertain output, δ f. This is given below in Equation 3.10.

$$\delta f = \sqrt{(\delta x)^2 + ... + (\delta z)^2} \tag{3.10}$$

Defining the full-scale voltage of the power supply to be 500 VDC, the output supply to the heat pump is calculated with an uncertainty of 0.054 VDC. These results are summarized in Table 3.8, where $\Delta V_{controlled}$ represents the 350 VDC measured operating condition.

Table 3.8. DC power supply output uncertainty.

Uncertainty Condition	Uncertainty [%]	Voltage Error [VDC]
Line Regulation	0.01	$V_{controlled} \pm 0.05$
Load Regulation	0.004	$V_{controlled} \pm 0.02$
Output Supply	0.011	$V_{controlled} \pm 0.054$

Using the power supply to monitor the heat pump power consumption, the measurement accuracy must then be considered. The manufacturer specifies a voltage readback uncertainty of ±0.2% of full-scale voltage, and a current readback uncertainty of ±0.02% of full-scale current. Defining the full-scale current of the power supply to be 30 A, the cumulative power measurement uncertainty reading can be tabulated as shown in Table 3.9. Since the power is calculated by the multiplication of the DC voltage and current, the resulting uncertainty is defined as the quadratic sum multiplied by the power measurement.

Table 3.9. DC power supply measurement uncertainty.

Uncertainty Condition	Uncertainty [%]	Error
Voltage Reading	0.02	$V_{measured} \pm 0.1$ [V]
Current Reading	0.02	$I_{measured} \pm 0.006$ [A]
Power Measurement	0.011	$P_{measured} \pm 0.100$ [W]

3.3.7 Testing Summary and Conlusions

This study presented the psychrometric evaluation of a retrofitted hybrid heat pump unit under a variety of environmental conditions using both AC and DC electrical configurations. The intent of this research is to demonstrate the feasibility of DC retrofits of devices traditionally configured for AC inputs, and to analyze improvements in performance and energy efficiency through the avoidance of AC and DC conversions. The DC power was supplied using a variable voltage power supply, which was implemented to represent a DC Nanogrid operating in a residential setting. The unit functioned successfully using a 350 VDC input, and was able to perform under each of the five test conditions described in Table 3.4. Based

on the thermal and electrical measurements obtained, a need for additional instrumentation and further testing was identified. DC-based watt transducers are planned for installation on the indoor and outdoor units to provide insight into their representative energy consumption. This data coupled with supporting manufacturer measurements will be used to both verify the results obtained within this paper and analyze the difference in behavior between the AC and DC modes of operation.

Beyond the laboratory setting, additional studies will analyze the hybrid heat pump results described here against an unmodified heat pump unit installed in the DC House using load-based testing methodology. These subsequent investigations will assist in confirming the hybrid heat pump AC and DC data obtained in this paper, and further support the potential energy improvement opportunities under DC operation. In addition, coordinated testing between the hybrid heat pump and unmodified heat pump is planned in order to establish a proportional relationship between testing results. Under this methodology, ambient temperature and humidity from the residential testing environment will be relayed in real-time to the test setup in the psychrometric chambers, allowing it to be recreated and applied to the heat pump under scrutiny there.

4. DC NANOGRID DESIGN AND IMPLEMENTATION

4.1 Motivation for a DC-Driven Architecture

The development of the AC-based power grid has been rife with challenges since inception in the late 19th century. The advent of increasing energy demands within the U.S. has resulted in escalated strain on power grids around the world, bringing into question their capacities to support future needs. The systematic and spatial layout of power grids makes it especially vulnerable to cascading failures, as described in the Introduction chapter. Modern technological innovations have fostered a greater dependency on the grid, coupling it with nearly every aspect of contemporary society. Unfortunately, grids have not experienced a parallel rate of global growth alongside technology, with some estimates reporting on the order of trillions of dollars necessary for repairs and upgrades on a country-wide basis to establish a nominal performance level. In addition, the variation in AC frequency used in transmission lines between North America and Europe has been a longstanding issue challenging appliance manufacturers, industrial factories, and standards working groups. A transition to a common DC voltage reference seeks to alleviate many of these issues, and establish electrical unification both intra- and intercontinentally.

A major proponent for a transition from AC to DC power distribution originates from the use of DERs. DERs, such as solar PV and wind energy, are naturally configured to produce DC power but suffer from the multitude of inversion losses to integrate with AC for distribution and transmission. These losses are further exacerbated when DC-based devices, such as LEDs, cell phones, computers, TVs, etc. must convert again from AC to DC. A consistent DC voltage offers to mitigate these losses through the avoidance of unnecessary conversion losses and stability concerns inherent in AC-based systems. Many studies have been conducted indicating the potential energy savings from moving to a DC-driven system, especially those with significant lighting elements [134].

Other devices with considerable energy consumption needs, such as HVAC equipment, employ DC-driven devices such as variable-speed drives (VSDs), fans, pumps, and other power electronics. These devices rely heavily on AC-DC conversions, increasing power losses and decreasing energy efficiency. According to recent research, it is estimated that approxi-

mately 30% of all generated AC power is processed through conversion electronics before it reaches the end point of use [135]. These conversions are associated with a nontrivial amount of power dissipation, and based on studies performed by the EMerge Alliance, the amount of energy lost may range up to 25% on average across all household devices and appliances [25].

Furthermore, DC transmission lines offer greater energy transfer potential than their AC counterparts, owing to the circumvention of line-losses inherent with AC frequency components, such as the skin and proximity effects [45]. In addition, DC lines only require two conductors to transfer power, while AC must have three; this results in decreased real-estate costs over long distances. AC transmission line towers also most occupy more space, known as right-of-way (ROW), compared to those carrying DC power as a result of conductor spacing needs in AC lines. These effects culminate in a break-even cost for DC vs. AC systems, with some estimates determining distances of approximately 300 km or longer to be more economical employing high voltage DC (HVDC) transmission than the functional AC equivalent [53]. In short, investigation across both macro-scale (country-wide transmission) and micro-scale (individual power electronic components) levels has revealed the benefits of a DC-based architecture, motivating the creation of new DC topologies to support it [136].

4.2 Microgrid and Nanogrid Formulation

4.2.1 Electrical Topologies

The ideas of the microgrid and nanogrid designs have existed for decades, but the rapid growth in renewable energy has stimulated additional research into these concepts. According to the DOE and California Energy Commission (CEC), a microgrid is a system which contains energy generation capability with the capacity to offset the demands of a significant number of loads connected to it. Similarly as defined by LBNL, a microgrid is represented by a group of loads and DERs, which have a defined electrical boundary from other entities, can be controlled as a single body, and maintain the ability to either interact with the grid, or disconnect and operate independently in an islanding mode [137]. CIGRÉ provides a similar interpretation, further specifying that DERs include all manner of energy genera-

tion in the microgrid (e.g., fossil fuels, CHP, PV, wind, etc.), and that storage devices can possess a diverse collection of implementations (e.g., electrical, mechanical, gravitational, thermal, chemical, etc.) [68]. To this end, a microgrid is a unit which can coexist alongside conventional electrical distribution mechanisms, but affords the capability to operate on its own if necessary. Furthermore, the microgrid can distribute energy back to the macrogrid if required, offering an additional advantage to stability.

Nanogrids are quite similar to microgrids, with one caveat: nanogrid systems do not require the presence of energy storage. According to definitions supplied by LBNL, a nanogrid is an entity which must have at least one load and one connection outside itself. The critical responsibility of the nanogrid is to distribute power between connections and loads, and serve as an intermediary between outside systems and internal devices. A nanogrid can often function alongside a larger microgrid or external power grid (often referred to as the macrogrid), functioning as a highly flexible infrastructure [82]. Also similar to microgrids, nanogrids offer much of the same benefits on a smaller scale. While a microgrid might encompass an entire neighborhood of interconnected houses, a power plant, and local energy storage, a nanogrid could be comprised of a single home with a solar installation. Nordman (2010) defines a nanogrid to represent a single controllable entity with at least one load, and at least one connection to external grids (e.g., a larger microgrid, the overall macrogrid, etc.). A critical difference from the microgrid, however, is the requirement for storage; a nanogrid may or may not have energy storage integrated into its design. As a result, by its formal definition a nanogrid is not required to support islanding operation.

Microgrids and nanogrids are not required to stipulate a specific voltage type for distribution, although DC and other hybrid combinations are common. These systems benefit from their flexibility to integrate into a panoply of applications, ranging from industrial facilities, commercial buildings, cul-de-sacs, individual homes, and many other structures. Microgrids and nanogrids offer a bottom-up solution to transmission and distribution challenges, requiring minimal coordination and the flexibility to function alongside the existing AC infrastructure. With integrated battery storage, these topologies offer resiliency to grid disruptions, load-balancing opportunities, and ready-compatibility with DC-power producing renewable energy sources. Nanogrids advocate these benefits another step further, yielding

configurations with reduced conversions between distribution and devices, and increasing the potential for energy savings. Combining these systems with DC-compatible devices and furthering retrofit-research into additional appliances capable of supporting DC could render AC the minority in power distribution, rather than the predominant entity.

Two possible microgrid topologies are demonstrated in Figure 4.1, with the left side indicating an AC/DC hybrid structure, and the right side presenting a pure DC structure. In these diagrams, darkened circles represent a switch, open circles represent power electronics, and arrows represent the direction of power flow. Under both schemes, the electrical storage could be removed without affecting the overarching integrity of the design. The hybrid structure affords some of the benefits of the microgrid architecture without fundamentally altering the common distribution mechanism. The right style, however, yields an ideal configuration for a DC-based solution. In this case, all conversions from AC to DC have been eliminated (with the exception of the primary grid-tie), and renewable energy generation, energy storage, and loads can benefit from direct-DC supplies with minimal and highly efficient DC-DC conversions.

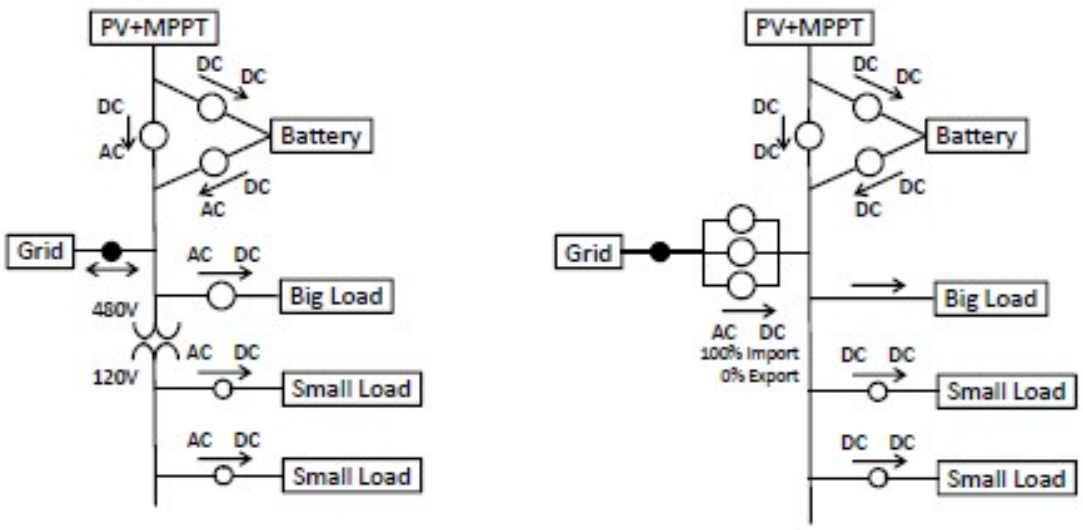

Figure 4.1. Sample AC and DC microgrid/nanogrid topology reference layouts [27].

4.2.2 The Residential Nanogrid

Owing to the explosion of growth in renewable energy generation in residential locations, and the aforementioned benefits from the inclusion of DERs within the existing macrogrid infrastructure, the application of DC-based architectures within residential spaces has become a compelling topic. In its 2020 World Energy Outlook publication, the IEA states that, "for projects with low-cost financing that tap high-quality resources, solar PV is now the cheapest source of electricity in history" [138, para. 5]. Even while global electricity demand curtailed due to the COVID-19 pandemic, renewables maintained a year-over-year growth of nearly 7% during the 2020 year [139]. According to Solar Energy Industry Associates (SEIA), this international advancement was fueled in-part by a 43% increase in new electricity production of solar PV within the U.S. in the same year, and incidentally was also the single largest increase of that category during the previous decade. Contributions to new production included a 14% increase in residential solar installations between the second and third quarters of 2020 within the U.S., and new residential solar capacity additions of approximately 3 GWdc during the same year [140].

From the perspective of consumption, the majority of modern devices and appliances consume DC power either directly or indirectly, yielding further credence to DC-based topologies. In a residential setting where DERs are present, maintaining conventional AC distribution results in a multitude of potentially dissipative AC to DC and DC to AC conversions, which diminish the capacity for micro/nanogrid benefits. As a result, a centralized DC-distribution architecture affords the capability to mitigate these impacts, reducing the need for complex and expensive power electronics, and offering viable high efficiency DC-DC conversions. Hybrid structures of the layouts previously described in Figure 4.1 can also be attainable, where DERs and DC-compatible loads can share a common DC bus, while conventional AC loads and DC-indifferent loads can remain on a traditional AC infrastructure. As [27, p. 2] enumerates, there are nine key performance indicators (KPIs) that can be applied to analyze an electrical architecture's benefit:

1. Safety and Protection

2. Reliability

3. Capital Costs

4. Energy Efficiency

5. Operating Costs

6. Engineering Costs

7. Environmental Impact

8. Power Quality

9. Resilience

After reviewing numerous studies for evidence and implementation details, including [29], [30], [75], [141] and many others, these nine KPIs were summarized over various AC and DC topologies to reveal distinct advantages of DC designs for categories (3), (4), (6), and (8), and neutral or marginal benefits for the remaining categories [27]. A high-level comparison in AC and DC micro/nanogrid layouts within a residential setting is depicted in Figure 4.2. Based on the performance metrics previously outlined, architectures including significant DC composition certainly merit additional investigation.

4.2.3 Design Objectives

Within this project, the design objectives comprising a nanogrid-topology are sought using a DC powered configuration. Since microgrids typically envelope small communities with multiple buildings, storage devices, and energy generation facilities, the nanogrid nomenclature and characteristics were determined to be a better fit for this study. In total, a whole-home conversion is desired, such that every device and appliance would be compatible with a DC input voltage. This can be achieved under two different approaches:

1. Retrofit a given device/appliance to support a DC input

2. Supply a DC-AC inverter at the device/appliance input

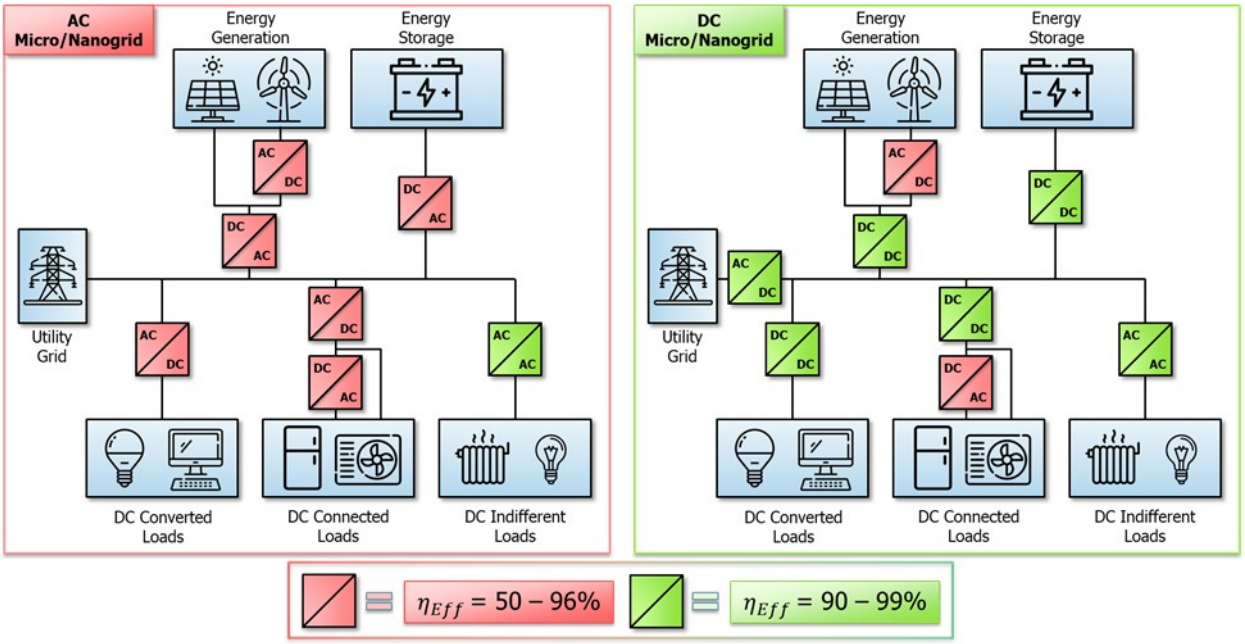

Figure 4.2. DC vs AC micro/nanogrid architectural depiction highlighting relative conversion efficiencies

Through either of these mechanisms, a common DC bus can be employed throughout the entire home, avoiding the need to maintain both separate AC and DC infrastructures.

4.3 DC Nanogrid Design and Implementation

4.3.1 Equipment Sizing and Specifications

In pursuit of the previous objectives outlined in Section 4.2, the electrical framework and specifications were established based on the analysis of data collected from previous years of the project. Sizing of the equipment requires an assessment of two critical factors: power and energy consumption. Since the nanogrid supplies both AC and DC loads, an appropriate kVA rating of a bidirectional inverter must be first determined. Following this, the energy consumption in terms of daily and monthly increments is necessary to evaluate an appropriate sizing of renewable energy generation and storage. Finally, appropriate DC voltages must be established to define the infrastructure of the nanogrid, which will also influence the selection of downstream DC-DC converters and DC-AC inverters for individual devices and appliances.

To survey the electrical characteristics of the instrumented loads outlined in Section 2.3.1, the collected data from the EMCB and TED modules are analyzed and represented as performance metrics. Each measurement performed by either DAQ system occurs through two steps. First, the elapsed time of a given sampling period is established by taking the difference of the beginning and ending timestamps, as indicated in Equation 4.1. Following this period, the maximum and average real and reactive power quantities are determined by examining the maximum and mean values of the n collected data points, as indicated in Equations 4.2 and 4.3. In these equations, X can represent either the real or reactive power quantities. Finally, the sampled period's energy consumption in kWh is determined by summing the individual sampled power measurements and converting from kJ to kWh as shown in Equation 4.4.

$$\Delta t_{sample} = t_2 - t_1 \tag{4.1}$$

$$X_{max}\Big|_{\Delta t_{sample}} = \max_{\Delta t_{sample}} \{X_1, X_2, ..., X_n\} \tag{4.2}$$

$$\bar{X}\Big|_{\Delta t_{sample}} = \frac{1}{n}\sum_{i=1}^{n} X_i \tag{4.3}$$

$$E\Big|_{\Delta t_{sample}} = \frac{1}{3600}\sum_{i=1}^{n} P[t_i] \tag{4.4}$$

Sampling periods occur once every 15 minutes for EMCB modules, and once every minute for TED modules. As a result, a huge number of samples occur over the course of all collected measurements. To determine suitable metrics to size the nanogrid equipment, the surveyed electrical load data is processed in timescales of individual days, with N respective samples each day, over the entire project period, T_{net}. To this end, maximum real power, reactive power, and consumed energy can be tabulated over each day in the period as indicated in Equation 4.5. The maximum from this set of values can be obtained to provide a global maximum characteristic across each individual load. The net sum of these global maxima, shown in Equation 4.6, represents an impractical load condition, since such maximum values

typically occur during an inrush period (i.e., a transient surge of power when equipment first switches on) and would need to occur simultaneously across every load. However, it does provide an absolute upper bound to further refine adequate specifications of the nanogrid equipment.

$$X_{max}\Big|_{\Delta t=24hrs} = \max_{N}\left\{X_{max\,|\,\Delta t_1}, X_{max\,|\,\Delta t_2}, ..., X_{max\,|\,\Delta t_N}\right\} \tag{4.5}$$

$$X_{max,\,\Sigma app}\Big|_{\Delta t=T_{net}} = \sum_{app=1}^{32} \max_{T_{net}}\left\{X_{max}^{app}\Big|_{\Delta t=24hrs}\right\} \tag{4.6}$$

To approximate a more practical specification target, the average electrical quantities for an individual day can be collected across all loads. The maximum value of this set of averages for each load over the entire project period can be evaluated, and then summed together over all loads as indicated in Equations 4.7 and 4.8. While this still represents a generally excessive demand scenario, this value serves as a reasonable liberal estimate upon which equipment can be sized. The results of these metrics are summarized in Table 4.1, and the summary of all energy consumption across each month of the project is visualized in Figure 4.3. Energy and power consumption by device, as outlined in Equations 4.6 and 4.8, are visualized in Figures 4.4 and 4.5.

$$\bar{X}\Big|_{\Delta t=24hrs} = \frac{1}{N}\sum_{i=1}^{N}\bar{X}_{\Delta t_i} \tag{4.7}$$

$$\bar{X}_{\Sigma app}\Big|_{\Delta t=T_{net}} = \sum_{app=1}^{32} \max_{T_{net}}\left\{\bar{X}^{app}\Big|_{\Delta t=24hrs}\right\} \tag{4.8}$$

Table 4.1. Summary of instrumented AC electrical load characteristics.

	Real Power [kW]	Reactive Power [kVA]	Energy [kWh]
Maximum	62.36	6.89	239.45
Average	26.68	2.79	39.19

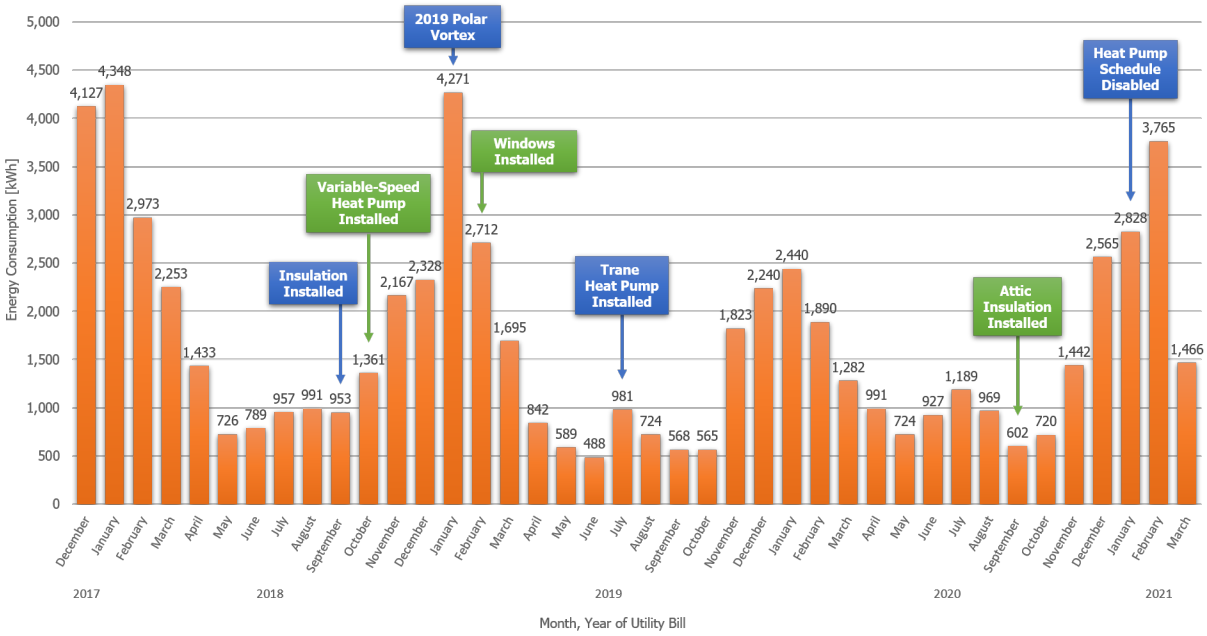

Figure 4.3. DC Nanogrid House electrical energy consumption by month from 2017 to 2021.

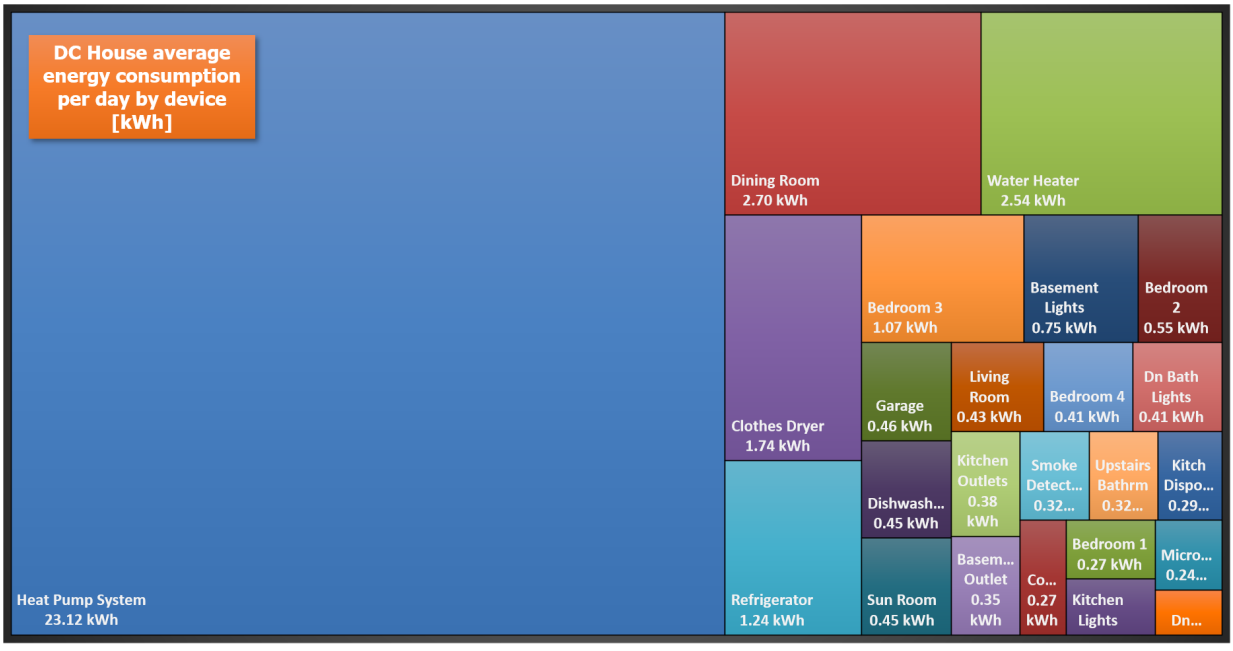

Figure 4.4. DC Nanogrid House appliance average energy consumption per day.

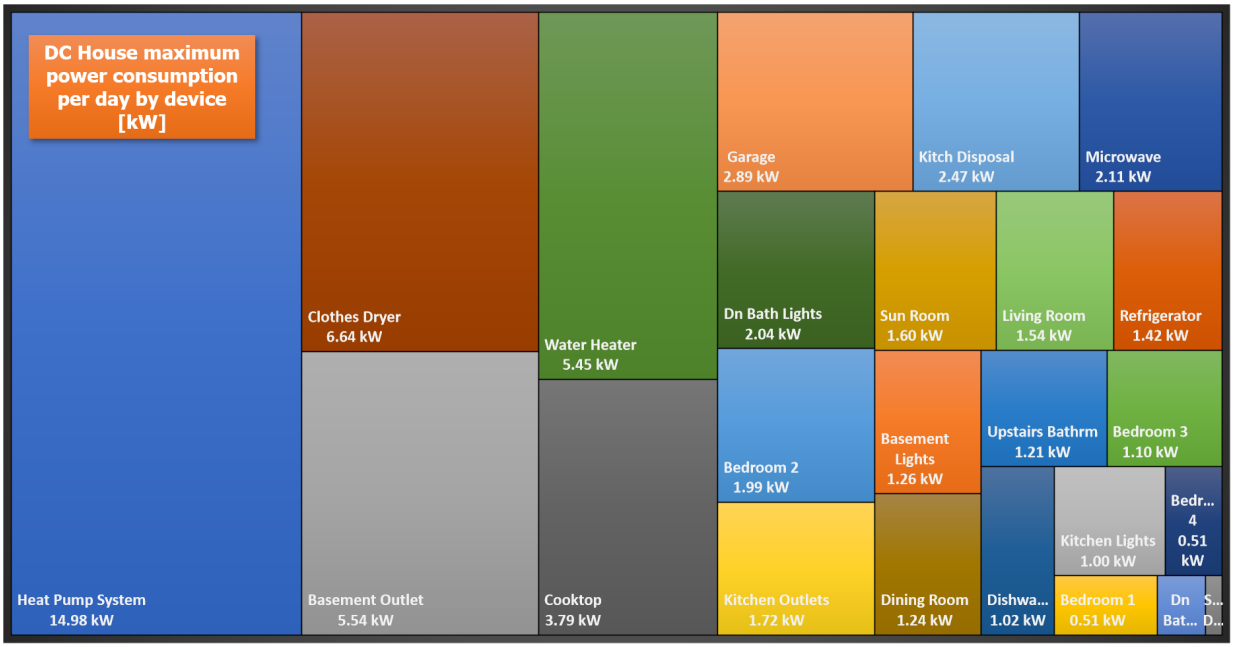

Figure 4.5. DC Nanogrid House appliance maximum average power consumption per day.

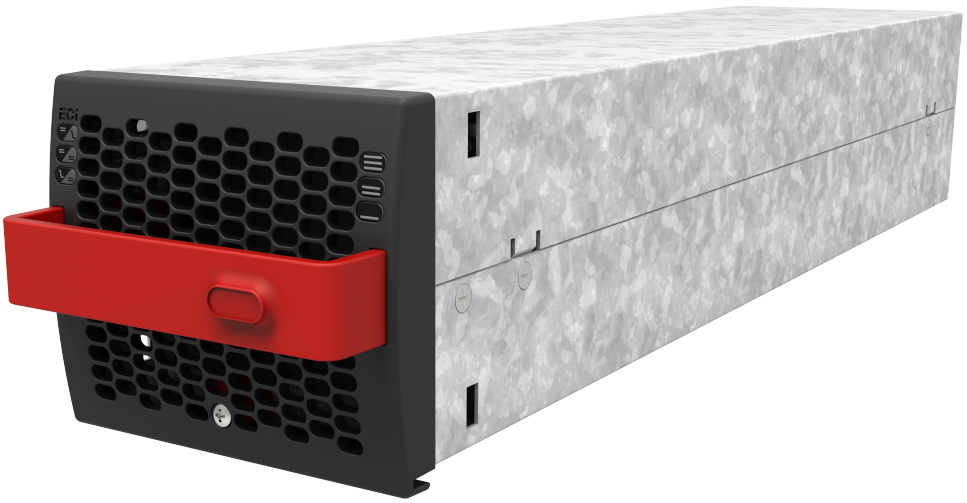

Figure 4.6. CE+T Bravo ECI bidirectional inverter module [142].

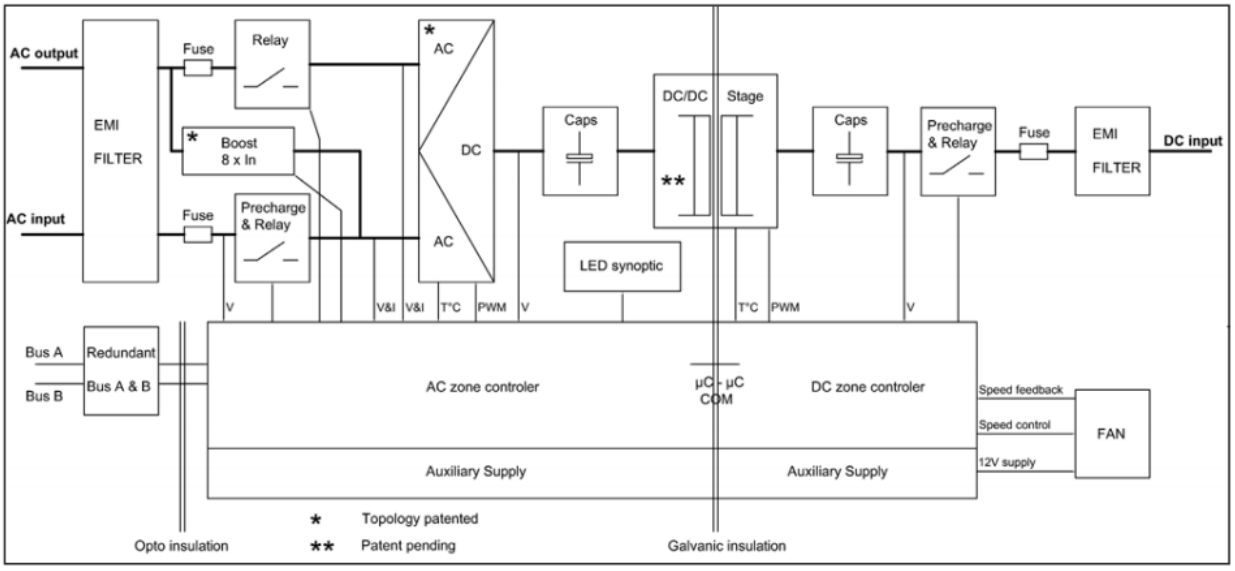

Figure 4.7. CE+T ECI module block diagram and circuit topology [142].

To satisfy the needs outlined in Table 4.1, a bidirectional AC/DC inverter manufactured by CE+T was selected with a nominal 35 kVA nameplate rating. This rating was determined from the average power conditions combined with a 25% buffer in the event of unexpected demand. The inverter is known as the Sierra Modular Inverter Power System (MIPS), and utilizes Bravo Enhanced Conversion Innovation (ECI) modules which can be added to the Sierra system as needed to increase its available capacity. An ECI module is illustrated in Figure 4.6 and its representative block diagram emphasizing its galvanic isolation is shown in Figure 4.7. The Sierra system provides up to 96% efficiency between AC-AC conversions, and 94% efficiency between AC-DC conversions [142]. To operate at maximum capacity, the system requires a three phase AC input, which was not immediately available at the DC Nanogrid House location. In order to mitigate this, two input/output AC transformers were selected to: 1) provide isolation between the inverter and other circuitry, and 2) step up and down the single phase AC voltage to three phase AC voltage. The transformers procured for this project are manufactured by Maddox, and have nameplate ratings of 50 kVA.

In addition to the supply of existing AC loads, the bidirectional inverter must also be capable of handling DC loads. However, the net load demand is expected to remain constant, since if a load is retrofitted from AC to DC, it will merely change its physical supply input

from the AC distribution bus to the DC distribution bus while requiring at most the same amount of power. In an ideal scenario, the DC-retrofitted loads will operate with higher efficiency than their AC counterparts, and the overall net load demand of the house would actually decrease. This situation is demonstrated in Section 3.3, with load consumption improvements under the DC configuration achieving 3% to 7% less power than the AC configuration for the same performance.

4.3.2 Renewable Energy Generation and Storage

Performing the same analysis with the rest of the circuits indicated in Table 2.2 provides a means to estimate the electrical power and energy demands on the DC nanogrid design. Both of these parameters are critical to consider, because each one caters to a separate need. If there is exceedingly adequate battery storage, but a significant limitation of power distribution through the nanogrid equipment, the storage will be wasted. In the reverse scenario, if the power throughput is sufficient but energy storage is underutilized, the nanogrid effectivity will be reduced. Optimizing both of these values is a nontrivial effort, and a similar study has been performed for the implementation of a microgrid in a residential setting [143].

Investigation of the electrical data from the loads in the home revealed a maximum combined potential power demand during the winter months when resistive heating from the heat pump unit consumes a significant amount of energy. In addition, the month with the largest energy consumption occurred in February, 2018, with a net usage of 4,348 kWh. This usage averages to approximately 155 kWh each day of the month. Given that solar photovoltaics are planned to be the primary source of energy generation each month, the amount of sunlight is directly proportional to the ability of the nanogrid to satisfy this demand. From weather data, February in Indiana provides approximately 10 to 10.25 hours of sunlight each day, and thus the solar array would be required to generate 15.5 kW to satisfy this demand.

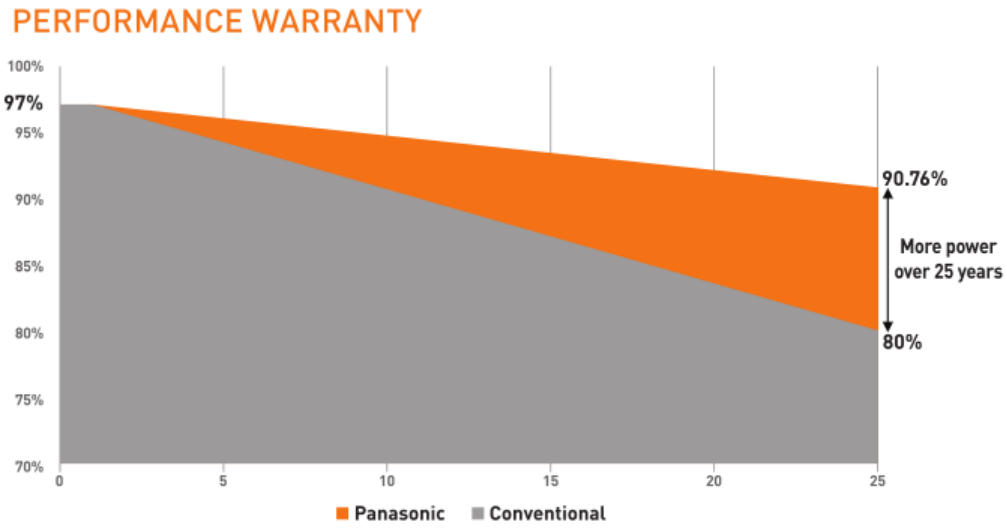

Figure 4.8. Panasonic 325 W solar panel warranty performance over a 25 year period.

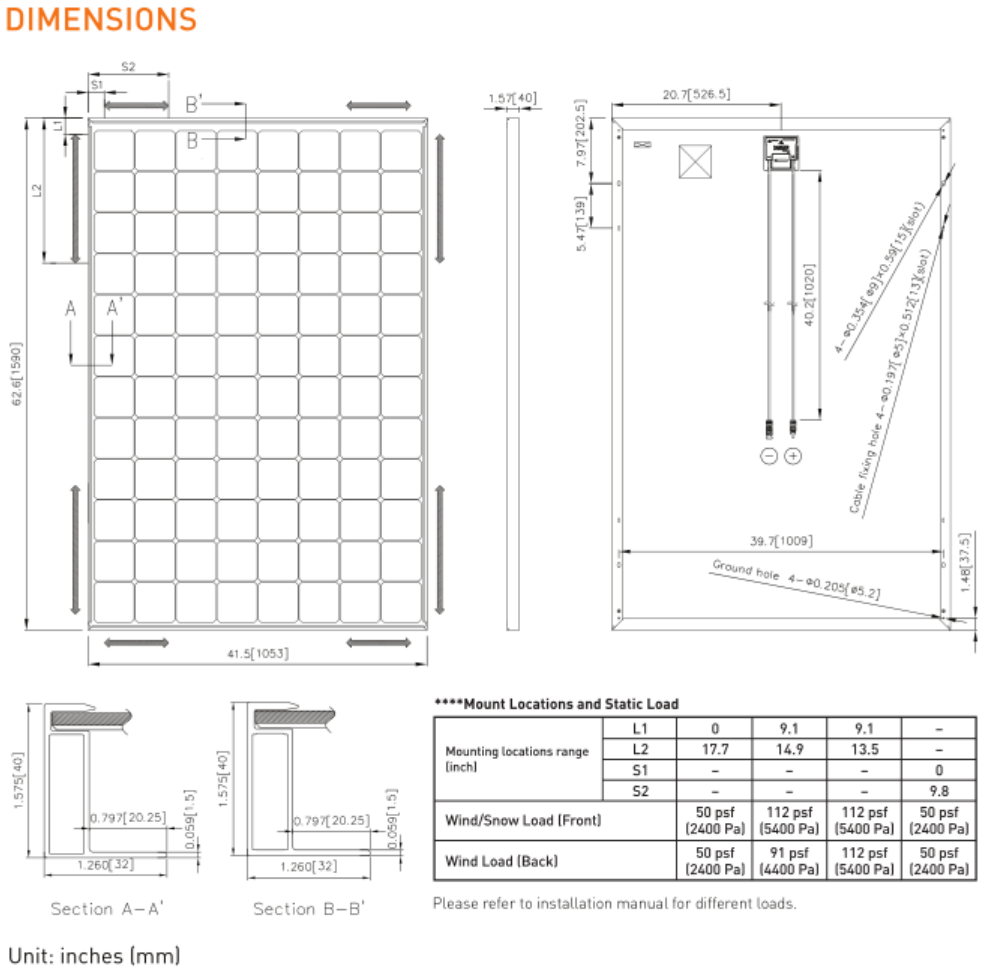

Mounting locations range (inch)	L1	0	9.1	9.1	–
	L2	17.7	14.9	13.5	–
	S1	–	–	–	0
	S2	–	–	–	9.8
Wind/Snow Load (Front)		50 psf (2400 Pa)	112 psf (5400 Pa)	112 psf (5400 Pa)	50 psf (2400 Pa)
Wind Load (Back)		50 psf (2400 Pa)	91 psf (4400 Pa)	112 psf (5400 Pa)	50 psf (2400 Pa)

Figure 4.9. Panasonic 325 W solar panel dimensions and mechanical properties.

After collaborating with solar-installers in the area, Panasonic 325 W N325K panels were selected as the best fit and economical choice for the project. Performance of these panels and their dimensions are detailed in Figures 4.8 and 4.9. Survey of the roof yielded enough area to install a maximum of 44 panels, providing up to a 14.3 kW DC nameplate output. While this is slightly below the needs indicated by the previous needs in February, 2018, the home has undergone significant renovations to improve its energy efficiency, including foam-injection insulation, replacement of single-pane windows with triple-pane insulated high efficiency models, and the substitution of the fixed-speed heat pump with a variable-speed unit. As a result, the 14.3 kW is expected to be sufficient for an adequate apportionment of the energy needs during the winter months. Using the HelioScope software application, a monthly projection estimate was generated for the solar panel layout, as shown in Figure 4.10 [144]. Based on model predictions, the solar configuration is expected to generate approximately 14.94 MWh during the course of each year. An image of the solar array near the end of installation can be viewed in Figure 4.12, and a real-time snapshot of the installed solar panel optimizer voltage readings is displayed in Figure 4.13. Initial production from the installed panels during the month of April, 2021, is illustrated in Figure 4.14.

In addition to the generation capabilities, the energy efficiency of the solar installation under both AC and DC configurations merits investigation. Since this project is focused on the reduction of energy conversion and increasing energy efficiency, the losses associated with an AC configuration are important to recognize. Figure 4.11 outlines the individual losses by percentage, with the AC system and corresponding inverters representing up to 3.8% of the total system power dissipated. The module DC nameplate for the solar installation is 14.3 kW, so this loss amounts to approximately 0.54 kW. Although this amount can't be completely reclaimed by transition to a DC system, the percentage lost will be significantly less.

With respect to storage, average power and energy consumption determined in Table 4.1 insinuates that heavier load demands occurring during the heating season will render any substantial storage capacity mostly unproductive. However, the cooling seasonal months are excellent candidates for storage considerations. As revealed by Figure 4.3, during the month of June in 2019, 488 kWh was expended by the DC Nanogrid House, while the projected solar

production detailed in Figure 4.10 indicates an estimated 1,700 kWh of generation capacity for the same month. Taking the average difference over each day, this represents a daily surplus production of 40 kWh. Performing a similar analysis over each month of the year for the average energy consumption and production, a surface approximation of the ideal storage capacity falls into the range of 10 kWh to 15 kWh. As a result, a battery of LiFePO4 chemistry manufactured by POMCube was selected with 20 kWh of storage capacity, slightly above the aforementioned average estimated need for the year. This additional bandwidth of energy storage will enable greater utilization during the summer months, and support optimal control strategy development for charging/discharging scenarios during other months. The installed battery system is depicted in Figure 4.15.

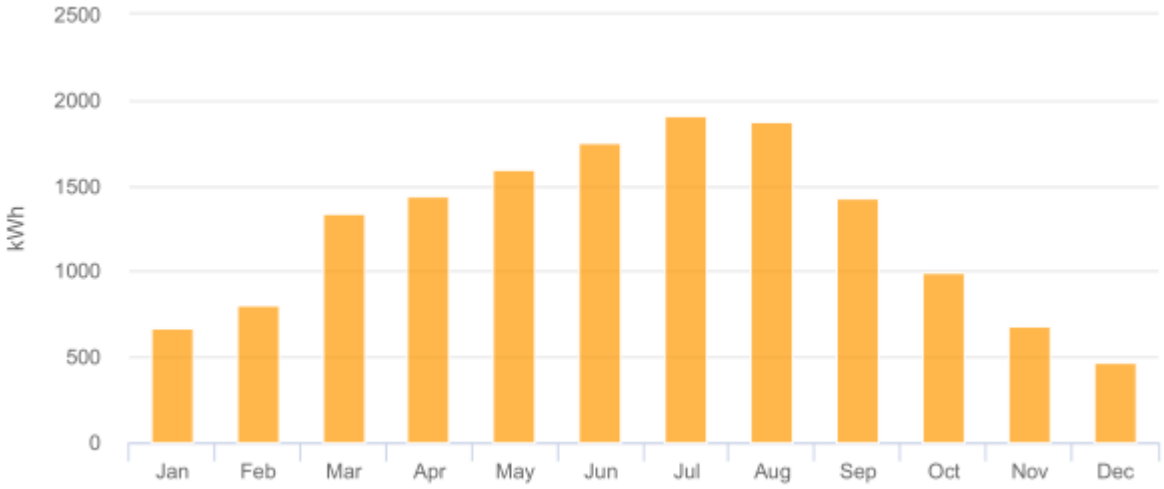

Figure 4.10. Projected solar panel installation energy generation each month.

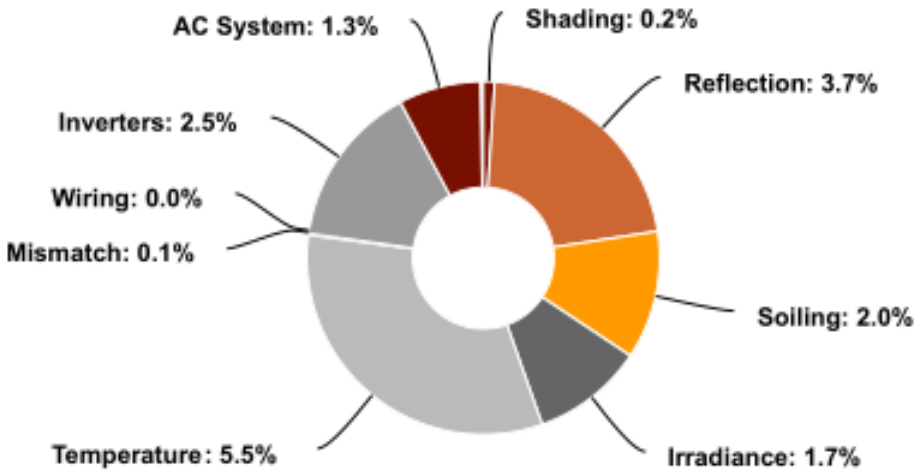

Figure 4.11. Sources of loss by percentage in the rooftop solar installation.

Figure 4.12. In-progress installation of the 14.3 kW solar array.

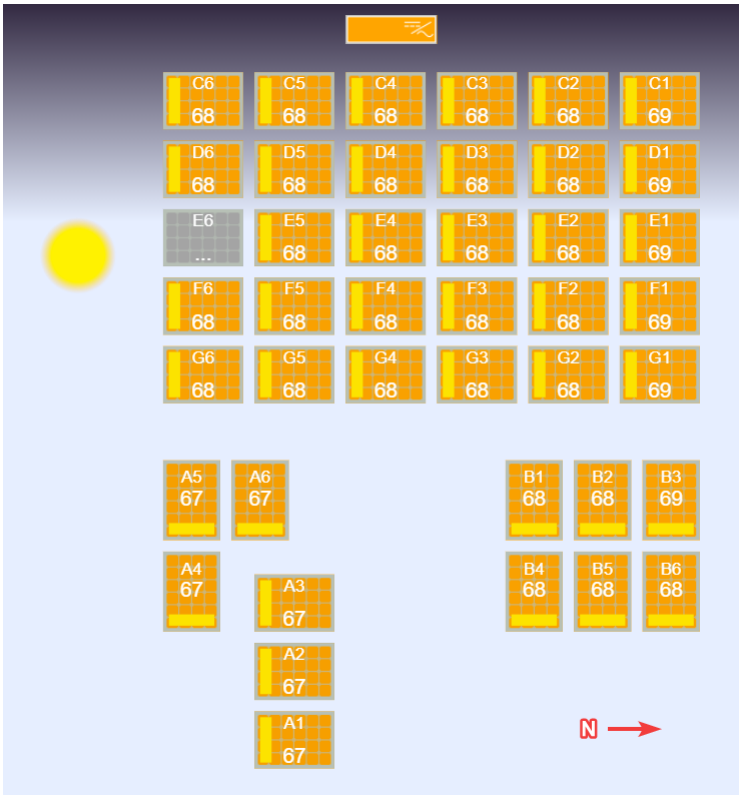

Figure 4.13. DC Nanogrid House solar panel visualization with real-time optimizer voltage output.

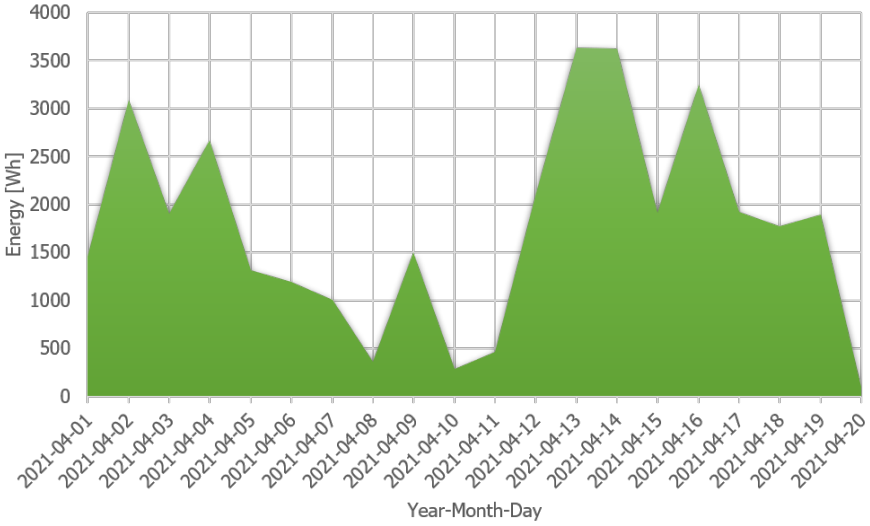

Figure 4.14. Solar panel energy production during the month of April, 2021.

Figure 4.15. Installation of the 20 kWh battery system.

4.3.3 Construction, Implementation, and Safety

With the nanogrid equipment selected and sized sufficiently, the next step was to determine the corresponding layout and connections. A unique challenge of the DC infrastructure arises from the multiple sources and bidirectional nature of the storage and inverter. To resolve this issue, a novel DC combiner and distribution panel was designed to interface between the primary DC bus and the individual loads. It also serves as a focal point for power and energy measurements to be conducted, as well as a means to troubleshoot individual connections during development and experimentation. The AC connections of the nanogrid, load centers, and DC interface through the combiner panel is summarized in a one-line diagram of the nanogrid layout depicted in Figure 4.16.

Based on the maximum power ratings of the nanogrid equipment, 6 American Wire Gauge (AWG) wire was selected as the primary conductor for AC and DC connections. This wire is rated for up to 600 VDC of continuous operation, and up to 70 A in peak load conditions, as confirmed in Figure 4.17. DC wiring of the nanogrid was installed in a unipolar scheme, with two conductors maintaining a voltage potential of 380 VDC, and a third wire functioning as a ground wire. Electrical disconnects were installed both inside and outside of the home at every interface, including the main utility AC branch input to the transformers, solar PV string combination box, and battery storage. These safety mechanisms are illustrated in Figures 4.16, 4.18, 4.19, 4.20, 4.21, and 4.22.

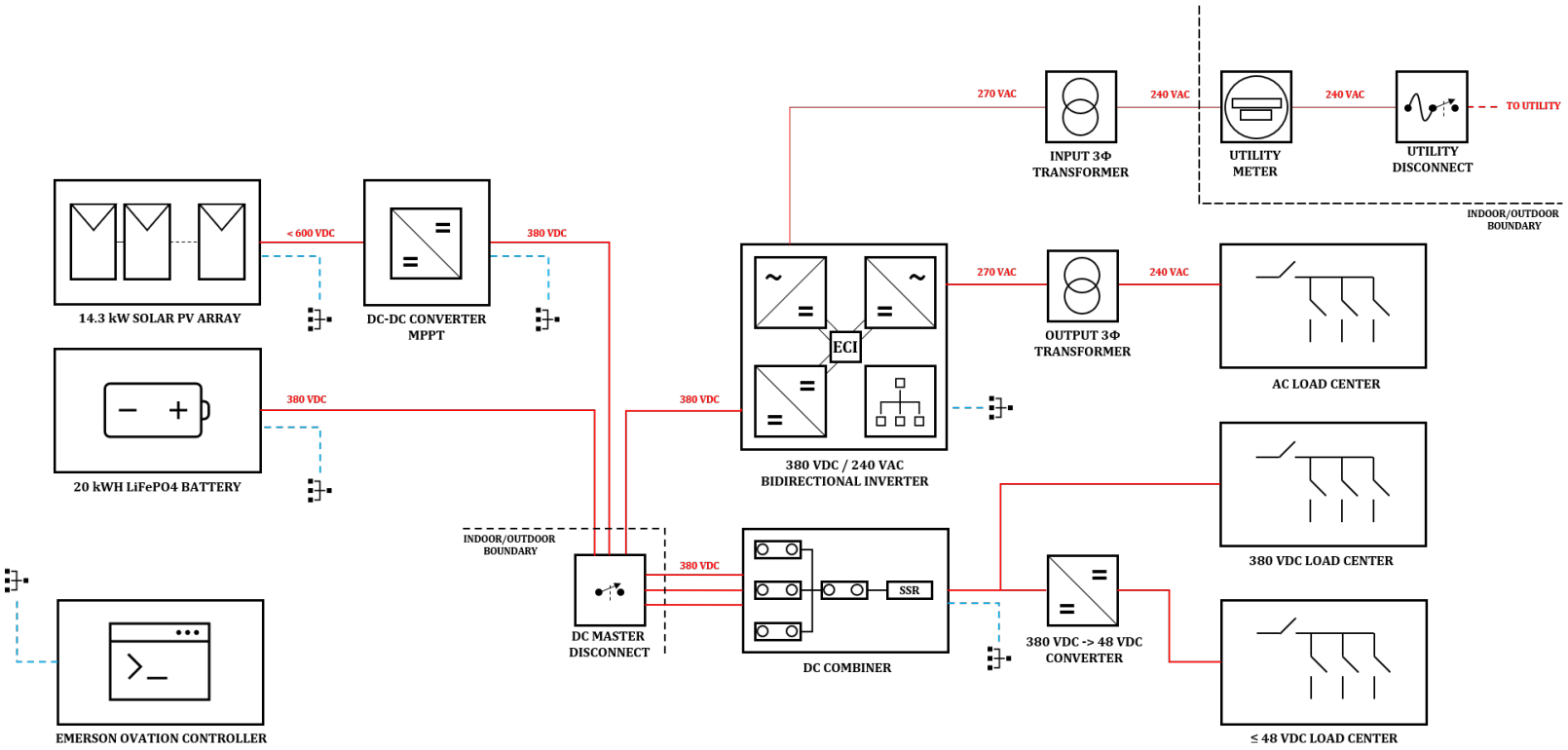

Figure 4.16. DC nanogrid one-line schematic.

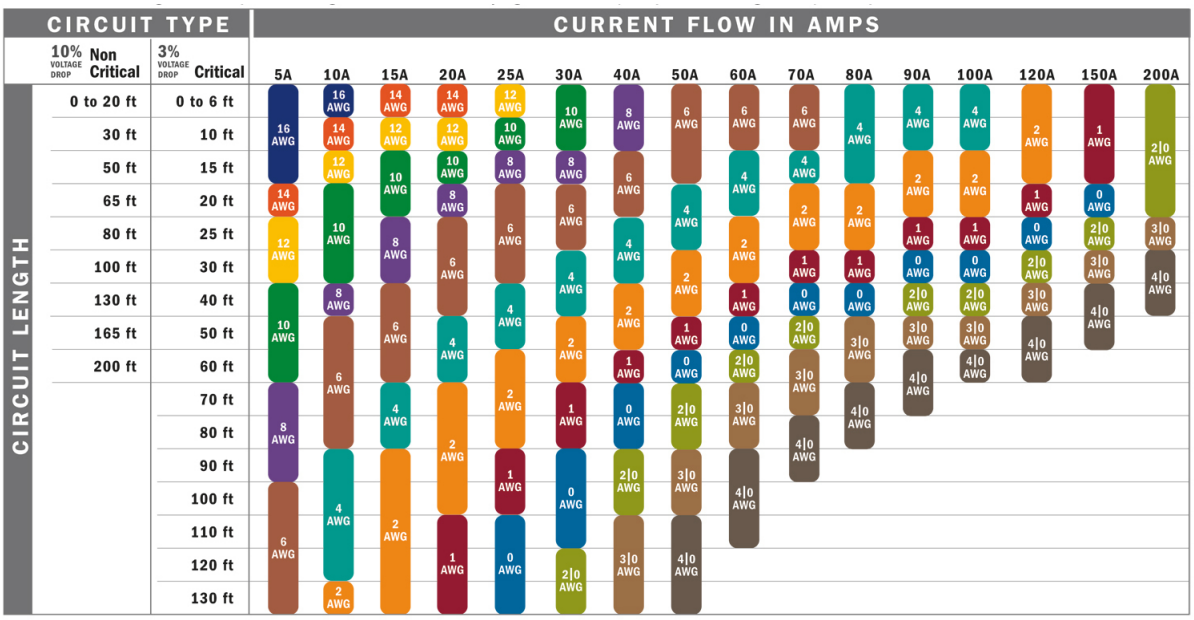

Figure 4.17. DC current capacity rating by wire gauge and conductor length.

Figure 4.18. Nanogrid AC input utility disconnect location.

Figure 4.19. Solar PV combiner and disconnect location.

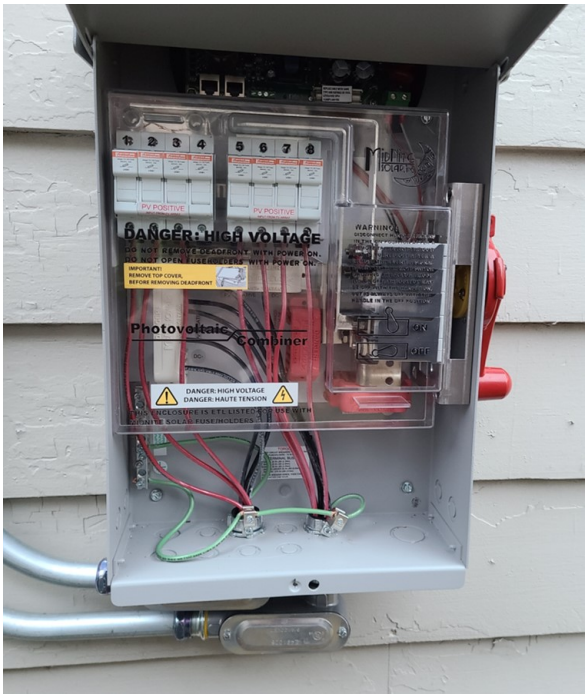

Figure 4.20. Solar PV combiner and disconnect internal circuitry and connections.

Figure 4.21. Solar PV and battery indoor disconnect locations.

Figure 4.22. Bidirectional inverter AC input and output indoor disconnect locations.

The DC combiner and distribution panel are individually composed of solid state relays (SSRs), current shunts, fuses, distribution busses, monitoring circuits and devices, and DC-DC converters. A critical aspect of this panel is the electrical isolation it affords between DC connections. As defined by the Institute of Electrical and Electronics Engineers (IEEE), a ground loop is a "A potentially detrimental loop formed when two or more points in an electrical system that are nominally at ground potential are connected by a conducting path such that either or both points are not at the same ground potential" [145, p. 494]. In some systems this can result in a minor nuisance (e.g., buzzing from a speaker, etc.), but in other systems this can result in destructive and dangerous outcomes. To mitigate these risks, electrical components with built-in isolation are used between interfaces and loads. In the case of the DC distribution panel, the input DC connections are isolated through the digital shunts and downstream DC-DC converters. This ensures that: (1) all input DC connections are isolated from each other, and (2) all downstream DC loads are isolated from the inputs. The individual components of the DC panel are identified in Figure 4.23, and the current construction of the panel is shown in Figure 4.24 with a live voltage reading in Figure 4.25.

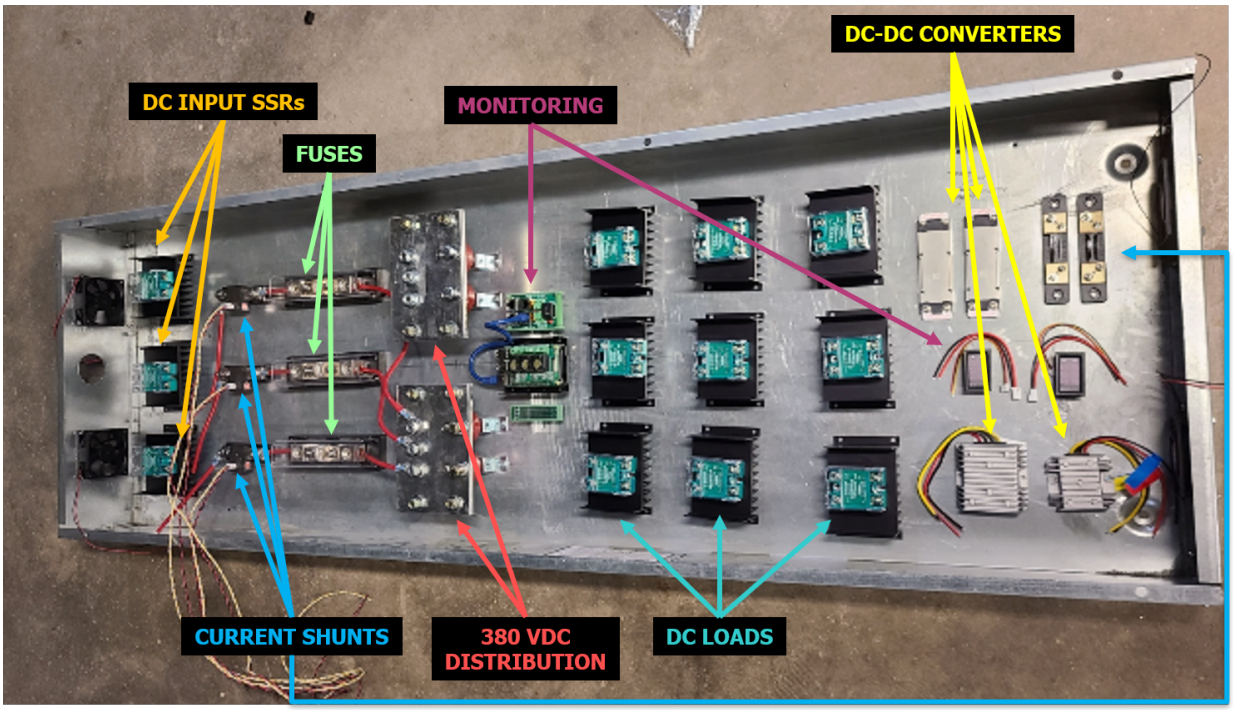

Figure 4.23. DC distribution panel component designation and layout.

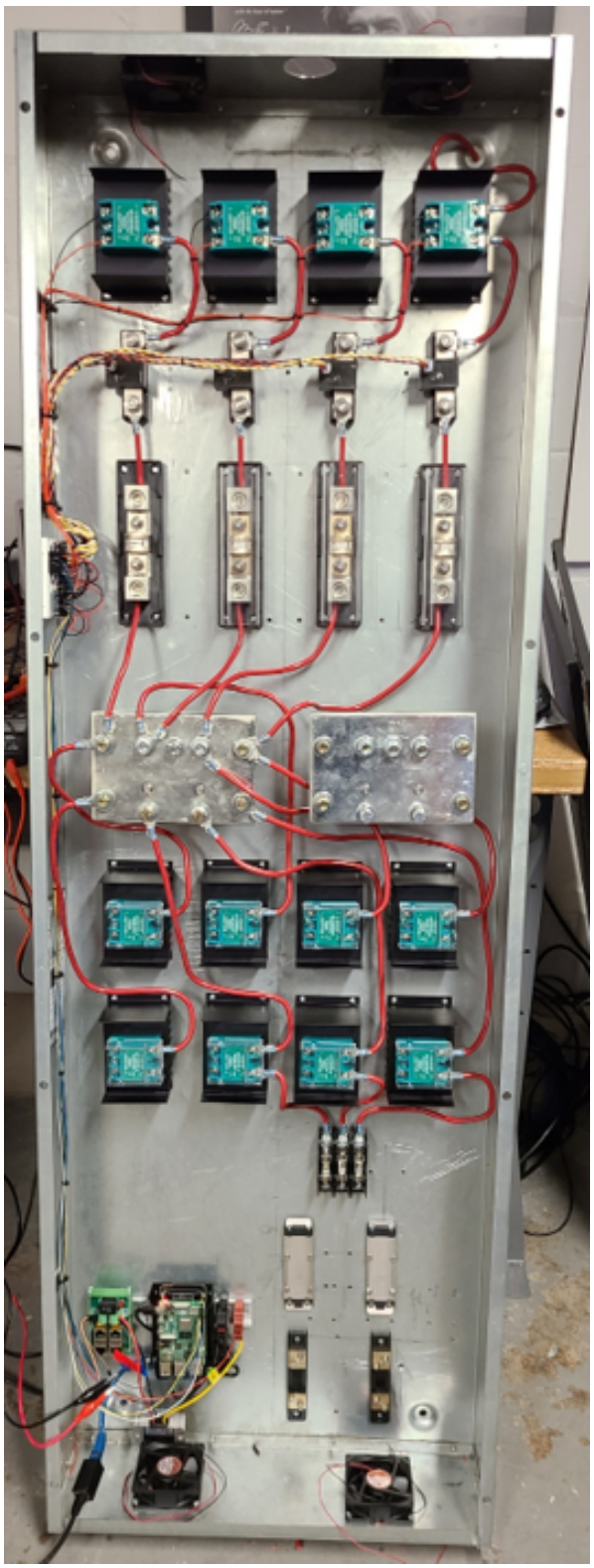

Figure 4.24. Installed DC distribution panel with wired connections to the DC nanogrid sources and loads.

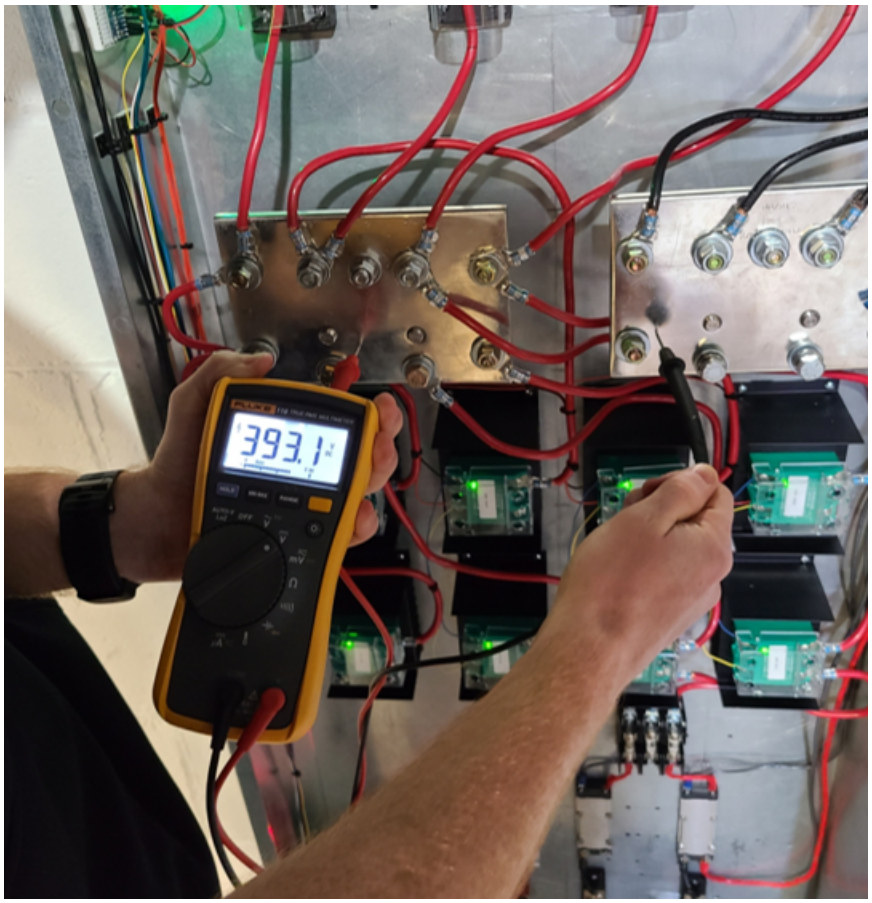

Figure 4.25. Demonstration of the DC distribution panel 380 VDC primary bus.

The final component of the DC nanogrid is the maximum power point tracking (MPPT) equipment used to optimize the collected solar PV energy. An MPPT system from CE+T, known as the Stabiliti module, was selected to process the generated DC power from the solar panels and simultaneously function as a DC-DC converter to stabilize the central nanogrid DC bus. The Stabiliti MPPT system and the Sierra inverter system operate in conjunction with one another to ensure a consistent DC voltage and proper flow of power (either into or out of the nanogrid). At the present, the DC nanogrid has been successfully commissioned by the equipment manufacturer, and has performed the following initial functions:

- Powered on using AC supplied by the utility
- Back-fed power out to the utility generated by the solar PV and battery system
- Fully charged the battery using generated power from the solar PV
- Supplied DC from the inverter to charge the battery

An overview of the nanogrid and the equipment during the commissioning process is detailed in Figures 4.26, 4.27, 4.28, and 4.29, and a demonstration of the nanogrid's functionality is illustrated on the control screen shown in Figure 4.30.

Figure 4.26. Assembled and installed DC nanogrid equipment.

Figure 4.27. Layout of the low-voltage DC load center cabinets.

Figure 4.28. Commissioning of the bidirectional Sierra inverter system and modular Bravo ECI components.

Figure 4.29. Commissioning of solar PV Stabiliti MPPT system.

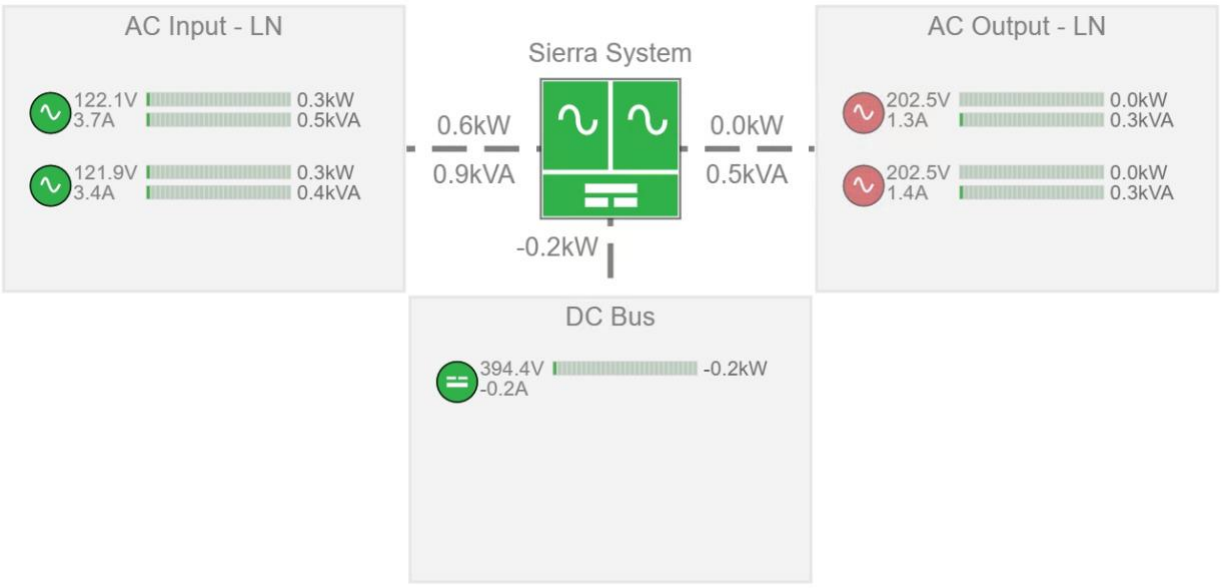

Figure 4.30. Control screen display of the individual DC nanogrid electrical connections.

4.3.4 Control System Development

In addition to the electrical nanogrid equipment, a control system manufactured by Emerson was selected to manage and communicate with each system, as well as maintain and host the EMS and BMS systems. The control system communication connections are detailed in Figure 4.16, and the physical controller itself, referred to as the Ovation system, is illustrated in Figure 4.31. The control system is responsible for managing the critical Nanogrid operations, including:

- AC/DC grid interaction and power flow
- Energy distribution and management
- Load shedding behavior
- Power optimization
- Safety/fault management and handling

Figure 4.31. Emerson Ovation controller equipment.

The Emerson Ovation system features distributed control methodology, and is built on top of a real-time operating system (RTOS) platform. This platform provides high-level functional processes which can be managed in a graphical programming environment (similar to MATLAB Simulink, ANSYS SCADE, etc.), and performs operations such as

proportional-integral-derivative (PID) control, boolean logic, data acquisition, event processing, input/output (I/O) interfacing, and many others. Up to 32,000 individual virtual points can be managed within the system, which interacts with other equipment through a supervisory control and data acquisition (SCADA) interface. Logic can be implemented using control sheets built in the RTOS platform, and the Ovation system supports up to five simultaneous process executions. Each process can be maintained at specified loop speeds ranging between 10 ms up to 300 s each. The control loop configurations are critical for the nanogrid's operations, as certain safety and electrical responses require guaranteed processing times within limited windows. Finally, the controller also operates in a hot-backup mode in which a backup processor can perform an automatic failover in the event the primary processor encounters a fault. Both processors are continually synchronized to ensure that operations are identical under either configuration.

The control system main panel is illustrated in Figure 4.32. Communication configurations using the SCADA environment is shown in Figure 4.33, and example control functions using the graphical library are demonstrated in Figures 4.34 and 4.35.

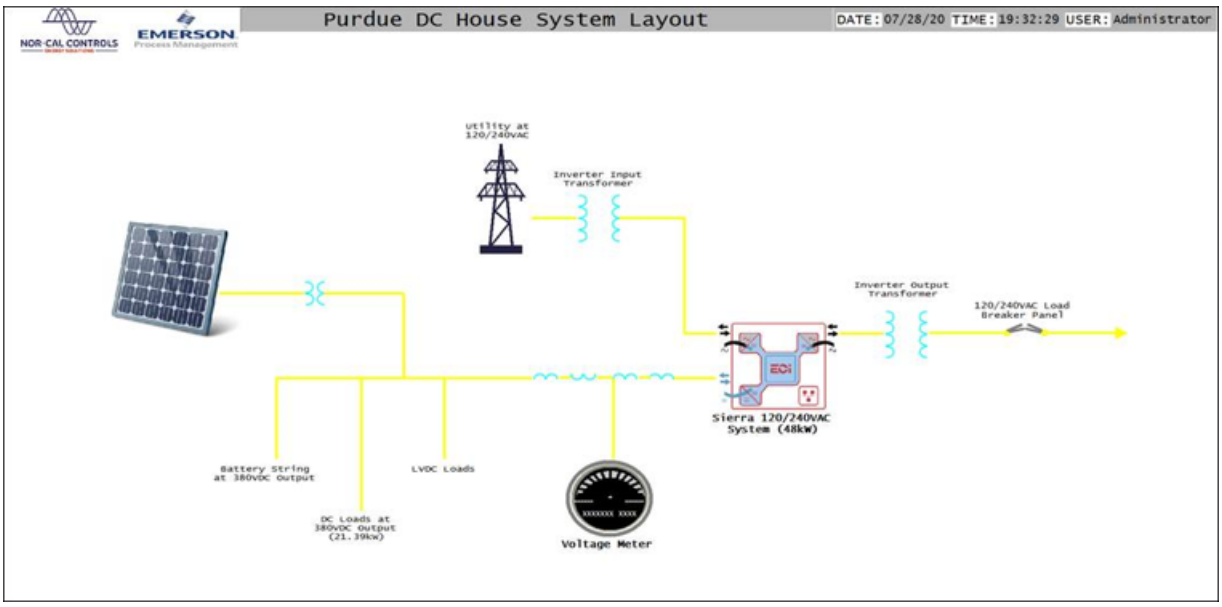

Figure 4.32. Ovation control system main monitoring panel.

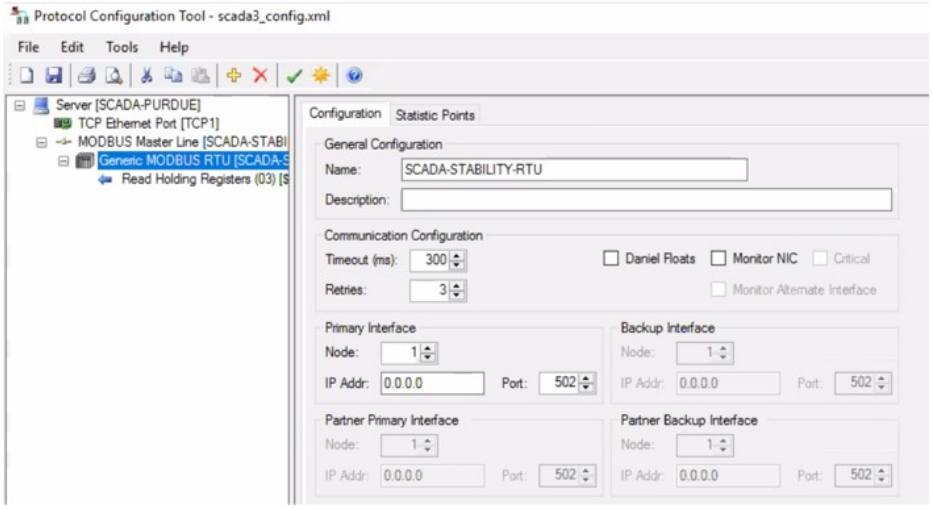

Figure 4.33. Ovation control system SCADA environment for configuring communications.

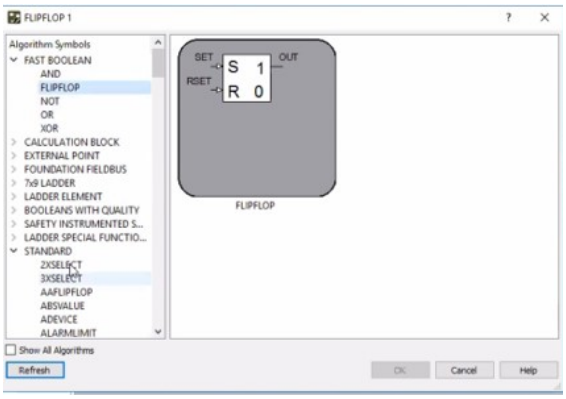

Figure 4.34. Ovation RTOS control logic block demonstration.

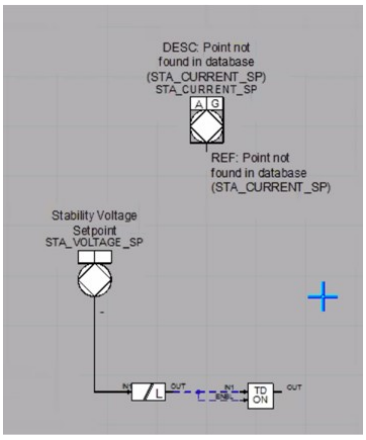

Figure 4.35. Ovation RTOS control logic sheet demonstration.

5. IOT SYSTEM DEVELOPMENT AND APPLICATION

5.1 System Synopsis and Demonstration

The concept of smart devices has existed for decades, dating back to the inception of the internet itself. Within the 21st century, this idea has continued to evolve into more advanced and integrated technologies, collectively known as the Internet of Things, or IoT. These technologies have been applied to numerous different settings, including home automation, healthcare and medical science, and industrial applications. IoT affords the capability to monitor and control a huge variety of devices over an ever-increasing range of protocols. From this perspective, the system of IoT can be analyzed in an analogous manner to the Open System Interconnection (OSI) model, which divides telecommunications into seven individual layers: Physical, Data Link, Network, Transport, Session, Presentation, and Application [146]. In the landscape of IoT, corresponding layers include Infrastructure, Transport, Data Protocol, Device Type, Storage, and Application. Table 5.1 below illustrates these various layers, and existing representations of each one.

Table 5.1. IoT layers and corresponding instances.

Layer	Instances
Infrastructure	IPv4/IPv6, 6LoWPAN, UDP, NanoIP
Transport	Wi-Fi, Bluetooth, ZigBee, LTE
Data Protocol	MQTT, AMQP, REST, Websocket
Device Type	ESP32, Arduino, RaspberryPi
Storage	MySQL, PostgresSQL, MongoDB
Application	Monitoring, Analysis, Data Mining

Among each of the layers, arguably some of the most important are the Transport and Data Communication Protocol layers, which are often dictated in part by the environment and specific application setting. There are a variety of advantages and disadvantages for each type, which is a central focus of this individual subtopic.

5.1.1 Communication Protocols

For intra-communication between sensors, three primary types of communication methods exist. These include Universal Asynchronous Receiver Transmitter (UART), Inter-Integrated-Circuit (I2C), and Serial Peripheral Interface (SPI). Each method has distinct advantages and disadvantages which serve as critical determinants in a particular application. Specific applications of UART include RS232, RS422, and RS485, while I2C and SPI can often be found together or interchangeably on various sensors and devices (Analog to Digital Converters (ADCs), Digital to Analog Converters (DACs), etc.).

A primary benchmark for each communication option is the complexity and scalability. UART and I2C dominate this category, requiring only half as many wires (I2C), or a quarter as many (UART) compared to SPI to establish communication as SPI. However, UART is limited in terms of its scalability, only supporting a maximum of two devices in each communication chain. I2C supports up to 127 devices, while SPI has no theoretical limit at all, only being bound by the hardware employed or the intricacy of the messages being broadcast. In terms of speed, SPI provides the fastest option of the three types, followed by I2C, with UART finishing last. Finally, in terms of features provided, SPI and UART support full duplex communication, while I2C offers only half duplex. In essence, I2C does not support bidirectional simultaneous communication on the same channel. However, I2C supports multiple master and slave relationships in a specific communication channel, while SPI permits only one master with many slaves. UART has no applicability to these relationships due to its one-to-one relationship between devices [147]. In summary, the specific attributes of each communication protocol can be summarized in a tabular form as shown in Table 5.2.

From these details, it is clear the choice of protocol is highly dependent on its application. For instances with device to device connection only, UART is a common selection. However, for IoT applications with the potential to add large numbers of sensors communicating on a single network, I2C or SPI may be better suited. For a single controller, SPI is a logical option, while I2C offers more decentralized communication and fewer single points of failure (SPOFs). Demonstrations of I2C and SPI are shown in Figure 5.1 and Figure 5.2.

Table 5.2. Intra-communication protocol benchmarks.

Benchmark	**Protocol**		
	UART	**I2C**	**SPI**
Complexity	Simple	Simple	Complex
Speed	Slow	Moderate	Fast
Device Support	2	127	Unlimited
Duplex Support	Full	Half	Full

Pins used in I2C and SPI communication include Serial Data (SDA), Serial Clock (SCL), Master-In Slave-Out (MISO), Master-Out Slave-In (MOSI), and Chip Select (CS). Of these, the CS pin is especially unique to SPI communication, which serves as a unique identifier for each downstream device to be controlled.

Beyond the small-scale distances between immediate sensors and corresponding microcontrollers, other mediums of communication must be employed to maintain system feasibility and interconnectivity. Table 5.1 indicates many of these options, including Wi-Fi, various Bluetooth protocols, ZigBee, etc. These methods need not be mutually exclusive within a given network, as patents currently exist outlining their conjoint operation [148].

Unlike local communication methods, additional mechanisms are typically necessary to support these longer-range connections, which are exemplified under the data protocol row in Table 5.1. Often an intermediary buffer is established between the individual elements of an IoT network, which forms the basis of message-oriented middleware (MOM) communication

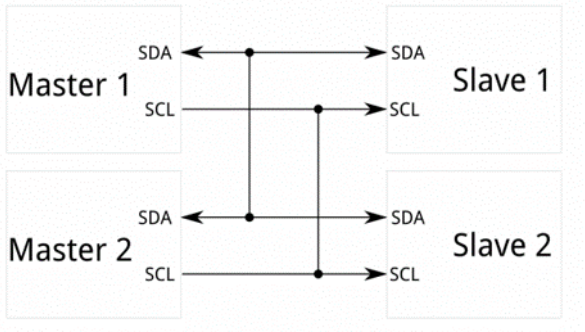

Figure 5.1. I2C communication.

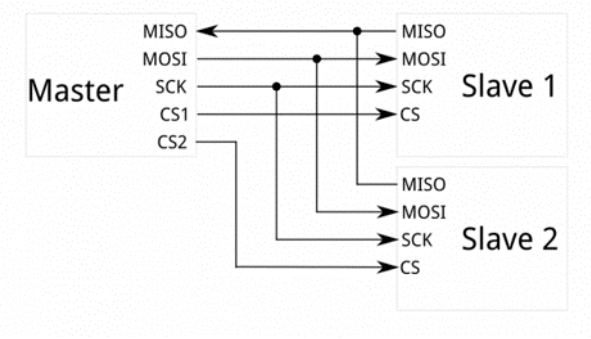

Figure 5.2. SPI communication.

[149]. A MOM architecture provides a multitude of benefits in a communication network, most notably the flexibility for asynchronous and synchronous communication, decentralization between devices, and priority specification between messages. This is most often achieved through the use of publish/subscribe, in which a topic or queue serves as a buffer for messages. A queue provides point-to-point relationships, whereas a topic offers one-to-many. Using the transportation medium of any of the available infrastructures, messages can be transmitted from individual IoT elements and processed by interested subscribers.

A common IoT MOM implementation is the MQ Telemetry Transport protocol, or MQTT. MQTT is a lightweight protocol (among both computational and energy considerations), and provides significant resilience even in the presence of networks with high latency or unreliability. These features make it highly attractive for IoT networks, which are often composed of low-power devices and a unique variety of data exchanges and characteristics. The publish/subscribe nature of MQTT enables integration of devices with differing transmission rates, without impacting subscribers or data processing elements. In essence, each aspect of the network can be decoupled from the other components, using the MQTT broker as the intermediary. An illustration of these attributes in practice is demonstrated in Figure 5.3.

An additional characteristic critical for these networks is the Quality of Service (QoS). The QoS represents the confidence of message delivery and reception between each communicating element of the IoT system. Specifically, there are three defined QoS levels in MQTT representing the guarantee of delivery for a transmitted message. QoS 0 guarantees at most

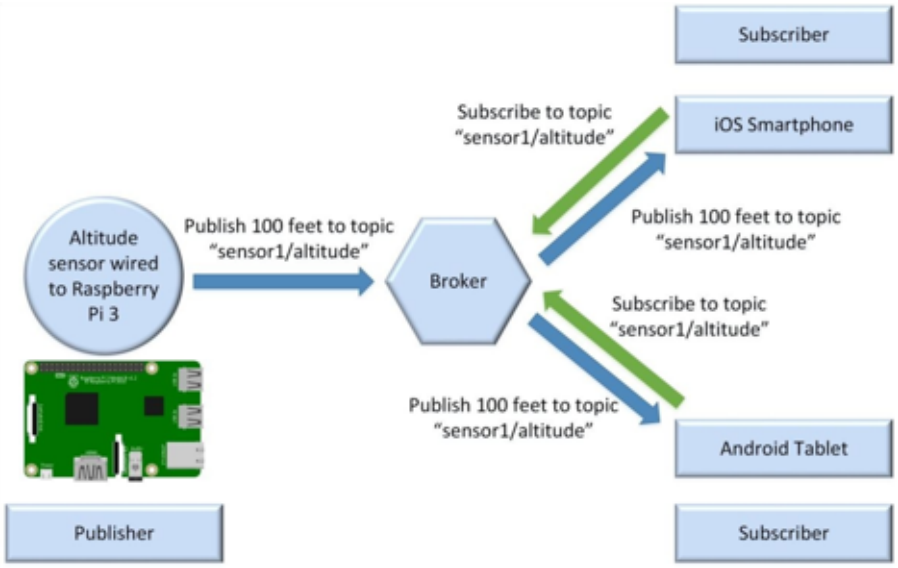

Figure 5.3. MQTT broker demonstration [150].

once, QoS 1 guarantees at least once, and QoS 2 guarantees exactly once. These levels are individually clarified in Figure 5.4.

As the illustration confirms, QoS 2 is the most complex but secure form of transaction. The client sends a request to publish a message, which is confirmed with an acknowledgement from the broker. Until this acknowledgement is received, the client will continue posting publish requests with a duplicate message flag. Once the acknowledgement is received, the message payload is transmitted to the broker. After the broker successfully processes the message, it responds with a final confirmation to the client. Until this confirmation is received, the client maintains a copy of the message for safekeeping in case processing by the broker was unsuccessful. Ultimately, this four-part handshake ensures complete message delivery and receipt between two IoT entities [150].

A final aspect of the QoS relationship is the potential for a downgrade of service. If two clients are involved between a given broker, each may maintain a different level of QoS. If the first client is equipped with QoS 2 (and the broker supports it), the message will be delivered to the broker with QoS 2. However, if the second client subscribing to the broker has QoS 1, the broker will only deliver the message to the subscriber with QoS 1. As a result, the totality of the message delivery between client one and client two have QoS 1. Other

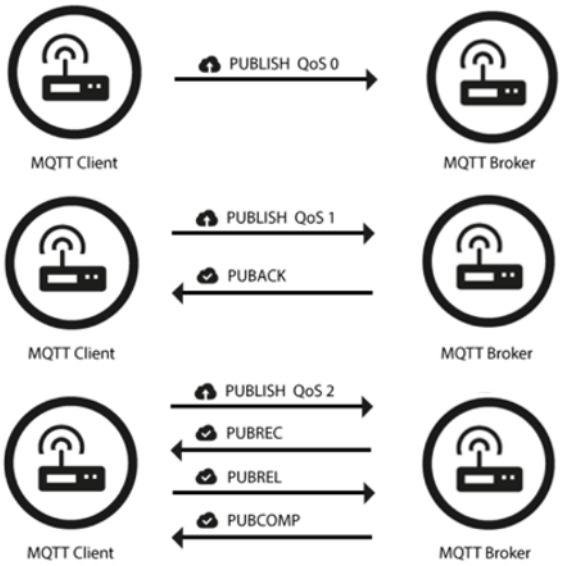

Figure 5.4. QoS levels of communicating devices.

situations may arise where a given client is capable of QoS 2 delivery, but the corresponding broker only supports QoS 1 or QoS 0. As in the previous example, the overall message transmission is then limited by the entity with the least QoS level. This is an important consideration when evaluating IoT network performance [150].

5.1.2 Messaging Configuration

Although MQTT may exist as the predominant choice of messaging in the IoT space, other protocols may also be present (including Advanced Message Queuing Protocol (AMQP), Simple Text Oriented Message Process (STOMP), etc.), making it important to choose a messaging service with sufficient flexibility. Some of the most popular choices include RabbitMQ, HiveMQ, ActiveMQ, JoramMQ, Apollo, and Mosquitto. A distributed technology organization, ScalAgent, compared several of these technologies in a benchmark MQTT study and evaluated their capabilities and latencies [151]. While RabbitMQ is a highly flexible and capable server, it is computationally intensive in terms of size and resources and thus unsuitable for implementation within many System on a Chip (SoC) devices. Instead, the Mosquitto server is a much better choice and satisfies the device communication needs.

Alternatively, the devices comprising the Single-Board Computer (SBC) category are far better adapted for the additional features afforded by the RabbitMQ server while satisfying its computational demands. As a result, both the Mosquitto and RabbitMQ servers can be integrated together, each working in tandem to support the needed communication mechanism. A depiction of this network is illustrated in Figure 5.5.

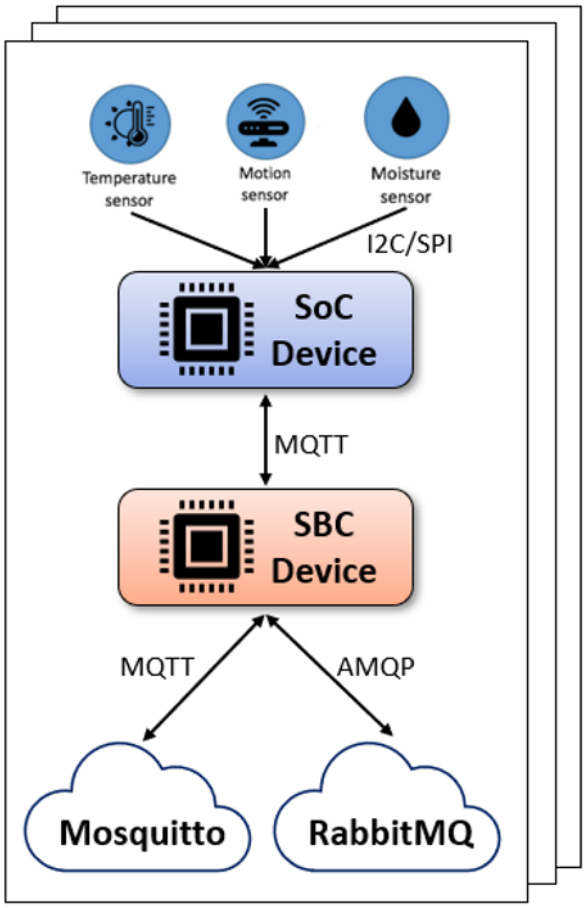

Figure 5.5. Mosquitto/RabbitMQ network integration.

5.1.3 Power Distribution and PoE Protocols

In addition to the communication channel, individual IoT devices must also be supplied with a DC power source. In smaller scale environments, it may be feasible to achieve this with USB cables or even batteries. However, in the case of a multi-floor home, as in the DC House, Wi-Fi may be insufficient in certain locations, and a multitude of devices renders a

battery-based solution impractical. The DC House's LVDC network is advantageous for the IoT devices, which all require various DC voltage inputs (e.g., 5 VDC, 3.3 VDC, etc.). As a result, a solution satisfying both the power and communication needs is highly desirable, and can be achieved through a specific DC technology: PoE.

PoE was initially developed under IEEE 802.3af in 2003, which supported 15.4 W of DC power under a minimum supply of 44 VDC and 350 mA of current [152]. This has increased under the latest IEEE 802.3bt protocol released in 2018, which now affords up to 100 W under a minimum supply of 52.0 VDC and 960 mA of current (per pair of wires in 4-pair mode) [153]. In this study, a PoE Power Injector satisfying the IEEE 802.3at "PoE+" protocol was employed, capable of producing a maximum of 25.5 W at the output under a minimum supply 50.0 VDC and 500 mA [152], [153]. A typical use case is illustrated in Figure 5.6 and Figure 5.7.

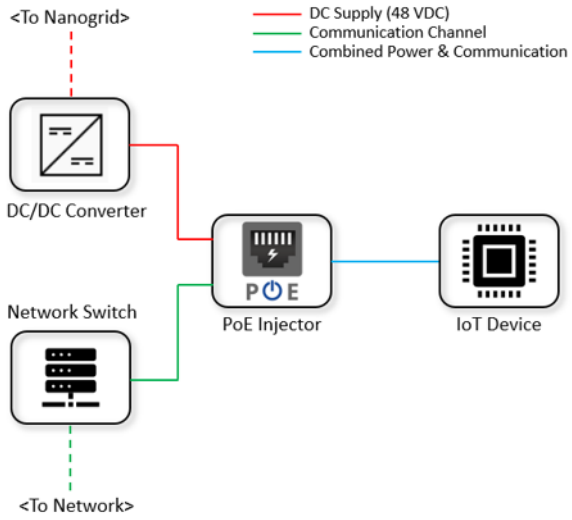

Figure 5.6. DC nanogrid integration with IoT using PoE.

SBC devices, such as a Raspberry Pi, often come equipped with 5 VDC and 3.3 VDC rails which are capable of powering local SoC devices. In the specific case of a Raspberry Pi 4 Model B, the manufacturer specifications indicate a power requirement of 5 VDC at a minimum of 3 A, providing 15 W of power. Studies of the device under heavy load indicated a maximum current draw of approximately 1 A, leaving 2 A remaining for peripheral devices and other components. Tests of SoC devices, such as an ESP32, reveal typical current

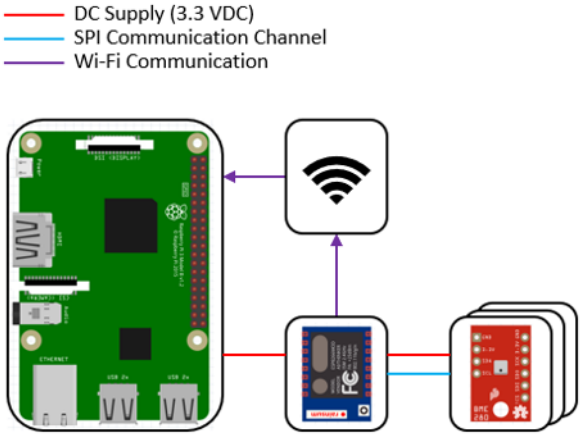

Figure 5.7. IoT SBC interconnection with SoC sensors.

consumptions of approximately 100 mA to 200 mA, with current spikes around 500 mA. As a result, the SBC is more than sufficient to supply individual SoCs.

In the reverse case, it is also necessary to consider each SBC device's current draw with respect to the IEEE 802.3 PoE protocol. These measurements are not solely necessary for determining whether or not the PoE mechanism can satisfy them, but for the specific level of PoE required. As discussed in the previous section, a range of PoE levels exist, which are summarized in Table 5.3 [152]–[154].

Table 5.3. IEEE protocol electrical characteristics.

Attribute	**IEEE Protocol**			
	802.3af [PoE]	**802.3at [PoE+]**	**802.3bt [4PPoE]**	**802.3bt [PoE++]**
Max Power at Device [W]	12.95	25.50	51	71
Max Voltage at Device [V]	57.0	57.0	57.0	57.0
Max Current at Device [A]	0.350	0.600	1.200	1.920
Min Ethernet CAT Needed	3	5	5	5

As the IEEE protocol level increases, the corresponding cost of the devices supporting them increases rapidly. For example, low-power 802.3af 15 W injectors can be obtained for around for 10 to 20 US dollars, while a single high-power 802.3bt 100 W injector can reach into the hundreds of US dollars [152], [153]. For a practical system implementation, the

appropriate injector must be selected for each device to ensure adequate power is supplied without unnecessarily incurring additional cost.

In the case of this IoT system, the SBC of choice was designated to be the Raspberry Pi models. To establish the required PoE protocol, power consumption was studied on each of the available models. This data is tabulated in Table 5.4.

Table 5.4. Raspberry Pi SBC power consumption.

Model	**Max Power Draw [W]**	**Max Current Draw [A]**
4B	6.4	1.280
3B+	5.1	0.980
3B	3.7	0.730
2B	2.1	0.450
Zero	0.7	0.120

These values were obtained under worst case conditions simulated by executing the Linux command “stress -cpu 4”, which spawns four processes on the SBC CPU to perform mathematical computations. HDMI outputs were disconnected along with all other USB devices. It is worth noting that thermal considerations become necessary at these levels for a sufficient period of elapsed time.

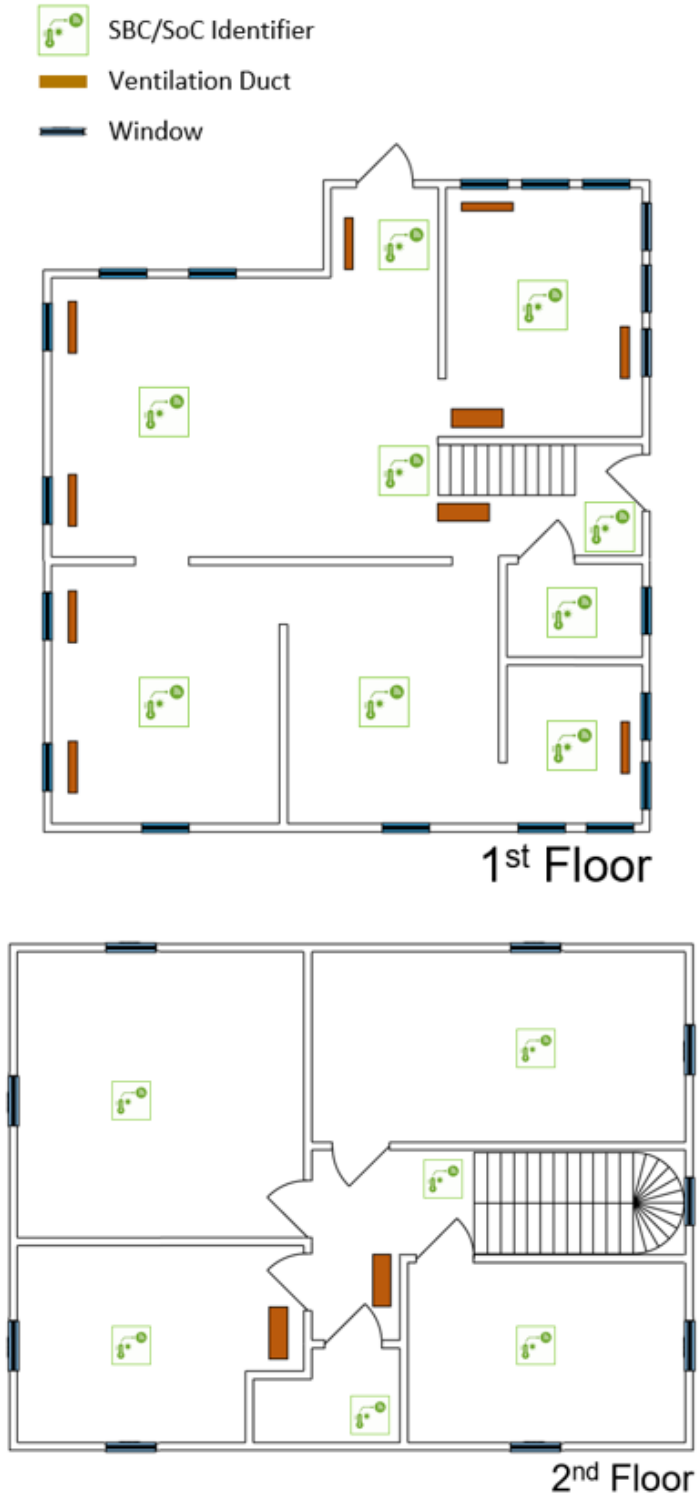

Figure 5.8. Residential IoT Network Implementation.

5.1.4 Residential Implementation

From the findings in Table 5.4 and the architecture detailed in Figure 5.6, the IoT network design can be extended throughout the house. Combining the SBC IoT device and downstream sensors as an individual identifier, a depiction of the layout for the DC House can be developed as shown in Figure 5.8. A prototype of the IoT modules was presented previously in Section 2.3.3 and Figure 2.43.

The results of Table 5.4 indicate that PoE protocol IEEE 802.3af is satisfactory to sustain an individual SBC device, even under maximum power consumption. Using the worst-case conditions for the Raspberry 4B model, approximately 6.6 W are available for additional SoC consumption. From the upper limit of typical consumption, 200 mA, at an input supply of 3.3 VDC, each device consumes approximately 0.4 W, yielding a sustainable ratio of SoC devices to a single SBC of 16:1. As a result, a highly affordable and scalable PoE-based network is feasible employing IEEE 802.3af 15 W injectors connected to SBCs and corresponding SoCs in strategic locations.

An active PoE splitter is used to provide both power and communication to the Raspberry Pi from the DC nanogrid, as illustrated previously in Figure 5.6. The Raspberry Pi provides a 3.3 VDC power supply to the ESP32, and the ESP32 3.3 VDC power rail drives each of the downstream sensors. The ESP32 is programmed in C++ using the PubSubClient library to post messages to the MQTT broker residing on the Raspberry Pi. The code responsible for posting messages to the broker is achieved through a successful Wi-Fi connection, connection to the broker, sensor read, and finally data postage to the broker topic. The key steps of this process are detailed in Appendix B.

While this code executes on the ESP32, Python code to establish and host the MQTT broker is performed on the Raspberry Pi. The serial output from the ESP32 can then be used to verify the building data against that being posted to the MQTT broker on the Raspberry Pi. Figure 5.9 shows the output of the serial monitor from the ESP32, and Figure 5.10 indicates the temperature data processed in the MQTT broker on the Raspberry Pi.

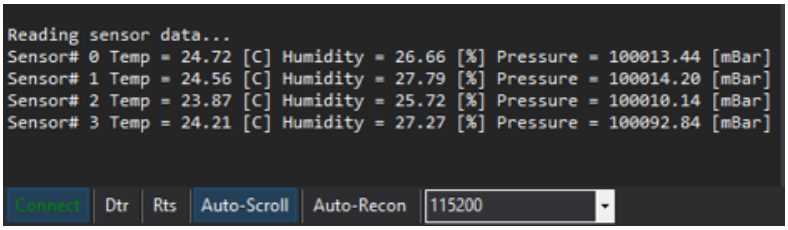

Figure 5.9. Serial output of the ESP32.

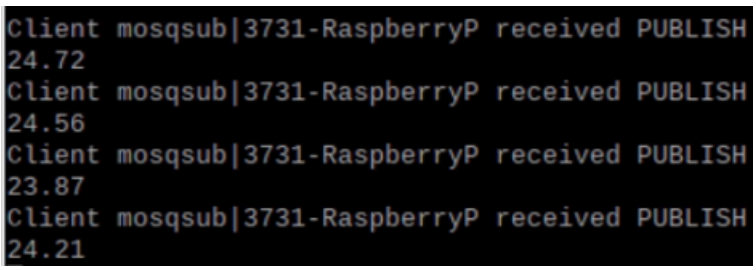

Figure 5.10. Data processed from the MQTT broker on the Raspberry Pi.

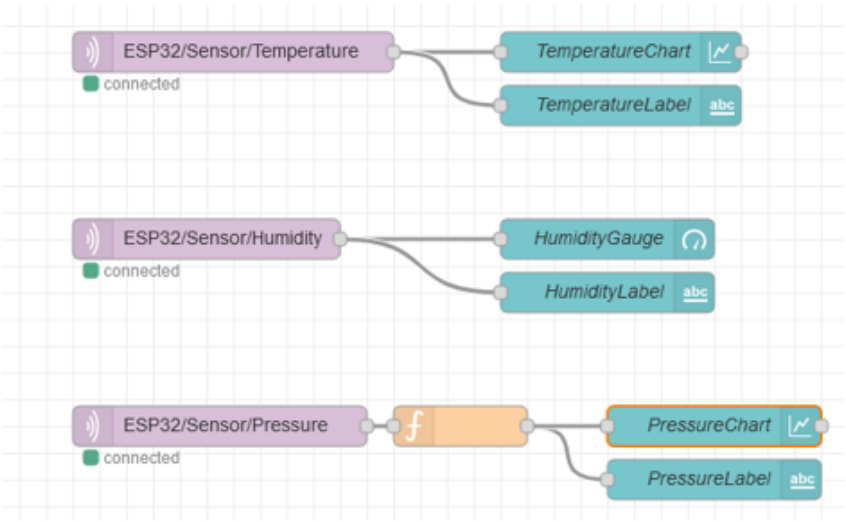

Figure 5.11. Node-RED data visualization tool.

5.1.5 Data Visualization and Summary

Following the successful demonstration of the IoT system, the collected data in the MQTT broker can be utilized by any other subscriber for further analysis, safety reporting, or informational dashboards. Node-RED is a popular tool which provides a variety of gauges, charts, and other flow-tools which can be used to display, manipulate, and signal events. An illustration of this tool used with the previous data collection is detailed in Figure 5.11 and Figure 5.12. In addition, another open source tool called InfluxDB can be used to store timeseries data, and create visualizations from it. An InfluxDB dashboard showing the server resources available from one of the IoT devices is presented in Figure 5.13.

A DC nanogrid affords a unique opportunity to transform a residential building into a "smart home" through the employment of an IoT sensor network. Galvanizing the IoT system with PoE technology repurposes the Ethernet cable beyond high communication throughput to simultaneously supply power alongside data transmission. In addition, power provided to these devices can be further leveraged to support devices even further downstream without imposing additional complexity within the power distribution network.

In terms of the system architecture, the coexistence of both the Mosquitto and RabbitMQ servers within the SBC provides the highest level of QoS service between devices, and also enables increased interfacing potential outside the MQTT communication structure. The dual servers increase the overall reliability and robustness of the system, and support a decentralized network independent from a single entity (and thus a SPOF). As the IEEE PoE protocol continues integrating into other popular connections (USB-C, Thunderbolt, etc.), the utility of these networks will also benefit, providing opportunities for faster communication networks, increased resilience to cyberthreats, advanced control strategies, and more comprehensive building metrics and assessments. In addition, the RabbitMQ broker can be leveraged for additional data processing, or data storage in a database.

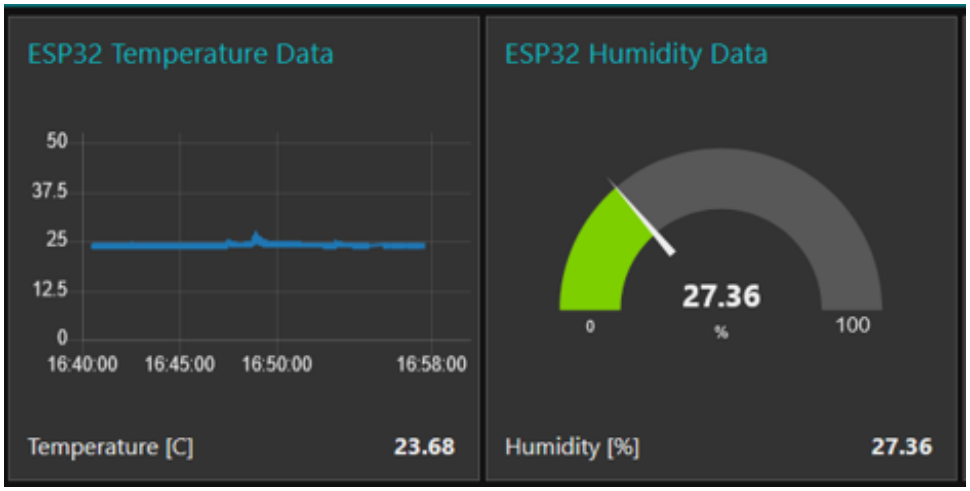

Figure 5.12. Node-RED dashboard display.

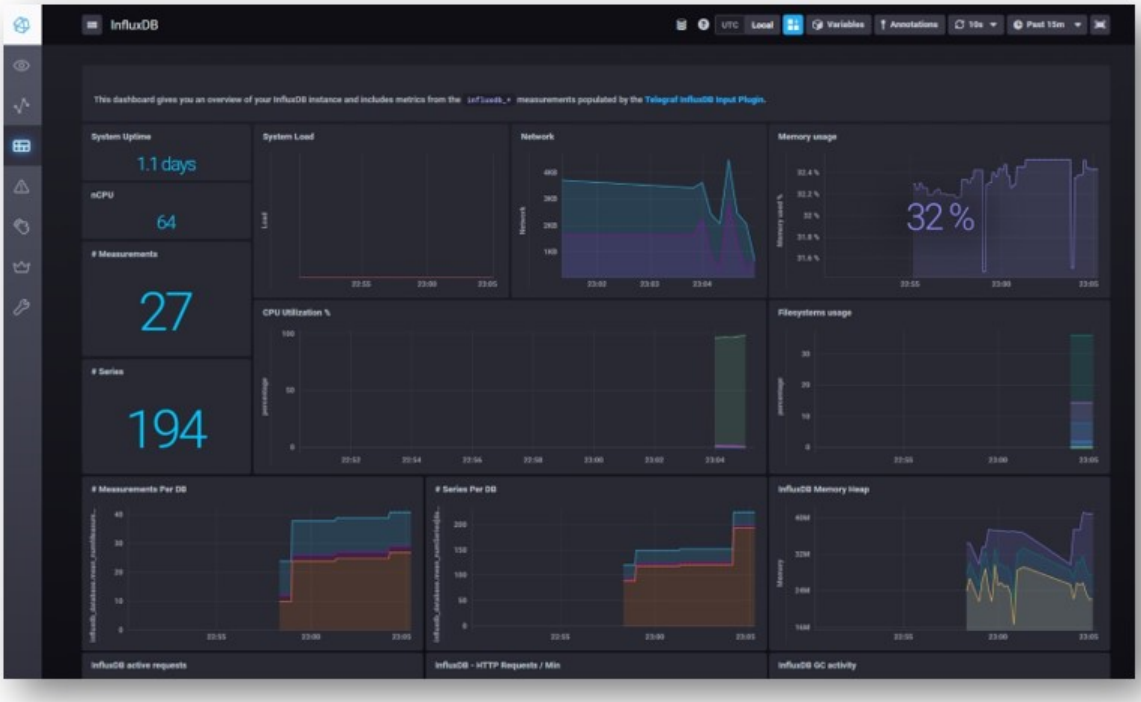

Figure 5.13. InfluxDB dashboard illustrating available server resources.

5.2 Techno-Economic Analysis and Data Validation

One of the fundamental objectives of the DC Nanogrid House's IoT system is to implement an economical infrastructure based on low-cost, high-performance devices operating with a sufficient degree of reliability. Inline with this ideal, a research project entitled the *Eco-IoT-DAQ* was launched, using sensors and microcontrollers to process and visualize data collected from sensors and equipment. The components and individual sensor specifications employed within this system are previously described in Section 2.3.3 and Table 2.6. Depending on the specific application space, these customized IoT systems can cost on the order of $1/10^{\text{th}}$ to $1/100^{\text{th}}$ of a commercially-equivalent system. The generalized concept of the Eco-IoT-DAQ is illustrated in Figure 5.14. Due to the significant minimization in expense, a corresponding techno-economic analysis of the system's performance was necessary to justify its credibility.

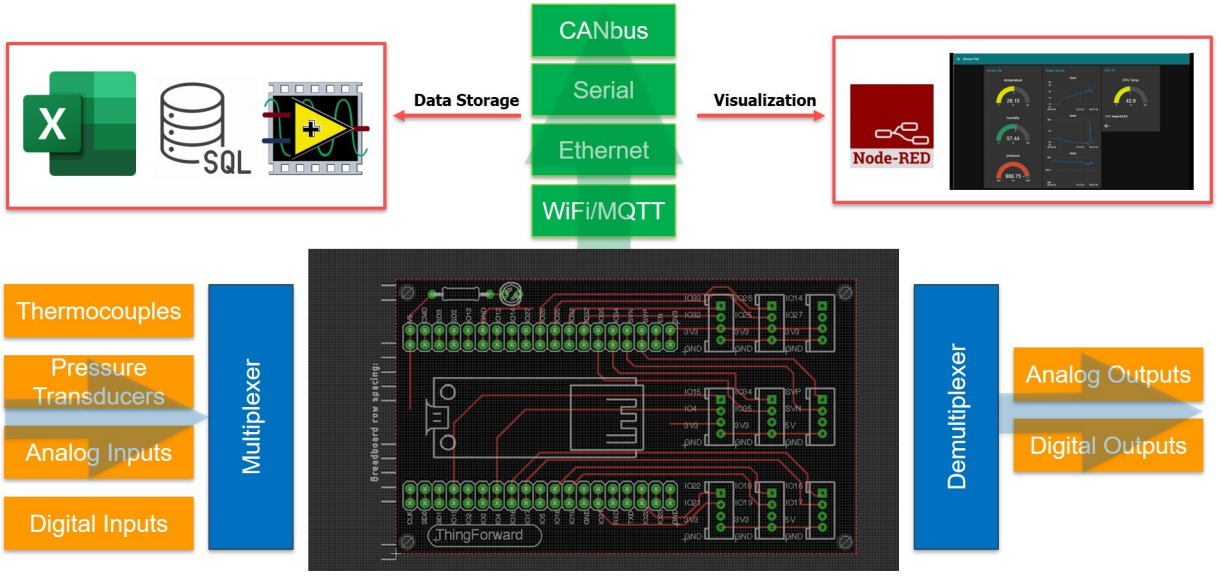

Figure 5.14. System concept of the customized Eco-IoT-DAQ system.

5.2.1 Commercial Solutions

A considerable variety of robust DAQ systems are available for selection from a wide array of manufacturers, several of which are described and utilized in Section 2.3. These systems

offer an assortment of benefits, including robustness, extensive sensor interfaces, electrical protection mechanisms, and a high degree of accuracy and reliability. National Instruments (NI) is a frequently used system in the thermal science research area, providing modules for measurements ranging from voltage, current, temperature, acoustics, pressure, to mechanical forces [155]. Although such systems are replete with desirable qualities, there are several impediments exhibited in their application for research environments and testbeds.

The first difficulty involves the communication interface specified by the manufacturer's DAQ solution. These often take the form of Ethernet, controller area network (CAN) bus, Modbus, USB, or other common interfaces. Although the physical interface presents in a conventional format, the underlying communication method is ordinarily masked in a proprietary configuration, restricting the user's access via the manufacturer's custom software implementation or decryption process. In addition to the equipment's base cost, the DAQ interface can occasionally impose additional costs, requiring subscription and electronic fees for compatible software tools such as MATLAB, LabVIEW, etc.

The topic of financial burdens segue into the second challenge, surrounding the cost of equipment and software itself. Depending on the system application, implementing a comprehensive solution can cost thousands, if not tens of thousands of USD to setup and deploy. Consider the scenario of a psychrometric test stand under analysis, requiring at least 20 thermocouples, 10 digital inputs, and 10 analog outputs for experimentation. A viable solution using the NI product line with current manufacturer's suggested retail price (MSRP) could include:

- NI cDAQ-9137 Controller, 1.91 GHz, 32GB, 8-slot Standard ($7,176.00)
- Two NI-9214 16 channel C-Series Temperature Input Modules ($2,009.00 each)
- Two NI-9262 DSUB 6 channel 16-bit AO C-Series Modules ($1,512.00 each)
- Two NI-9401 8 channel, 100 ns Digital Input/Output Modules ($392.00 each)
- Two NI 9924 front-mount terminal block for DSUB modules ($141.00 each)
- NI PS-15 Power Supply, 24 VDC, 5 A, 120-240 VAC input ($292.00)

- Moxa 5-port Industrial Unmanaged Ethernet Switch ($309.00)
- TRC-8542 NI-XNET CAN HS/FD Transceiver Cable ($476.00)
- Standard Service Program for CompactDAQ Systems, 3 years ($3,788.32)
- LabVIEW Full Development System, 1 year ($3,569.00)

The total system cost for this setup courtesy of the NI official website is **$24,086.32**, not including local taxes and delivery charges [155]. In this specific prototyping example, the costs incurred in purchasing the measurement system could very well rival those associated with the actual test stand equipment.

The third obstacle is concerned with troubleshooting efforts. With the multitude of diverse hardware and software elements involved, conflicts commonly emerge and can demand substantial time and technical expertise to resolve. In addition, though commercial DAQ solutions typically include technical support as part of their packages, the cost of inconvenience and delay when performing experimental work cannot be disregarded. Furthermore, once outside of the manufacturer warranty period, costs involved with repair and replacement can introduce secondary charges outside of those described previously. Alongside unexpected fees, repair and replacement can also increase delay times involved with shipping and handling.

5.2.2 The Eco-IoT-DAQ Alternative

The custom DAQ solution developed in Section 5.1 introduces an alternative to those of commercial origin previously described in Section 5.2.1. Sensors and components used in this system are described and detailed in Section 2.3.3, with additional integrated circuits (ICs) used for communication and data handling to the SBC and SoC. Low-cost microprocessor and microcontroller devices are frequently hindered by the lack of I/O ports available (e.g., Arduino Nano, NodeMCU, etc.), or the inability to process analog I/O (e.g., Raspberry Pi, etc.). To rectify this, inexpensive ICs such as the CD74HC4067 16-channel bidirectional analog multiplexer/demultiplexer [156], and the MCP3008 10-bit eight-channel ADC [157] can

be used in conjunction with the microprocessor or controller to achieve the same I/O functionality as their commercial-equivalents. The current market MSRP for the CD74HC4067 and the MCP3008 through popular electronic vendors such as Digi-Key are approximately $0.99 and $2.41, respectively [158]. If desired, similar ICs with additional channels, higher sampling rates, and improved resolutions can also be procured to closely match available commercial options.

Protection mechanisms and durable I/O are advantageous attributes of industrial solutions, and are not easily replicated by custom solutions. Manufactured systems traditionally withstand a collection of electrical safety tests outlined by the International Electrotechnical Commission (IEC), which include safety checks such as dielectric-voltage testing, insulation-resistance testing, vibration testing, and electromagnetic interference (EMI) testing [159]. Beyond these tests, industrial equipment is commonly accompanied with waterproofing, dust-proofing, electrostatic discharge (ESD) protection, and conformal coating for additional protection and durability. These individual qualities, along with supplemental quality assurance (QA), contributes to the valuation of the DAQ systems and corresponding package solutions.

Although the Eco-IoT-DAQ system omits the majority of these inspections and verifications, there are several mitigation strategies employed to enhance its overall resiliency and stability. The first of these surrounds input protection to the microcontroller, which can be achieved through the use of a Zener diode as shown in Figure 5.15.

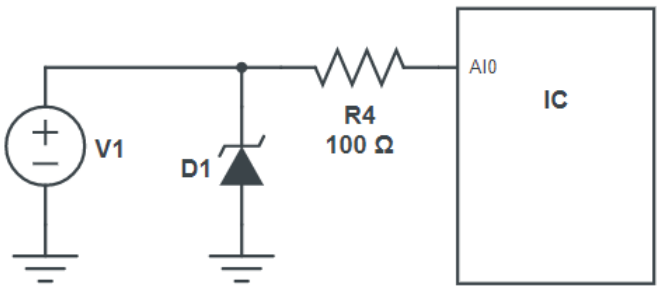

Figure 5.15. Microcontroller input protection circuit monitoring an analog signal.

By applying a combination of Zener diode and resistor, the voltage input to the microcontroller can be safely clamped at a desired level and the current can be sufficiently dissipated. Another mechanism involves the use of decoupling capacitors, placed between the voltage source and ground nodes of the microcontroller. Under a DC voltage, capacitors act as open circuits, nominally preventing any current flow. When used in parallel with a microcontroller's voltage source, however, they function as a buffer device, minimizing noise and voltage spikes while maintaining a consistent voltage input to the microcontroller. A practical implementation is shown in Figure 5.16,

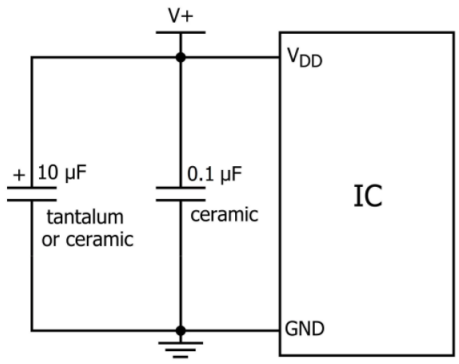

Figure 5.16. Microcontroller voltage source protection using decoupling capacitors [160].

In addition to the decoupling capacitors, a reverse-blocking Zener diode can also be affixed to the voltage source input to prevent damage through the same method as previously described with the analog input. If a sufficiently high voltage for the diode is selected, such as 50 VDC, the microcontroller can then withstand unintended supply voltages under this threshold without being destroyed (so long as the thermal limitations of the diode are not exceeded).

Beyond these protection features, other economical-circutry modifications are also provided with the Eco-IoT-DAQ design to improve its functionality. Many research experiments involve the use of DAQ systems to control an output, such as a switch or relay. While digital and analog outputs are commonplace on microcontrollers, activation of an output can sporadically result in undesirable ramifications to the microcontroller or circuit being controlled. In the case of a switch or button, the mechanical vibration can result in a bouncing effect,

leading to misinterpreted values and signals. To alleviate this situation, a debouncing mechanism can be introduced either via hardware or software implementation. Through hardware solution, this can be achieved using a Schmitt-Trigger inverter, such as the 74HC14 [161]. This IC can operate in conjunction with an example circuit shown in Figure 5.17 to mitigate the undesirable bouncing behavior. In this circuit, the resistor and capacitor form an RC-filter to attenuate voltage ripples, and the Schmitt-Trigger provides hysteresis to address the signal fluctuations from the switch.

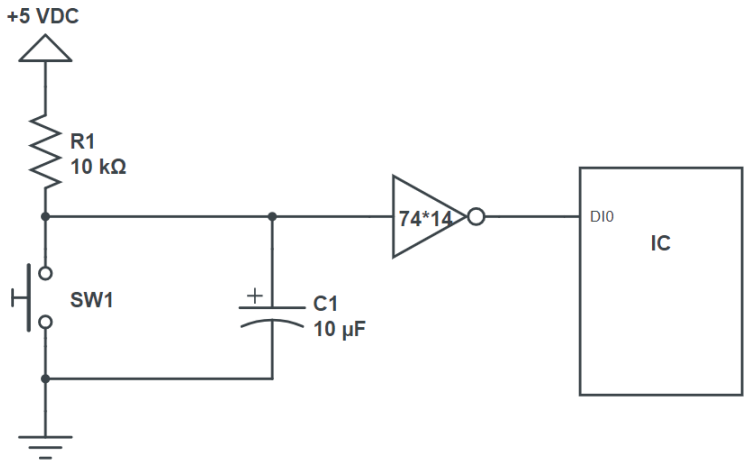

Figure 5.17. Microcontroller debouncing hardware solution using a Schmitt-Trigger IC.

In a similar vein to the previous modification, microcontrollers are often leveraged to control a significantly larger signal, such as that from a traditional wall-outlet in a building, or a high voltage DC value described in Chapter 4. The challenge associated with this example arises from the limitations of the microcontroller I/O current, which is frequently on the order of a few hundred milliamps or less. As a result, switching a load requiring a higher current can often produce unsatisfactory (if not unpredictable) behavior. Thankfully, a simple circuit employing a transistor can adequately resolve this difficulty, such as that shown in Figure 5.18. When the Bipolar Junction Transistor (BJT) in this circuit receives a sufficient current into its base, a proportionally greater current can be driven through its collector terminal, and thus through the load. If even larger load controls are desired, modified transistor configurations such as a Darlington pair can be utilized instead. These

circuits can be used for a variety of other applications, including motor controls, LED arrays, charge/discharge circuits, and energy measurements.

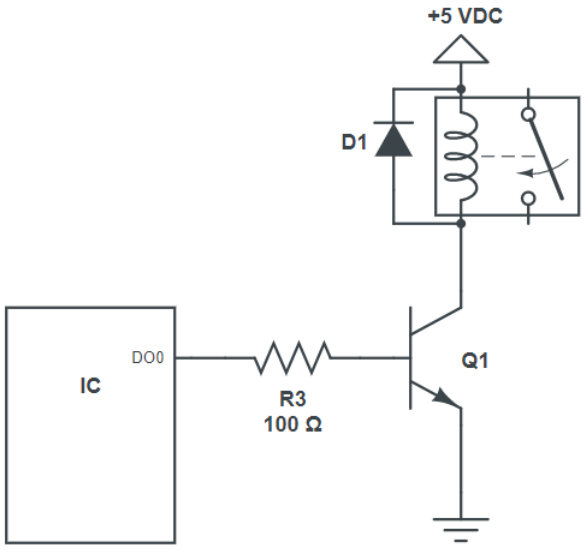

Figure 5.18. Microcontroller control of a large load using a transistor.

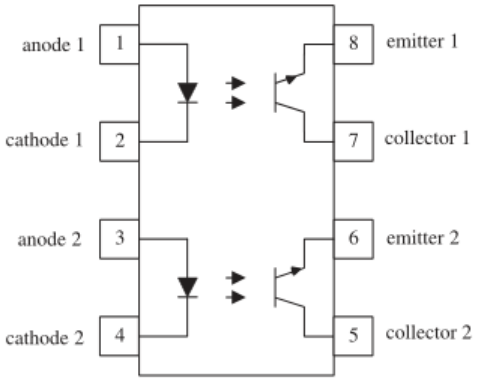

Figure 5.19. Optocoupler IC circuit representation [162].

Transistors can also be used for a specialized isolation circuit known as an optocoupler, which leverages an LED and phototransistor to control a circuit. The more intense the light from the LED, the more current can be passed through the associated phototransistor. A representation of an optocoupler circuit in an enclosed IC is illustrated in Figure 5.19.

Since the LED/phototransistor circuit-pair operates without any physical contact, electrical isolation is afforded to both input (microcontroller) and output (load).

Utilizing the hardware circuit modifications previously outlined, and given the same testbed scenario described in Section 5.2.1, a corresponding cost of an Eco-IoT-DAQ can be estimated. To achieve the same basic DAQ functionality as a commercial equivalent model, the following components would be required:

- SBC Device (e.g., Raspberry Pi) ($55.00)
- SoC Device (e.g., ESP32 Devkit) ($2.02)
- 32GB MicroSD Memory Card ($21.23)
- 5 VDC Power Supply ($10.95)
- Four 74HC4067N 16-channel Bidirectional Multiplexer ($2.94 each)
- Two MCP3008 8-channel ADC ($2.41 each)
- Two CD74HC595E 8-bit Shift Register ($0.91)
- Ten MAX5216BGUA 16-bit DAC ($2.80 each)
- Two MAX31856 Thermocouple Amplifier Signal Conditioner ($17.50 each)
- Assorted components (e.g., resistors, capacitors, transistors, etc.) (approx. $25.00)
- Assorted wires, terminals, and tools (approx. $100.00)

All MSRP values are courtesy of Digi-Key's product pages, and do not include any shipping, handling, or taxes. The total estimated cost to satisfy the testbed requirements is approximately **$295.60**, about $1/100^{\text{th}}$ of the cost previously determined for a commercially-equivalent DAQ system. A simplified system demonstrating this concept is illustrated in Figure 5.20.

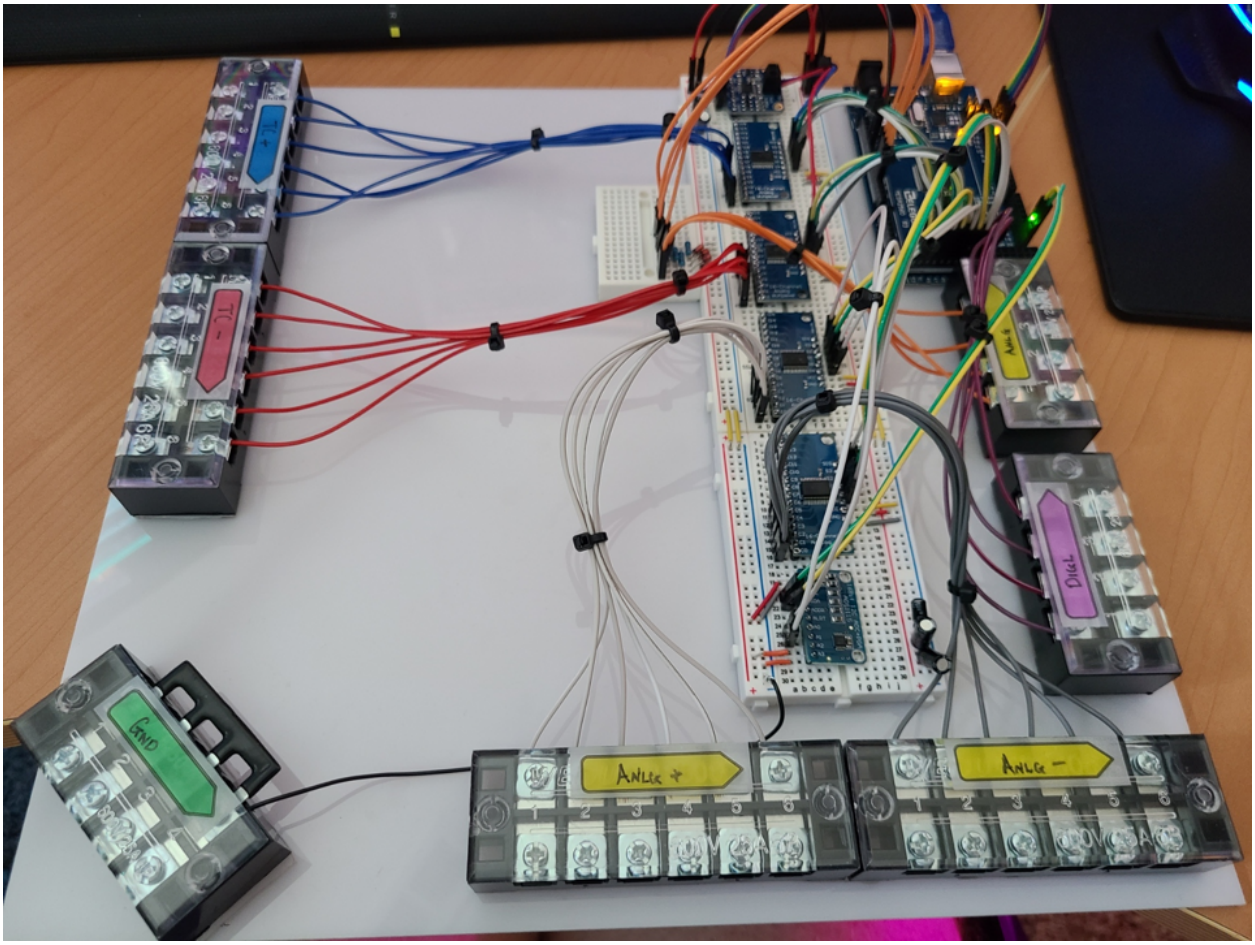

Figure 5.20. Eco-IoT-DAQ demonstration supporting thermocouple, analog, and digital I/O measurements.

5.2.3 Sensor and Data Validation

Following the outline and design of the Eco-IoT-DAQ's hardware implementation, the next step was to verify its physical performance. As part of this assessment, a PoC IoT system arrangement was deployed in the Purdue Herrick psychrometric chambers as shown in Figure 5.21, and validated against a wide array of test data. Each chamber is equipped with a highly-sensitive temperature and relative-humidity monitor, establishing a reliable baseline to compare sensor measurements against. Each Eco-IoT-DAQ module was positioned within close proximity of the psychrometric chamber sensors and airflow locations to obtain the most accurate possible readings. Two sets of calibration and validation tests were performed; the

first of which occurred on September 11th, 2020 as shown in Figures 5.22 and 5.23, and the second on April 2nd, 2021 as shown in Figures 5.24 and 5.25. The data collected in these graphics is fundamentally rudimentary; that is, there are no calibration or offsets applied to any raw IoT data presented. However, the unprocessed data clearly mirrors the trend of the baseline psychrometric data, yielding some initial confidence in the Eco-IoT-DAQs' operation.

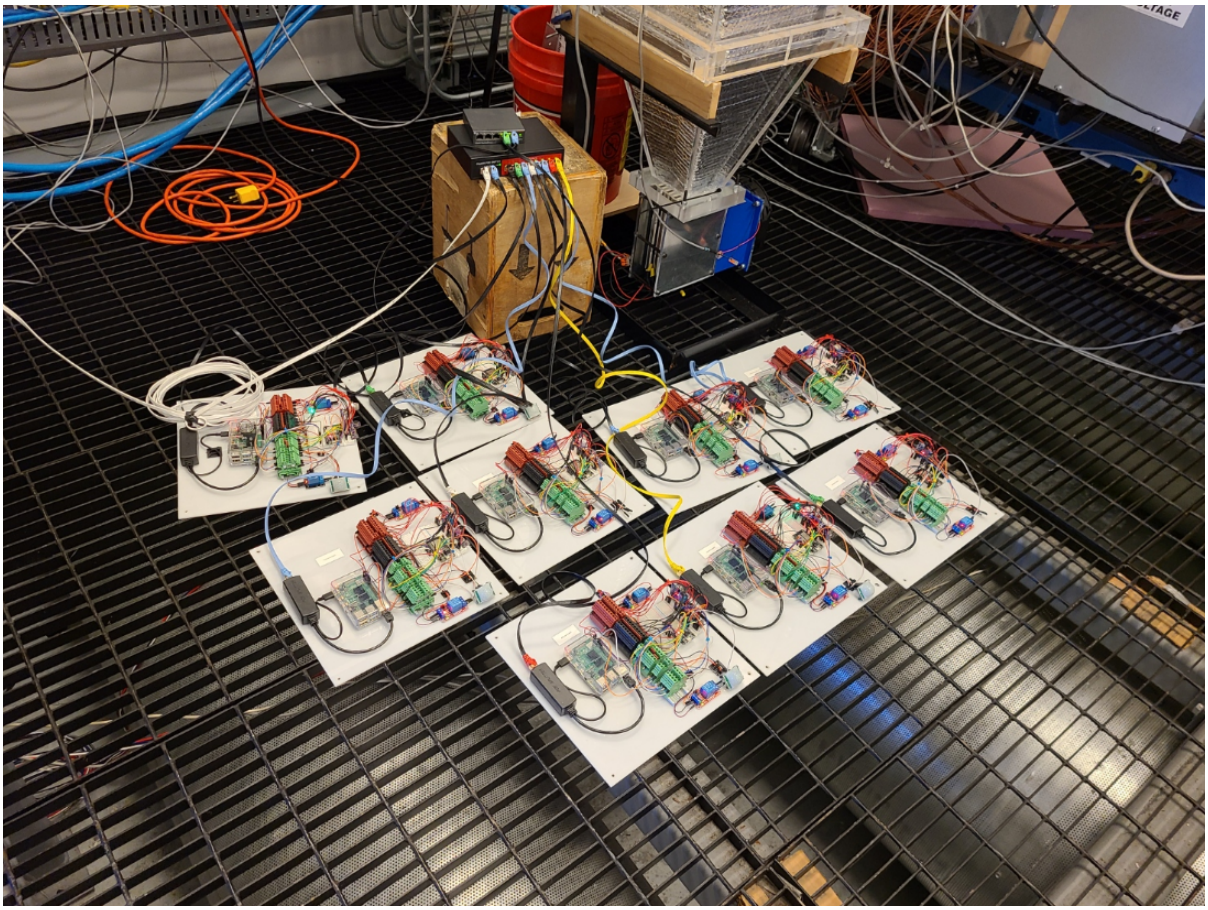

Figure 5.21. Psychrometric testing setup of the PoC IoT systems.

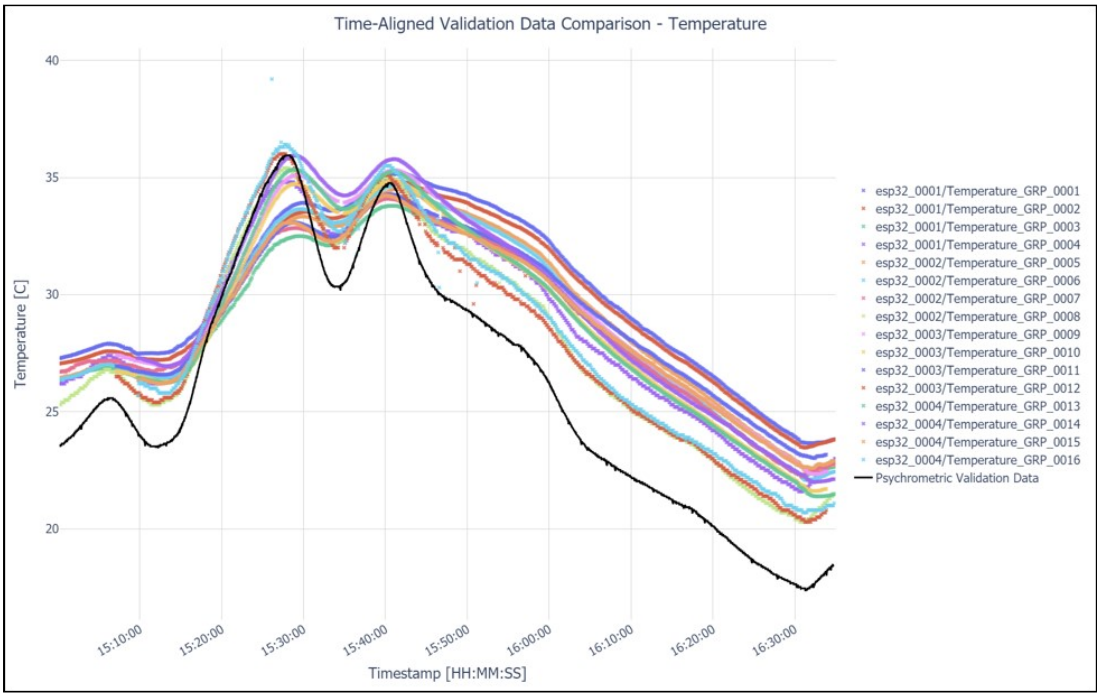

Figure 5.22. Baseline performance evaluation of the Eco-IoT-DAQ system temperature sensors on September 9th, 2020.

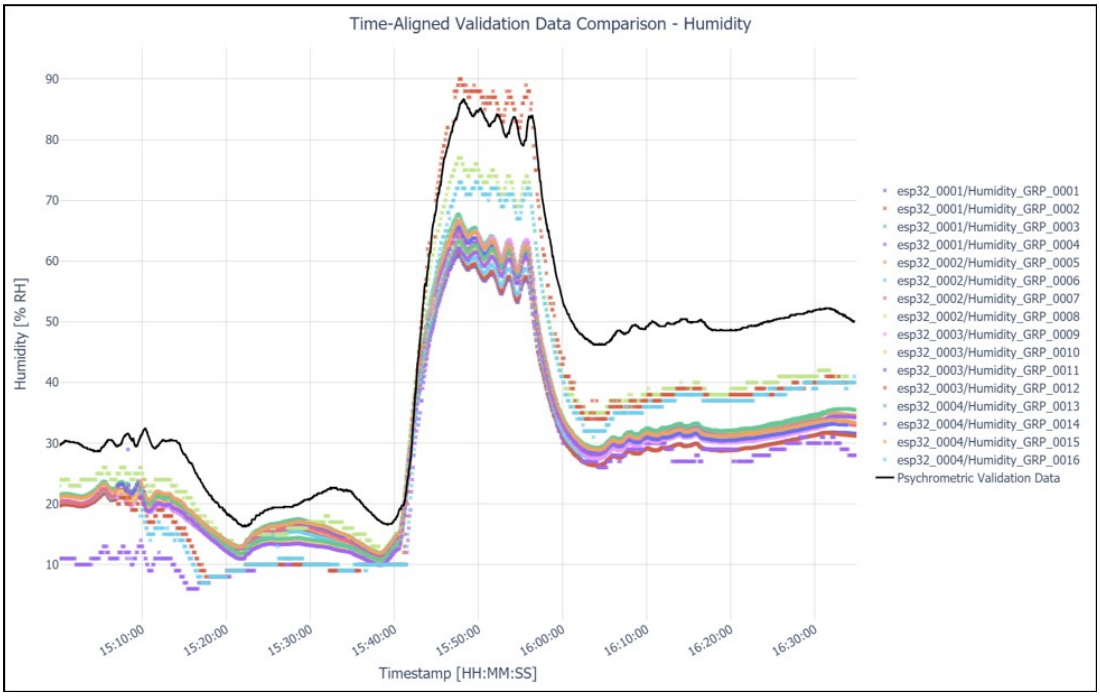

Figure 5.23. Baseline performance evaluation of the Eco-IoT-DAQ system relative humidity sensors on September 9th, 2020.

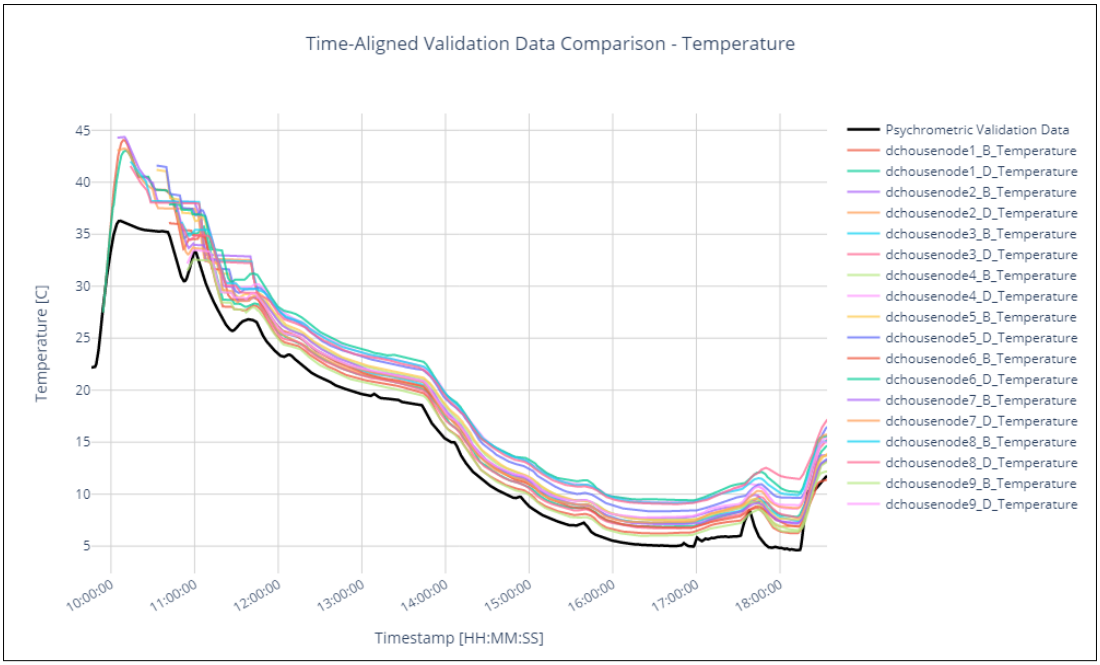

Figure 5.24. Baseline performance evaluation of the Eco-IoT-DAQ system temperature sensors on April 2nd, 2021.

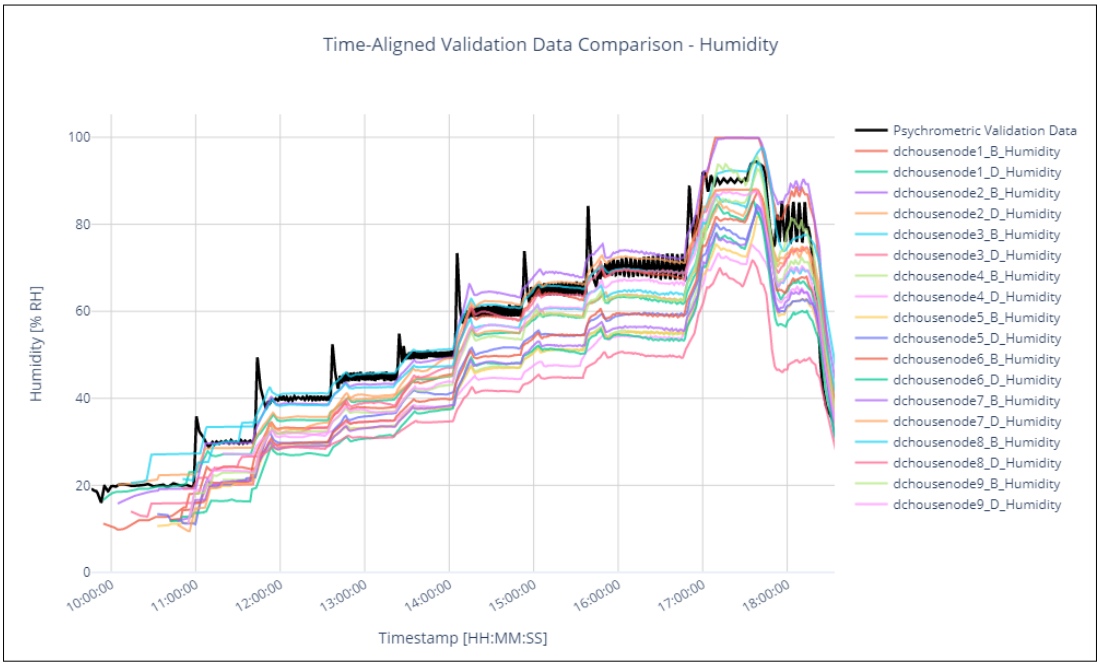

Figure 5.25. Baseline performance evaluation of the Eco-IoT-DAQ system relative humidity sensors on April 2nd, 2021.

Calibrating the data stipulates can be achieved by plotting the measured data from the individual Eco-IoT-DAQ modules against the psychrometric validation data, and deriving a relationship between them. In order to directly compare the two discrete data sets, a uniform dependent variable (time) must be established first. Although Figures 5.22, 5.23, 5.24, and 5.25 visualize each data set as being comparatively time-aligned to one another, the individual discrete points composing them are not directly identical. For example, the psychrometric validation data may have one data point recorded at 11:00:00.020, while an Eco-IoT-DAQ module has its correspondingly nearest point recorded at 11:00:00.150. While relatively similar, these two points cannot be directly equated to generate the needed calibration curve.

This difficulty can be remedied through a two step process. First, the psychrometric validation data and individual Eco-IoT-DAQ measurements can be fitted to a spline function, comprised of individual piecewise polynomials. Splines offer a variety of benefits over a conventional polynomial fit, most significantly that of their piecewise nature, enabling non-periodic and indiscriminate data sets to be approximated by a curve [163]. Second, the fitted spline functions for each data set can be sampled over a common timeseries sample, providing a one-to-one calibration between the IoT and validation data sets.

This procedure was performed using SciPy Interpolation library, which supports both one and two dimensional curve fitting for applicable data sets [164]. From the data recorded in Figures 5.24, and 5.25, 56,458 data points were collected in the psychrometric validation data set and 53,875 corresponding sensor measurements were collected across all of the Eco-IoT-DAQ modules. One dimensional spline curves were fitted to each data set, using a quadratic polynomial interpolation between points for smoothing. Following this, the validation data set spline and corresponding IoT data set spline were sampled an equal number of times and charted against each other. Finally, a least squares regression line can be calculated between the compared data sets. A visualization of this process for the validation and one of the IoT module's temperature sensor is depicted in Figure 5.26 and 5.27.

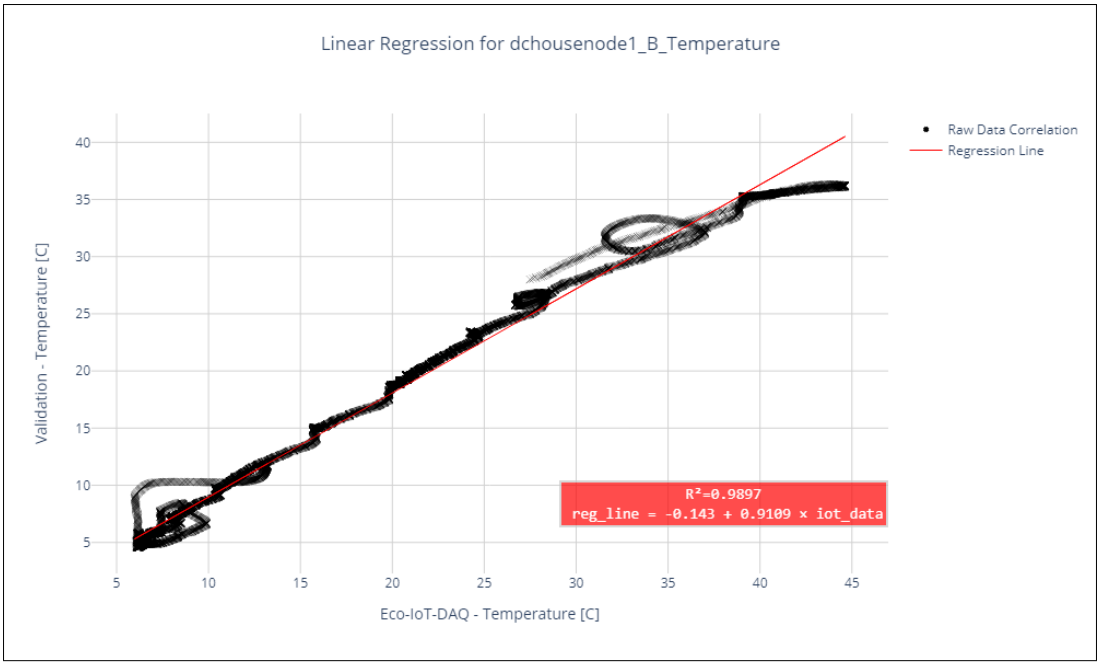

Figure 5.26. Least squares regression line of the validation and Eco-IoT-DAQ temperature sensor.

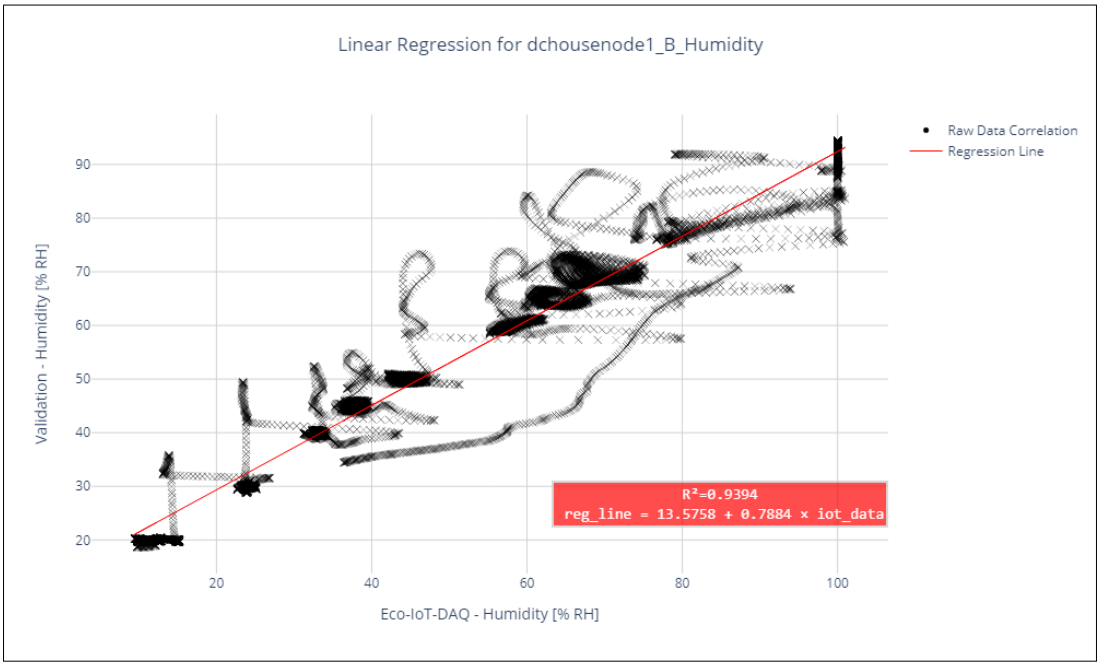

Figure 5.27. Least squares regression line of the validation and Eco-IoT-DAQ humidity sensor.

The applied linear regression technique illustrates a substantial degree of correspondence between the measured IoT and validation data sets, as verified by the R^2 values on the respective plots. However, there are some interesting features observed within the linear-fit graphics, which can be discerned through examination of the original timeseries data. In Figure 5.27, multiple crossing behavior of the regression line can be observed resulting from the overshooting behavior in Figure 5.25. These effects are elucidated by understanding the PID controls present in the psychrometric chambers, which occasionally introduce windup and overshoot behaviors influenced by the integral (I) component. This in turn produces a type of hysteresis-effect in the regression plots, which is much more pronounced on the humidity validation. Ultimately, however, the resulting calibration performance indicates satisfactory agreement with the validation data, as confirmed by Figures 5.28 and 5.29, and the continuous error evaluation of all collected IoT measurements shown in Figures 5.30 and 5.31.

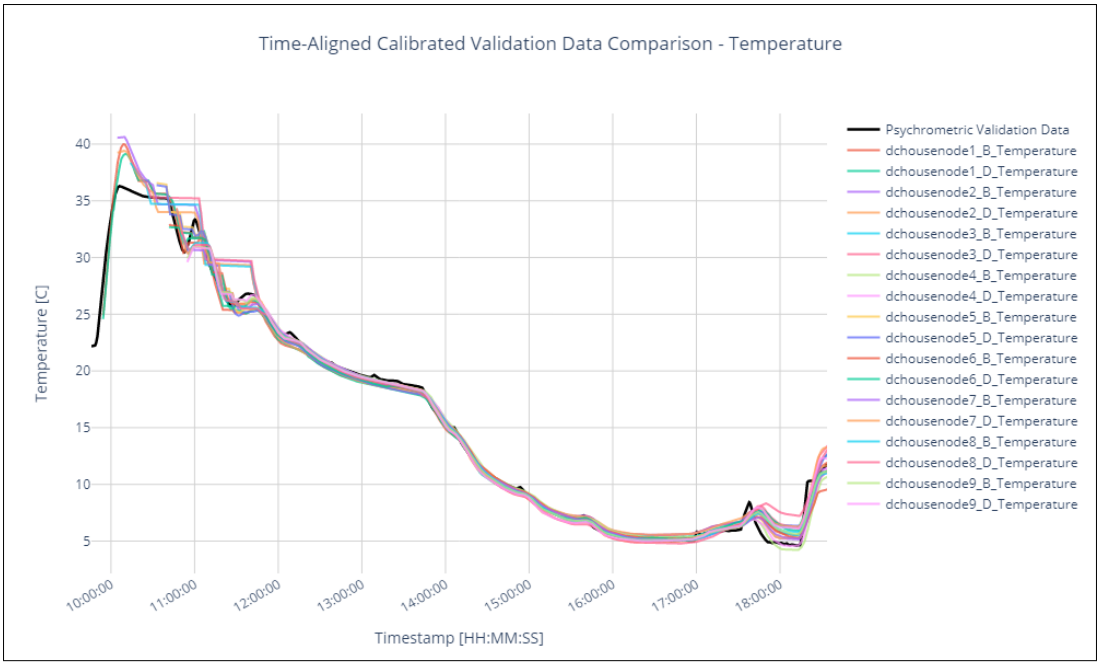

Figure 5.28. Calibrated performance evaluation of the Eco-IoT-DAQ system temperature sensors on April 2nd, 2021.

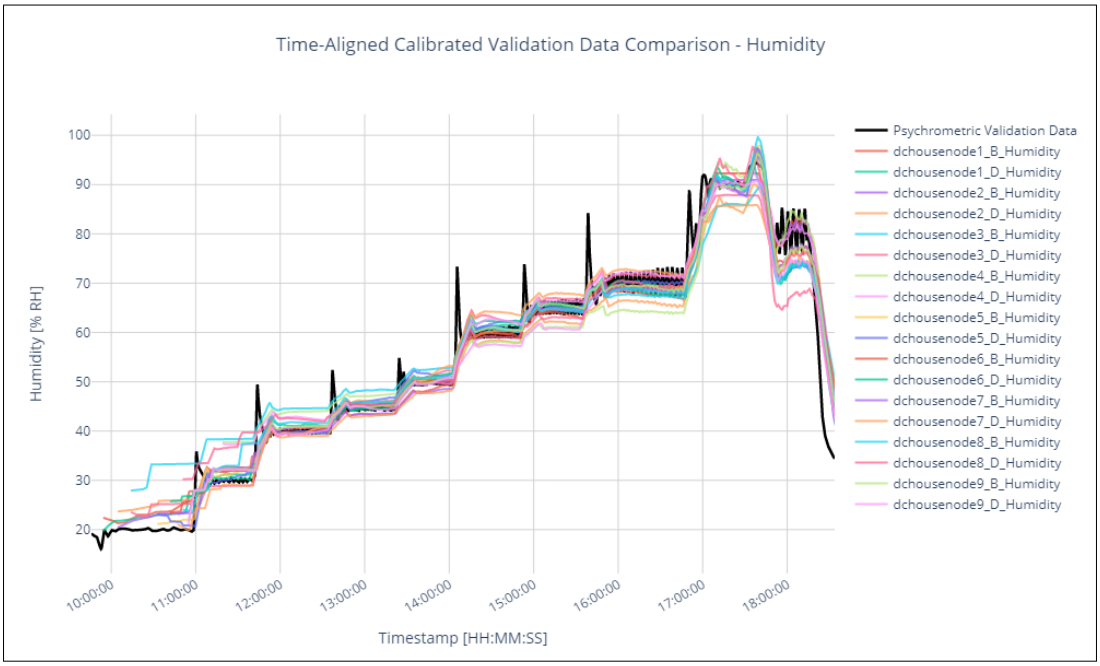

Figure 5.29. Calibrated performance evaluation of the Eco-IoT-DAQ system relative humidity sensors on April 2nd, 2021.

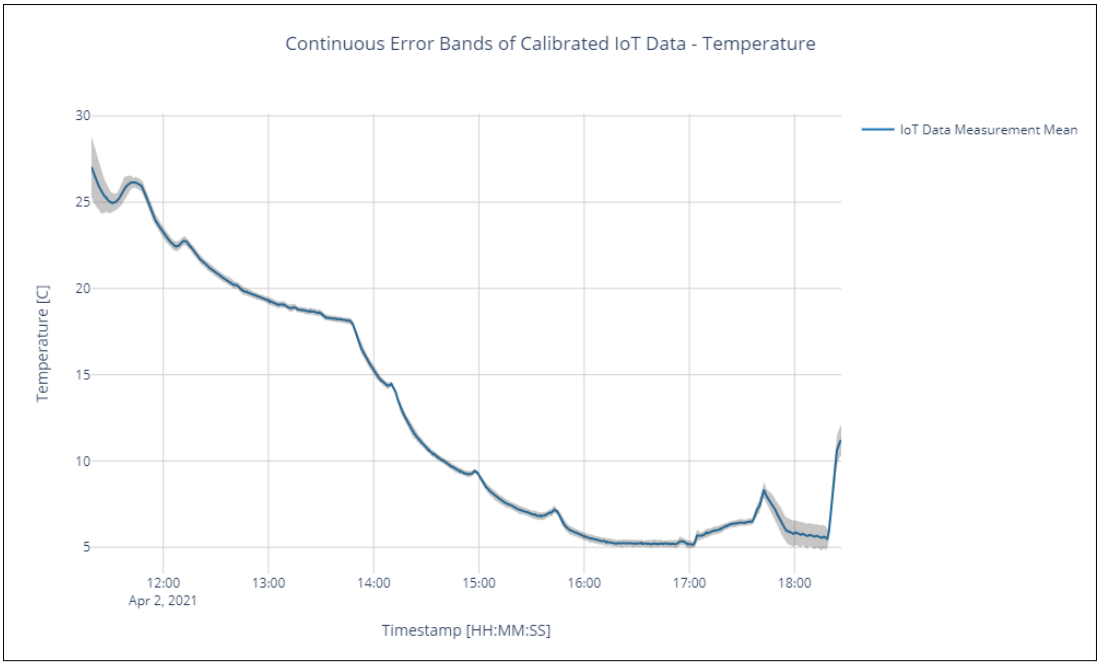

Figure 5.30. Continous error evaluation of the Eco-IoT-DAQ system temperature sensors on April 2nd, 2021.

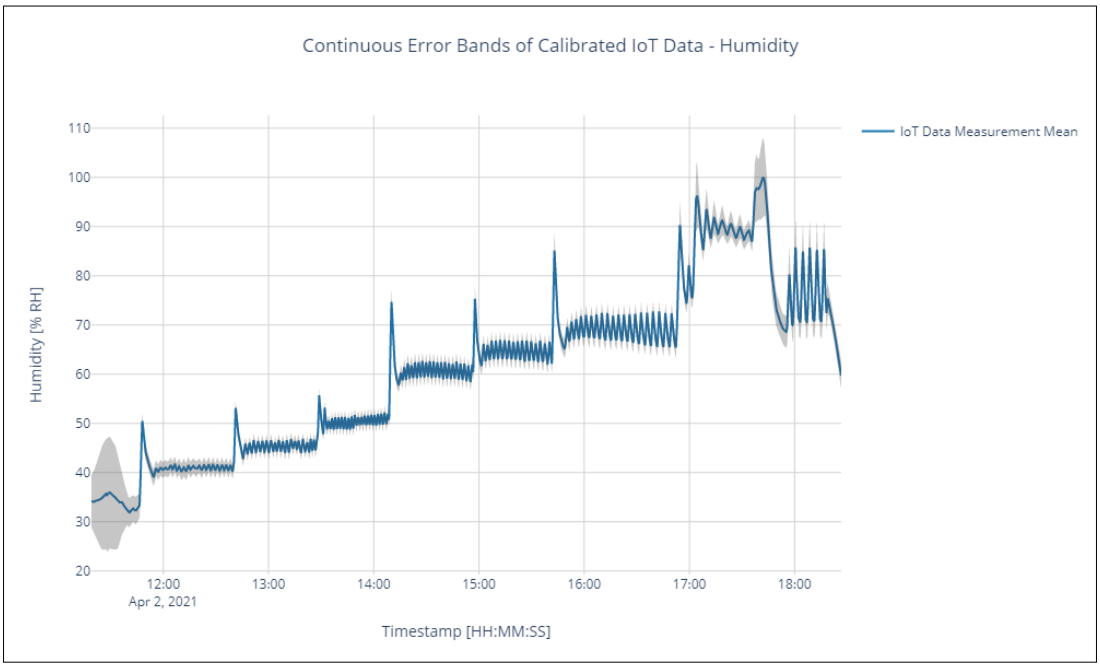

Figure 5.31. Continous error evaluation of the Eco-IoT-DAQ system relative humidity sensors on April 2nd, 2021.

5.3 Software Development

5.3.1 Application Construction

In the previous sections, the IoT architecture was developed and tested through a PoC demonstration. Undergirding this architecture are the individual software components that support the data collection, processing, storage, and presentation to the user. The software implementation created for this purpose is based on a wide variety of programming languages, including Python, C, C++, SQL, Javascript, Angular, and many others. The individual components comprising this application are maintained in individual repositories on the DC Nanogrid House Github page, illustrated in Figure 5.32. The corresponding IoT communication layout is summarized in Figure 5.33.

As discussed in Section 5.1.2, a combination of messaging servers via Mosquitto MQTT and RabbitMQ are used to support data exchange between various layers of the application. To present this to a user, an intermediary application contained in Docker is used to subscribe to data-messages, and respond to requests from the user interface (UI). Docker is a platform as a service (PaaS) which allows individual applications to be *containerized*, which is similar to operating an application within a virtual machine (VM). Unlike a VM, however, containers are significantly lighter on system resources and can be deployed rapidly to desired locations. In addition, individual application dependencies can also be managed from a high-level, ensuring functionality across multiple environments and independent of the operating system (OS) [165].

5.3.2 Network Framework

To support all of the systems within the DC Nanogrid House, from consumer electronics, to IoT devices, to critical nanogrid equipment, a novel network framework was constructed. Within this setup, the overall house's network is *segmented* into individual virtual local area networks (VLANs), which subdivides a network into independent partitions through a specialized network switch. While VLANs can serve important security functions within Information Technology (IT) environments, their application with the nanogrid control system

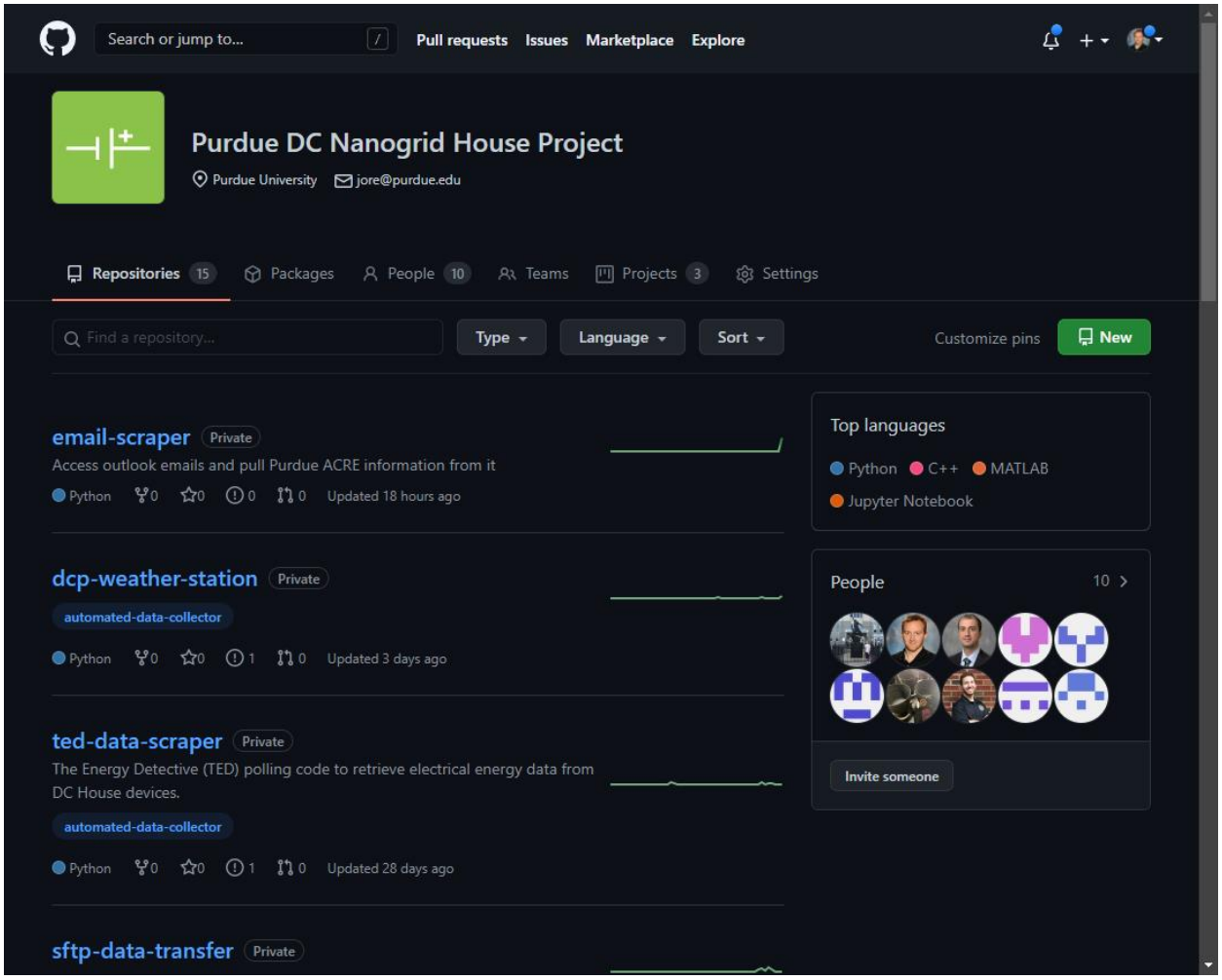

Figure 5.32. DC Nanogrid House project Github homepage.

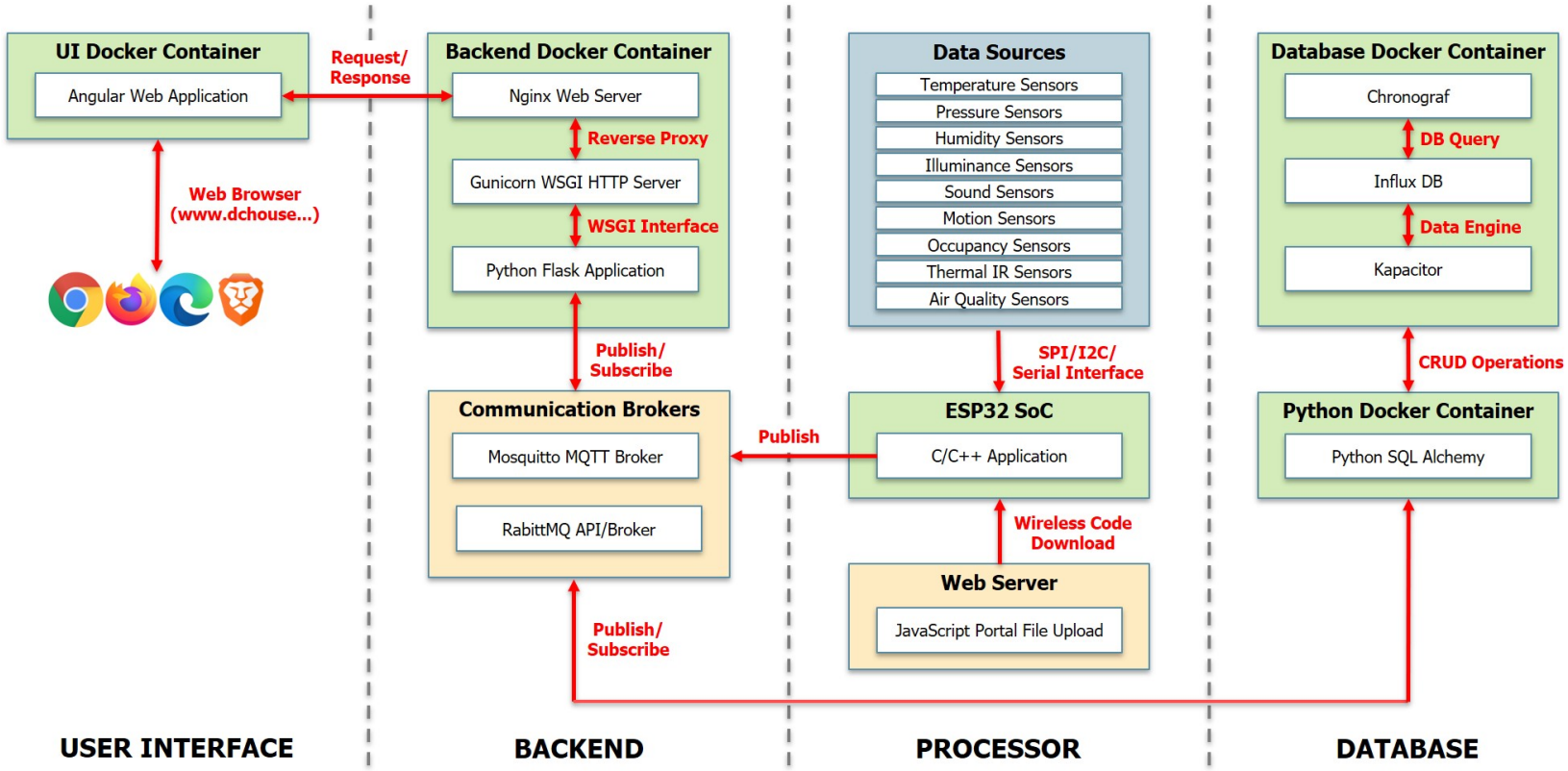

Figure 5.33. IoT software application communication flow diagram.

is essential for its intended operation. Due to the strict specifications of timing and communication of the Ovation Control system outlined in Section 4.3.4, cross-communication and other network traffic must be prevented. A VLAN resolves this obstacle by ensuring that the nanogrid equipment and control system operates within a separate networking allocation without outside interference. To this end, the entire network within the house is segmented to isolate communications and organize networking resources. The physical construction of the server rack containing this infrastructure is shown in Figures 5.34 and 5.35, and a system outline is depicted in Figure 5.36.

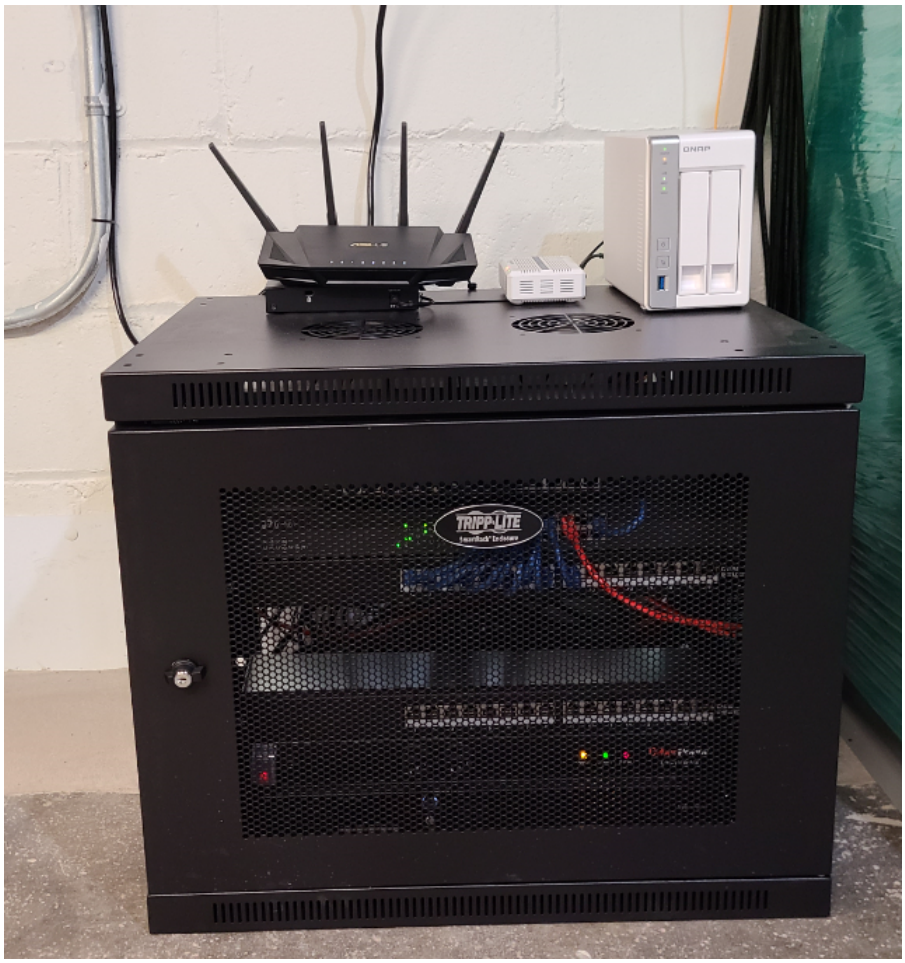

Figure 5.34. Networking server rack construction.

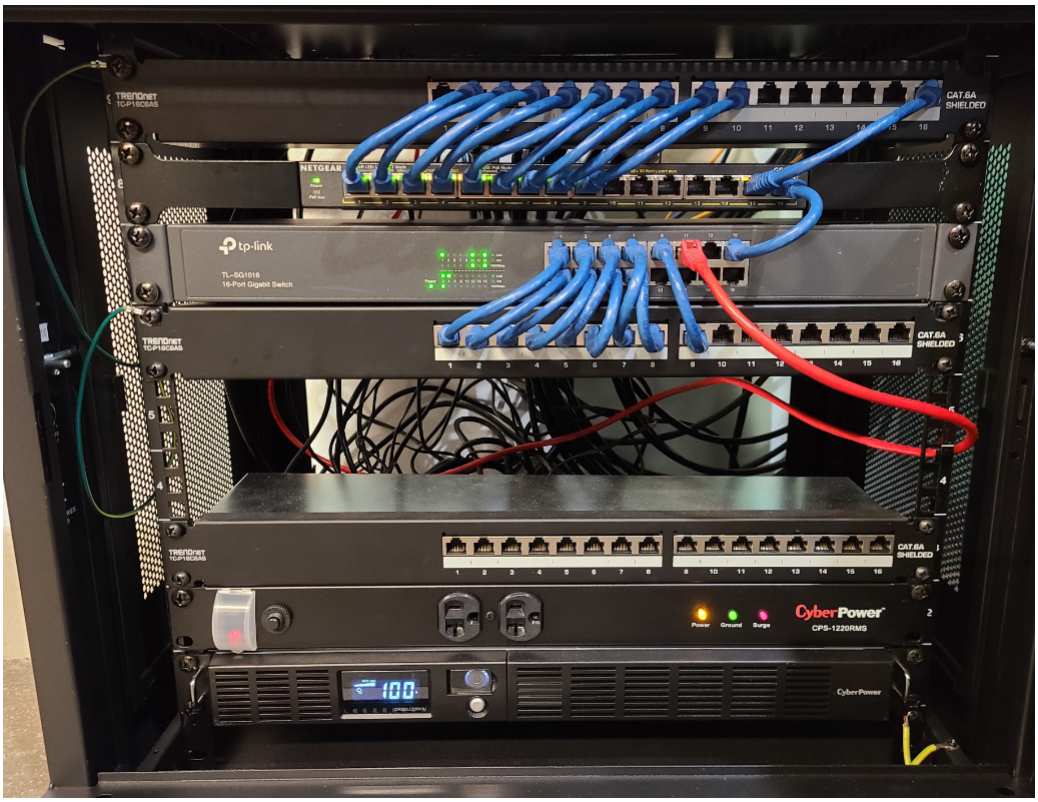

Figure 5.35. Networking server rack internals.

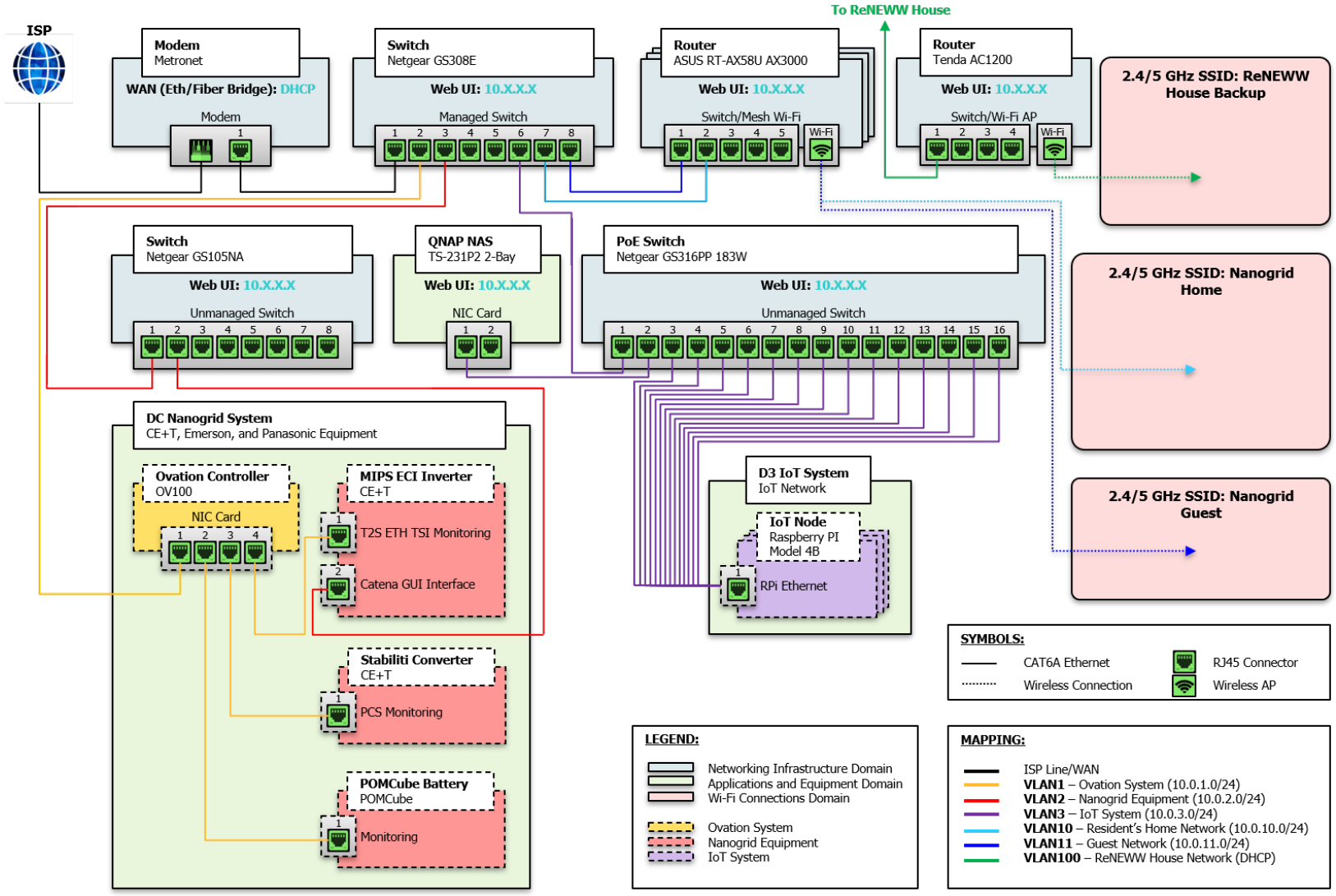

Figure 5.36. DC Nanogrid House network segmentation diagram.

6. SUMMARY AND FUTURE WORK

In the work presented within this thesis, a wide range of topics were addressed surrounding the implementation of a DC nanogrid design within a residential home to improve energy efficiency. Of crucial importance is the comprehension of the role of DC power within the current U.S. macrogrids, and the various benefits it affords over traditional AC-based systems. The concept of the microgrid and nanogrid are not fundamentally novel, but have lacked concentrated research and experimental study within residential settings. This research effort seeks to approach all aspects of this electrical topology, which naturally introduces interdisciplinary exercises.

The heat pump unit was a prime candidate for study in this project, as it represents a significant amount of energy consumption in residential homes across the U.S., in nearly any climate. Since it functions as one of the largest energy consumers among other appliances, it possesses the potential to demonstrate a nontrivial energy savings through a retrofit to DC power. The DC Nanogrid House currently maintains an unmodified AC-based variable speed air-source heat pump, which has been collecting energy baseline measurements since July of 2019. The hybrid retrofitted unit currently installed in the Ray W. Herrick Laboratory psychrometric chambers will continue to undergo study to fully understand its electrical and thermal performance under a variety of test conditions. In addition to this equipment, many others have also been procured for immediate compatibility with the nanogrid's DC bus voltages, or can be designed to operate on DC following a retrofit operation. These include a water heater, refrigerator, sump pump, lighting, and clothes dryer.

The novel DC nanogrid system has been fully implemented and commissioned at the DC Nanogrid House, representing a pivotal moment in the project's history. Although almost every aspect of the system has been custom designed for operation within a residential environment, the system was successful during its initial testing and functionality as described in Section 4.3.3. Following the approval of the application for interconnection with the local utility, the system will be authorized to continuously distribute energy back to macrogrid during moments of surplus production. The control system has also been set up for consistent use in the system, and can be modified as needed to implement desired control strategies.

Finally, the IoT system and network have been deployed throughout the entire DC Nanogrid House, providing a wealth of information from a variety of sensor sources and PoE power wherever necessary. This data is also useful with respect to the evaluation of renovation efforts, as was demonstrated in Section 2.4. Additional opportunities for automation and processing still exist, with the potential to expand this data collection into machine learning models for innovative insights into building energy consumption, occupancy comfort and behaviors, and even novel control strategies.

Although this project's central focus surrounded the development and construction of the DC nanogrid, a considerable range of interdisciplinary activities have evolved since its inception. As a result, there remain a substantial number of opportunities for continued research and development within this space. These include, but are certainly not limited to:

1. Continue the installation of a wind turbine for integration into the DC nanogrid system. Beyond its value as another source of DC power, this energy source also functions in a complementary fashion to the existing solar installation. This presents additional opportunities for distribution optimization, and novel control strategies.

2. Expand the existing control system development. At the current moment, the control system is operating in a maintenance mode for the majority of the nanogrid equipment's typical operating conditions. This Ovation platform is a powerful tool with many logic and data functions available, and can be utilized to further optimize the energy and power distribution within the DC nanogrid, as well as ensure its safe operation.

3. Install new DC devices and appliances, and continue retrofit activities on existing items. This is a topic which has been pursued by many other national laboratories and equipment manufacturers, and the DC Nanogrid House affords an ideal location to implement and test them.

4. Complete psychrometric testing of the hybrid AC/DC heat pump, and perform load-based testing methodology against the baseline AC unit installed in the DC House. This will yield more definitive conclusions about the performance improvements of the

DC system against the reference AC design, and will prepare the hybrid device for smoother integration into the DC nanogrid.

5. Automate all IoT data sources and collection. Presently, about half of the critical data sources are collected autonomously, and the remaining sources require occasional manual intervention. These data exchanges can be completed automated, which requires software provisions to ensure operation, fault handling, backup storage locations, and notifications to user in the event of a severe failure.

6. Perform additional measurement validation studies similar to that in Section 5.2.3 for the additional IoT parameters outline in 2.6. Audio measurements could leverage the anechoic chamber, and illuminance data can be verified in the same manner as the weather station. Proximity sensors can be tested using human and smaller animal subjects to ensure adequate performance is achieved.

7. Implement automatic intelligent-controls using the collected IoT data. Illuminance and proximity sensors could be used to control motorized blinds and switch or dim light fixtures. Proximity and environmental sensors could be used to control mechanized dampers for selective heating and cooling management of individual rooms. Air quality sensors could be integrated into safety mechanisms to detect the presence fire or other harmful gases and chemicals. These individual subsystems can ultimately be processed through adaptive control and feedback from each of the DC Nanogrid House residents to achieve optimal comfort and safety.

8. Construct custom AC and DC energy monitors. To date, the DC Nanogrid House project has evaluated two sets of AC DAQ systems, described in Section 2.3.1, which have each illustrated specific weaknesses and defects. A customized energy monitoring solution could be created inline with the IoT efforts outline in Chapter 5, and leveraged for additional insights into building metrics and performance.

9. Integrate weather data into HVAC operation, nanogrid equipment, and control system development. The 3D printed weather system described in Section 2.3.4 provides the capability to measure crucial metrics, such as outdoor temperature, relative humidity,

wind measurements, and ambient light. These can be incorporated into corresponding equipment to drive heating and cooling functions, predict solar and wind energy production, and provide insights into the house's thermal comfort and distribution.

10. Transform IoT modules into miniature picogrids. Each IoT module could maintain its own battery source and a charge controller managed by an associated software implementation. Through this mechanism, the modules can continue operation during power-failures, system faults, and can reduce the overall load on the DC nanogrid.

11. Construct an indoor vertical farm in partnership with the Department of Horticulture and Landscape Architecture. This system offers a multitude of potential benefits, including edible food for the residents of the home, PoE integration with the nanogrid through grow lights, potential collaboration and publication opportunities with another research group, and a general aesthetic improvement to the area surrounding it.

12. Develop a custom weather research and forecasting (WRF) model in partnership with the School of Earth, Atmosphere, and Planetary Sciences (EAPS). Currently, major weather models are available primarily for the Purdue airport location, which introduces a potential disparity in data collected from local sources. To improve these discrepancies, a WRF model can be constructed through (1) additional validation of the DC Nanogrid House's weather data, and (2) formulation of a model with sufficient prediction capabilities. This work also offers another interdisciplinary opportunity to collaborate with groups such as the Indiana State Climate Office and Purdue Agronomy Center for Research and Education (ACRE) research center.

A wealth of previous studies and research endeavors have reiterated the pressing necessity to evaluate DC and hybrid AC/DC based electrical topologies to satisfy the ever-increasing demands of the modern power grid. Though many articles frame this issue as a dilemma of proper choice between AC or DC, or even Tesla versus Edison, the reality is more fundamental to simply using the right tool for the job. In the same way obsolete wooden waterwheels are viewed today, doubtlessly too will fossil fuels and other similar power sources seem primitive to those of the coming centuries. However, the present time must commit to continual

examination of constructive and propitious distribution strategies, independent from political or commercial inclinations, and remain focused on the ultimate goal of preserving the environment and promoting sustainability.

As the well-known anthropologist Joseph Tainter wrote in his book, The Collapse of Complex Societies, "sociopolitical systems require energy for their maintenance, [and] increased complexity carries with it increased costs per capita…a new energy subsidy is necessary if a declining standard of living and a future global collapse are to be averted" [166, pp. 194-215]. This admonition has held true through the ages, and continues through today; for the survival of both our individual societies and world as a whole, we must ceaselessly seek practical and effective means of leveraging our available resources to supply our civilization.

REFERENCES

[1] A. Hirshfeld, *The Electric Life of Michael Faraday*. New York, New York: Walker Publishing Company, Inc., 2006.

[2] Encyclopaedia Britannica Online, *Electromagnetism*, 2020. [Online]. Available: https://www.britannica.com/science/electromagnetism.

[3] L. Keesey, *High-Voltage Transmission Lines to Act as Antenna in First-of-its-Kind NASA Space-Weather Project*, 2014. NASA.gov. [Online]. Available: https://www.nasa.gov/content/goddard/high-voltage-transmission-lines-are-antenna-for-space-weather/.

[4] NERC, "NERC Interconnections," 2019. [Online]. Available: https://www.nerc.com/AboutNERC/keyplayers/Pages/default.aspx.

[5] S. Backhaus and M. Chertkov, "Getting a grip on the Electrical Grid," *Los Alamos National Laboratory*, pp. 42–48, 2013.

[6] J. A. deChalendar, J. Taggart, and S. M. Benson, "Tracking emissions in the US electricity system," *Proceedings of the National Academy of Sciences*, vol. 116, no. 51, pp. 25497-25502, Dec 2019.

[7] U.S. Department of Energy, "The War of the Currents: AC vs. DC Power," *Energy.gov*, 2014. [Online]. Available: https://www.energy.gov/articles/war-currents-ac-vs-dc-power.

[8] R. Smith, "U.S. Risks National Blackout From Small-Scale Attack," *The Wall Street Journal*, 2014. [Online]. Available: https://www.wsj.com/articles/u-s-risks-national-blackout-from-small-scale-attack-1394664965.

[9] ASCE, "2017 Infrastructure Report Card," 2017. [Online]. Available: https://www.infrastructurereportcard.org/making-the-grade/.

[10] J. Tollefson, "US electrical grid on the edge of failure," *Nature*, 2013. [Online]. Available: https://www.nature.com/news/us-electrical-grid-on-the-edge-of-failure-1.13598.

[11] J. R. Minkel, "The 2003 Northeast Blackout–Five Years Later," *Scientific American*, vol. 13, 2008.

[12] B.K. Sullivan and N. S. Malik, "5 Million Americans Have Lost Power From Texas to North Dakota After Devastating Winter Storm," 2021. [Online]. Available: https://time.com/5939633/texas-power-outage-blackouts/#:~:text=5%20Million%20Americans%20Have%20Lost,on%20Feb.%2015%2C%202021..

[13] I. Ivanova, "Texas winter storm costs could top $200 billion — more than hurricanes Harvey and Ike," 2021. [Online]. Available: https://www.cbsnews.com/news/texas-winter-storm-uri-costs/#:~:text=Now%20many%20homeowners%20are%20dealing, as%20much%20as%20%24295%20billion..

[14] A. Goard, "Texas' power grid set a new winter peak demand record Sunday evening," 2021. [Online]. Available: https://www.kxan.com/news/texas/texas-power-grid-set-a-new-winter-peak-demand-record-sunday-evening/.

[15] V. Penney, "How Texas' Power Generation Failed During the Storm, in Charts," 2021. [Online]. Available: https://www.nytimes.com/interactive/2021/02/19/climate/texas-storm-power-generation-charts.html.

[16] E. Douglas, "Texas was 'seconds and minutes' away from catastrophic monthslong blackouts, officials say," 2021. [Online]. Available: https://www.texastribune.org/2021/02/18/texas-power-outages-ercot/.

[17] P. Hines, K. Balasubramaniam, and E. C. Sanchez, "Cascading failures in power grids," *IEEE Potentials*, pp. 24–30, 2009.

[18] D. Stanglin, "Almost 1 million lose power after intense Halloween storm rolls through eastern US," *USA Today*, 2019. [Online]. Available: https://www.usatoday.com/story/news/nation/2019/11/01/power-outages-halloween-storm-maine-new-york-connecticut-vermont/4120890002/.

[19] A. Gonzalez, "Utilities Scramble to Restore Power," *The Wall Street Journal*, 2011. [Online]. Available: https://www.wsj.com/articles/-SB10001424053111903352704576-536770913696248?mod=googlenews_wsj.

[20] A. T. Elsayed, A. A. Mohamed, and O. A. Mohammed, "DC microgrids and distribution systems: An overview," *Electric Power Systems Research*, vol. 119, pp. 407–417, 2015.

[21] D. Kumar, F. Zare, and A. Ghosh, "DC Microgrid Technology: System Architectures, AC Grid Interfaces, Grounding Schemes, Power Quality, Communication Networks, Applications, and Standardizations Aspects," *IEEE Access*, vol. 5, pp. 12230–12256, 2017.

[22] K. Fowler, "Power Supply Design and Distribution," *IEEE Instrumentation and Measurement*, vol. 3, no. 4, pp. 42–46, 2000.

[23] P. Ponce, A. Molina, O. Mata, L. Ibarra, and B. MacCleery, *Power System Fundamentals*. Boca Raton, FL, USA: CRC Press, 2018.

[24] G. F. Reed, "DC technologies: solutions to electric power system advancements," *IEEE Power Energy*, vol. 10, pp. 10–17, 2012.

[25] B. T. Patterson, "DC, come home: DC microgrids and the birth of the Enernet," *IEEE Power Energy*, vol. 10, pp. 60–69, 2012.

[26] D. Magdefrau, T. Taufik, M. Poshtan, and M. Muscarella, "Analysis and Review of DC Microgrid Implementations," *International Seminar on Application for Technology of Information and Communication*, pp. 241–246, 2016.

[27] S. N. Backhaus et. al., "DC microgrids scoping study. Estimate of technical and economic benefits," (No. LA-UR-15-22097), Los Alamos National Lab, 2015.

[28] A. F. B. Santos, G. P. Duggan, C. D. Lute, D. J. Zimmerle, "An efficiency comparison study for small appliances operating in DC and AC in minigrids," *2018 IEEE Global Humanitarian Technology Conference (GHTC)*, pp. 1-2, 2018.

[29] D. Burmester, R. Rayudu, W. Seah, and D. Akinyele, "A review of nanogrid topologies and technologies," *Renewable and Sustainable Energy Reviews*, vol. 67, pp. 760-775, 2017.

[30] V. Vossos, K. Garbesi, and H. Shen, "Energy savings from direct-DC in U.S. residential buildings," *Energy and Buildings*, vol. 68, pp. 223-231, 2014.

[31] D. L. Gerber, R. Liou, and R. Brown, "Energy-Saving Opportunities of Direct-DC Loads in Buildings," *Applied Energy*, vol. 248, pp. 274–287, 2018.

[32] J. Hofer, B. Svetozarevic, and A. Schlueter, "Hybrid AC/DC building microgrid for solar PV and battery storage integration," *2017 IEEE Second International Conference on DC Microgrids (ICDCM)*, pp. 188-191, 2017.

[33] R. L. Boylestad, *Introductory Circuit Analysis*. 13th ed. Harlow, Essex, England: Pearson Education Limited, 2016.

[34] P. Kundur, *Power System Stability and Control*. New York, NY, USA: McGraw-Hill, 1994.

[35] N. T. Hawkins, "Voltage collapse and its avoidance," *IEE Colloquium on Voltage Collapse*, no. 101, pp. 1–6, 1997.

[36] F. Alvarado, I. Dobson, and Y. Hu, "Computation of closest bifurcations in power systems," *IEEE Transactions on Power Systems*, vol. 9, no. 2, pp. 918–928, 1994.

[37] J. Loughran, "Renewables threaten power grid stability in the US, energy department claims," *Engineering and Technology*, 2017. [Online]. Available: https://eandt.theiet.org/content/articles/2017/08/renewables-threaten-power-grid-stability-in-the-us-energy-department-claims/.

[38] U.S. Department of Energy, "Staff Report to the Secretary on Electricity Markets and Reliability," 2017. [Online]. Available: https://www.energy.gov/sites/prod/files/2017/08/f36/Staff%20Report%20on%-20Electricity%20Markets%20and%20Reliability_0.pdf.

[39] NREL, "Western Grid Can Handle High Renewables in Challenging Conditions," 2015. [Online]. Available: https://www.nrel.gov/docs/fy16osti/65302.pdf.

[40] M. Bragard, N. Soltau, S. Thomas, and R. W. D. Doncker, "The Balance of Renewable Sources and User Demands in Grids: Power Electronics for Modular Battery Energy Storage Systems," *IEEE Transactions on Power Electronics*, vol. 25, no. 12, pp 3049–3056, 2010.

[41] EIA, "How much electricity is lost in electricity transmission and distribution in the United States?" 2019. [Online]. Available: https://www.eia.gov/tools/faqs/faq.php?id=105&t=3.

[42] ——, "How much electricity does an American home use?" 2019. [Online]. Available: https://www.eia.gov/tools/faqs/faq.php?id=97&t=3.

[43] EIA, "U.S. energy facts explained," 2020. [Online]. Available: https://www.eia.gov/energyexplained/us-energy-facts/.

[44] R. Jackson, O. C. Onar, H. Kirkham, E. Fisher, K. Burkes, M. Starke, O. Mohammed, and G. Weeks, "Opportunities for Energy Efficiency Improvements in the U.S. Electricity Transmission and Distribution System," *Oak Ridge National Laboratory*, 2015.

[45] A. Gómez-Expósito, A. J. Conejo, and C. A. Cañizares, *Electric Energy Systems Analysis and Operation*. 2nd ed. Boca Raton, FL, USA: CRC Press, 2018.

[46] F. R. Thrash, "Transmission Conductors – A Review of the Design and Selection Criteria," *Technical Support Article, Southwire Company*. [Online]. Available: http://southwire.com/support/TransmissionConductoraReviewOfTheDesignandSelection-Criteria.htm.

[47] C. P. Steinmetz, "Transient Electric Phenomena and Oscillations," pp. 361–393, 1920.

[48] H. B. Dwight, "Proximity Effect in Wires and Thin Tubes," *Trans. A. I. E. E.*, vol. 42, pp. 850–859, 1923.

[49] F. W. Peek, "Dielectric Phenomena in High-Voltage Engineering," *McGraw-Hill*, pp. 169–214, 1929.

[50] F. C. Lu, S. H. You, Y. P. Liu, Q. F. Wan, and Z. B. Zhao, "AC conductors' corona-loss calculation and analysis in corona cage," *IEEE Transactions on Power Delivery*, vol. 27., no. 2, pp. 877–885, 2012.

[51] J. Arrillaga, "High Voltage Direct Current Transmission," 2nd ed., Stevenage, UK: The Institution of Engineering and Technology, 1998.

[52] L. Ying, L. Zhenqiang, X. Liang, and W. Lei, "Research on overvoltage and minimum air clearance on 1000 kV AC side of converter transformer in ±1100 kV Guquan converter station," *Journal of Engineering*, vol. 2019, no. 16, pp. 2159–2164, 2019.

[53] M. H. Rashid, "Power Electronics Handbook: Devices, Circuits, and Applications," 3rd ed., Jordan Hill, Oxford, UK: Elsevier, pp. 823–849, 2011.

[54] G. Migliavacca, *Advanced Technologies for Future Transmission Grids*, London: Springer, 2013.

[55] M. P. Bahrman, "HVDC transmission overview," *IEEE/PES Transmission and Distribution Conference and Exposition*, pp. 1–7, 2008.

[56] IEA, "Tracking Transport," 2019. [Online]. Available: https://www.iea.org/reports/tracking-transport-2019.

[57] ——, "4 Charts That Show Renewable Energy is on the Rise in America," 2016. [Online]. Available: https://www.energy.gov/eere/articles/4-charts-show-renewable-energy-rise-america.

[58] ——, "Solar," 2019. [Online]. Available: https://www.iea.org/fuels-and-technologies/solar.

[59] ——, "Global EV Outlook 2019, Scaling up the transition to electric mobility" 2019. [Online]. Available: https://www.iea.org/reports/global-ev-outlook-2019.

[60] IEA, "Largest end-uses of energy by sector in selected IEA countries," 2018. [Online]. Available: https://www.iea.org/data-and-statistics/charts/largest-end-uses-of-energy-by-sector-in-selected-iea-countries-2018.

[61] M. Anzar, S. Ejaz, R. Iqra, M. S. Alvarez-Alvarado, A. Kousar, and A. K. Zafar, "Optimization of Home Energy Management System in Smart Grid for Effective Demand Side Management," *International Renewable and Sustainable Energy Conference*, pp. 1-6, 2017.

[62] R. K. Chauhan, C. Phurailatpam, B. S. Rajpurohit, F. M. Gonzalez-Longatt, and S. N. Singh, "Demand-Side Management System for Autonomous DC Microgrid for Building," *Technology and Economics of Smart Grids and Sustainable Energy*, vol. 2, no. 1, pp. 1-6, 2017.

[63] D. L. Gerber, R. Lion, and R. Brown, "Energy-saving opportunities of direct-DC loads in buildings," *Applied Energy*, vol. 248, pp. 274-287, 2019.

[64] F. Luo, G. Ranzi, S. Wang, and Z. Y. Dong, "Hierarchical Energy Management System for Home Microgrids," *IEEE Transactions on Smart Grid*, vol. 10, no. 5, pp. 5536-5545, 2019.

[65] NERC, "Distributed Energy Resources: Connection Modeling and Reliability Considerations," 2017. [Online]. Available: https://www.nerc.com/comm/other/essntlrlbltysrvcstskfrcdl/distributed_energy_resources_report.pdf.

[66] N. W. Miller, M. Shao, S. Pajic, and R. D'Aquila, *Western Wind and Solar Integration Study Phase 3 –Frequency Response and Transient Stability*, 2014. NREL, No. KAGN-4-23474-01.

[67] U.S. Department of Energy, "Microgrid Definitions," 2019. [Online]. Available: https://building-microgrid.lbl.gov/microgrid-definitions.

[68] CIGRÉ, "Working Group C6.22 Terms of Reference," 2010.

[69] B. Nordman, "Nanogrids Evolving our electricity systems from the bottom up," *LBNL*, 2010.

[70] EMerge Alliance, "DC Power Distribution Systems," 2015.

[71] D. Becker and B. Sonnenberg, "DC microgrids in buildings and data centers," *IEEE 33rd International Telecommunications Energy Conference*, pp. 1–7, 2011.

[72] LBNL, "DC power distribution cuts data center energy use," 2014. [Online]. Available: http://hightech.lbl.gov/documents/data.centers/CEC-TB-40.PDF.

[73] D. Kintner and Duke Energy, "EPRI DC Powered Data Center Demonstration," *EPRI*, 2011.

[74] C. J. Daly, D. L. Moore, R. J. Haddad, A. Specht, and S. Neal, "PicoGrid Smart Home Energy Management System," *SoutheastCon 2018*, pp. 1–3, Apr. 2018, doi: 10.1109/SECON.2018.8479129.

[75] K. Garbesi, V. Vossos, W. Feng, C. Marnay, B. Nordman, and R. Brown, "Optimizing Energy Savings from Direct-DC in U.S. Residential Buildings," (No. LBNL-5193E), Lawrence Berkeley National Laboratory (LBNL), 2011.

[76] V. Webb, "Design of a 380 V/24 V DC micro-grid for residential DC distribution," dissertation, The University of Toledo, 2013.

[77] H. E. Gelani, F. Dastgeer, K. Siraj, M. Nasir, K. A. K. Niazi, and Y. Yang, "Efficiency Comparison of AC and DC Distribution Networks for Modern Residential Localitiesm" *Applied Sciences*, vol. 9, no. 3, p. 582, 2019.

[78] G. Raman, G. Raman, J. C. Peng, and W. Xiao, "Bridging the transition to DC distribution: A hybrid microgrid for residential apartments," *IEEE Innovative Smart Grid Technologies - Asia (ISGT-Asia)*, pp. 1–6, 2017.

[79] S. Moussa, M. J. Ghorbal, and I. Slama-Belkhodja, "DC voltage level choice in residential remote area," *2018 9th International Renewable Energy Congress (IREC)*, pp. 1–6, Mar. 2018 doi: 10.1109/IREC.2018.8362444.

[80] L. R. Jie and R. T. Naayagi, "Nanogrid for Energy Aware Buildings," *2019 IEEE PES GTD Grand International Conference and Exposition Asia (GTD Asia)*, pp. 92–96, Mar. 2019, doi: 10.1109/GTDAsia.2019.8715905.

[81] T. Taufik, "The DC House project: An alternate solution for rural electrification," *IEEE Global Humanitarian Technology Conference (GHTC 2014)*, pp. 174–179, Oct. 2014, doi: 10.1109/GHTC.2014.6970278.

[82] B. Nordman, "Nanogrids Evolving our electricity systems from the bottom up," *LBNL*, 2010.

[83] N. C. Sahoo, S. Mohapatro, A. K. Sahu, and B. S. Mohapatro, "Loss and cost evaluation of typical DC distribution for residential house," *2016 IEEE International Conference on Power and Energy (PECon)*, pp. 668–673, Nov. 2016, doi: 10.1109/PECON.2016.7951644.

[84] T. Shibata, K. Sakai, and Y. Okabe, "The Design and Implementation of an On-demand DC Grid in Home," *2011 IEEE/IPSJ International Symposium on Applications and the Internet*, pp. 152–159, Jul. 2011, doi: 10.1109/SAINT.2011.29.

[85] Y. Ji, E. Buechler, and R. Rajagopal, "Data-Driven Load Modeling and Forecasting of Residential Appliances," *IEEE Transactions on Smart Grid*, vol. 11, no. 3, pp. 2652–2661, May 2020, doi: 10.1109/TSG.2019.2959770.

[86] J. Pellis, "The DC Low-Voltage House," dissertation, Energy Center, The Netherlands, 1998.

[87] S. C. Joseph, A. A. Mohammed, P. R. Dhanesh, and S. Ashok, "Smart Power Management for DC Nanogrid Based Building," *2018 IEEE Recent Advances in Intelligent Computational Systems (RAICS)*, pp. 142–146, Dec. 2018.

[88] C. B. Rasmussen and E. Ritchie, "Variable Speed Brushless DC Motor Drive for Household Refrigerator Compressor," *Eighth International Conference on Electrical Machines and Drives*, pp. 128–132, 1997.

[89] G. Ciampi, A. Rosato, M. Scorpio, and S. Sibilio, "Retrofitting Solutions for Energy Saving in a Historical Building Lighting System," *Energy Procedia*, vol. 78, pp. 2669–2674, Nov. 2015, doi: 10.1016/j.egypro.2015.11.343.

[90] A. M. Iuoras, N. C. Szekely, L. D. Vitan, M. Bojan, and P. D. Teodosescu, "AC home appliances retrofiting for DC microgrids," *2020 12th International Conference on Electronics, Computers and Artificial Intelligence (ECAI)*, pp. 1–6, Jun. 2020, doi: 10.1109/ECAI50035.2020.9223183.

[91] Ó. Lucía, I. Cvetkovic, H. Sarnago, D. Boroyevich, P. Mattavelli, and F. C. Lee, "Design of Home Appliances for a DC-Based Nanogrid System: An Induction Range Study Case," *IEEE Journal of Emerging and Selected Topics in Power Electronics*, vol. 1, no. 4, pp. 315–326, Dec. 2013, doi: 10.1109/JESTPE.2013.2283224.

[92] G. Makarabbi, V. Gavade, R. Panguloori, and P. Mishra, "Compatibility and performance study of home appliances in a DC home distribution system," *2014 IEEE International Conference on Power Electronics, Drives and Energy Systems (PEDES)*, pp. 1–6, Dec. 2014, doi: 10.1109/PEDES.2014.7042151.

[93] T. J. C. Sousa, V. Monteiro, J. S. Martins, M. J. Sepúlveda, A. Lima, and J. L. Afonso, "Comparative Analysis of Power Electronics Topologies to Interface dc Homes with the Electrical ac Power Grid," *2019 International Conference on Smart Energy Systems and Technologies (SEST)*, pp. 1–6, Sep. 2019, doi: 10.1109/SEST.2019.8849046.

[94] A. Bracale, P. Caramia, G. Carpinelli, E. Mancini, and F. Mottola, "Optimal control strategy of a DC micro grid," *International Journal of Electrical Power & Energy Systems*, vol. 67, pp. 25–38, May 2015, doi: 10.1016/j.ijepes.2014.11.003.

[95] Y. Hakuto, T. Tsuji, and J. Qi, "Autonomous decentralized stabilizing control of DC microgrid," *2017 IEEE Second International Conference on DC Microgrids (ICDCM)*, pp. 292–296, Jun. 2017, doi: 10.1109/ICDCM.2017.8001059.

[96] L. E. Zubieta, "Power management and optimization concept for DC microgrids," *2015 IEEE First International Conference on DC Microgrids (ICDCM)*, pp. 81–85, Jun. 2015, doi: 10.1109/ICDCM.2015.7152014.

[97] K. Friansa, I. N. Haq, B. M. Santi, D. Kurniadi, E. Leksono, and B. Yuliarto, "Development of Battery Monitoring System in Smart Microgrid Based on Internet of Things (IoT)," *Procedia Engineering*, vol. 170, pp. 482–487, Jan. 2017, doi: 10.1016/j.proeng.2017.03.077.

[98] S. C. Joseph, V. Chandrasekar, P. R. Dhanesh, A. A. Mohammed, and S. Ashok, "Battery Management System for DC Nanogrid," *2018 20th National Power Systems Conference (NPSC)*, pp. 1–5, Dec. 2018, doi: 10.1109/NPSC.2018.8771838.

[99] C. Lebrón, F. Andrade, E. O'Neill, and A. Irizarry, "An intelligent Battery management system for home Microgrids," *2016 IEEE Power Energy Society Innovative Smart Grid Technologies Conference (ISGT)*, pp. 1–5, Sep. 2016.

[100] E.-K. Lee, W. Shi, R. Gadh, and W. Kim, "Design and Implementation of a Microgrid Energy Management System," *Sustainability*, vol. 8, no. 11, Art. no. 11, Nov. 2016, doi: 10.3390/su8111143.

[101] E. Rodriguez-Diaz, J. C. Vasquez, and J. M. Guerrero, "Potential energy savings by using direct current for residential applications: A Danish household study case," *IEEE Second International Conference on DC Microgrids (ICDCM)*, pp. 547–552, 2017.

[102] K. E. Thorvaldsen, S. Bjarghov, and H. Farahmand, "Representing Long-term Impact of Residential Building Energy Management using Stochastic Dynamic Programming," *2020 International Conference on Probabilistic Methods Applied to Power Systems (PMAPS)*, pp. 1–7, Aug. 2020, doi:10.1109/PMAPS47429.2020.9183623.

[103] J. Yue, Z. Hu, C. Li, J. C. Vasquez, and J. M. Guerrero, "Optimization scheduling in intelligent Energy Management System for the DC residential distribution system," *2017 IEEE Second International Conference on DC Microgrids (ICDCM)*, pp. 558–563, Jun. 2017, doi: 10.1109/ICDCM.2017.8001102.

[104] C. Zhou, S. Liu, and P. Liu, "Neural Network Pattern Recognition Based Non-intrusive Load Monitoring for a Residential Energy Management System," *2016 3rd International Conference on Information Science and Control Engineering (ICISCE)*, pp. 483–487, Jul. 2016, doi: 10.1109/ICISCE.2016.110.

[105] K. Keller, "Electrical Safety Code Manual," Kidlington, Oxford, UK: Elsevier, 2010.

[106] DOE, "Weatherize: Insulation," 2020. [Online]. Available: https://www.energy.gov/energysaver/weatherize/insulation.

[107] Lowes, "Energy Efficiency: Glass Options,", 2020. [Online]. Available: https://www.pella.com/features-options/energy-efficiency/.

[108] ENERGY STAR, "Benefits of ENERGY STAR Qualified Windows, Doors, and Skylights," 2020. [Online]. Available: https://www.energystar.gov/products/building_products/residential_windows_d-oors_and_skylights/benefits.

[109] Efficient Windows, "Frequently Asked Questions (FAQ)," 2020. [Online]. Available: https://www.efficientwindows.org/faq.php.

[110] Eaton, "Energy Management Circuit Breaker," 2020. [Online]. Available: https://www.eaton.com/us/en-us/markets/innovation-stories/energy-management-circuit-breaker.html.

[111] *Molded-Case Circuit Breakers, Molded-Case Switches, and Circuit-Breaker Enclosures*, UL 489, 2019.

[112] TED, "TED Pro Home - complete system," 2020. [Online]. Available: https://www.theenergydetective.com/tedprohome.html.

[113] Yokogawa, "Data Acquisition System GM: General Specifications," 2020. [Online]. Available: https://web-material3.yokogawa.com/GS04L55B01-01EN.pdf.

[114] T. Hong, W.-K. Chang, and H.-W. Lin, "A fresh look at weather impact on peak electricity demand and energy use of buildings using 30-year actual weather data," *Applied Energy*, vol. 111, pp. 333–350, Nov. 2013, doi: 10.1016/j.apenergy.2013.05.019.

[115] I. Staffell and S. Pfenninger, "The increasing impact of weather on electricity supply and demand," *Energy*, vol. 145, pp. 65–78, Feb. 2018, doi: 10.1016/j.energy.2017.12.051.

[116] D. Jose, M. Mathew, and A. Krishnan, "Weather dependency of electricity demand: A case study in warm humid tropical climate," *2016 3rd International Conference on Electrical Energy Systems (ICEES)*, pp. 102–105, Mar. 2016.

[117] F. Nhita and K. Adiwijaya, "A rainfall forecasting using fuzzy system based on genetic algorithm,", pp. 111–115, Mar. 2013, doi: 10.1109/ICoICT.2013.6574557.

[118] S. L. Caskey, D. Kultgen, E. A. Groll, W. Hutzel, and T. Menzi, "Simulation of an Air-Source Heat Pump with Two-Stage Compression and Economizing for Cold Climates," *International Refrigeration and Air Conditioning Conference*, 2012.

[119] J. Proctor, "Field Measurements of New Residential Air Conditioners in Phoenix, Arizona," *ASHRAE Transactions*, vol. 103, pp. 406–416, 1997.

[120] ANSI/ASHRAE Standard 62-1989, "Ventilation for acceptable indoor air quality," 1989.

[121] S. L. Caskey and E. A. Groll, "Hybrid air-hydronic HVAC performance in a residential net-zero energy retrofit," *Energy and Buildings*, vol. 158, pp. 342–355, 2017.

[122] ASHRAE, "ASHRAE Handbook of Fundamentals," 2017.

[123] National Park Service, U.S. Department of the Interior, "National Register of Historic Places," 2020. [Online]. Available: https://npgallery.nps.gov/NRHP.

[124] "TM 41 Degree-days: theory and application, Chartered Institution of Building Services Engineers - Publication Index | NBS." https://www.thenbs.com/PublicationIndex/documents/details?Pub=CIBSE&DocID=280950.

[125] Z. J. Zhai and J. M. Helman, "Climate change: Projections and implications to building energy use," *Build. Simul.*, vol. 12, no. 4, pp. 585–596, Aug. 2019, doi: 10.1007/s12273-019-0509-5.

[126] I. Cooper, "Adapting to the impact of climate change on buildings, neighborhoods and cities," 2010. [Online]. Available: http://www.eclipseresearch.co.uk/download/sustainability_climate_change/Adapting%20to%20the%20impact%20of%20climate.pdf.

[127] Y. Parshina-Kottas, K. Patanjali, J. White, B. Wilhelm, and E. Grothjan, "A Closer Look at the Polar Vortex's Dangerously Cold Winds," The New York Times, Jan. 30, 2019.

[128] H. Kakigano, M. Nomura, and T. Ise, "Loss evaluation of DC distribution for residential houses compared with AC system," *The 2010 International Power Electronics Conference - ECCE ASIA -*, pp. 480–486, Jun. 2010, doi: 10.1109/IPEC.2010.5543501.

[129] V. Baxter, K. Sikes, R. Domitrovic, and K. Amrane, "IEA HPP Annex 42: Heat Pumps in Smart Grids. Task 1: Market Overview," ORNL/TM-2014/73, 2014.

[130] P. Krause, O. Wasynczuk, S. Sudhoff, and S. Pekarek, "Analysis of Electric Machinery and Drive Systems, 3rd Edition," John Wiley & Sons, Inc: Hoboken, NK, 2013.

[131] S. Klein, "Engineering Equation Solver," *F-Chart Software*, v.10.268, 2018.

[132] ASHRAE, "Methods of Testing for Rating Electrically Driven Unitary Air-Conditioning and Heat Pump Equipment," ASHRAE Standard 37, 2009.

[133] AHRI, "Performance Rating of Unitary Air-conditioning & Air-source Heat Pump Equipment," AHRI Standard 210/240, 2017.

[134] W. Yu, J. S. Lai, H. Ma, and C. Zheng, "High-efficiency DC–DC converter with twin bus for dimmable LED lighting," *IEEE Transactions on Power Electronics*, vol. 26, pp. 2095–2100, 2011.

[135] C. H. Tsai, Y. W. Bai, M. B. Lin, R. J. R. Jhang, and C. Y. Chung, "Reduce the standby power consumption of a microwave oven," *IEEE Transactions on Consumer Electronic*, vol. 59, pp. 54–61, 2013.

[136] P. Fairley, "DC versus AC: the second war of currents has already begun [in my view]," *IEEE Power and Energy Magazine*, vol. 10, pp. 103–104, 2012.

[137] D. Black, "Microgrids and Vehicle-Grid Integration," 2021. [Online]. Available: https://gridintegration.lbl.gov/microgrids-vehicle-grid-integration.

[138] IEA, "World Energy Outlook", 2020. [Online]. Available: https://www.iea.org/reports/world-energy-outlook-2020.

[139] IEA, "Renewables", 2020. [Online]. Available: https://www.iea.org/reports/renewables-2020.

[140] SEIA, "Solar Market Insight Report 2020 Q4," 2020. [Online]. Available: https://www.seia.org/about-solar-market-insight-report.

[141] C. Wang and P. Jain, "A quantitative comparison and evaluation of 48V DC and 380V DC distribution systems for datacenters," *2014 IEEE 36th International Telecommunications Energy Conference (INTELEC)*, pp. 1-7, 2010.

[142] CE+T, "ECI: the Future of Power Conversion," 2021. [Online]. Available: https://cet-energrid.com/enhanced-conversion-innovation-eci/.

[143] R. Atia and N. Yamada, "Sizing and Analysis of Renewable Energy and Battery Systems in Residential Microgrids," *IEEE Trasnactions on smart grids*, vol. 7, no. 3, pp. 1204–1213, 2016.

[144] HelioScope, "The new standard in solar design software," 2020. [Online]. Available: https://www.helioscope.com/..

[145] "The Authoritative Dictionary of IEEE Standards Terms, Seventh Edition," *IEEE Std 100-2000*, pp. 1–1362, Dec. 2000, doi: 10.1109/IEEESTD.2000.322230.

[146] H. Zimmerman, "OSI Reference Model-The IS0 Model of Architecture for Open Systems Interconnection," *IEEE Transactions on Communications*, vol. 28, no. 4, pp. 425-432, 1980.

[147] F. Leens, "An Introduction to I2C and SPI Protocols," *IEEE Instrumentation and Measurement Systems*, vol. 12, no. 1, pp. 8–13, 2009.

[148] T. L. Dickey, C. L. McCrank, J. I. Masters, D. M. Markuson, and M. S. Evans, *United States Patent No. US 9980277B2*, 2018.

[149] M. Albano, L. L. Ferreira, L. M. Pinho, and A. R. Alkhawaja, "Message-oriented Middleware for Smart Grids," *Computer Standards and Interfaces*, vol. 38, pp. 133–143, 2015.

[150] G. C. Hillar, *MQTT Essentials – A Lightweight IoT Protocol*, Birmingham, UK: Packt Publishing, 2017.

[151] ScalAgent, "Benchmark of MQTT servers," 2015. [Online]. Available: http://www.scalagent.com/IMG/pdf/Benchmark_MQTT_servers-v1-1.pdf..

[152] IEEE802.3af, *IEEE Standard for Information Technology - Telecommunications and Information Exchange Between Systems*, 2003.

[153] IEEE802.3bt, *IEEE Standard for Ethernet Amendment 2: Physical Layer and Management Parameters for Power over Ethernet over 4 pairs.*, 2018.

[154] IEEE802.3at, *IEEE Standard for Information technology - Local and metropolitan area networks.*, 2009.

[155] National Instruments, "Data Acquisition (DAQ)," 2021. [Online]. Available: https://www.ni.com/en-us/shop/data-acquisition.html.

[156] Texas Instruments, "CD74HC4067," 2021. [Online]. Available: https://www.ti.com/lit/ds/symlink/cd74hc4067.pdf.

[157] Microchip, "MCP3008," 2021. [Online]. Available: https://www.microchip.com/wwwproducts/en/en010530.

[158] Digi-Key, "Product Index," 2021. [Online]. Available: https://www.digikey.com/en/products.

[159] Safety of machinery - Functional safety of safety-related electrical, electronic and programmable electronic control systems: international standard IEC 62061, ed. 1.0, Geneva: IEC, 2005.

[160] S. Sattel, "What Are Decoupling Capacitors?" 2021. [Online]. Available: https://www.autodesk.com/products/eagle/blog/what-are-decoupling-capacitors/.

[161] Texas Instruments, "CD74HC4067," 2021. [Online]. Available: https://www.ti.com/lit/ds/symlink/sn74hc14.pdf.

[162] P. Scherz and S. Monk, *Practical Electronics for Inventors*, 4th ed. McGraw Hill Professional, 2016.

[163] Q. Kong, T. Siauw, and A. Bayen, *Python Programming and Numerical Methods*, 1st ed. London: Elsevier, 2021.

[164] P. Virtanen, R. Gommers, T. E. Oliphant, M. Haberland, T. Reddy, D. Cournapeau, E. Burovski, P. Peterson, W. Weckesser, J. Bright, S. J. van der Walt, M. Brett, J. Wilson, K. J. Millman, N. Mayorov, A. R. J. Nelson, E. Jones, R. Kern, E. Larson, C. J. Carey, İ. Polat, Y. Feng, E. W. Moore, J. VanderPlas, D. Laxalde, J. Perktold, R. Cimrman, I. Henriksen, E. A. Quintero, C. R. Harris, A. M. Archibald, A. H. Ribeiro, F. Pedregosa, P. van Mulbregt, and SciPy 1.0 Contributors, "SciPy 1.0: Fundamental Algorithms for Scientific Computing in Python," *Nature Methods*, vol. 17, pp. 261–272, 2020.

[165] Docker, "What is a Container? A standardized unit of software," 2021. [Online]. Available: https://www.docker.com/resources/what-container.

[166] J. A. Tainter, *The collapse of Complex Societies*. Cambridge University Press, 1988.

[167] "Phasor Diagrams and Phasor Algebra," 2019. [Online]. Available: https://www.electronics-tutorials.ws/accircuits/phasors.html.

A. PHASOR ANALYSIS METHODOLOGY

Phasors, otherwise known as a rotating vector, is a concept frequently used in AC analysis to represent complex quantities. A phasor, much like a vector, has both a *magnitude* and *direction*, which is typically represented using a phasor diagram, such as that in Figure A.1. In the case of an AC signal, voltage and current components are analyzed separately to determine their respective lead/lag relationship. To determine the voltage and current phasors, consider the voltage and current sinusoids in Figure A.2. As illustrated in the figure, the difference in phase between the voltage and current is 30°. Mathematical quantities representing the time-varying quantities and the relationship to the phase difference are indicated in Equations A.1 and A.2.

$$V(t) = V_m sin(\omega t) \tag{A.1}$$

$$V(t) = I_m sin(\omega t - \phi) \tag{A.2}$$

where ϕ represents the phase difference. In this case, the current is said to *lag* the voltage by the angle ϕ, or synonymously, the voltage is said to *lead* the current by the angle ϕ. This relationship can be represented by a phasor diagram, as indicated in Figure A.3.

With the convenient phasor quantities established, algebraic operations suddion as the addition and subtraction of two phasors is readily possible. The complex sinusoids can be rewritten in the general form given by Equation A.3.

$$v = V_m cos(\phi) + jV_m sin(\phi) \tag{A.3}$$

In this case, adding two phasors in the complex form given by Equation A.3 can be achieved as shown in Equations A.4, A.5, and A.6.

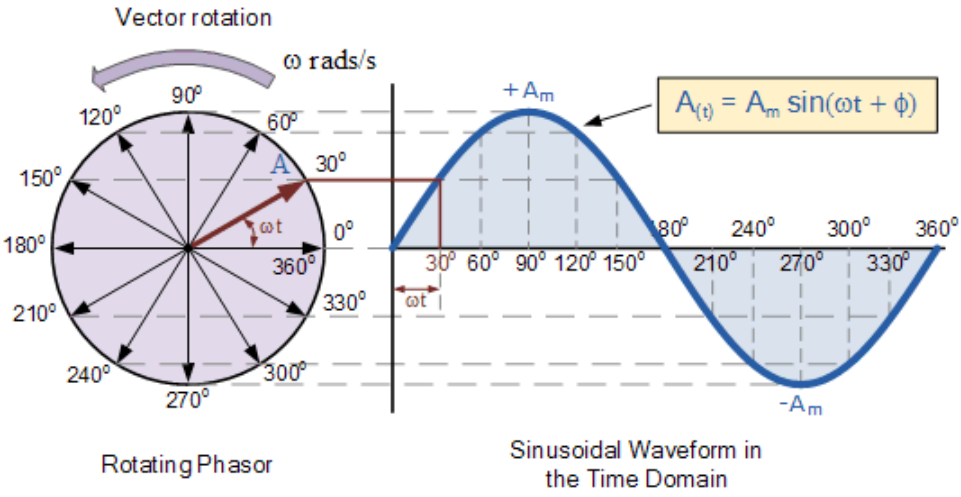

Figure A.1. Phasor Diagram of a Sinusoidal Waveform [167].

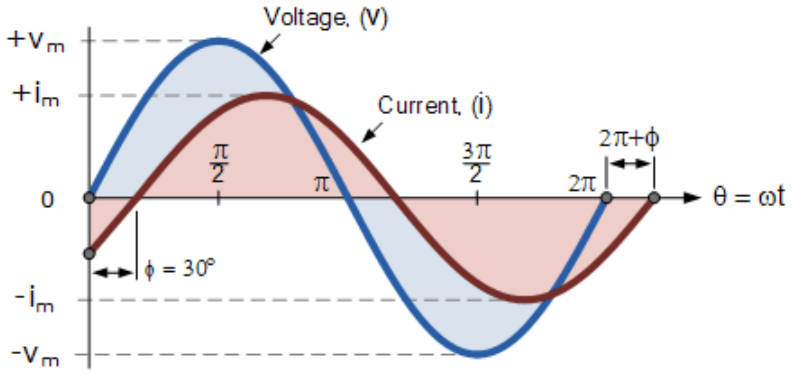

Figure A.2. Voltage and Current Sinusoidal Waveforms [167].

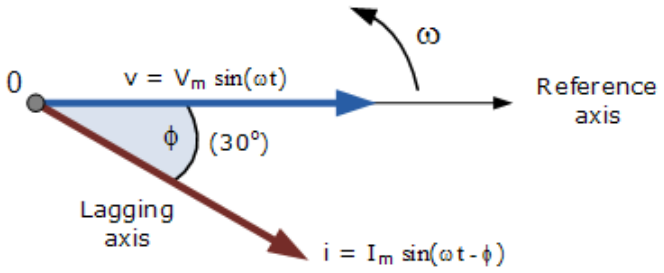

Figure A.3. Voltage and Current Phasor Diagram [167].

$$v_A = V_A sin(\theta) + jV_A cos(\theta) \tag{A.4}$$

$$v_B = V_B sin(\delta) + jV_B cos(\delta) \tag{A.5}$$

$$v_R = v_A + v_B = [V_A sin(\theta) + V_B sin(\delta)] + j[V_A cos(\theta) + V_B cos(\delta)] \tag{A.6}$$

B. MQTT COMMUNICATION PROCESS

```
static WiFiClient espClient;
static PubSubClient client(espClient);
static int maxConnectionAttempts = 3;
static int msecBetweenAttempts = 500;

bool EstablishMQTTConnection() {
    // Specify connection parameters
    client.setServer(Config::MQTT_SERVER_IP, Config::MQTT_SERVER_PORT);
    client.setSocketTimeout(msecBetweenAttempts);

    // Attempt to create connection
    int connectionAttempts = 0;
  bool isConnecting = client.connect(ObtainMACAddressString().c_str());
    while((!isConnecting) && (connectionAttempts < maxConnectionAttempts)) {
        isConnecting = client.connect(ObtainMACAddressString().c_str());
        connectionAttempts += 1;
    }

    bool isConnected = client.connected();
    LogDebugData(String("MQTT Connection Status: " + PubSubStateToString(client.state())).c_str()
        );
    return isConnected;
}

String PubSubStateToString(int state) {
    switch (state) {
        case -4: return "MQTT_CONNECTION_TIMEOUT";
        case -3: return "MQTT_CONNECTION_LOST";
        case -2: return "MQTT_CONNECT_FAILED";
        case -1: return "MQTT_DISCONNECTED";
        case 0: return "MQTT_CONNECTED";
        case 1: return "MQTT_CONNECT_BAD_PROTOCOL";
        case 2: return "MQTT_CONNECT_BAD_CLIENT_ID";
        case 3: return "MQTT_CONNECT_UNAVAILABLE";
        case 4: return "MQTT_CONNECT_BAD_CREDENTIALS";
        case 5: return "MQTT_CONNECT_UNAUTHORIZED";
        default: return "";
    }
}

void RecordData(String dataName, String payloadData, String payloadUnits, bool isMQTTConnected) {
    LogSensorData(dataName, payloadData, payloadUnits);
    if(isMQTTConnected) { PublishData(String(dataName + "," + payloadUnits), payloadData); }
```

```
}

void PublishData(String topicName, String topicPayload) {
    bool isPublishSuccessful = client.publish(String(ObtainMACAddressString() + "/" + topicName).
        c_str(), topicPayload.c_str());

    if (!isPublishSuccessful) {
        LogDebugData("Publishing unsuccessful, trying again");
        delay(msecBetweenAttempts);
        isPublishSuccessful = client.publish(String(ObtainMACAddressString() + "/" + topicName).
            c_str(), topicPayload.c_str());
    }

    if(!isPublishSuccessful) { LogDebugData("Publishing failed"); }
}
```

VITA

Jonathan Ore received three Bachelor of Science degrees in Mathematics, Physics, and Electrical Engineering from Penn State University in 2012, and a Master of Science in Engineering at Purdue University in 2015. Since this time he has pursued a doctoral degree in the school of Mechanical Engineering at Purdue University in the Thermal Science research discipline. After completing his undergraduate education, Jonathan has been continuously employed in a variety of engineering roles beginning as a System Engineer at Westinghouse Electric Company in 2012, then as a Lead Systems Engineer at Meggitt Aircraft Braking Systems in 2014, next as a Staff Electrical Engineer at The Goodyear Tire and Rubber Company in 2016, and presently as a Simulation Model Implementation Engineer at Emerson Automation Solutions as of 2021. He is also engaged in the field of renewable energy and smart-grid/microgrid development, serving as the co-chair on the EMerge Alliance's Residential Nanogrid Technical Standards Committee.